

General Disclaimer

One or more of the Following Statements may affect this Document

- This document has been reproduced from the best copy furnished by the organizational source. It is being released in the interest of making available as much information as possible.
- This document may contain data, which exceeds the sheet parameters. It was furnished in this condition by the organizational source and is the best copy available.
- This document may contain tone-on-tone or color graphs, charts and/or pictures, which have been reproduced in black and white.
- This document is paginated as submitted by the original source.
- Portions of this document are not fully legible due to the historical nature of some of the material. However, it is the best reproduction available from the original submission.

Further Seasat SAR Coastal Ocean Wave Analysis

Environmental Research Inst. of Michigan
Ann Arbor

Prepared for

National Aeronautics and Space Administration
Washington, DC

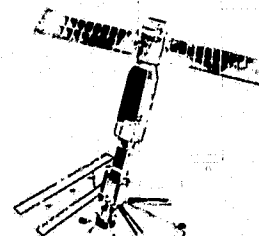
Sep 81

U.S. Department of Commerce
National Technical Information Service

NTIS

82052402

PB82-230350



138600-6-F

Final Report

FURTHER SEASAT SAR COASTAL OCEAN WAVE ANALYSIS

SEPTEMBER 1981

E.S. KASISCHKE
R.A. SHUCHMAN
G.A. MEADOWS
P.L. JACKSON
Y. TSENG
J.D. LYDEN
Radar and Optics Division

Contract No. MO-A01-78-00-4339
U. S. Department of Commerce
NOAA/NESS/SPOC Group S3X1
5200 Auth Road
Camp Springs, MD 20023

National Aeronautics and Space Administration
NASA Headquarter/OSTA-EB
600 Independence Avenue
Washington D. C. 20546

REPRODUCED BY
NATIONAL TECHNICAL
INFORMATION SERVICE
U.S. DEPARTMENT OF COMMERCE
SPRINGFIELD, VA. 22161

ENVIRONMENTAL
RESEARCH INSTITUTE OF MICHIGAN
BOX 8618 • ANN ARBOR • MICHIGAN 48107

NOAA FORM 25-13 (1-78)		BIBLIOGRAPHIC DATA SHEET		U. S. DEPARTMENT OF COMMERCE NATIONAL OCEANIC AND ATMOSPHERIC ADMINISTRATION	
1. NOAA ACCESSION NUMBER NOAA-82052402		2.		3. RECIPIENT'S ACCESSION NUMBER PDB2 230350	
4. TITLE AND SUBTITLE Further Seasat SAR Coastal Ocean Wave Analysis				5. REPORT DATE Sept 1981	
				6.	
7. AUTHOR(S) E.S. Kasischke, R.A. Shuchman, G.A. Meadows, P.L. Jackson, Y. Tseng and J.D. Lyden				8. REPORT NO. ERIM-138600-6-F	
9. PERFORMING ORGANIZATION NAME AND ADDRESS Environmental Research Institute of Michigan, Ann Arbor 48107, Radar and Optics Division				10. PROJECT/TASK NO.	
				11. CONTRACT/GRANT NO. MO-A01-78-00-4339	
12. SPONSORING ORGANIZATION NAME AND ADDRESS NOAA, National Earth Satellite Service, Camp Springs, MD 20023, SPOC Group S3X1; and National Aeronautics and Space Adm., Washington, DC 20546				13. TYPE OF REPORT AND PERIOD COVERED Final Rept. March 1980 - Sept 1981	
				14.	
15. PUBLICATION REFERENCE Environmental Research Institute of Michigan Final Report to NOAA/NESS No. 138600-6-F, September 1981. 192 p, 61 fig, 13 tab, 31 ref, 5 append.					
16. ABSTRACT Analysis techniques used to exploit Seasat Synthetic Aperture Radar (SAR) data of gravity waves are discussed and the Seasat SAR's ability to monitor large scale variations in gravity wave fields in both deep and shallow water is evaluated. SAR analysis techniques investigated included motion compensation adjustments and the semicausal model for spectral analysis of SAR wave data. From these studies, it was determined that spectra generated from fast Fourier transform analysis (FFT) of SAR wave data were not significantly altered when either range telerotation adjustments or azimuth focus shifts were used during processing of the SAR signal histories, indicating that Seasat imagery of gravity waves is not significantly improved or degraded by motion compensation adjustments. Evaluations of the semicausal (SC) model using Seasat SAR data from Rev. 974 indicates that the SC spectral estimates were not significantly better than the FFT results. Using a synthetically generated wave field with varying levels of background noise, the SC model produced more accurate spectral estimates than the FFT technique. Finally, it was determined that FFTs can be used to discriminate between two wave trains present in the same area if they are greater than					
17. KEY WORDS AND DOCUMENT ANALYSIS 20° apart. (Author modified)					
17A. DESCRIPTORS *Ocean waves, *Oceanographic data, Refraction, Optics, Synthetic aperture radar					
17B. IDENTIFIERS/OPEN-ENDED TERMS Seasat, Gravity waves, Fast Fourier Transforms (FFT)					
17C. COSATI FIELD/GROUP 8J					
18. AVAILABILITY STATEMENT Released for distribution: <i>Elaine S. Downs</i>				19. SECURITY CLASS (This report) UNCLASSIFIED	
				20. SECURITY CLASS (This report) UNCLASSIFIED	
				21. NO. OF PAGES 193 p.	
				22. PRICE	

TECHNICAL REPORT STANDARD TITLE PAGE

1. Report No.	2. Government Accession No.	3. Recipient's Catalog No.	
4. Title and Subtitle Further Seasat SAR Coastal Ocean Wave Analysis		5. Report Date September 1981	
		6. Performing Organization Code	
7. Author(s) E.S. Kasischke, R.A. Shuchman, G.A. Meadows, P.L. Jackson, Y. Tseng, J.D. Lyden		8. Performing Organization Report No. 138600-6-F	
9. Performing Organization Name and Address Environmental Research Institute of Michigan Radar and Optics Division P. O. Box 8618 Ann Arbor, Michigan 48107		10. Work Unit No.	
		11. Contract or Grant No. MO-A01-78-00-4339	
		13. Type of Report and Period Covered Final Report March 1980 through September 1981	
12. Sponsoring Agency Name and Address U. S. Department of Commerce NOAA/NESS/SPOC Group S3X1 5200 Auth Road Camp Springs, Maryland 20023		14. Sponsoring Agency Code	
15. Supplementary Notes The technical monitors for this report were Messrs. John W. Sherman, III and Patrick Deleonibus.			
16. Abstract This report discusses analysis techniques used to exploit Seasat Synthetic Aperture Radar (SAR) data of gravity waves and evaluates the Seasat SAR's ability to monitor large scale variations in gravity wave fields in both deep and shallow water. SAR analysis techniques investigated included motion compensation adjustments and the semicausal model for spectral analysis of SAR wave data. From these studies, it was determined that spectra generated from fast Fourier transform analysis (FFT) of SAR wave data were not significantly altered when either range telerotation adjustments or azimuth focus shifts were used during processing of the SAR signal histories, indicating that Seasat imagery of gravity waves is not significantly improved or degraded by motion compensation adjustments. Evaluations of the semicausal (SC) model using Seasat SAR data from Rev. 974 indicates that the SC spectral estimates were not significantly better than the FFT results. Using a synthetically generated wave field with varying levels of background noise, the SC model produced more accurate spectral estimates than the FFT technique. Finally, it was determined that FFTs can be used to discriminate between two wave trains present in the same area if they are greater than 20° apart. Using optical Fourier transforms (OFTs) from over 100 positions in deep water regions, transformations of the deep water gravity wave field were studied. The sources causing these variations were identified as the source of the gravity wave field (Hurricane Ella) and an interaction between gravity			
17. Key Words Oceanography Seasat Synthetic Aperture Radar Gravity Waves Fast Fourier Transforms (OVER)		18. Distribution Statement (OVER) Distribution of this report is unlimited.	
19. Security Classif. (of this report) Unclassified	20. Security Classif. (of this page) Unclassified	21. No. of Pages xv + 200	22. Price

16. Abstract (concluded)

waves and the Gulf Stream current. Seasat SAR data was used to hindcast the position of Hurricane Ella to within ± 50 kms and also was used to map the position and velocity profile of the Gulf Stream. Two shallow water bathymetric refraction models were run and wavelengths predicted from these models compared favorably to the SAR-observed values.

17. Key Words (concluded)

Optical Fourier Transforms
Image Enhancement
Currents
Wave Refraction
Semicausal Model

PREFACE

The work described in this report was conducted by the Radar and Optics Division of the Environmental Research Institute of Michigan (ERIM). This work was jointly supported by the National Oceanic and Atmospheric Administration (NOAA) and the National Aeronautics and Space Administration (NASA) as a part of the Seasat Announcement of Opportunity Program under Contract No. MO-A01-78-00-4339. The technical monitors for this contract were John W. Sherman III and Patrick Deleonibus of NOAA.

The Principal Investigator for this project was Robert A. Shuchman. Eric S. Kasischke contributed the sections on shallow water wave refraction, image enhancement of Seasat SAR data and comparison of the semicausal model to other data reduction routines. Philip Jackson contributed the sections on the semicausal model. James D. Lyden performed all the computer analysis for this project and contributed the section on discriminating two wave trains through fast Fourier Transform spectral analysis. Guy A. Meadows and Y. Tseng contributed the section on wave/current interactions.

ACKNOWLEDGMENTS

This study would not have been possible without the cooperation and efforts of many people. It is a pleasure to acknowledge the help of the following individuals: A. Klooster and J. Losee of ERIM generated digital SAR data for the study; R. Shounia of ERIM generated all the optical Fourier transforms; Vincent J. Cardone of Ocean Weather, Inc. and Duncan Ross of NOAA's Sea-Air Interaction Laboratory provided their expertise on hurricane Ella; Benjamin Holt of the Jet Propulsion Laboratory provided Seasat SAR data from Rev. 974; D. Lodge of the Royal Air Force Establishment and the European Space Agency (ESA) provided the use of Seasat SAR data collected during the JASIN experiment; and James Hammack of the Defense Mapping Agency, Hydrographic Center provided information and bathymetric charts for the test sites.

It should be noted that the algorithms used to analyze the SAR wave data discussed in Chapter 3 of this report were partially developed under Office of Naval Research sponsorship. The ONR-developed algorithms include: optical and digital slant-to-ground range conversion, wave focusing corrections, and the optical and digital spectral estimation programs. The ONR Contract Number is N00014-76-C-1048 and is monitored by Mr. Hans Dolezalek.

Finally, thanks go to D. Lyzenga, R. Larson, and R. Mitchel of ERIM for reviewing the technical contents of this report, to D. Clarke and L. Walls for typing the manuscript and to B. Termatt and K. Newstead for preparing the figures.

TABLE OF CONTENTS

PREFACE	iii
ACKNOWLEDGMENTS	v
LIST OF FIGURES	ix
LIST OF TABLES	xiii
1. INTRODUCTION	1
2. SUMMARY	3
3. IMAGE ENHANCEMENT AND DIGITAL SPECTRAL ANALYSIS TECHNIQUES FOR SAR OCEAN WAVE DATA	5
3.1 Motion Compensation Adjustments and their Effects on Spectral Estimates	5
3.1.1 Background and Theory	6
3.1.2 Experiment	8
3.1.3 Results	14
3.2 Generation of Spectral Estimates from Seasat SAR Data	29
3.2.1 Background	29
3.2.2 Comparison Data Base	31
3.2.3 Effects of Sampling Rate and Aperture Size on Semicausal Estimates	38
3.2.4 Effects of Noise on Semicausal Spectral Estimates	52
3.3 Multiple Wave Train Discrimination	55
3.4 Summary	67
4. WAVE REFRACTION STUDIES	69
4.1 Background	71
4.2 Methodology	72
4.2.1 Data Description	76
4.3 Analysis of Deep Water Wave Transformations	83
4.3.1 Wave/Current Interaction Theory	86
4.3.2 Data Analysis	93
4.3.3 Calculation of the Seasat SAR Inferred Current Field	109
4.4 Shallow Water Analysis	113
4.5 Discussion	131
5. RECOMMENDATIONS FOR ADDITIONAL INVESTIGATIONS	135
REFERENCES	137
APPENDIX A: "HIGH RESOLUTION SPECTRAL ESTIMATION OF SAR OCEAN WAVE IMAGERY"	A-1

TABLE OF CONTENTS
(Concluded)

APPENDIX B:	AN ASSESSMENT OF JPL DIGITALLY PROCESSED SEASAT SAR DATA FROM REV. 974	B-1
APPENDIX C:	FURTHER SEMICAUSAL VERSUS FAST FOURIER TRANSFORM COMPARISONS	C-1
APPENDIX D:	PRECISION AND ACCURACY OF OPTICAL FOURIER TRANSFORMS	D-1
APPENDIX E:	WAVE/CURRENT INTERACTION ANALYTICAL DEVELOPMENT	E-1

LIST OF FIGURES

1. Seasat SAR Image of Range Traveling Ocean Gravity Waves and Its Resultant Two-dimensional Fourier Transforms	10
2. Examples of Computer-generated Two-dimensional and One-dimensional Wave Spectra from Seasat SAR Data	13
3. Seasat SAR Imagery of Azimuth Traveling Waves Collected During Rev. 1087, 11 September 1978	15
4. Peak-to-Background Ratio Versus Telerotation Adjustment, Seasat Rev. 762	17
5. Two-dimensional Fast Fourier Transforms of Seasat SAR Wave Data Using Variable Telerotation Settings	20
6. One-dimensional Wave Number Spectra Using Variable Telerotation Settings	21
7. One-dimensional Wave Direction Spectra Using Variable Telerotation Settings	22
8. Peak-to-Background Ratio Versus Azimuth Focus Shift, Seasat Rev. 1087	24
9. Two-dimensional Fast Fourier Transforms of Seasat SAR Data Using Variable Azimuth Focus Shifts	26
10. One-dimensional Wave Number Spectra Using Variable Azimuth Focus Shifts	27
11. One-dimensional Wave Direction Spectra Using Variable Azimuth Focus Shifts	28
12. Positions of Areas Used for the Semicausal/Fast Fourier Transform Comparison	32
13. Two-dimensional Fast Fourier Transform and One-dimensional Spectra for Seasat Rev. 974, Position A	33
14. Two-dimensional Fast Fourier Transform and One-dimensional Spectra for Seasat Rev. 974, Position B	34
15. Two-dimensional Fast Fourier Transform and One-dimensional Spectra for Seasat Rev. 974, Position C	35
16. Two-dimensional Fast Fourier Transform and One-dimensional Spectra for Seasat Rev. 974, Position D	36

LIST OF FIGURES
(Continued)

17.	Fast Fourier Transform Versus Semicausal Two-dimensional Spectra Using Variable Sampling Rates	40
18.	Fast Fourier Transform Versus Semicausal One-dimensional Wave Direction Spectra Using Variable Sampling Rates	41
19.	Fast Fourier Transform Versus Semicausal One-dimensional Wave Number Spectra Using Variable Sampling Rates	42
20.	Fast Fourier Transform Versus Semicausal Two-dimensional Spectra Using Variable Wave Cycles per Aperture	44-45
21.	Fast Fourier Transform Versus Semicausal One-dimensional Wave Direction Spectra Using Variable Wave Cycles per Aperture	46-47
22.	Fast Fourier Transform Versus Semicausal One-dimensional Wave Number Spectra Using Variable Wave Cycles per Aperture	48-49
23.	Fast Fourier Transform Versus Semicausal Two-dimensional Spectral Estimates Using a Truncated, Synthetic Wave Field and Variable Signal-to-Noise Ratios	53-54
24.	Examples of the Effects of Random Variations in the Background Gaussian Noise on Two-dimensional Spectral Estimates of a Synthetic Wave Field	56
25.	Seasat SAR Imagery Collected During Rev. 1049 Illustrating Wave Diffraction Around an Island	58
26.	Hydrographic Chart of Diffraction Test Area	59
27.	Areas 1 to 5 in the Digitized Section (dashed lines) of Seasat Rev. 1049 Data from which Fast Fourier Transforms were Generated	61
28.	Two-dimensional SAR Wave Spectra Produced from Seasat Rev. 1049	62
29.	SAR-derived Wave Directions for Seasat Rev. 1049 Illustrating Wave Diffraction and Detection of Two Wave Components	64

LIST OF FIGURES
(Continued)

30. Enlargement of Two-dimensional Wave Spectra from Area 3, Seasat Rev. 1049 Showing a Dominant and a Secondary Wave Component	65
31. Enlargement of Two-dimensional Wave Spectra from Area 4, Seasat Rev. 1049 Showing Two Wave Components of Equal Spectral Strength	66
32. SAR Ground Coverage of Seasat Rev. 974, 3 September 1978, in the Cape Hatteras, North Carolina Coastal Region	70
33. Flow Diagram Outlining Methodology of Examination of Deep and Shallow Water Wave Refraction Using Seasat SAR Data	74
34. Positions of 116 Optical Fourier Transforms with Examples of OFT Spectra	77
35. Area of Digital Depth Data Available from NOAA National Ocean Survey Smooth Sheets, 1930-1973	79
36. Gulf Stream Flow Conditions on 30 August 1978	81
37. Position of Hurricane Ella from 1 through 3 September 1978 . . .	82
38. Input Sea Conditions from Hurricane Ella	84
39. Projected Wave Rays in the Cape Hatteras Region from Hurricane Ella	85
40. Illustrations of Wave and Current Interactions in a Slowly Varying Cross Current	92
41. Summary of Seasat-sensed Dominant Wave Crests	94
42. Seasat SAR-observed Dominant Wave Directions	95
43. Average Wave Rays Constructed from Orthogonals to Seasat SAR-observed Wave Crests	96
44. SAR Wave Ray Hindcasts to Determine Wave Generation Regions . .	98
45. Comparison of SAR-observed Wave Rays with Projected Wave Rays without Consideration of the Correction of the Refraction Due to the Gulf Stream	99

LIST OF FIGURES
(Continued)

46. SAR-observed Wave Rays, Hurricane-projected Wave Rays, and the Gulf Stream	104
47. Clockwise and Counterclockwise Bending of Projected Wave Ray due to Refraction within the Gulf Stream's Non-uniform Velocity Field	105
48. Computer-generated Wave Rays Using SAR-measured Deep Water Wave Inputs Show the Effects of Topographically-induced Wave Refraction	108
49. SAR-observed Wave Numbers and Vectors from Seasat Rev. 974 Used to Calculate the Gulf Stream Current Velocity Field	112
50. Cross-track Velocity Components (M/S) of the Gulf Stream Current Calculated from SAR-observed Wave Numbers	114
51. Along-track Velocity Components (M/S) of the Gulf Stream Current Calculated from SAR-observed Wave Numbers	115
52. Total Current Velocity (M/S) Calculated from SAR-observed Wave Numbers	116
53. Spatially-smoothed (Three-point Moving Average) Current Velocity Profile Calculated from SAR-observed Wave Numbers . .	117
54. Comparison of SAR-derived Current Profile to U.S. Coast Guard-predicted Current Profile	118
55. Deep Water Wave Strata Locations, Seasat Rev. 974, 3 September 1978	119
56. SAR-predicted Depth (Using Inverted Airy Wave Theory Model) Versus Actual Depth	122
57. Comparison of Wavelength from Airy Wave Theory Model Versus SAR-observed Wavelengths	124
58. Position of ERIM-generated Shallow Water OFTS	127
59. Position of CERC-generated Shallow Water OFTS	128
60. Comparison of Wavelengths and Directions from Computer-based Model Versus SAR-observed Values	129

LIST OF FIGURES
(Concluded)

61. Model-predicted Wavelengths Versus SAR-observed Wavelengths Eliminating Points Where Wavelength (SAR) <120 Meters	132
--	-----

LIST OF TABLES

1. Peak-to-Background Ratio Versus Telerotation Setting, Revolution 762	16
2. Fast Fourier Transform Estimates of Dominant Wavelength and Direction as a Function of Range Telerotation Adjustments for Revolution 762	19
3. Peak-to-Background Ratio Versus Azimuth Focus Shift, Revolution 1087	23
4. Fast Fourier Transform Estimates of Dominant Wavelength and Direction as a Function of Range Azimuth Focus Shift for Revolution 762	25
5. Comparison of Dominant Wavelengths and Directions from Optical Fourier Transforms and Fast Fourier Transforms	37
6. Comparison of Semicausal Spectral Estimates Versus Fast Fourier Transform Spectral Estimates Using Variable Sampling Rates	43
7. Comparison of Semicausal Spectral Estimates Versus Fast Fourier Transform Spectral Estimates Using Variable Aperture Sizes	50
8. Fast Fourier Transform Spectral Estimates for the Five Areas Shown in Figure 27	63
9. Summary of SAR-Predicted (OFT) Dominant Wavelength and Direction from Deep-Water Areas of Revolution 974	87-90
10. Comparison of SAR-Observed Wave Rays with Hurricane Ella-Projected Wave Rays	102
11. Comparison of SAR-Observed Wave Rays with Hurricane Ella-Projected Wave Rays	106
12. Dominant Wavelengths and Directions for Deep Water Strata	121
13. Data Points for Computer Wave Refraction Model Comparisons	125-126

FURTHER SEASAT SAR COASTAL OCEAN WAVE ANALYSIS

1
INTRODUCTION

This report presents the results of a continuation of a previous Seasat gravity wave study conducted for NOAA and NASA under the Seasat Announcement of Opportunity (see Shuchman et al., 1979). This study investigates in detail Seasat synthetic aperture radar (SAR) data collected over oceanic areas where refracting and diffracting gravity waves were imaged.

The report is divided into two parts. The first part (Chapter 3) considers various image enhancement and spectral analysis techniques to extract wave information from SAR data. Part two (Chapter 4) is a case study of Seasat gravity wave data collected during Revolution 974 off the coast of Cape Hatteras, North Carolina.

Found within Chapter 3 of this report are sections covering the following topics:

1. Comparison of digital fast Fourier transforms (FFTs) and their resultant one-dimensional wave-directional and wave-number spectra obtained from Seasat SAR data that were processed using different SAR processor settings to account for the motion of gravity waves.
2. Comparison of estimates of dominant wavelength and direction obtained from optical Fourier transforms (OFTs) with estimates obtained from FFTs and from semicausal techniques.
3. Examination of the effects of reducing the aperture size and changing the sampling rate on the spectral estimates produced by fast Fourier transforms and spectral estimates obtained by semicausal techniques, and

4. Examination of the use of FFTs to discriminate between two distinct wave trains present within a given SAR data set.

The case study of the Cape Hatteras SAR data (Chapter 4) first discusses an analysis of the deep-water waves whose source is traced back to the location of the hurricane Ella. Next the refraction of these deep water waves due to the Gulf Stream is quantified. Then using wave data obtained from the deep-water analysis, a shallow water wave refraction study is performed by comparing SAR-derived estimates of dominant wavelength and direction of propagation to those obtained from a NASA developed shallow water wave refraction model which uses digital depth information as an input.

A discussion section outlining the utility of SAR to study synoptic wave climates is then presented, followed by a recommendations section.

2
SUMMARY

The purpose of this study was to further investigate the utility of Seasat synthetic aperture radar (SAR) data to provide useful information about ocean gravity waves. To accomplish this, two separate, but related investigations were performed. The first investigation considered various image enhancement and spectral analysis techniques to extract gravity wave information from SAR data. The second investigation was a case study of Seasat gravity wave data collected off the Coast of Cape Hatteras, North Carolina on 3 September 1978 during Revolution 974.

During the first investigation, it was determined that wave spectra generated from digitized Seasat SAR wave imagery were not significantly altered when either range telerotation adjustments or azimuth focus shifts were used during processing of the SAR signal histories. This result indicates that Seasat SAR imagery of gravity waves is not significantly improved or degraded by adjustments made in the SAR processor for scatterer motion effects, unlike previously studied aircraft SAR data which are sometimes quite sensitive to these adjustments.

Also during this first investigation, an advanced high resolution spectral analysis technique, the semicausal (SC) model, was studied. Applied to a synthetically generated wave field with varying levels of background Gaussian noise, the SC model appears to produce more accurate spectral estimates than conventional fast Fourier transform (FFT) techniques. Using Seasat SAR data from Rev. 974, the SC model spectral estimates were not significantly better than the FFT results, even when the aperture size was reduced to two wave cycles. The spectral analysis investigation also determined that FFTs could be used to discriminate between two distinct wave fields present on the Seasat SAR data if the waves are greater than 20° apart.

Estimates of dominant ocean wavelength and direction of propagation derived from SAR images collected during Rev. 974 were used to study gravity wave transformations in both deep and shallow water areas near Cape Hatteras, North Carolina. Using SAR data from one-hundred positions within the 400 x 100 km test area, it was determined that the deep water wave field was non-uniform in both wavelength and wave direction. By using wave hindcasting, the major source of this variation was identified as hurricane Ella. Another source of variation in the deep water region were wave/current interactions caused by the Gulf Stream. The SAR was able to document subtle changes in wavelength and direction due to this wave/current interaction. Finally, it was shown that a Gulf Stream current profile could be constructed using SAR inputs.

The results of the deep water analysis were used as inputs into two shallow water wave refraction models which included a basic Airy wave theory model and a more sophisticated computer-based wave refraction model. The present investigation, which utilized more accurate water depth information than used in the first study, and the updated deep water inputs did not improve results obtained from the initial study. It appears that the Seasat SAR detects shorter wavelengths than the wave refraction models predict. Possible reasons for this discrepancy include a bias in the manner the Seasat SAR imaged refracting coastal waves and the presence of additional tidal or along shore currents in the Cape Hatteras region.

3

IMAGE ENHANCEMENT AND DIGITAL SPECTRAL ANALYSIS
TECHNIQUES FOR SAR OCEAN WAVE DATA

This chapter of the report considers several image enhancement and spectral analysis techniques to extract gravity wave information from Seasat SAR data. The first section of this chapter addresses the question whether special wave motion compensation adjustments performed during image processing change the character of spectral estimates obtained from fast Fourier transform (FFT) analysis.

Next, a section is presented on the use of advanced data processing techniques to extract spectral information from SAR wave data. This section evaluates a technique referred to as a semicausal (SC) model used to extract estimates of dominant wavelength and direction from SAR data. First, a general discussion on the semicausal model is presented. Next, the results of an analysis of Seasat SAR data from Rev. 974 using the SC model are compared to those obtained from optical and fast Fourier transforms. Then, the performance of the semicausal model using different sampling rates and reduced aperture sizes (i.e., fewer wave trains included in the data set), and the effects of system noise on the SC model are discussed.

The next section of this chapter investigates how well the Seasat SAR can discriminate two distinct wave fields in an image. For this study, a test site was chosen where diffraction around an island occurred, causing two wave fields to be present within the scene.

3.1 MOTION COMPENSATION ADJUSTMENTS AND THEIR EFFECTS ON SPECTRAL ESTIMATES

Studies using aircraft SAR data have shown that the visibility or detectability of gravity waves is often sensitive to motion compensation adjustments made during the processing of the SAR signal histories (Kasischke, et al., 1979; Kasischke and Shuchman, 1981).

Because these motion compensation adjustments are inversely proportional to the velocity of the SAR platform, it was theoretically determined by early Seasat investigators that the motion adjustments may be necessary for optimum contrast wave imagery if the SAR is processed to full resolution. Furthermore, it was determined by Shuchman and Zelenka (1978) that the adjustment, if necessary, would be quite small and the effect on the SAR wave imagery quite subtle.

The purpose of the present investigation was to determine the sensitivity of Seasat SAR data to motion compensation adjustments. This was accomplished in two separate experiments. First, wave detectability or contrast was measured as a function of both the range telerotation adjustment and azimuth focus shift adjustment. Next, SAR imagery processed with various telerotation and focus adjustments were digitized and fast Fourier transformed to determine if the spectral estimates varied.

3.1.1 BACKGROUND AND THEORY

The initial work quantifying the effects of target motions on the synthetic aperture radar imaging mechanism was performed by Raney (1971). SARs are sensitive to both the azimuth and range velocity components of moving targets. A moving target being imaged by the SAR will sometimes result in a degraded image of that target.

A velocity in the range (line-of-sight) direction affects the SAR imaging process in several ways. One such effect is an azimuthal displacement of the moving target's image relative to a stationary target's image. When a target is accelerating in the range direction, this azimuthal displacement changes during the imaging time, resulting in a smearing in the azimuthal direction. Neither one of these effects is correctable during processing.

A range velocity component will also cause a smearing or defocusing in the range direction due to a rotation of the phase history of

the target. This effect can be corrected for during correlation of the data by rotating the lenses in the optical processor as described below.

Finally, motion of a SAR imaged target in the along track direction results in a defocusing of the image in the azimuthal direction. This defocusing can be compensated for during processing by adjusting the focal length of the azimuthal lens. For a more detailed discussion of the problems associated with imaging moving targets with a SAR, the reader is referred to articles by Shuchman (1981) or Shuchman, et al. (1981).

Shuchman (1981) presented equations to calculate adjustments to use during processing of the signal histories for the range and azimuth velocity components present in gravity waves. These velocity adjustments are directly proportional to the velocity of the target and inversely proportional to the velocity of the SAR platform. The motion compensation adjustments are of two types: telerotation adjustments which compensate for motion in the range (line-of-sight) direction and focus shifts which compensate for motion in the azimuth direction.

The calculation for the telerotation adjustment (Shuchman, 1981) is:

$$\phi = \frac{V_r P}{V_{AC} Q} \quad (1)$$

where ϕ is the rotation angle for correction,
 V_r is the line-of-sight velocity of the target,
 V_{AC} is the SAR platform velocity,
 P is the azimuth scale factor, and
 Q is the range scale factor.

According to this calculation, SAR imagery of gravity waves should be most visible when the correction in Eq. (1) is used during

processing of the SAR signal histories. Previous studies by Kasischke, et al. (1979) showed that greater detectability of range traveling waves (as indicated by modulation depths) was obtained from aircraft SAR data collected at the Marineland Experiment when a tele-rotation correction was used which adjusted for the phase speed of the waves. Recent studies by Kasischke and Shuchman (1981) have shown similar results using aircraft SAR imagery of wind driven waves on Lake Michigan.

In a similar fashion, an adjustment can also be made to compensate for azimuth velocity distortions in the SAR data. As derived by Shuchman and Zelenka (1978), the focal length (F_0) for SAR processing is defined as:

$$F_0 = \frac{R\lambda}{2M^2\lambda_0} \left(\frac{v_f}{V_{AC}} \right)^2 \quad (2)$$

where R is the slant range to the target,

λ is the radar wavelength,

λ_0 is the optical processor wavelength,

M is azimuth demagnification of the optical processor, and

v_f is the film velocity.

Using the focal length (F_0) calculated in Eq. (2), the shift in focal length (δF) produced by a moving target is defined as

$$\delta F = 2F_0 \frac{v_A}{V_{AC}} \quad (3)$$

where v_A is the target velocity parallel to the SAR platform direction.

3.1.2 EXPERIMENT

The above mentioned motion compensation calculations were tested on Seasat SAR data collected during the Joint Air/Sea Interaction

(JASIN) experiment (Allan and Guymer, 1980). Two examples were selected: one where range traveling waves were present and a second with azimuth traveling waves.

Seasat SAR imagery from Revolution 762 was optically processed at ERIM using a variety of different telerotation settings. Revolution 762 data used in this experiment were collected northwest of the coast of Scotland in the North Atlantic at 06:50 (GMT) on 19 August 1978 and had a range traveling wave field present. An example of the 25 meter resolution SAR imagery from this orbit and the resultant two-dimensional Fourier transforms (both optical and digital) are presented in Figure 1.

Surface measurements, made coincident with and near to the SAR ground coverage area, indicate a wave field with a dominant wavelength of 210 meters (phase speed, $C = 18.1$ m/sec) with a significant wave height ($H_{1/3}$) of 5.5 meters from 240° (T) was present at this time. The sea truth also reported a wind speed of 12 m/sec from 186° (T). Spectral measurements derived from SAR data (OFTs) result in a dominant wavelength of 241 meters ($C = 19.4$ m/sec). The telerotation adjustment ($\phi = 8.9 \times 10^{-4}$ radians) calculated for Revolution 762 data assumed the gravity waves had a phase speed of 19.4 m/sec. Revolution 762 data were processed using the following telerotations: -9ϕ , -7ϕ , -5ϕ , -3ϕ , -2ϕ , $-\phi$, 0 , $+\phi$, $+2\phi$, $+3\phi$, $+5\phi$, $+7\phi$, and $+9\phi$. A negative (-) telerotation assumes the waves are moving towards the radar (along the line-of-sight) while a positive (+) telerotation assumes the waves are moving away. (The waves present during Rev. 762 were moving away from the SAR look direction.)

Wave visibility was then measured on this imagery using a recently developed wave crest-to-trough contrast measurement called a peak-to-background ratio or PBR (see Kasischke, 1980; or Kasischke and Shuchman, 1981). Each PBR presented in this report represents

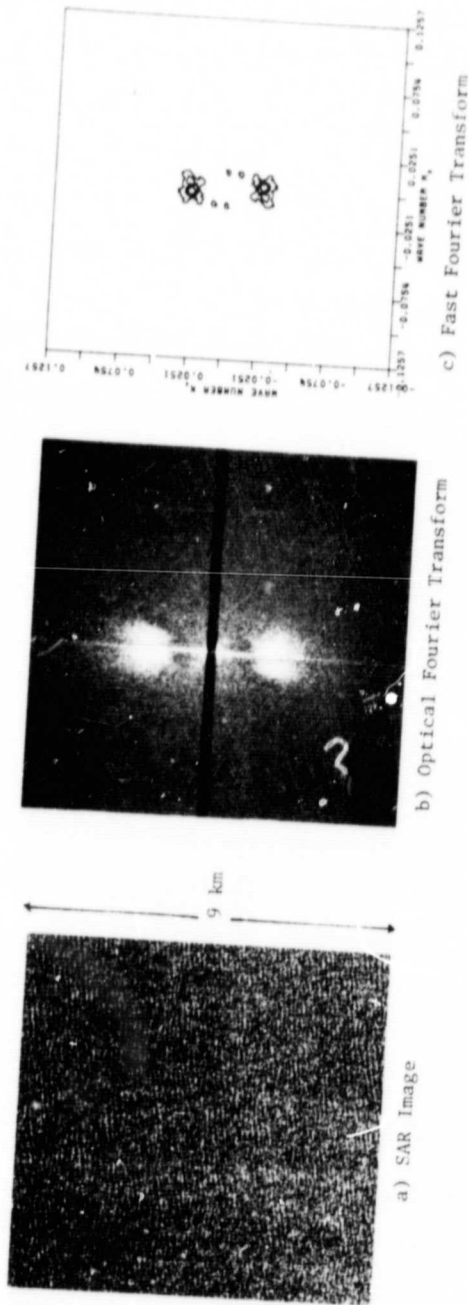


FIGURE 1. SEASAT SAR IMAGE OF RANGE TRAVELING OCEAN GRAVITY WAVES AND ITS RESULTANT TWO-DIMENSIONAL FOURIER TRANSFORMS. (Rev. 762, 19 August 1978)

the average of five separate measurements. From these five measurements, the standard deviation of the mean was calculated. Also, a 95 percent confidence interval was calculated as $2\sigma_x$, where σ_x was calculated (after Shaeffer, et al., 1979) as:

$$\sigma_x = \frac{s_x}{n} \quad (4)$$

where s_x = the standard deviation of the mean, and
 n = the number of samples.

The dependence of wave visibility on telerotation can be determined from a graph of PBR versus ϕ .

The next part of this experiment involved studying the effects of telerotation adjustments on the spectral estimates derived from these data. Results of SAR aircraft studies indicate that gravity waves are usually not detectable on SAR imagery when the telerotation adjustment made is greater than 2ϕ away from the optimum setting (Kasischke and Shuchman, 1981). Since results (discussed below) of the Seasat experiments showed that the optimum setting for these data are at 0 (or stationary focus), it was decided to digitize SAR data from the -2ϕ , $-\phi$, 0, ϕ and 2ϕ imagery.

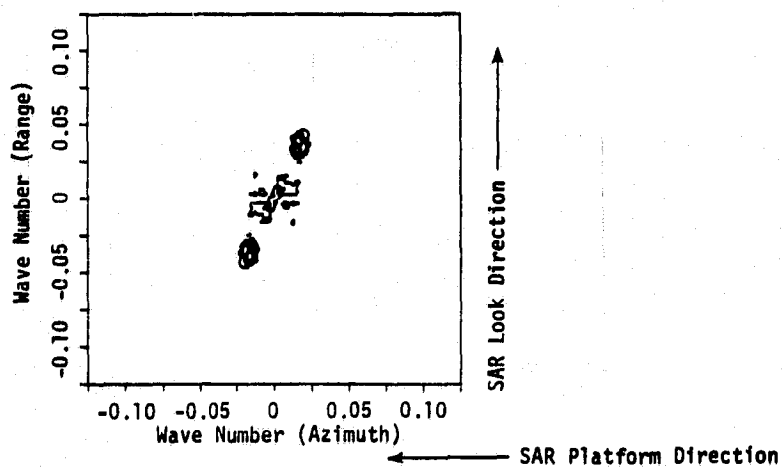
All digital data (except for the JPL-digital data presented in Appendix B) discussed in this report were generated by ERIM's hybrid optical-digital processor (Ausherman, et al., 1975). The SAR image film (either ERIM or JPL produced) of ocean gravity waves were digitized using a 12.5 meter by 12.5 meter pixel. A 1024 by 1024 pixel area was digitized and the data recorded on a computer compatible tape (CCT).

The digitized SAR ocean wave imagery was then analyzed using a standard computer package developed by ERIM under sponsorship of the Office of Naval Research (see Shuchman, et al., 1979a). A 512 by 512 pixel subset of the digitized data is extracted from the CCT.

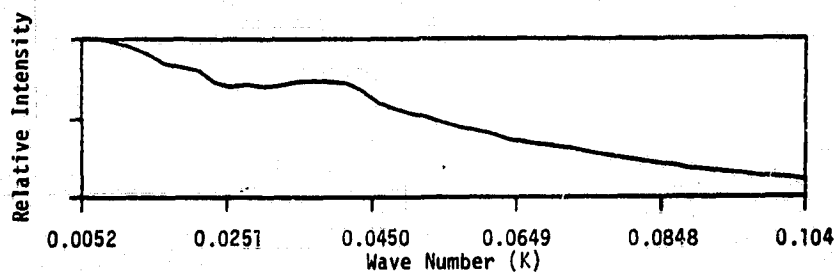
Usually the SAR data are geometrically rectified, but since both the JPL and ERIM data had been previously geometrically corrected when the data were optically correlated, this step was not necessary. The data are then corrected for long-period variations (such as power loss or antenna gain) to remove D.C. bias, smoothed using a $(\sin x)/x$ filter on the data to reduce radar speckle and resampled to 256 by 256 pixels. This resampling results in a pixel size of 25 by 25 meters. These data are then inputted to either a fast Fourier transform or semicausal program to generate spectral estimates from the SAR data.

When the digital SAR data are fast Fourier transformed, the results are typically displayed as two-dimensional contour plots. Presented in Figure 2a is a typical two-dimensional contour plot produced from an FFT of SAR ocean wave data. Each of the three contour levels in Figure 2a represents 3 dB of energy from the SAR image. These three contour levels range from -3 dB to -9 dB (i.e., one-half to one-eighth of the peak value). Although this FFT produces no wave height information, the two-dimensional contour plot does accurately portray wave number and wave direction information. The x-axis of the plot represents azimuth direction and the y-axis the range direction, with the units on the axes being wave number (k). By finding the center of the highest contour level in the spectrum, and measuring k_{range} and k_{azimuth} , an estimate of the dominant wave number (and hence wavelength) can be calculated, as can an estimate of the wave's orientation. By knowing the SAR platform's direction, an estimate of the dominant wave direction can be calculated. Note, there is still a 180° ambiguity in the wave direction data.

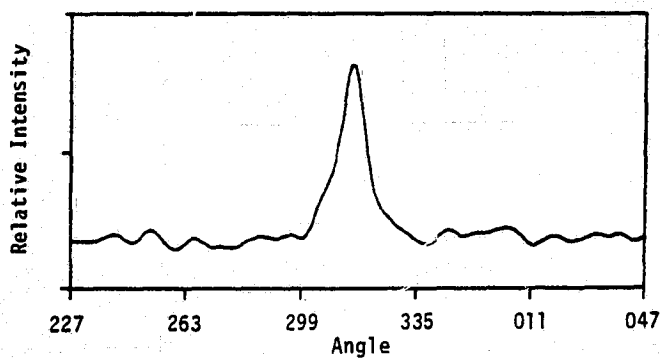
The information in the two-dimensional FFT spectrum can be more rigorously analyzed. To do so, one-half of the plot in Figure 2a is summed digitally over specified wave number ranges to produce a one-dimensional wave number spectrum, as is shown in Figure 2b. Finally,



a. Two-Dimensional Contour Plot



b. One-Dimensional Wave Number Spectra



c. One-Dimensional Wave Direction Spectra

FIGURE 2. EXAMPLES OF COMPUTER-GENERATED TWO-DIMENSIONAL AND ONE-DIMENSIONAL WAVE SPECTRA FROM SEASAT SAR DATA. (Rev. 974)

a one-dimensional wave direction spectrum (usually at the peak wave number) can be plotted, as is presented in Figure 2c. The digital output from these plots can be consulted to extract exact estimates of dominant wavelength and direction.

Seasat SAR imagery from Revolution 1087 was optically processed using a variety of different azimuth focus shifts. An example of this data is presented in Figure 3. No sea-truth was collected for this pass, but it is clear from Figure 3 that the waves are nearly azimuth traveling. The optical Fourier transform of this data indicates a 299 meter dominant wave is present ($C = 21.2$ m/sec). A focus shift ($\delta F = P = 1.82 \times 10^{-3}$ m) was calculated assuming the waves had a phase speed of 21.2 m/sec. Revolution 1087 data were processed using the following focus shifts: $-4P$, $-3P$, $-2P$, $-P$, 0 , P , $2P$, $3P$, $4P$. A negative ($-$) focus shift assumes the waves are moving in the same direction as the SAR platform while a positive ($+$) correction assumes the waves are moving in the opposite direction. (Since no sea truth was available, the assumption was made that the waves were moving towards the Scottish Coast, therefore opposite to the SAR platform direction.)

Peak-to-background ratio measurements were obtained for the various settings. Again, data from the $-2P$, P , 0 , $+P$, $+2P$ settings were digitized and fast Fourier transforms of the data generated.

3.1.3 RESULTS

Table 1 and Figure 4 summarize the telerotation (ϕ) versus wave contrast measurements. Table 1 presents the average ($n = 5$) PBR and the standard deviation, and the 95 percent confidence interval for each telerotation setting. A statistical analysis of variance (Scheffe, 1959) of these data reveals there is essentially no difference between the $+2\phi$, -2ϕ and 0 readings. Significant differences in wave detectability did not occur until a $\pm 5\phi$ telerotation was

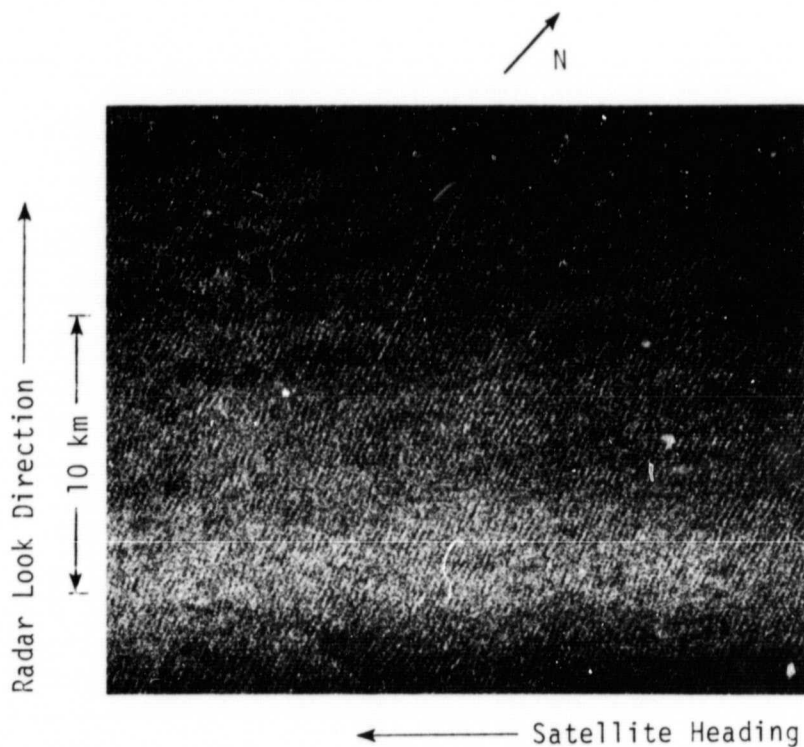


FIGURE 3. SEASAT SAR IMAGERY OF AZIMUTH TRAVELING WAVES COLLECTED DURING REV. 1087, 11 SEPTEMBER 1978.

TABLE 1
PEAK-TO-BACKGROUND RATIO VERSUS TELEROTATION SETTING,
SEASAT REVOLUTION 762

<u>Telerotation Setting</u>	<u>Average PBR</u>	<u>Standard Deviation</u>	<u>95 Percent Confidence Interval</u>
+9°	6.7	0.6	0.5
+7°	11.1	1.1	1.0
+5°	17.1	1.0	0.9
+3°	23.3	3.0	2.7
+2°	30.4	3.9	3.5
+ 0	31.2	2.3	2.0
0 (Stationary Focus)	33.3	3.0	2.7
-0	33.3	3.2	2.8
-2°	28.9	6.7	5.9
-3°	25.3	3.5	3.2
-5°	12.1	0.7	0.7
-7°	8.2	1.6	1.4
-9°	2.9	0.2	0.2

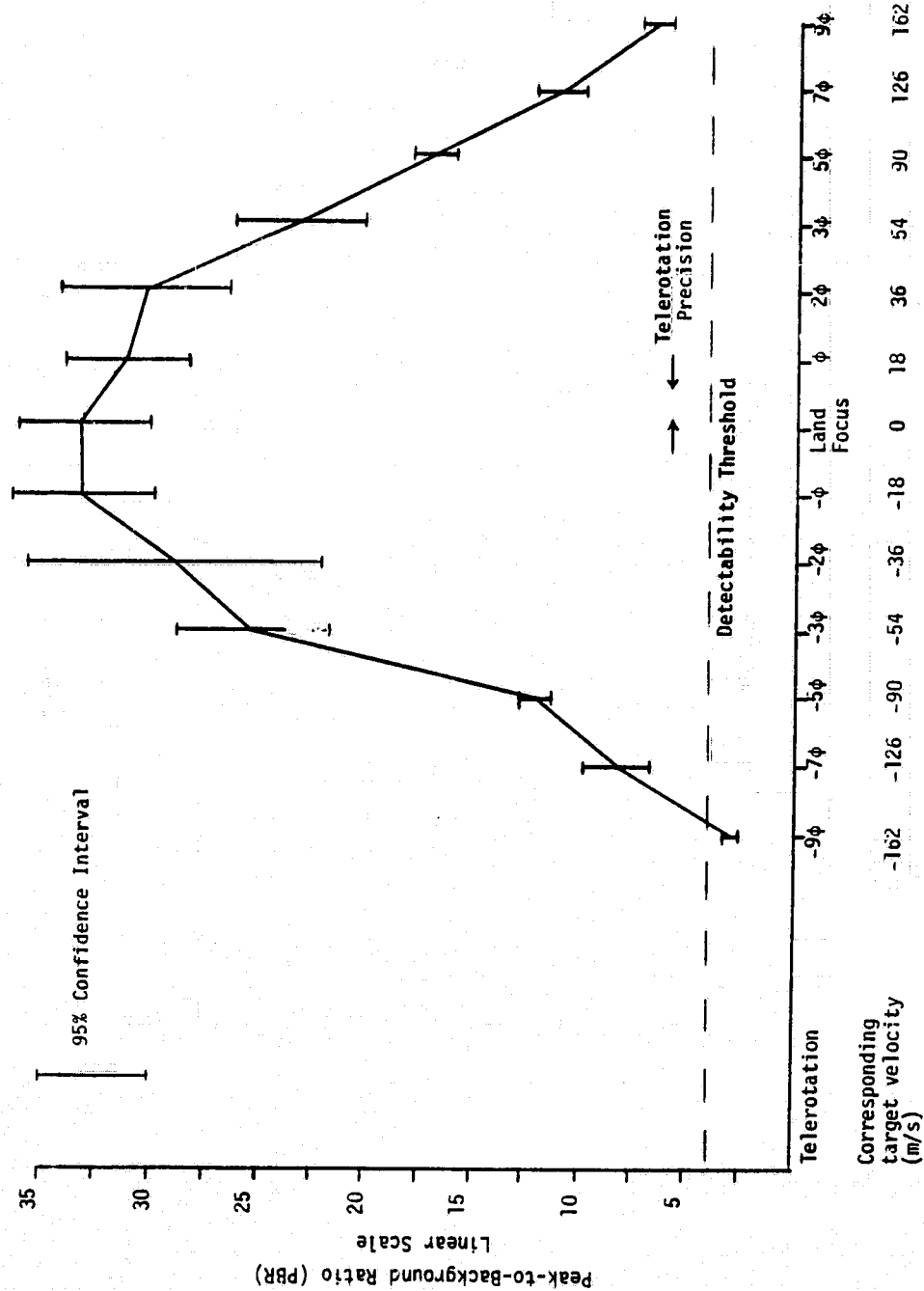


FIGURE 4. PEAK-TO-BACKGROUND RATIO VERSUS TELEROTATION ADJUSTMENT, SEASAT REV. 762.

used. Even so, range traveling waves were still visible on SAR imagery that was processed using telerotation adjustments of -7ϕ and $+7\phi$, indicating that a certain degree of latitude can be used when processing SAR imagery of range traveling waves from mid-ocean areas with no land present to focus on.

Table 2 lists the dominant wavelengths and directions obtained from the Rev. 762 SAR imagery processed using the different telerotation settings. Figures 5 through 7 present the two-dimensional Fourier transforms and the one-dimensional wave direction and wave number spectra generated from the -2ϕ , 0 and $+2\phi$ imagery. We can see from these figures and table that the SAR derived estimates of dominant wavelength and direction do not change as a function of telerotation and also that the shapes of the one-dimensional curves do not significantly change.

Table 3 and Figure 8 summarize the PBR versus the azimuth focus shift results. Table 3 presents the average ($n = 5$) PBR, the standard deviation, and the 95 percent confidence interval for each focus setting. An analysis of variance of these data indicates the highest PBR occurred at the 0 (stationary focus), with all the other settings being significantly lower. Waves were still visible out to the $+4P$ and $-4P$ focus shifts.

Table 4 lists the dominant wavelength and direction obtained from the digitized SAR imagery using different focus shift settings. Figures 9 through 11 present the two-dimensional Fourier transforms and the one-dimensional wave direction and wave number spectra generated from the $-2P$, 0 and $+2P$ focus shifts. Once again, we can see from these figures that the SAR derived estimates of dominant wavelength and direction do not change significantly as a function of focus shift.

In summary, this experiment has shown that SAR data collected by the Seasat satellite is relatively insensitive to motion compensation

TABLE 2
FAST FOURIER TRANSFORM ESTIMATES OF DOMINANT
WAVELENGTH AND DIRECTION AS A FUNCTION
RANGE TELEROTATION ADJUSTMENTS FOR
SEASAT REV. 762

<u>Telerotation Setting</u>	<u>Dominant Wavelength</u>	<u>Dominant Direction</u>
-2 ϕ	259 m	227°
- ϕ	259 m	227°
0 (Stationary Focus)	259 m	227°
+ ϕ	259 m	227°
+2 ϕ	259 m	227°

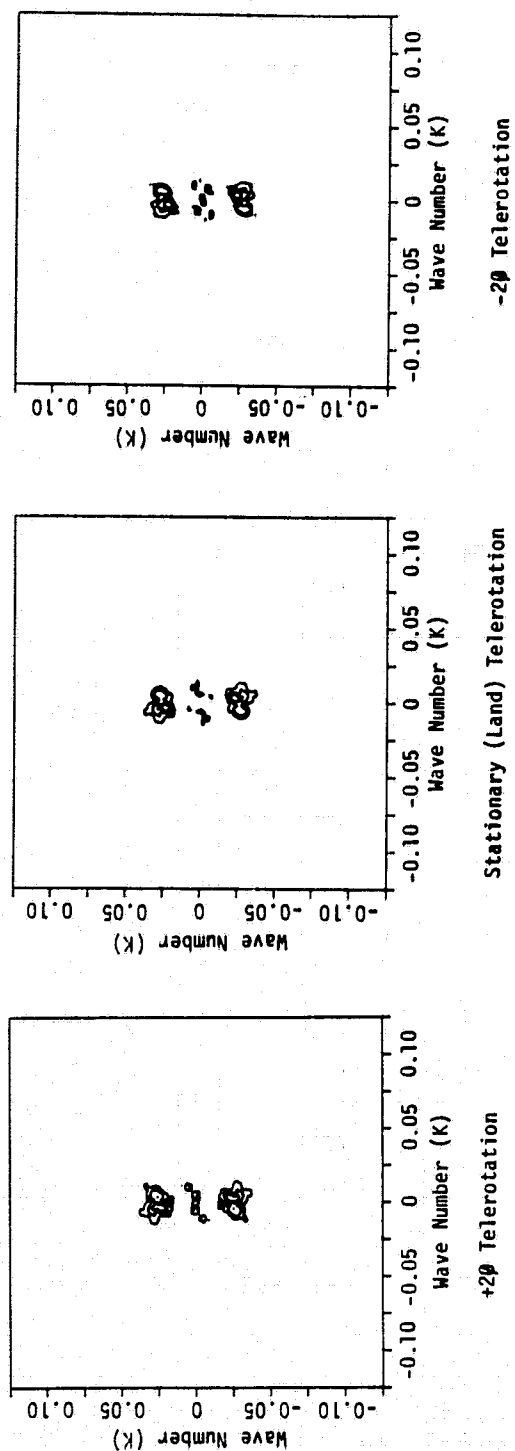


FIGURE 5. TWO-DIMENSIONAL FAST FOURIER TRANSFORMS OF SEASAT SAR WAVE DATA USING VARIABLE TELEROTATION SETTINGS. (Rev. 762, 19 August 1978)

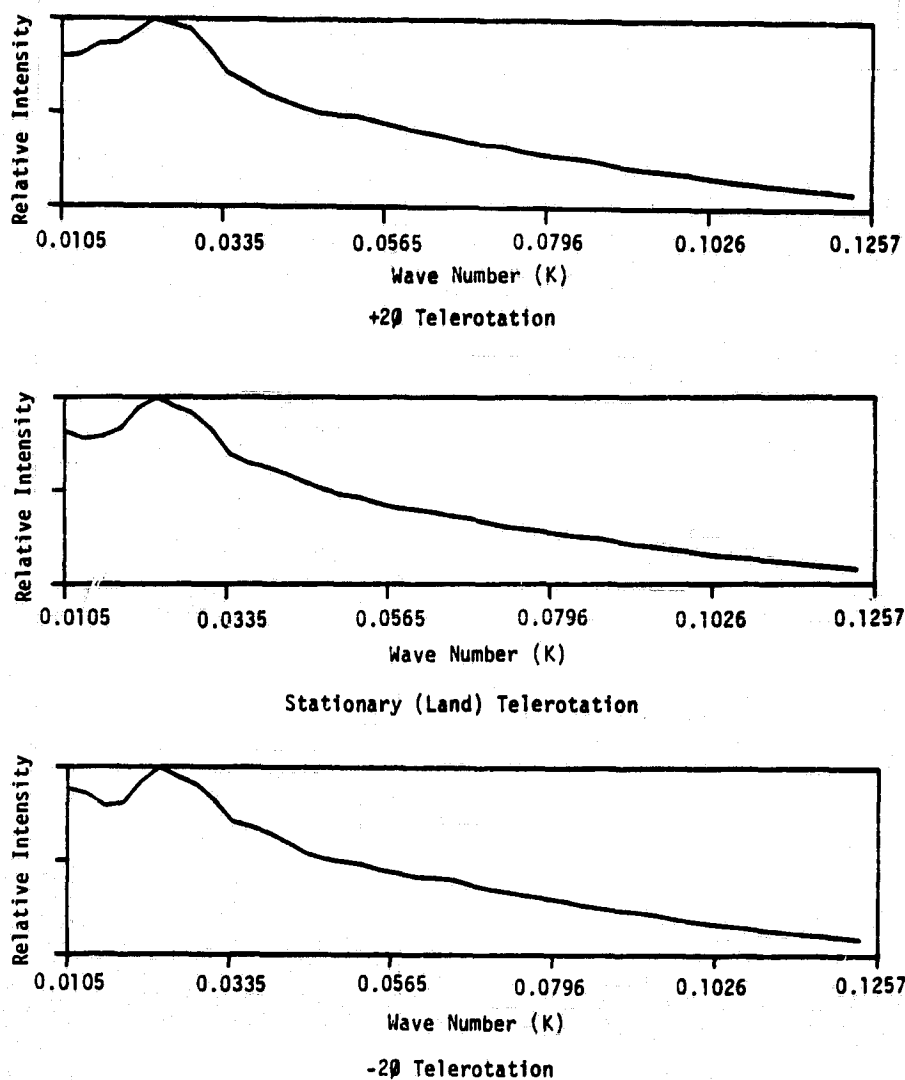


FIGURE 6. ONE-DIMENSIONAL WAVE NUMBER SPECTRA USING VARIABLE TELEROTATION SETTINGS.
(Seasat Rev. 762, 19 August 1978.)

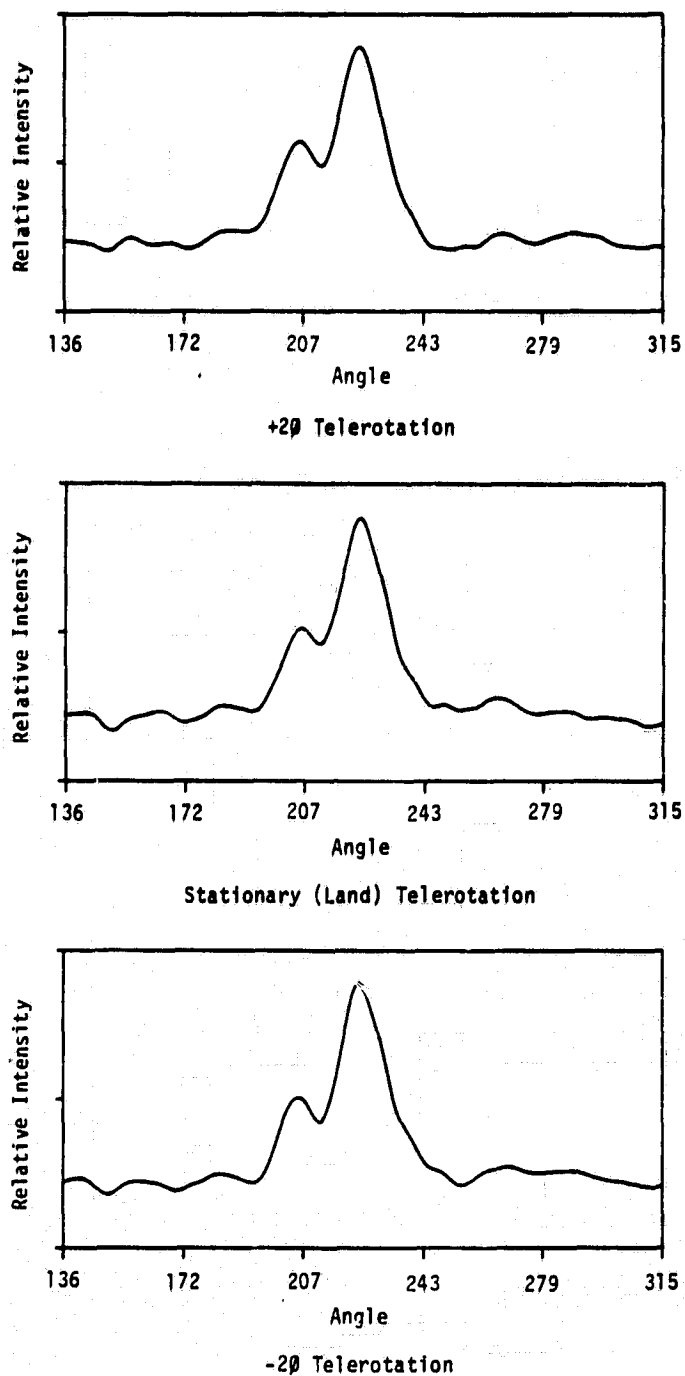


FIGURE 7. ONE-DIMENSIONAL WAVE DIRECTION SPECTRA USING VARIABLE TELEROTATION SETTINGS.
(Seasat Rev. 762, 19 August 1978.)

TABLE 3
PEAK-TO-BACKGROUND RATIO (PBR) VERSUS AZIMUTH
FOCUS SHIFT, SEASAT REVOLUTION 1087

<u>Focus Shift</u>	<u>Average PBR</u>	<u>Standard Deviation</u>	<u>95 Percent Confidence Interval</u>
+4P	6.0	1.3	1.2
+3P	10.2	1.4	1.2
+2P	12.7	2.3	2.0
+P	11.8	0.8	0.7
0 (Stationary Focus)	18.4	2.6	2.3
-P	14.7	2.8	2.5
-2P	13.5	1.8	1.6
-3P	8.3	0.9	0.8
-4P	6.0	0.9	0.8

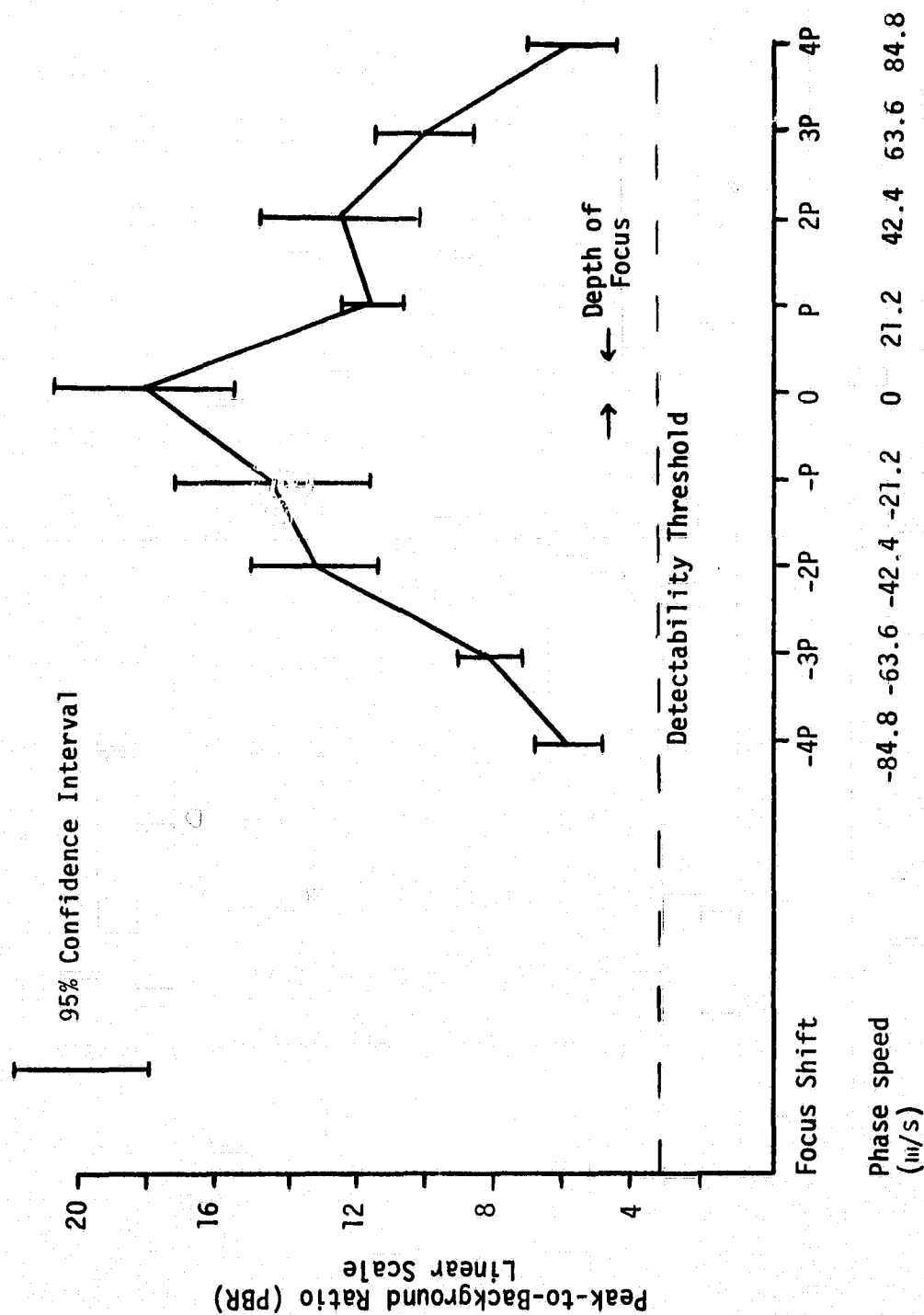


FIGURE 8. PEAK-TO-BACKGROUND RATIO VERSUS AZIMUTH FOCUS SHIFT, SEASAT REV. 1087.

TABLE 4
FAST FOURIER TRANSFORM ESTIMATES OF DOMINANT
WAVELENGTH AND DIRECTION AS A FUNCTION OF
AZIMUTH FOCUS SHIFT FOR
SEASAT REV. 762

<u>Azimuth Focus Setting</u>	<u>Wavelength</u>	<u>Direction</u>
-2P	289 m	254°
-P	289 m	253°
0 (Stationary Focus)	289 m	253°
+P	306 m	252°
+2P	306 m	250°

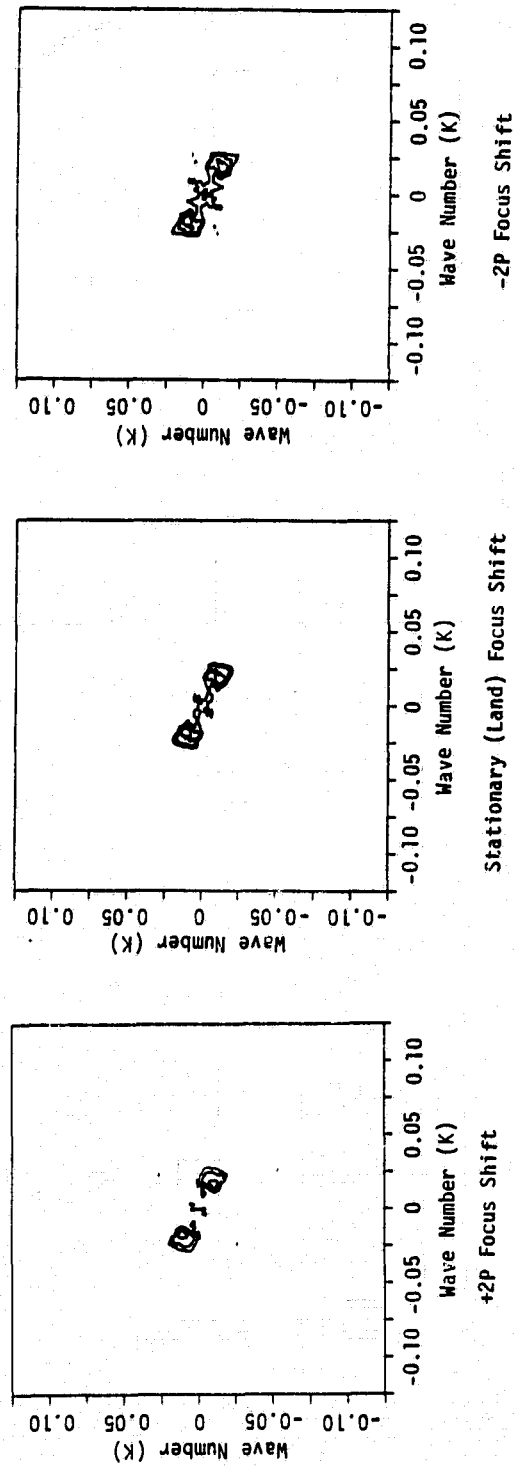


FIGURE 9. TWO-DIMENSIONAL FAST FOURIER TRANSFORMS OF SEASAT SAR DATA USING VARIABLE AZIMUTH FOCUS SHIFTS. (Rev. 1087, 11 September 1978.)

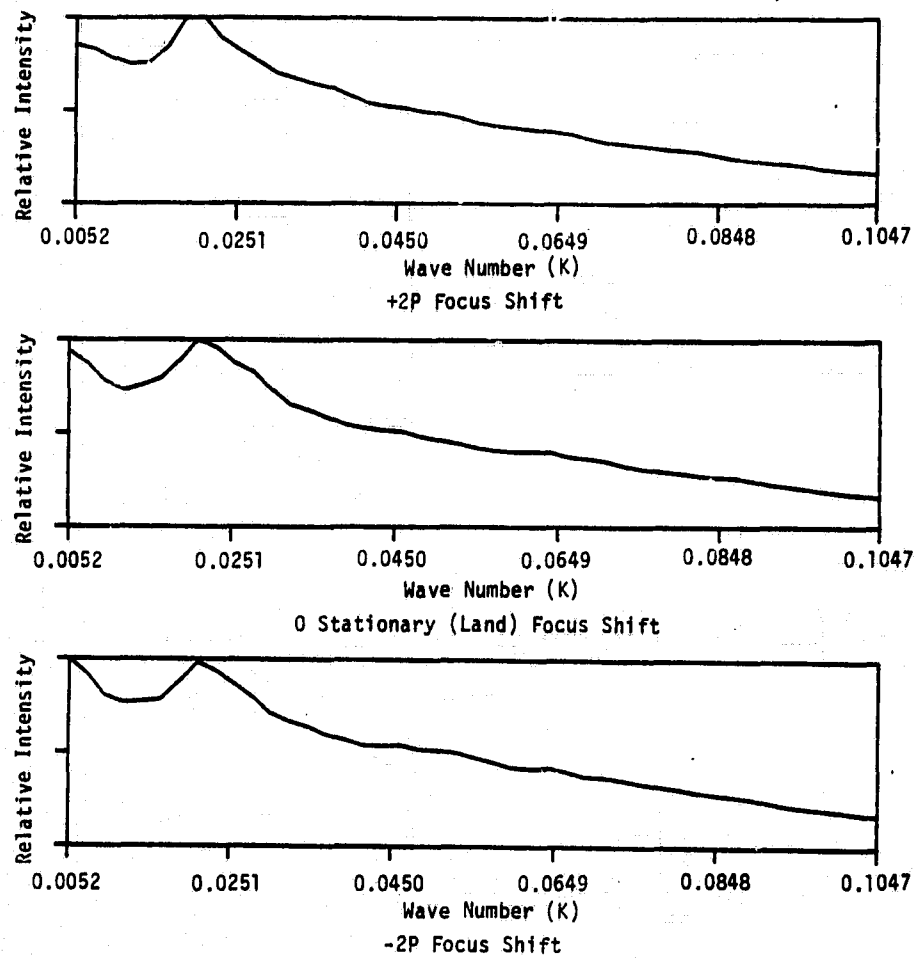


FIGURE 10. ONE-DIMENSIONAL WAVE NUMBER SPECTRA USING VARIABLE AZIMUTH FOCUS SHIFTS.
(Seasat Rev. 1087, 11 September 1978.)

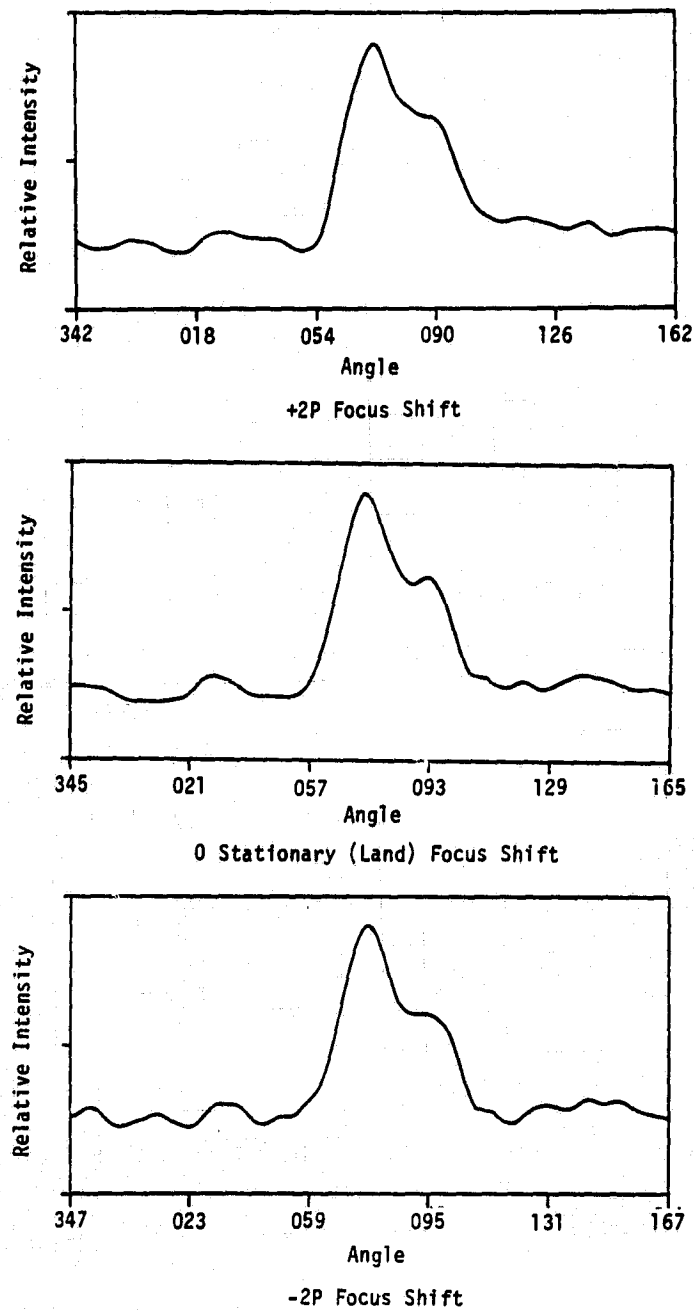


FIGURE 11. ONE-DIMENSIONAL WAVE DIRECTION SPECTRA USING VARIABLE AZIMUTH FOCUS SHIFTS.
(Seasat Rev. 1087, 11 September 1978.)

adjustments, as was predicted in theoretical studies. This indicates that given a stationary target to focus on (i.e., land), optimum imagery of gravity waves can be generated without making special motion compensations. Even when non-stationary settings were used to process Seasat SAR data, comparable spectral estimates of dominant wavelength and direction were obtained.

3.2 GENERATION OF SPECTRAL ESTIMATES FROM SEASAT SAR DATA

In this section, the utility of the semicausal model is further investigated using Seasat data collected during Rev. 974 and through the use of reference functions. First, the semicausal model is briefly discussed and results from previous studies summarized. Next, spectral estimates of dominant wavelength and direction obtained from optical Fourier transforms and fast Fourier transforms are presented to compare to the SC estimates. In addition, the effects of varying the sampling rate and the aperture size on the spectral estimates given by both the SC model and fast Fourier transform techniques are observed and a comparison made between the two techniques. Finally, the SC model is evaluated using a reference function with variable noise levels.

3.2.1 BACKGROUND

As was discussed previously, the spectral analysis technique which is most commonly utilized in determining the wavelength and direction of ocean waves from SAR data is the two-dimensional Fourier transform. The Fourier transform is adequate when a relatively large aperture (image size) is used. Usually, ten cycles of wave data are needed to resolve the waves. When the aperture is reduced in size, the Fourier transform is often degraded in resolution and this may cause difficulty in diagnosing waves. Also, when two wave components are sufficiently close in frequency or direction, the Fourier transform cannot resolve them.

In many oceanographic analyses, it is important to be able to either discriminate between two wave fields or use reduced aperture sizes to study wave transformations over short distances. An example of discriminating between two wavefields is the case where two sources of waves enter the same region. An example where a reduced aperture size is needed is when refraction of waves occurs in coastal regions and the waves change directions and wavelengths over very short periods. To accurately monitor these changes, smaller aperture sizes are necessary.

Fine resolution while using small apertures (or a few wave cycles) is one of the attributes of the new high resolution spectral analysis techniques. Such techniques show promise for more accurate analysis of refracting or diffracting ocean waves. These techniques are based on autoregression, or, its equivalent, maximum entropy analysis, and are continually being improved upon by many contributors (Burg, 1975; Jain and Ranganath, 1978; Swingler, 1980). In this section, we have applied one of these spectral analysis methods to radar images of ocean waves, and have additionally tested the technique on synthetic data. The method used is termed "semicausal" (Jain and Ranganath, 1978) and is one of the first available two-dimensional high resolution methods. A fuller discussion of the semicausal model is given in Appendix A to this report, where the derivation and algorithms of this method are presented.

During previous studies of the semicausal (SC) model (Shuchman, et al., 1979), it was determined that it could be used to estimate dominant wavelength and direction from both aircraft and satellite SAR data. The results of these earlier studies did not indicate conclusively whether the SC model was more beneficial than conventional fast Fourier transform techniques and indicated that more research was necessary to determine the effects of noise on the SC model.

3.2.2 COMPARISON DATA BASE

The objective of the studies summarized in the following sections was to further examine the utility of the semicausal model using Seasat SAR data. First it is necessary to develop a set of comparison data with which to evaluate the semicausal estimates.

Digital data from Rev. 974 were used in this analysis. An attempt was also made to extract gravity wave information from JPL-digitally processed Seasat SAR data of Rev. 974. But it became apparent that these data had not been correctly processed. A more complete discussion of these problems associated with the JPL digital data are presented in Appendix B of this report.

Four areas from Seasat Rev. 974 were chosen to be used in the SC model analysis. The positions of these areas, marked A, B, C, and D, are shown in Figure 12. To produce comparison data, OFTs and FFTs of these areas were generated and analyzed to produce estimates of dominant wavelength and direction. JPL optically processed data, with a 40 meter resolution, were used in this study. The optically processed imagery was digitized on ERIM's digital hybrid processor. The two-dimensional FFT spectra and the resultant one-dimensional wave number and wave direction plots are presented in Figures 13 through 16. Table 5 summarizes the OFT and FFT estimates of dominant wavelength and direction from the four positions. An equivalent ground area of 6.4 x 6.4 kilometers was used to produce each FFT while an area of 7.5 x 7.5 kilometers was used to produce each OFT.

From Table 5, it can be seen that the estimates of dominant wavelength and direction are all within ± 4 percent on wavelength and $\pm 2^\circ$ on wave direction. Previous studies, (Gonzalez, et al., 1981; Kasischke, 1980; Kasischke, et al., 1981) have established that the estimates of dominant wavelength and direction produced from Seasat SAR data from OFTs and FFTs compare favorably to those produced by surface instrumentation. A recent summary by Vesecky and Stewart (1981) of comparisons of Seasat SAR versus surface instrumentation

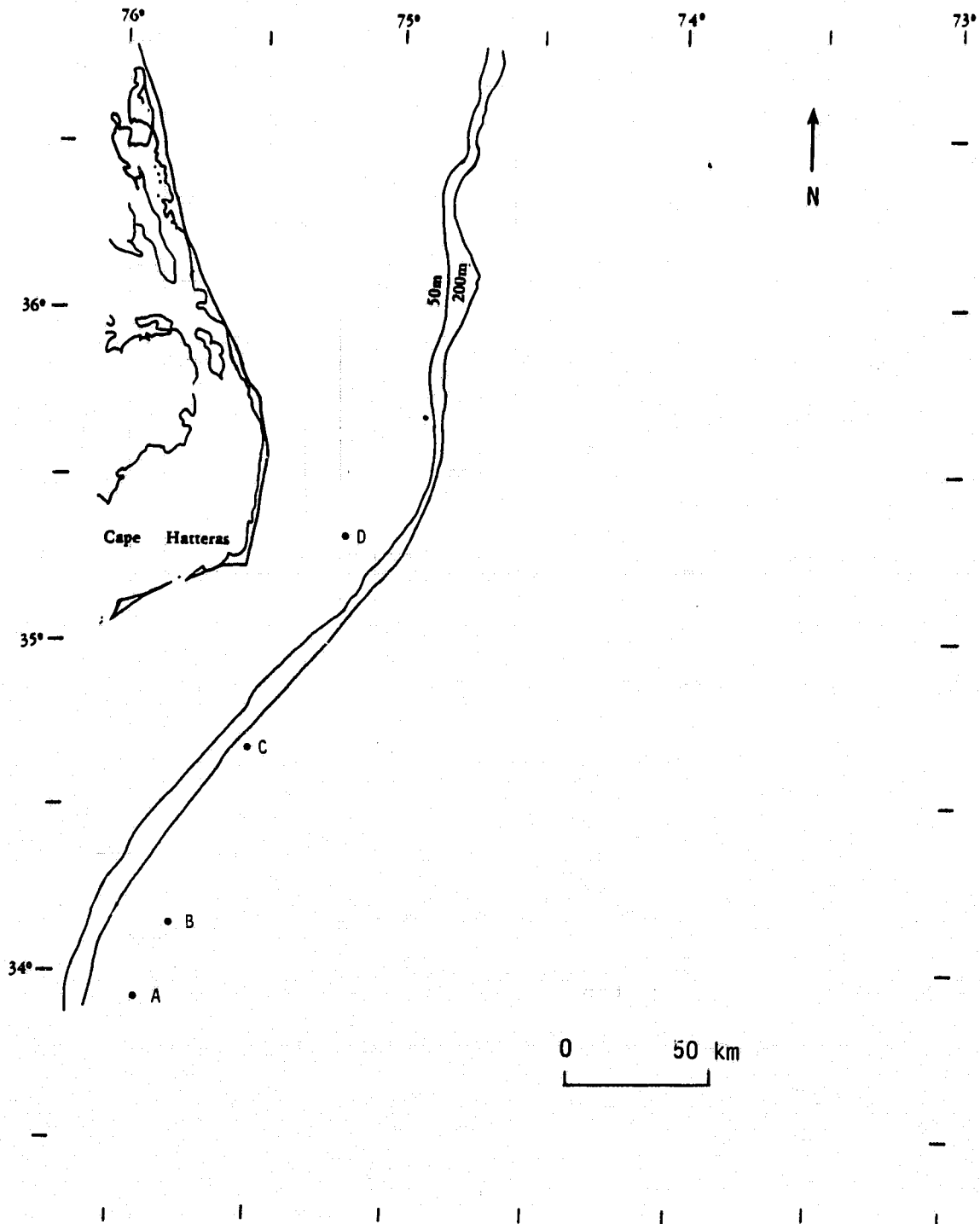
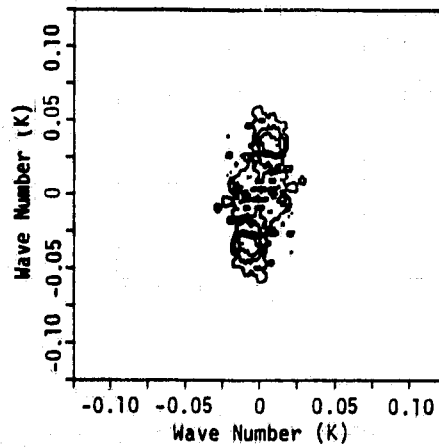
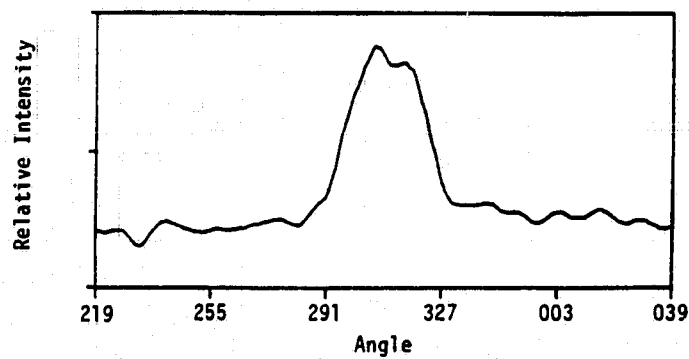


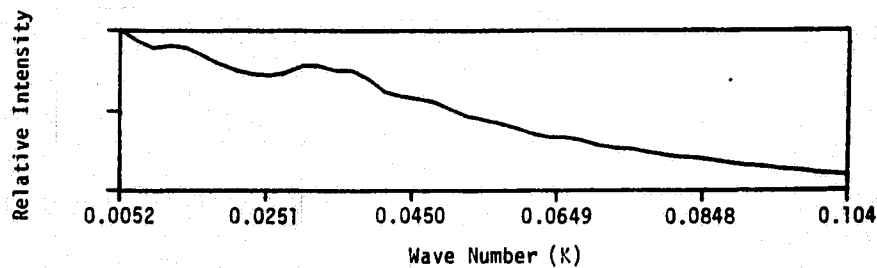
FIGURE 12. POSITIONS OF AREAS USED FOR THE SEMI-CAUSAL/
FAST FOURIER TRANSFORM COMPARISON.
(The 50 m and 200 m depth contours are also
shown.)



Two-Dimensional Fast Fourier Transform

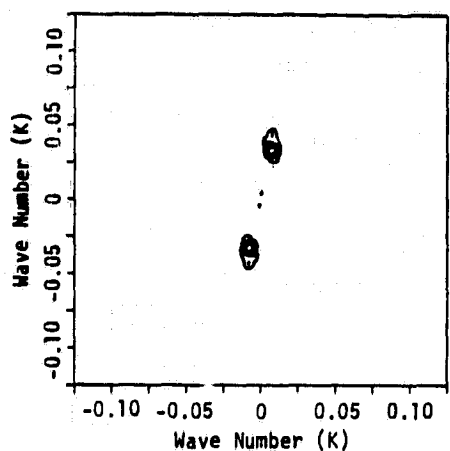


One-Dimensional Direction Spectrum

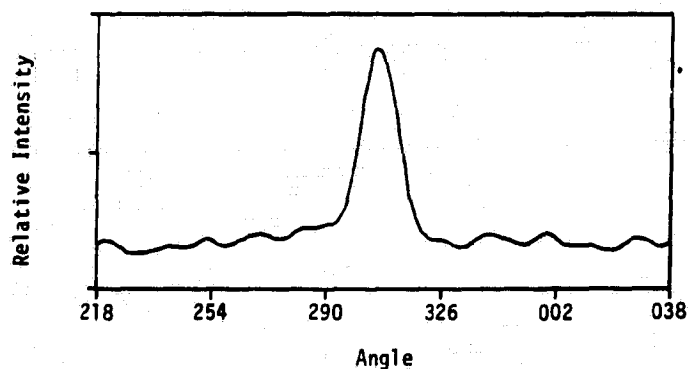


One-Dimensional Wave Number Spectrum

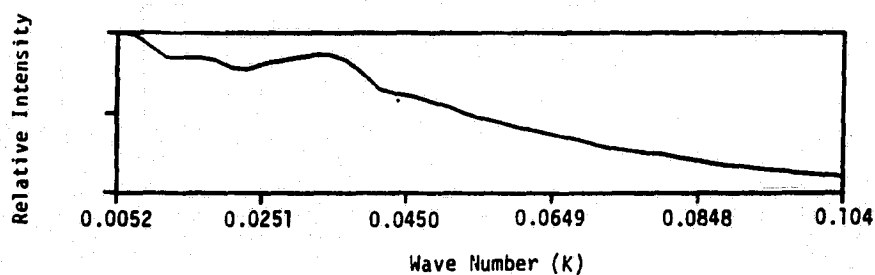
FIGURE 13. TWO-DIMENSIONAL FAST FOURIER TRANSFORM AND ONE-DIMENSIONAL SPECTRA FOR SEASAT REV. 974, POSITION A.



Two-Dimensional Fast Fourier Transform

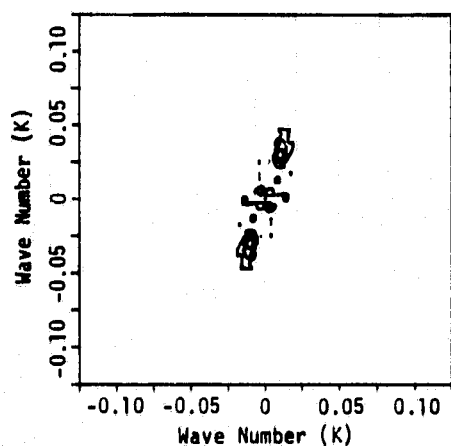


One-Dimensional Direction Spectrum

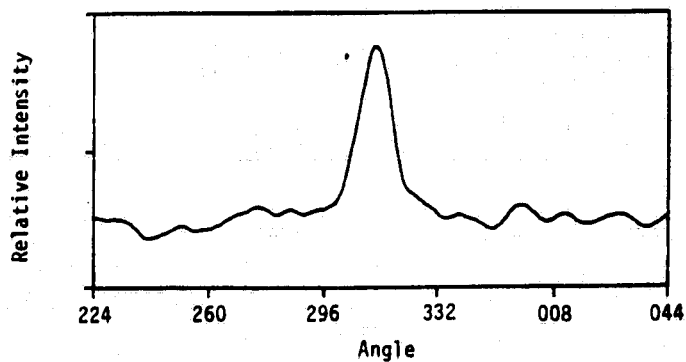


One-Dimensional Wave Number Spectrum

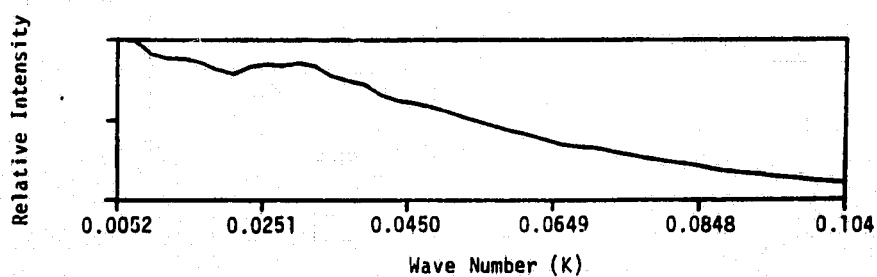
FIGURE 14. TWO-DIMENSIONAL FAST FOURIER TRANSFORM AND ONE-DIMENSIONAL SPECTRA FOR SEASAT REV. 974, POSITION B.



Two-Dimensional Fast Fourier Transform



One-Dimensional Direction Spectrum



One-Dimensional Wave Number Spectrum

FIGURE 15. TWO-DIMENSIONAL FAST FOURIER TRANSFORM AND ONE-DIMENSIONAL SPECTRA FOR SEASAT REV. 974, POSITION C.

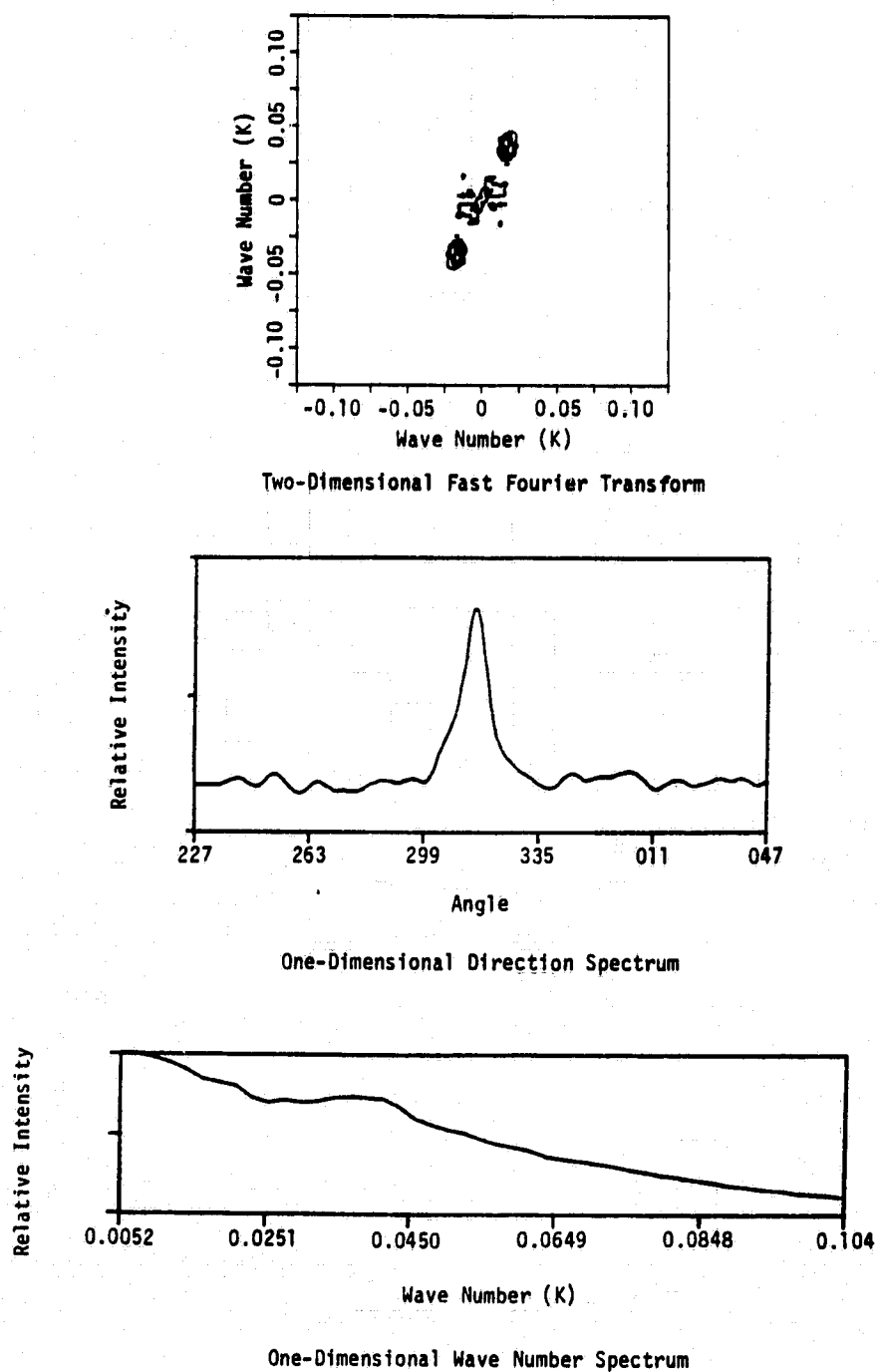


FIGURE 16. TWO-DIMENSIONAL FAST FOURIER TRANSFORM AND ONE-DIMENSIONAL SPECTRA FOR SEASAT REV. 974, POSITION D.

TABLE 5
COMPARISON OF DOMINANT WAVELENGTHS AND DIRECTIONS
FROM OPTICAL FOURIER TRANSFORMS (OFTs) AND FAST
FOURIER TRANSFORMS (FFT)

<u>Position</u> *	OFT		FFT	
	<u>Wavelength</u>	<u>Direction</u>	<u>Wavelength</u>	<u>Direction</u>
A	176 m	305°	172 m	307°
B	191 m	306°	183 m	308°
C	196 m	315°	196 m	313°
D	159 m	319°	153 m	318°

*See Figure 12.

indicates that the two are within ± 15 percent on wavelength and $\pm 11^\circ$ on wave direction. Therefore, it was determined that the baseline data accurately portrays the conditions present on the ocean surface at the time of the Seasat overflight.

3.2.3 EFFECTS OF SAMPLING RATE AND APERTURE SIZE ON SEMICAUSAL ESTIMATES

As previously discussed in Section 3.2.1, the expected advantage of using the semicausal model instead of the fast Fourier transform is that a smaller SAR data sample size is needed to produce estimates of dominant wavelength and direction. This reduction of SAR data can be accomplished in two ways:

1. reducing the number of wave cycles sampled, and
2. taking fewer samples per wave cycle.

The first data reduction can be accomplished by using a smaller aperture size, which essentially reduces the area and hence, the number of wave cycles used to generate the SC or FFT estimate. Reducing the number of wave cycles sampled has the advantage of reducing processing time (and therefore cost) and it enables the estimation of wave parameters in areas where they are changing over a few wave cycles, such as in shallow water areas where waves are refracted.

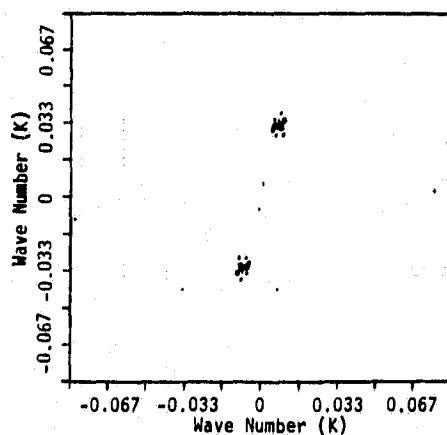
Taking fewer samples per wave cycle can be accomplished by changing the sampling rate in the SC program. It has the advantage of lowering processing times.

Two experiments were conducted to evaluate these concepts. In the first, the aperture size was held constant, while the sampling rate was varied. In the second, the sampling rate was held constant and the aperture size changed.

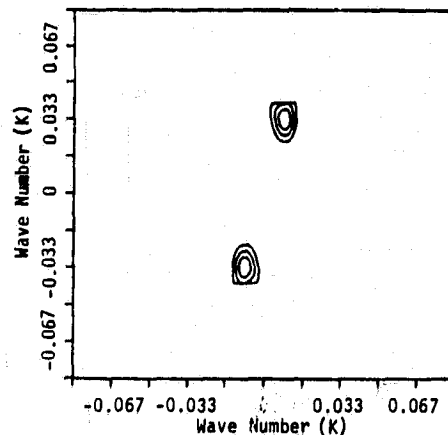
For the first experiment, position B data were used with an aperture size of 128 x 128 pixels. For an assumed wavelength of 183 meters, this would imply that approximately 17 wave cycles were included in the aperture. Three different sampling rates were tried: (1) every pixel; (2) every other pixel; and (3) every third pixel. These sampling rates are equivalent to 7 samples per wave cycle (every pixel); 3.5 samples per cycle (every other pixel), and 2.3 samples per cycle (every third pixel). The results of this experiment are presented in Figures 17-19 and Table 6. From Table 6 it can be seen that the SC and FFT estimates for each sampling size are in good agreement. Figure 17 presents the two-dimensional wave spectra for the different sampling rates while Figures 18 and 19 present the one-dimensional wave number and wave direction spectra, respectively. The only discrepancy is for the SC estimate of wave direction for the result which samples every pixel. The direction estimates otherwise match the estimate produced from the comparison data base quite closely. The wavelength data is all within approximately ± 10 percent of the baseline estimate. The conclusion to be drawn is that, when using a SAR image where waves are quite apparent (such as position B of Rev. 974), reduced sampling rates down to 2.3 samples per cycle will still produce reliable wave data for both the FFT and SC models.

For the next portion of this study, the aperture size was reduced while the sampling rate was kept constant at every other pixel. Aperture sizes used were 128 by 128 pixels (~16 wave cycles); 64 by 64 pixels (~8 wave cycles); 32 by 32 pixels (~4 wave cycles); 16 x 16 pixels (~2 wave cycles); and 8 by 8 pixels (~1 wave cycle). The above combinations were run for each test area. For position A, the data were first smoothed, and the full spectral analysis package run, resulting in the two-dimensional spectra in Figure 20, and the one-dimensional wave direction and wave number spectra in Figures 21 and 22, respectively. The SC and FFT estimates of dominant wavelength and direction for position A are summarized in Table 7.

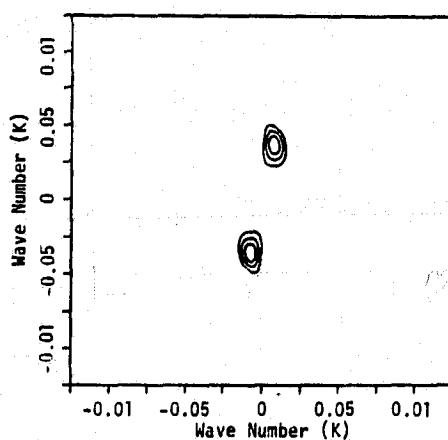
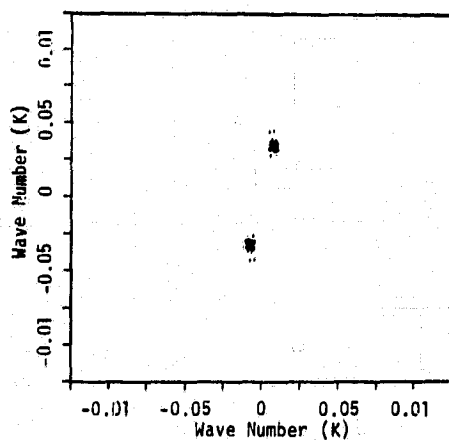
FFT



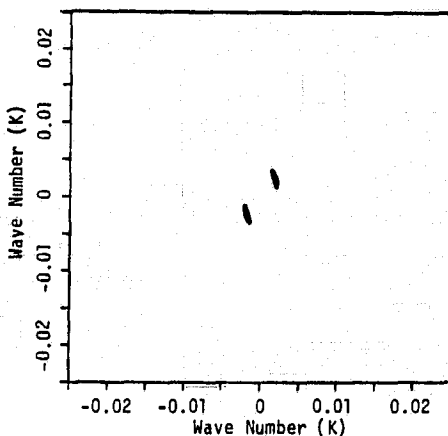
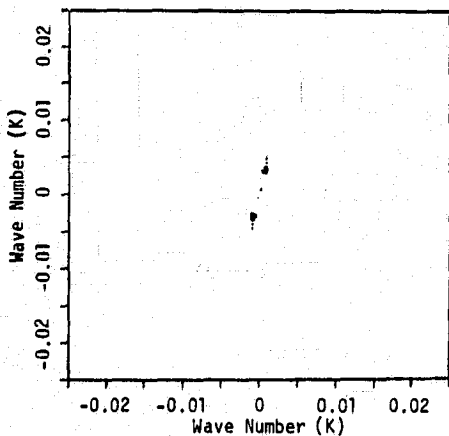
SC



2.3 Samples per Wave Cycle

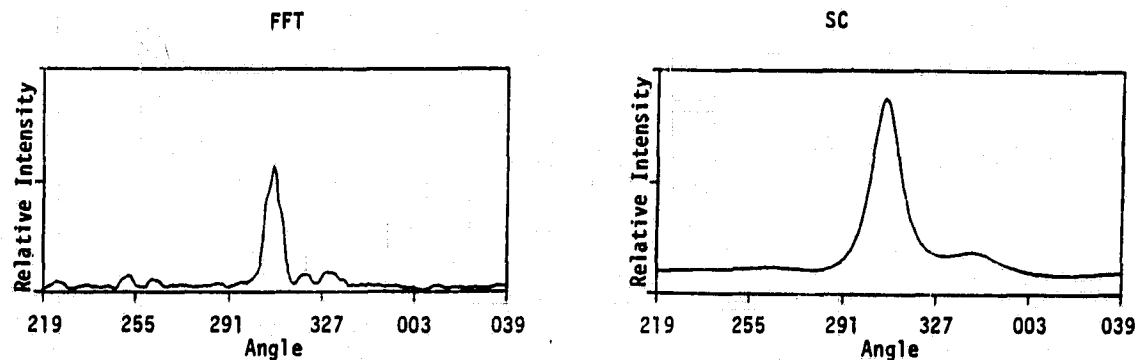


3.5 Samples per Wave Cycle

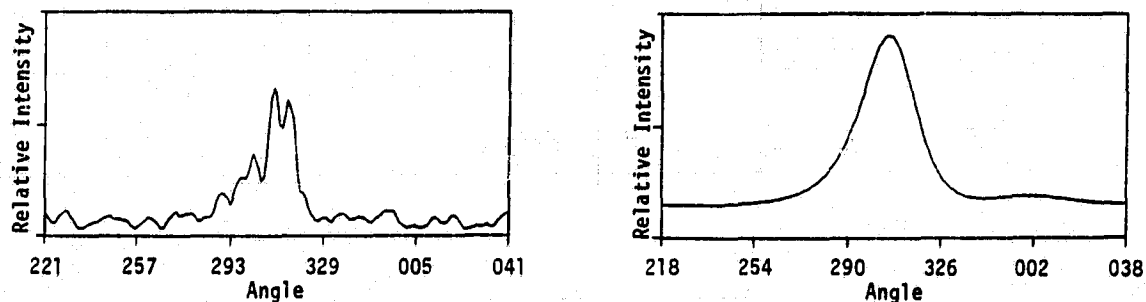


7 Samples per Wave Cycle

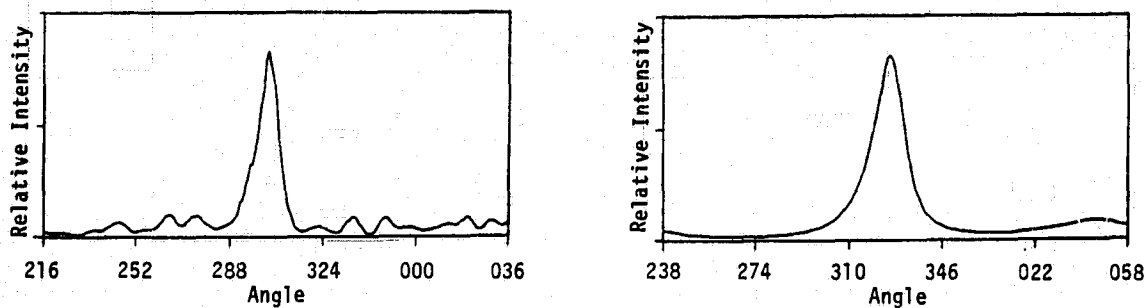
FIGURE 17. FAST FOURIER TRANSFORM VERSUS SEMICAUSAL TWO-DIMENSIONAL SPECTRA USING VARIABLE SAMPLING RATES. (A 128 x 128-pixel area from Rev. 974, Position B was used. See Figure 14 for a 256 x 256-pixel FFT of the same position.)



2.3 Samples per Wave Cycle



3.5 Samples per Wave Cycle



7 Samples per Wave Cycle

FIGURE 18. FAST FOURIER TRANSFORM VERSUS SEMICAUSAL ONE-DIMENSIONAL WAVE DIRECTION SPECTRA USING VARIABLE SAMPLING RATES. (A 128 x 128-pixel area from Rev. 974 Position B was used. See Figure 14 for the one-dimensional wave direction spectra produced from a 256 x 256-pixel FFT.)

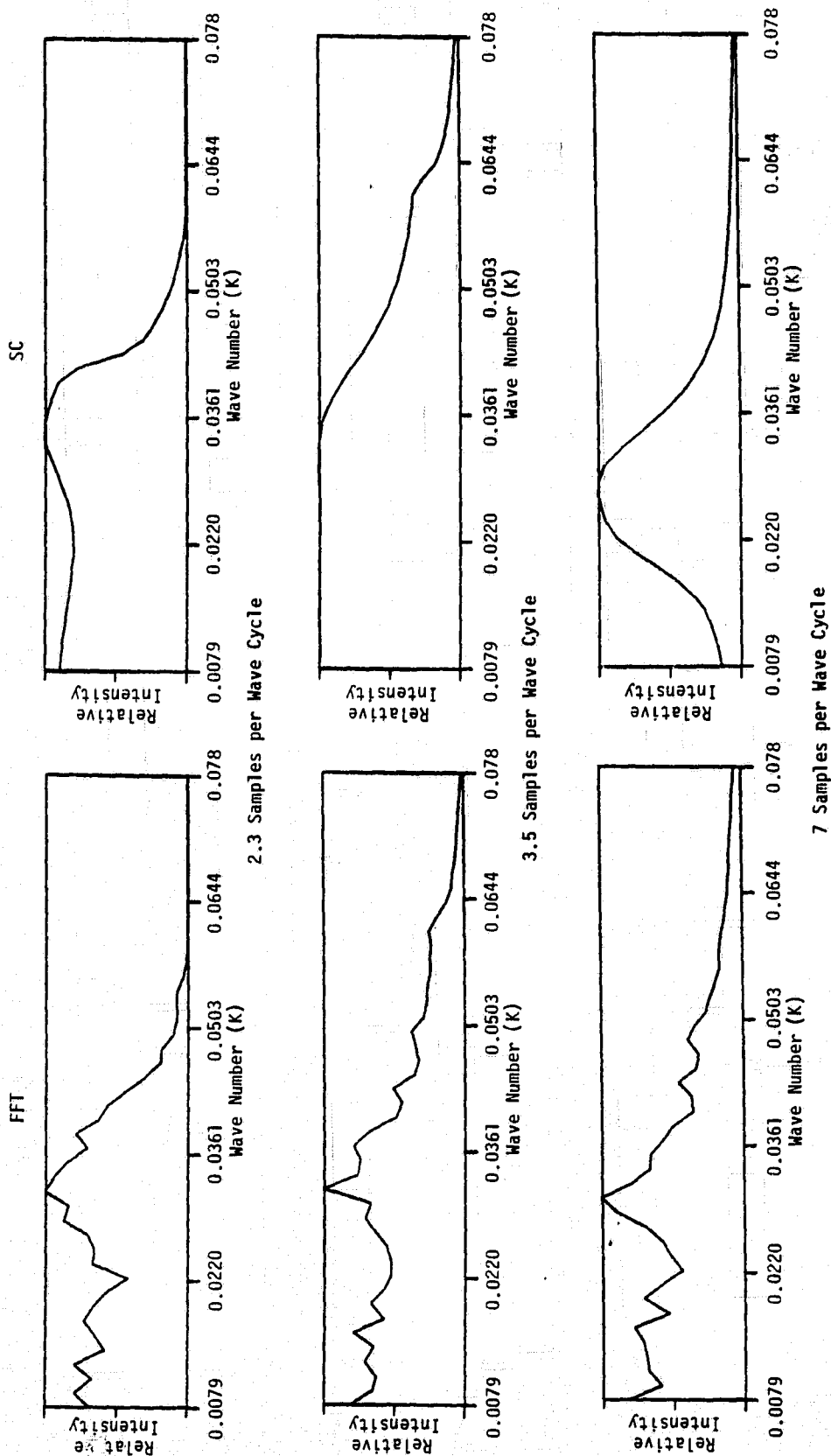


FIGURE 19. FAST FOURIER TRANSFORM VERSUS SEMICAUSAL ONE-DIMENSIONAL WAVE NUMBER SPECTRA USING VARIABLE SAMPLING RATES. (A 128 x 128-pixel area from Rev. 974, Position B was used. See Figure 14 for the one-dimensional wave number spectra produced from a 256 x 256-pixel FFT.)

TABLE 6
COMPARISON OF SEMICAUSAL SPECTRAL ESTIMATES VERSUS
FAST FOURIER TRANSFORM SPECTRAL ESTIMATES
USING VARIABLE SAMPLING RATES*

<u>Sampling Rate</u>	<u>Samples/ Wave Cycle</u>	FFT		SC	
		<u>λ</u>	<u>θ</u>	<u>λ</u>	<u>θ</u>
Every pixel	7.0	207 m	306°	197 m	328°
Every other pixel	3.5	171 m	304°	171 m	306°
Every third pixel	2.3	187 m	309°	187 m	309°

*Seasat Rev. 974, Position B data. A 256 x 256 pixel FFT of this data resulted in a dominant wavelength of 183 m and a dominant direction of 308° (T). A 128 x 128 pixel aperture (17.5 wave cycles) was used to generate the data summarized in this table.

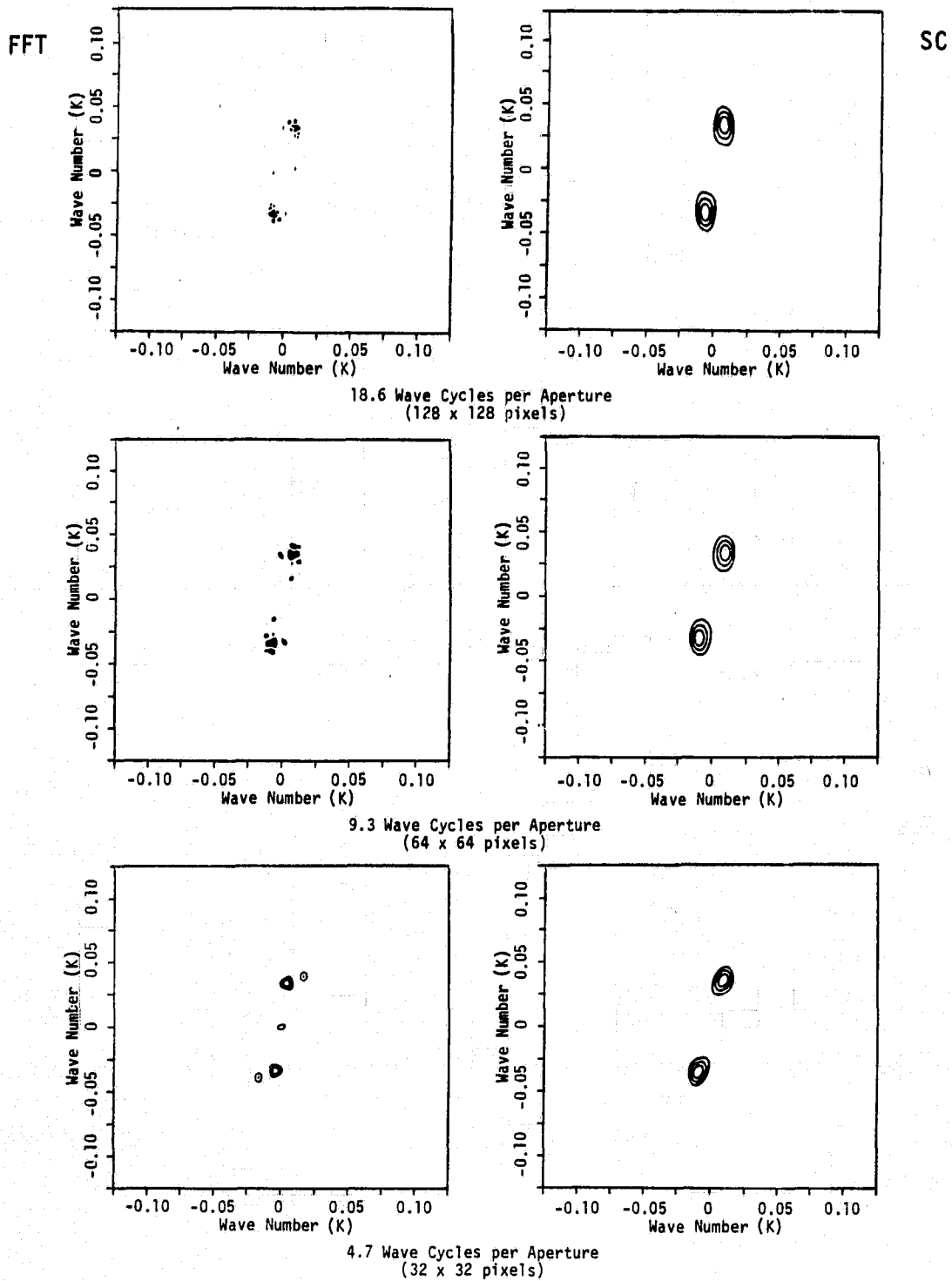


FIGURE 20. FAST FOURIER TRANSFORM VERSUS SEMICAUSAL TWO-DIMENSIONAL SPECTRA USING VARIABLE WAVE CYCLES PER APERTURE. (Seasat Rev. 974, Position A was sampled at every other pixel. See Figure 13 for a 256 x 256-pixel FFT of same area.)

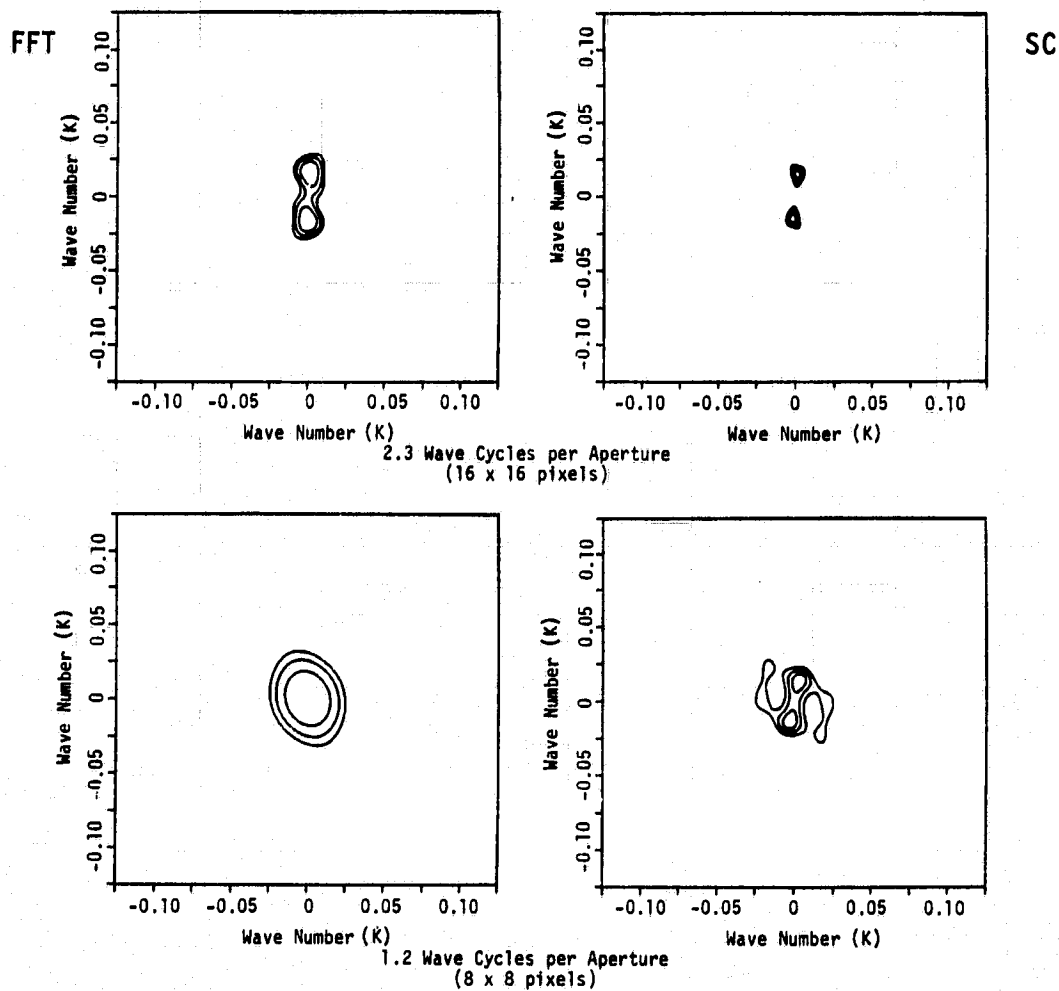


FIGURE 20. FAST FOURIER TRANSFORM VERSUS SEMICAUSAL TWO-DIMENSIONAL SPECTRA USING VARIABLE WAVE CYCLES PER APERTURE. (Seasat Rev. 974, Position A was sampled at every other pixel. See Figure 13 for a 256 x 256-pixel FFT of same area.)
(Concluded)

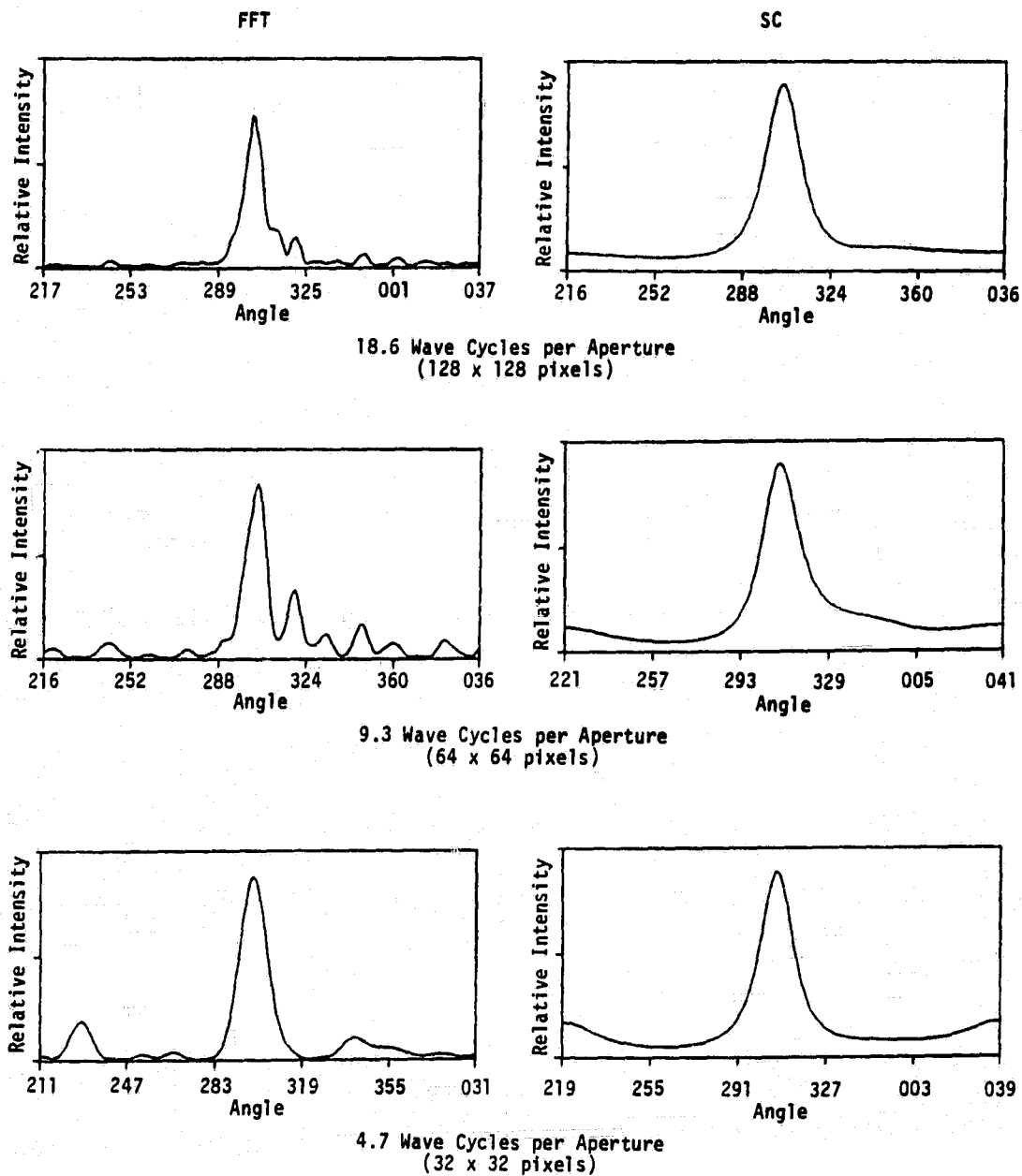


FIGURE 21. FAST FOURIER TRANSFORM VERSUS SEMICAUSAL ONE-DIMENSIONAL WAVE DIRECTION SPECTRA USING VARIABLE WAVE CYCLES PER APERTURE. (Seasat Rev. 974, Position A was sampled at every other pixel. See Figure 13 for the 256 x 256-pixel FFT results from the same area.)

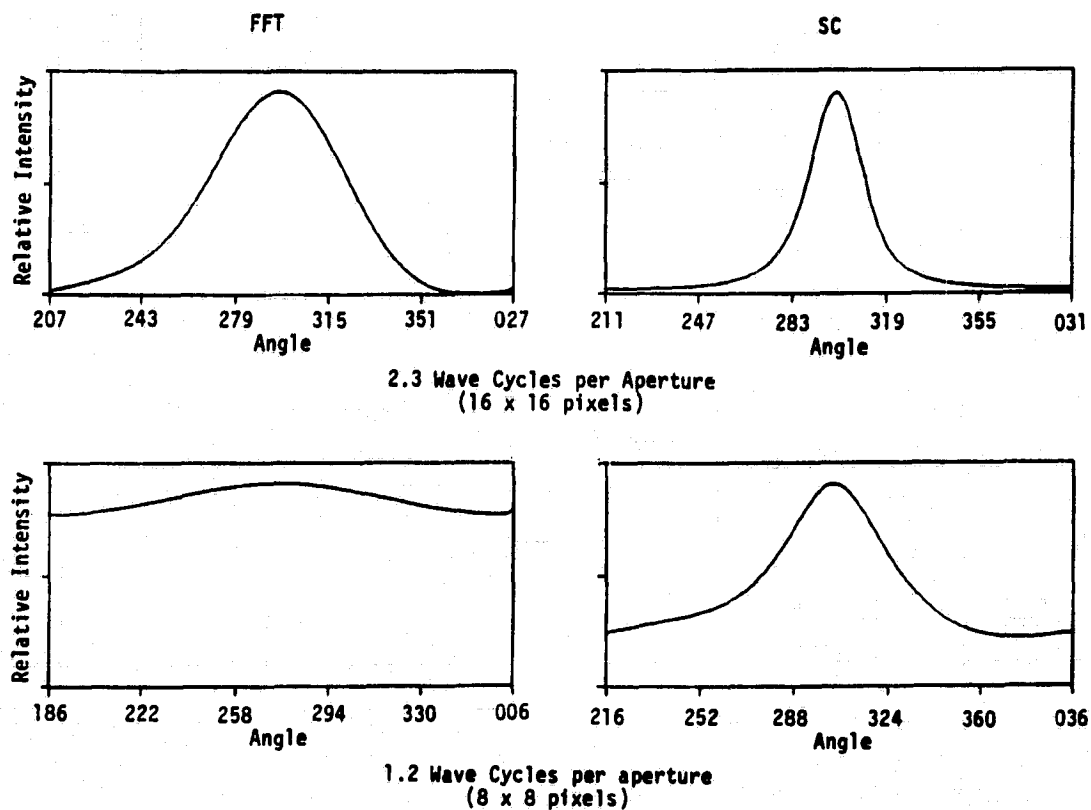


FIGURE 21. FAST FOURIER TRANSFORM VERSUS SEMICAUSAL ONE-DIMENSIONAL WAVE DIRECTION SPECTRA USING VARIABLE WAVE CYCLES PER APERTURE. (Seasat Rev. 974, Position A was sampled at every other pixel. See Figure 13 for the 256 x 256-pixel FFT results from the same area.)
(Concluded)

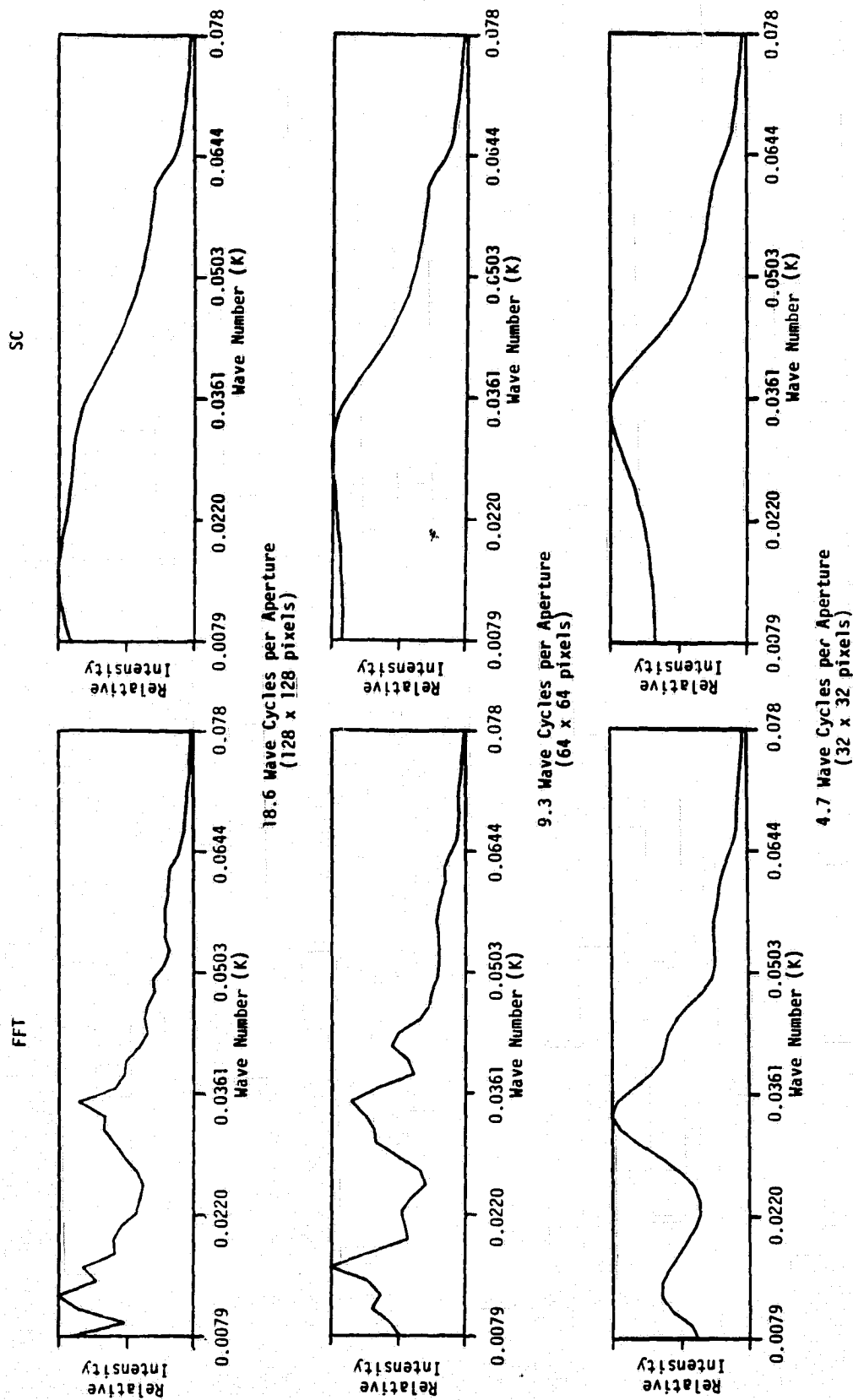


FIGURE 22. FAST FOURIER TRANSFORM VERSUS SEMICAUSAL ONE-DIMENSIONAL WAVE NUMBER SPECTRA USING VARIABLE WAVE CYCLES PER APERTURE. (Seasat Rev. 974, Position A was sampled at every other pixel. See Figure 13 for the 256 x 256-pixel FFT of the same area.)

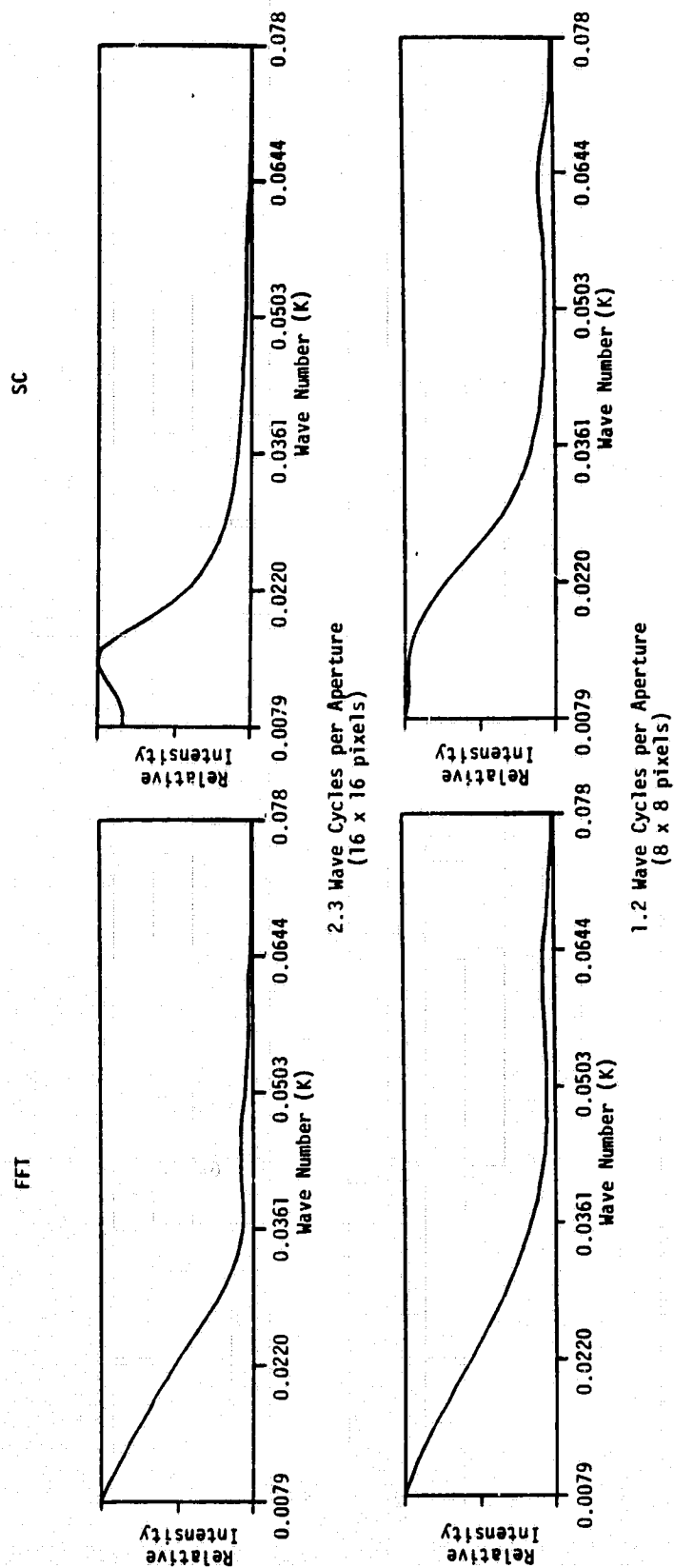


FIGURE 22. FAST FOURIER TRANSFORM VERSUS SEMICAUSAL ONE-DIMENSIONAL WAVE NUMBER SPECTRA USING VARIABLE WAVE CYCLES PER APERTURE. (Seasat Rev. 974, Position A was sampled at every other pixel. See Figure 13 for the 256 x 256-pixel FFT of the same area.) (Concluded)

TABLE 7
COMPARISON OF SEMICAUSAL SPECTRAL ESTIMATES VERSUS
FAST FOURIER TRANSFORM SPECTRAL ESTIMATES
USING VARIABLE APERTURE SIZES*

<u>Aperture Size</u>	<u>Wave Cycles/Aperture</u>	FFT		SC	
		<u>λ</u>	<u>θ</u>	<u>λ</u>	<u>θ</u>
128 x 128 pixels	18.6	178 m	308°	177 m	307°
64 x 64 pixels	9.3	178 m	307°	178 m	312°
32 x 32 pixels	4.7	183 m	302°	168 m	310°
16 x 16 pixels	2.3	366 m	298°	413 m	302°
8 x 8 pixels	1.2	not discernible		450 m	308°

*Seasat Rev. 974, Position A; A 256 x 256 FFT of this area results in a dominant wavelength of 172 meters and a dominant wave direction of 307° (T).

From Table 7, we can see that both the SC model and the FFTs produce comparable results to the comparison data down to a sampling size of approximately 5 wave cycles per aperture (32 x 32 pixels). The SC model does not appear to offer any significant improvement over the FFT approach in the estimation of dominant wavelength and direction, although the SC spectra appear to be smoother. The same comparisons were run on data from positions B, C, and D and similar results obtained. These results are summarized in Appendix C to this report.

In summary, it appears that FFTs produce comparable spectral estimates to those generated by the SC model. Results also show that using a 32 x 32 pixel aperture size (~ 5 wave cycles) with either the SC model or an FFT produces nearly the same estimate of dominant wavelength and direction as does a 256 x 256 pixel FFT. This somewhat unanticipated result appears to reinforce the utility of the FFT technique down to smaller aperture sizes than had been previously expected.

Another factor to consider in the SC/FFT comparison is the quality of the SAR-wave imagery. The gravity wave field present in the Cape Hatteras region was clearly imaged by the Seasat SAR in the areas where digital imagery was generated. It was not surprising when the FFT analysis using a reduced number of wave cycles or using a reduced number of samples per cycle produced comparable estimates (to the full 256 x 256 pixel FFT) of dominant wavelength and direction. It would probably not be possible to produce FFT estimates from SAR imagery where waves were not as clearly evident on SAR imagery as they were on Rev. 974 imagery. Whether or not the SC model could produce estimates of wavelength and direction from such data represents an area of future research.

3.2.4 EFFECTS OF NOISE ON SEMICAUSAL SPECTRAL ESTIMATES

Because the two-dimensional fast Fourier transform has been in existence and has been intensively studied for many years, the response of this spectral estimation technique to various perturbations is quite well known. An increase in Gaussian noise, for example, causes a widening in the main lobe of the two-dimensional spectrum. The width of the lobe, taken as the one-half power width (i.e., -3 dB power width) defines the Rayleigh resolution limits of the spectrum; a widening of the main lobe therefore decreases the precision of the FFT technique. If enough noise is present, the position of the lobe can shift as well. The effects of noise on the semicausal model are not well known and it was the intent of the present study to investigate them.

For the purposes of this study, a synthetically generated wave field (reference function) was used. Different levels of Gaussian noise were then added to this synthetic wave field. The signal-to-noise ratios (SNRs) tested were: 12 dB, 6 dB, 3 dB, 0 dB, -3 dB, -6 dB and -9 dB. Two-dimensional FFTs and SC contour plots were generated for each SNR level and are presented in Figure 23. To generate these estimates, only six samples and five-eighths of a wave-cycle were used. In Figure 23, we have plotted only the one-half power contours; therefore, the diameter of the contour represents the relative resolving power of the technique (i.e., either FFT or SC).

We can see from Figure 23 that even in the worst case where the spectrum is still distinguishable (i.e., -3 dB), the widening of the main lobe in the SC spectral estimate, caused by increased noise, is less than the widening of the FFT main lobe with identical added noise values. That is, in these examples, the main lobe of the semicausal spectrum is always significantly narrower than that of the FFT.

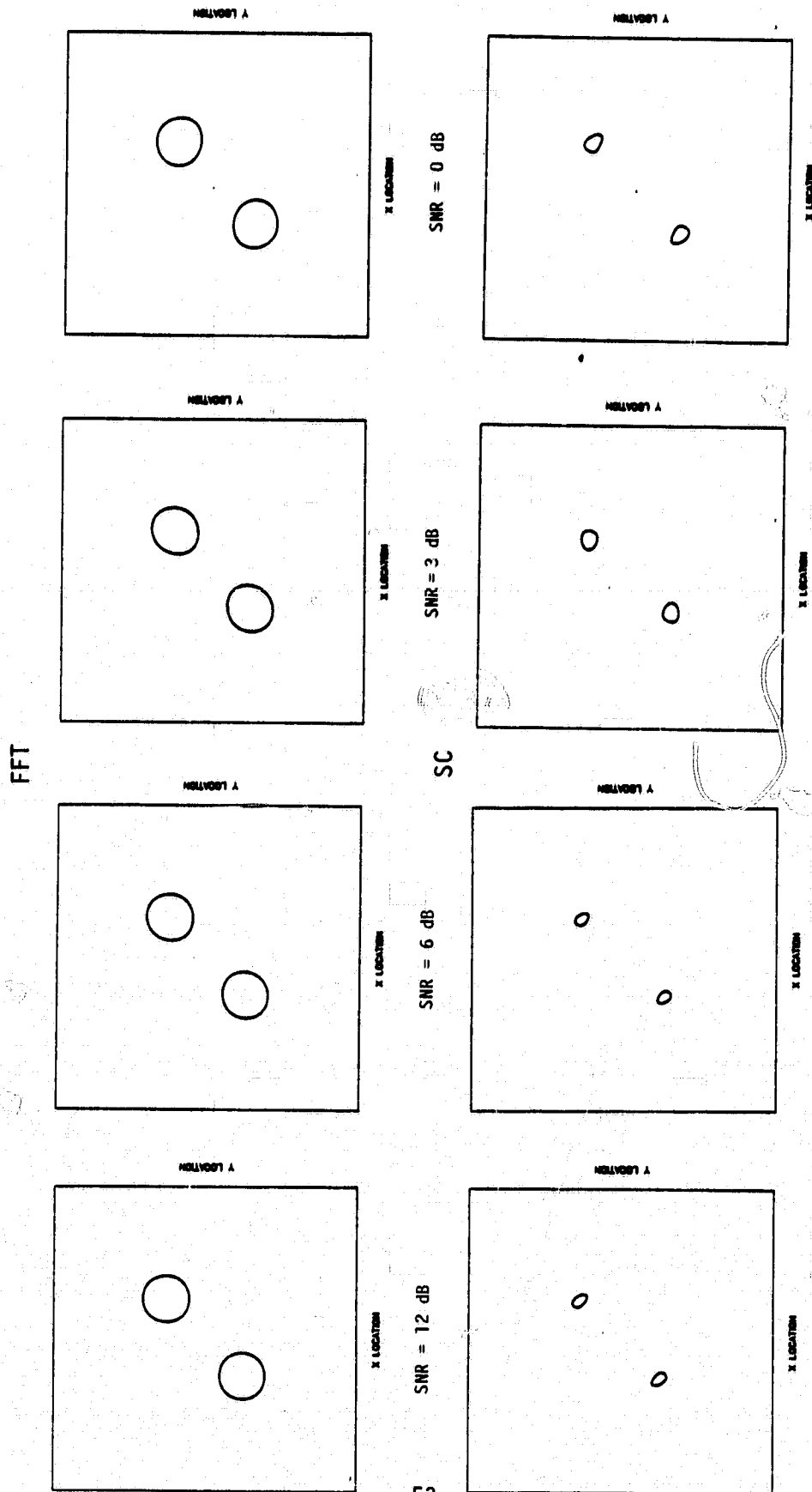


FIGURE 23. FAST FOURIER TRANSFORM VERSUS SEMICAUSAL TWO-DIMENSIONAL SPECTRAL ESTIMATES USING A TRUNCATED, SYNTHETIC WAVE FIELD AND VARIABLE SIGNAL-TO-NOISE RATIOS (SNR). (Contours are at the -3 dB level of the main lobe.)

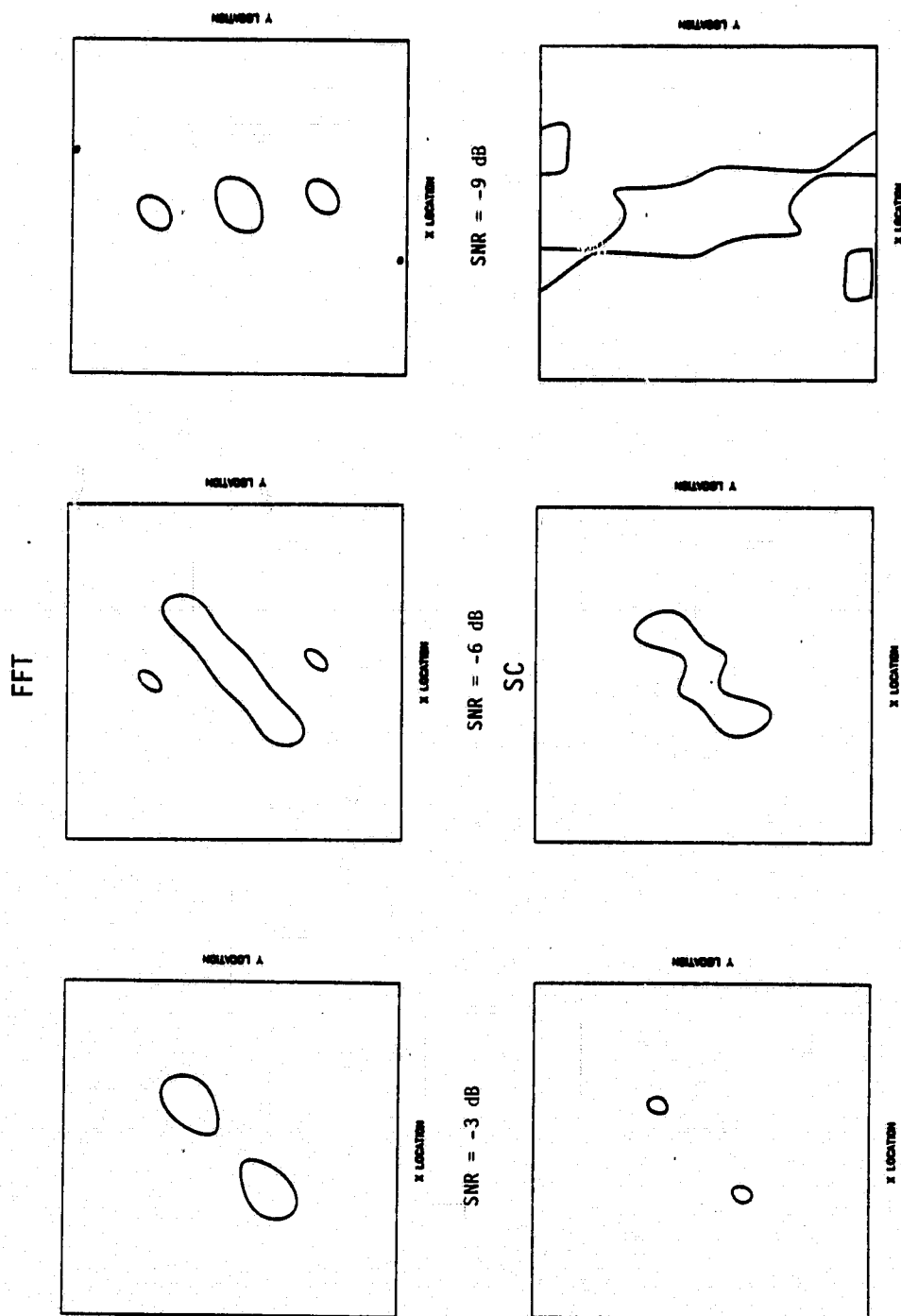


FIGURE 23. FAST FOURIER TRANSFORM VERSUS SEMICAUSAL TWO-DIMENSIONAL SPECTRAL ESTIMATES USING A TRUNCATED, SYNTHETIC WAVE FIELD AND VARIABLE SIGNAL-TO-NOISE RATIOS (SNR).
(Contours are at the -3 dB level of the main lobe.)
(Concluded)

When a small number of "noisy" samples is used in the spectral estimate, the spectrum estimated by the SC method varies somewhat depending on the set of samples selected, even though the underlying process is uniform. Figure 24 illustrates this point. The two-dimensional main lobe contours in Figure 24 were all generated using a data set with a SNR of 0 dB. In Figure 24a, the area within the main lobe of the SC estimate is approximately 1/400 of the area in the FFT lobe. In Figure 24b, this area ratio is about 1/7. Note that the FFT main lobes are essentially identical, apparently because the FFT does not resolve the differences between the noise-contaminated sample sets. In no case were the variations in the SC spectra such that the main lobe became larger than the main lobe of the FFT.

The results presented in this section indicate that Gaussian noise appears to have a less destructive effect on the resolution of the SC model than the FFT technique when a very short, truncated sinusoid is spectrally estimated. The variation of the SC main lobe can be large for different random noise inputs at identical SNR levels, but these variable main lobe widths are still smaller than those obtained with a fast Fourier transform.

3.3 MULTIPLE WAVE TRAIN DISCRIMINATION

This section of the report addresses two basic questions regarding the Seasat SAR's ability to resolve multiple gravity wave fields on a single image. The first is the SAR sensor's ability to successfully image and resolve two or more wave trains within a scene. The second is whether fast Fourier transform (FFT) spectral analysis techniques have sufficient resolution to identify multiple gravity wave trains imaged by SAR.

During the two-month 1978 JASIN Seasat experiment, surface wave measurements obtained by a pitch-and-roll buoy often indicated the

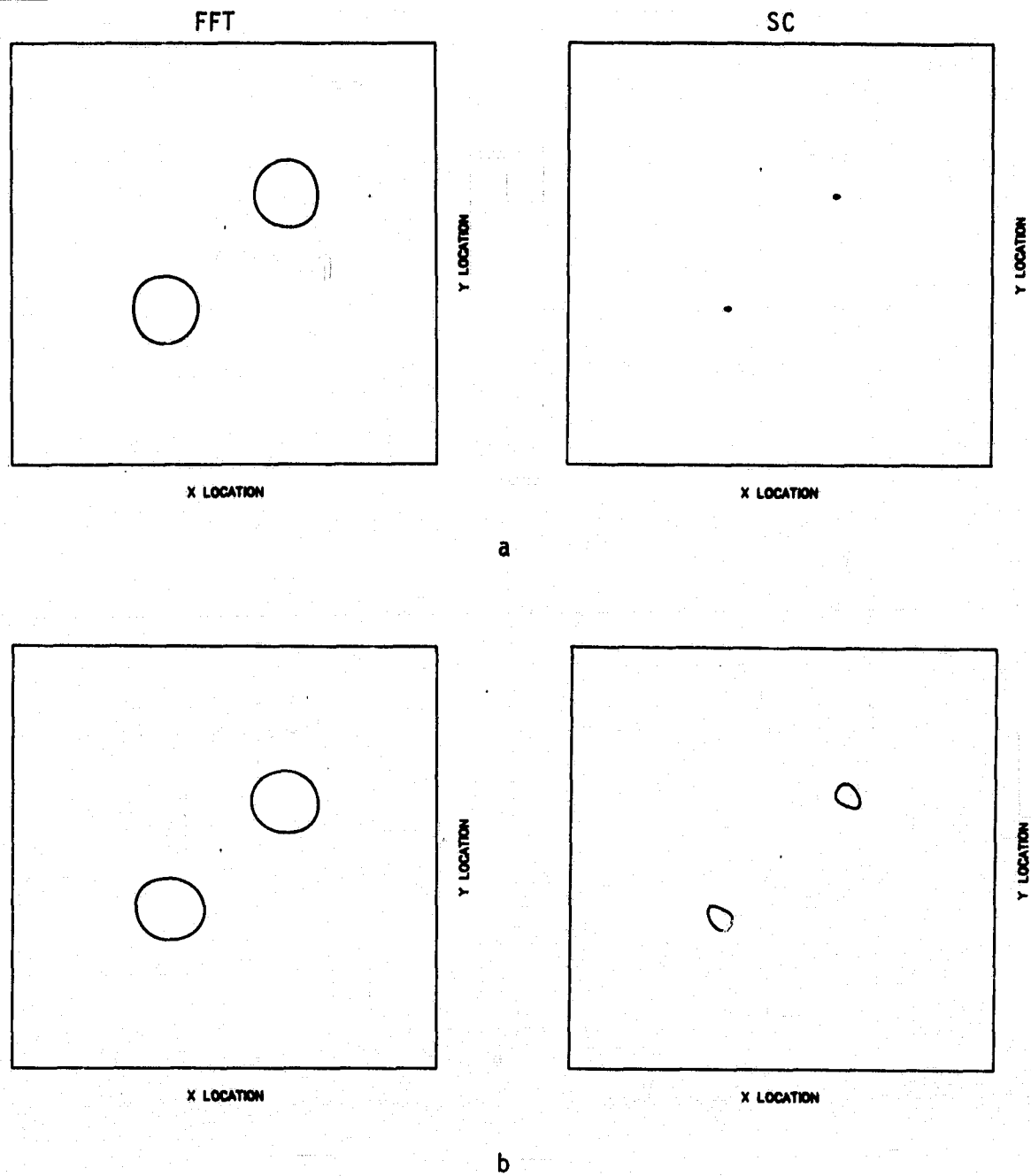


FIGURE 24. EXAMPLES OF THE EFFECTS OF RANDOM VARIATIONS IN THE BACKGROUND GAUSSIAN NOISE ON TWO-DIMENSIONAL SPECTRAL ESTIMATES OF A SYNTHETIC WAVE FIELD.

presence of two discrete wave systems present within the test site. Coincident (temporal and spatial) Seasat SAR coverage imaged either a single wave group or no waves for these cases.

The presence of multiple wave systems can result from several oceanographic processes, including: (1) the crossing of wave trains (swell) generated at different locations, (2) ocean swell passing through a region of wind-generated waves, and (3) complex diffraction occurring around islands. The relative inability of the Seasat SAR to detect multiple wave systems during JASIN raises doubts as to its utility in this application.

Beal (1980) detected two wave systems present in a section of Seasat Rev. 1339 using digital techniques. These waves had lengths of 177 and 93 meters, and were separated 20° in direction. Clearly, the Beal SAR observed waves were separated adequately in length to be detected. This however does not define the differences necessary in wave direction between two wave systems for them each to be detected. It is the directional resolving ability of the FFT technique using SAR data as an input that will be investigated here.

For this study, a portion of Seasat Rev. 1049 was used and is shown in Figure 25. The two islands in the image are St. Kilda and Boreray which are located approximately 25 km off the coast of Scotland. Figure 26 is a hydrographic chart of this test site. During this revolution, surface wave measurements made approximately 250 kms away indicated the presence of a swell with a dominant wavelength of 244 meters, significant wave height ($H_{1/3}$) of 5.0 meters, and a direction of propagation of 84° (T). These waves are visible in the SAR imagery and are observed to diffract as they pass the islands. The diffracted components appear to cross downwave of the islands. Classical wave refraction has been ruled out as a major cause of this wave bending because of the large depth values present very close to shore.

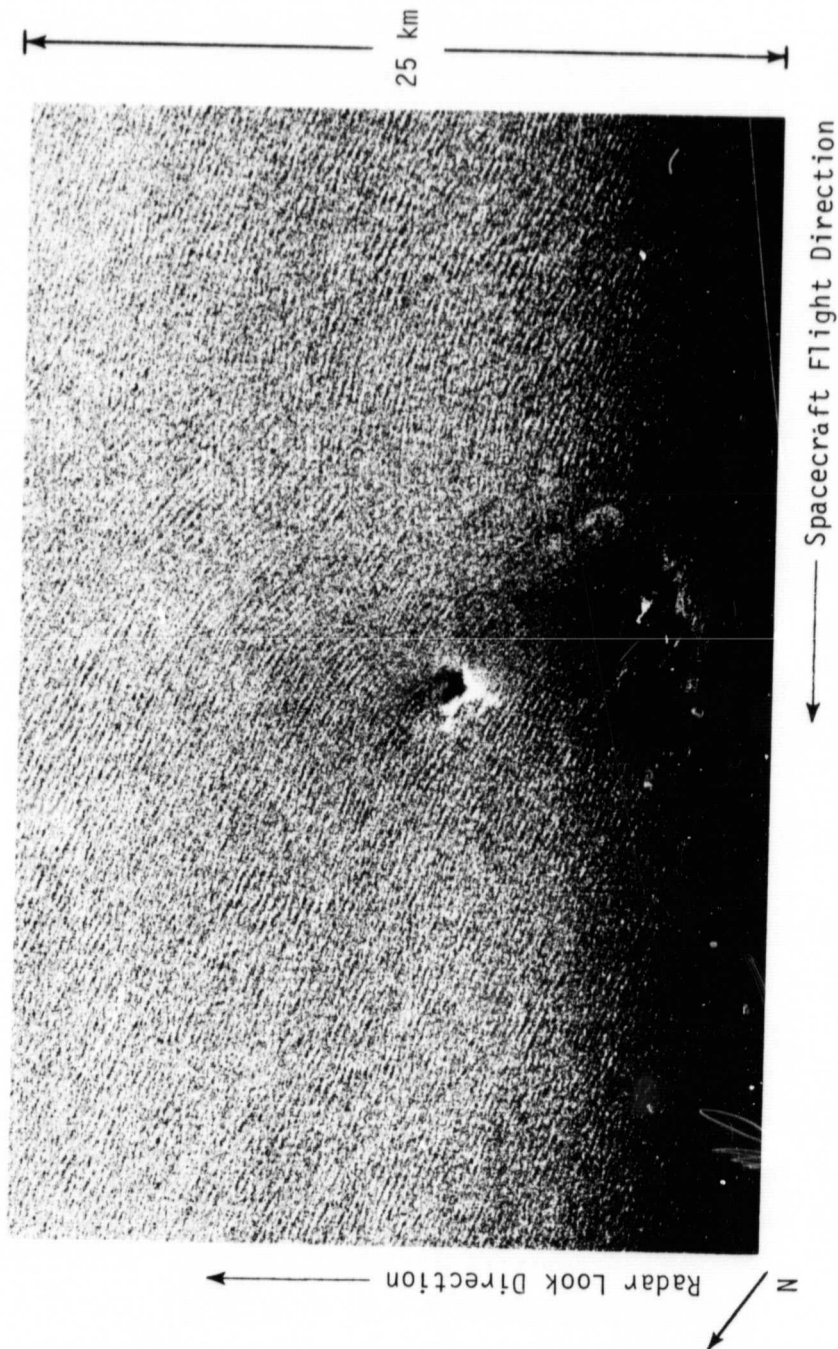


FIGURE 25. SEASAT SAR IMAGERY COLLECTED DURING REV. 1049 ILLUSTRATING WAVE DIFFRACTION AROUND AN ISLAND.

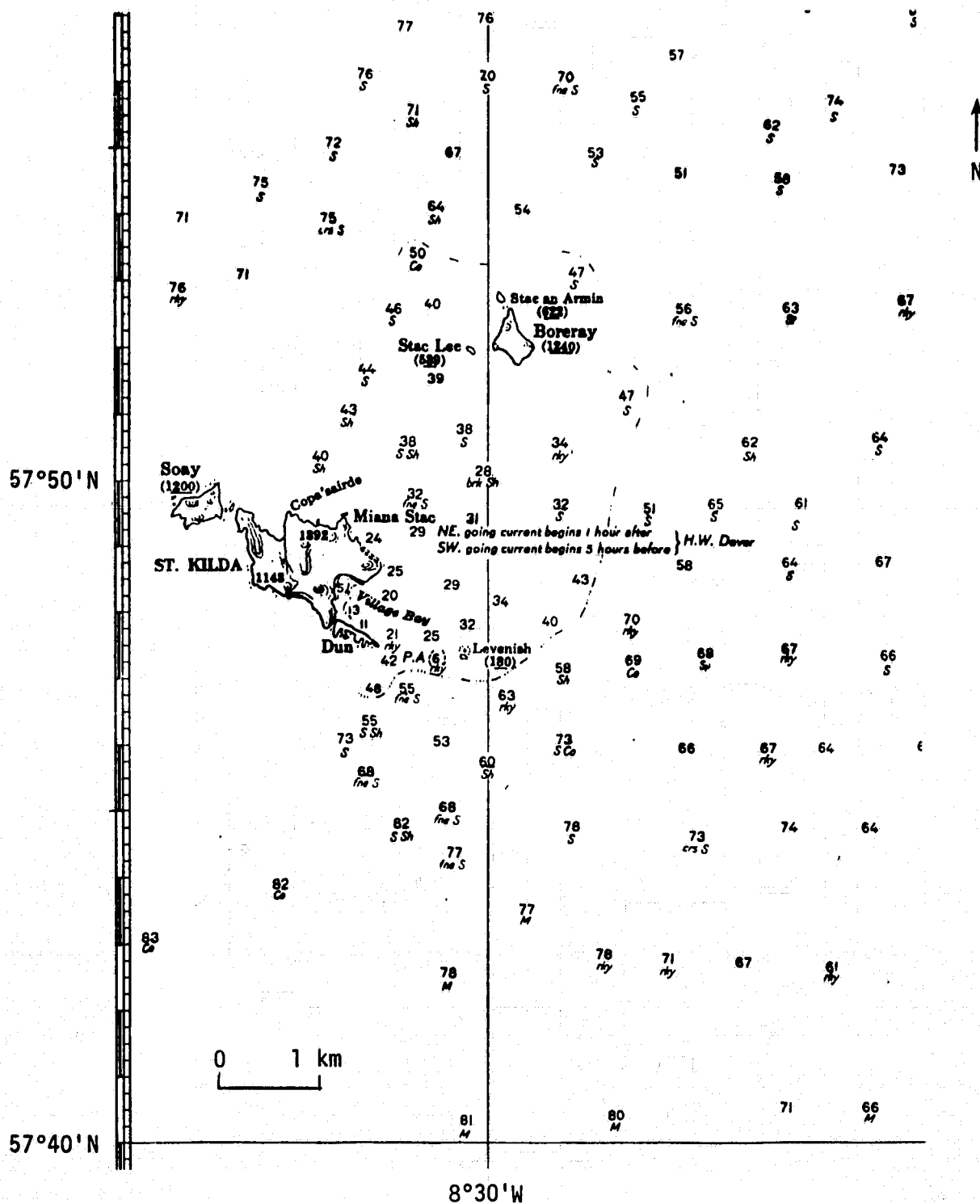


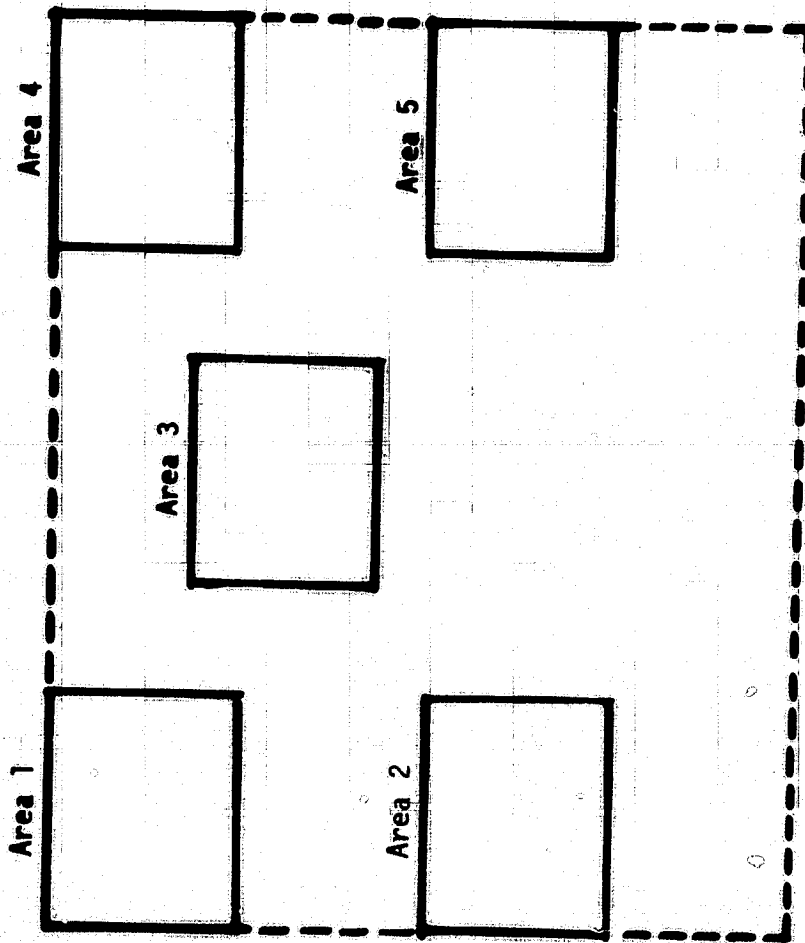
FIGURE 26. HYDROGRAPHIC CHART OF DIFFRACTION TEST AREA.
(Depth in fathoms.)

Recall that wave diffraction is the leakage of wave energy in a direction perpendicular to wave propagation. This phenomenon allows detectable wave amplitudes to be found inside the shadow region defined by geometrical optics. Diffraction does not have any appreciable effect on gravity wavelength.

To study the ability of Seasat SAR to directionally resolve more than one wave component, a section of the imagery shown in Figure 25 was digitized and fast Fourier transforms produced at five locations. Figure 27 shows the location of the digitized area as well as the locations of the five FFTs (areas 1-5). Contour plots produced from these FFTs are shown in Figure 28, and are summarized in Table 8 with respect to dominant wavelength and direction, as well as secondary wavelengths and directions when present. These results are also shown schematically by construction of wave orthogonals in Figure 29.

From these results, it appears that only one wave component is present in areas 1, 2, and 5. This is expected since these areas are not in the diffraction region. Areas 3 and 4 however do appear to contain two wave components based on analysis of the digital transforms. Enlarged contour plots from these two areas are shown in Figures 30 and 31. Examination of these enlargements indicates the spectral estimate from area 4 (Figure 31) clearly detected two discrete components. These two wave trains have equal spectral intensity as shown by the contour plot. Area 3 (Figure 30), on the other hand, has a clearly defined dominant wavelength and direction, and a less-defined secondary component. This is probably a result of this area being located only partially in the island "shadow" region.

To absolutely discriminate two wave components in a spectral estimate, they must be separated by a minimum of their -3 dB contour widths. This is analogous to spatial resolution measurements in radar. A review of the contour plots from the data set reveals an



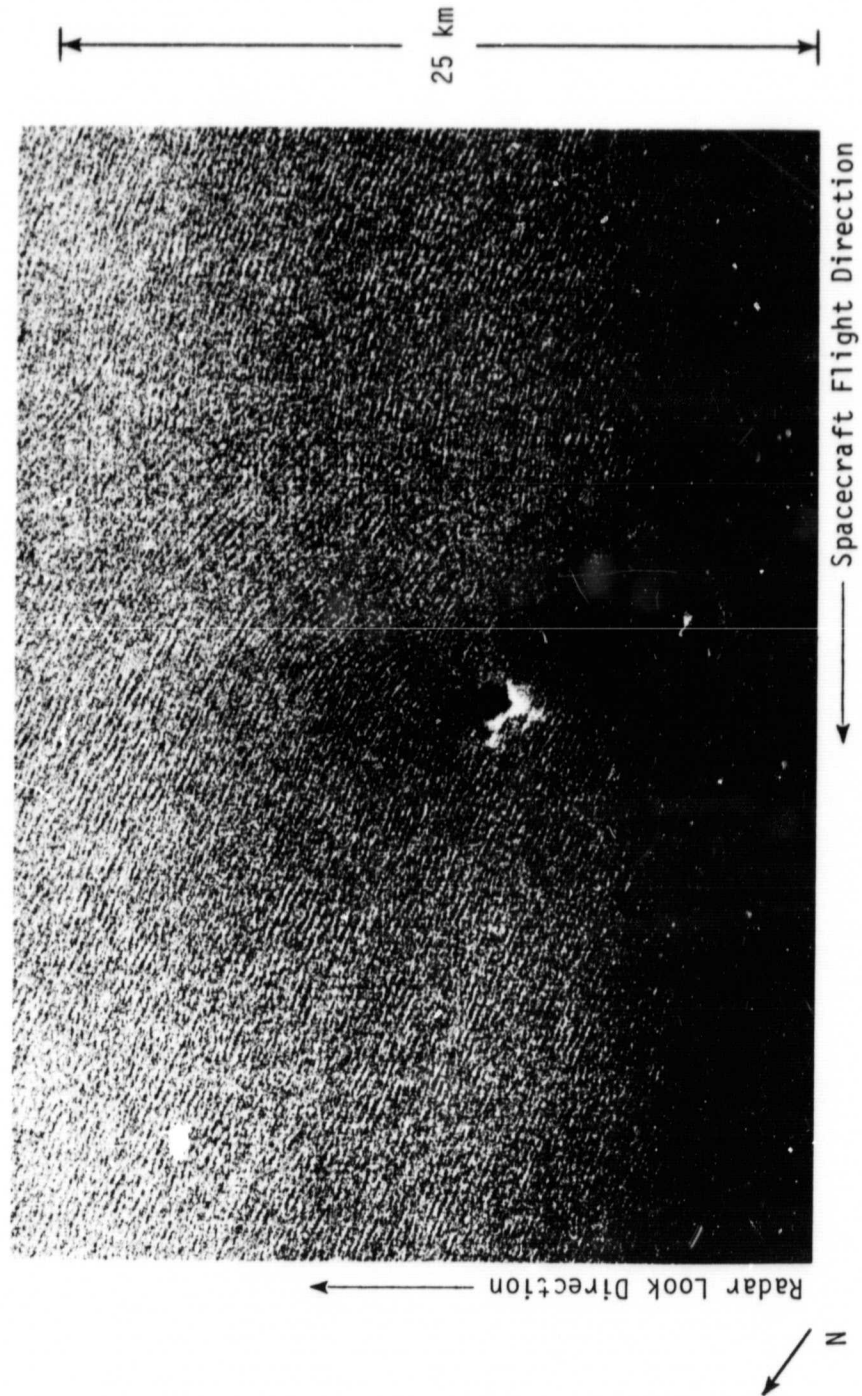


FIGURE 27. AREAS 1 TO 5 IN THE DIGITIZED SECTION (DASHED LINES) OF SEASAT REV. 1049 DATA FROM WHICH FAST FOURIER TRANSFORMS WERE GENERATED.

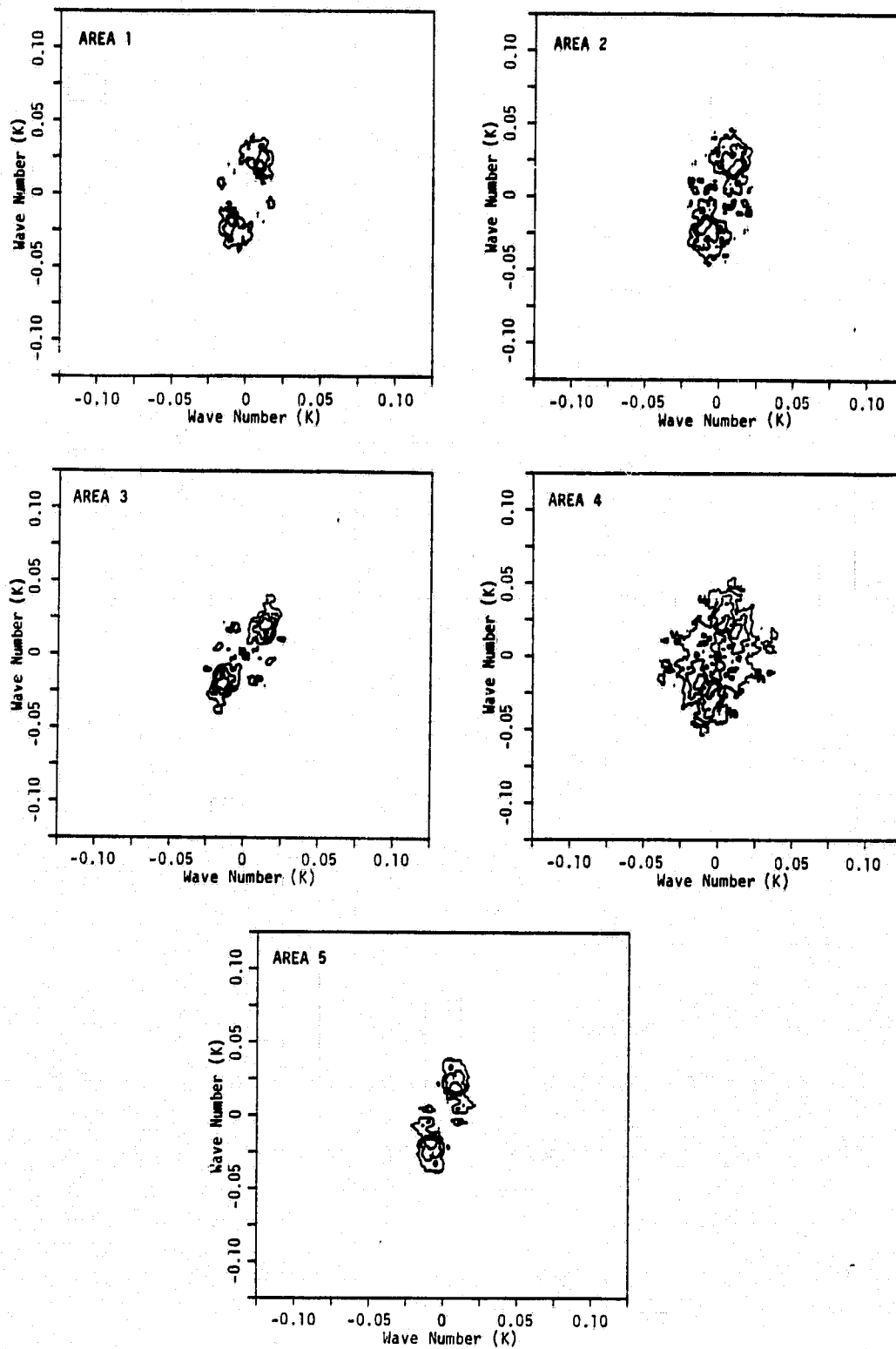


FIGURE 28. TWO-DIMENSIONAL SAR WAVE SPECTRA PRODUCED FROM SEASAT REV. 1049.
(See Figure 27 for the locations of these areas.)

TABLE 8
FAST FOURIER TRANSFORM SPECTRAL ESTIMATES FOR THE
FIVE AREAS SHOWN IN FIGURE 27

Area	Dominant		Secondary*	
	λ	θ	λ	θ
1	300 m	80°	---	---
2	300 m	78°	---	---
3	280 m	88°	330 m	101°
4	300 m	62°	300 m	85°
5	300 m	77°	---	---

*Note: For area 4, the two waves detected were of equal spectral density.

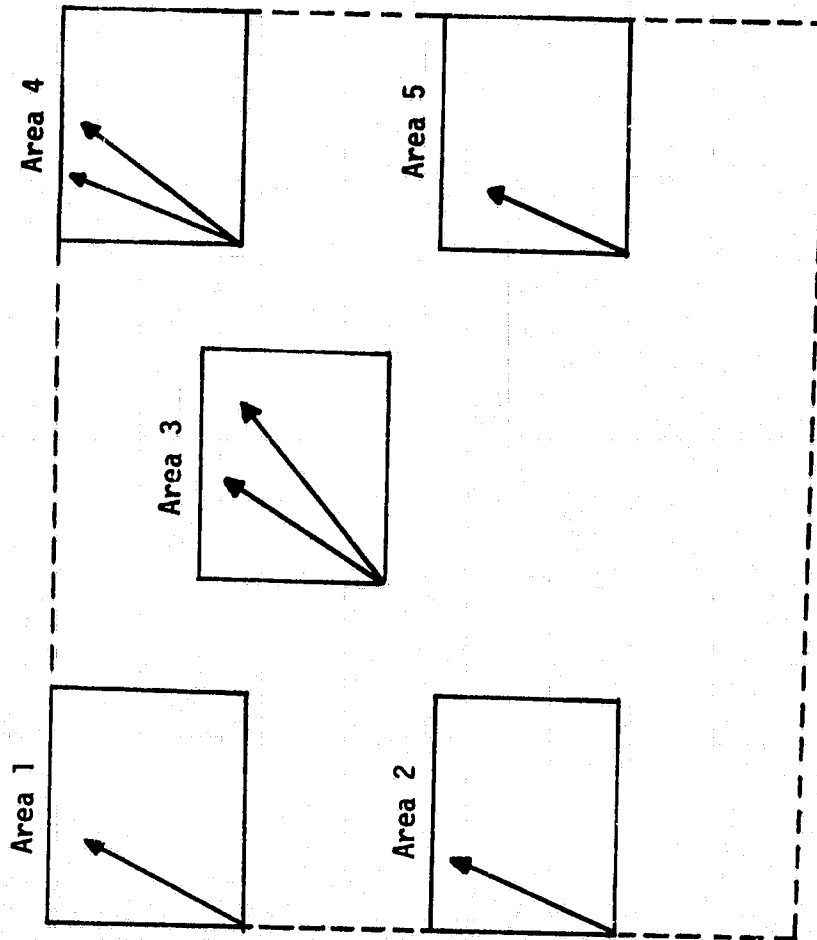


FIGURE 29. SAR-DERIVED WAVE DIRECTIONS FOR SEASAT REV. 1049
ILLUSTRATING WAVE DIFFRACTION AND DETECTION OF
TWO WAVE COMPONENTS.

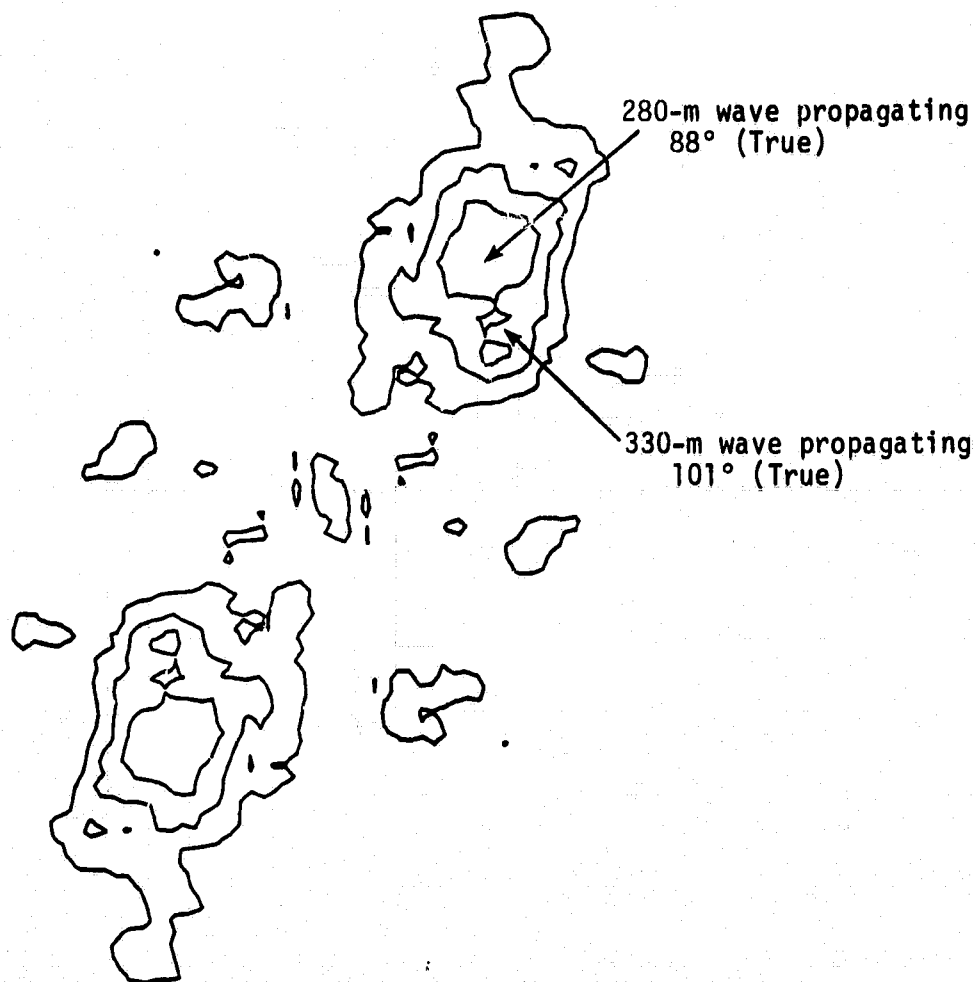


FIGURE 30. ENLARGEMENT OF TWO-DIMENSIONAL WAVE SPECTRA FROM AREA 3, SEASAT REV. 1049 SHOWING A DOMINANT AND A SECONDARY WAVE COMPONENT.

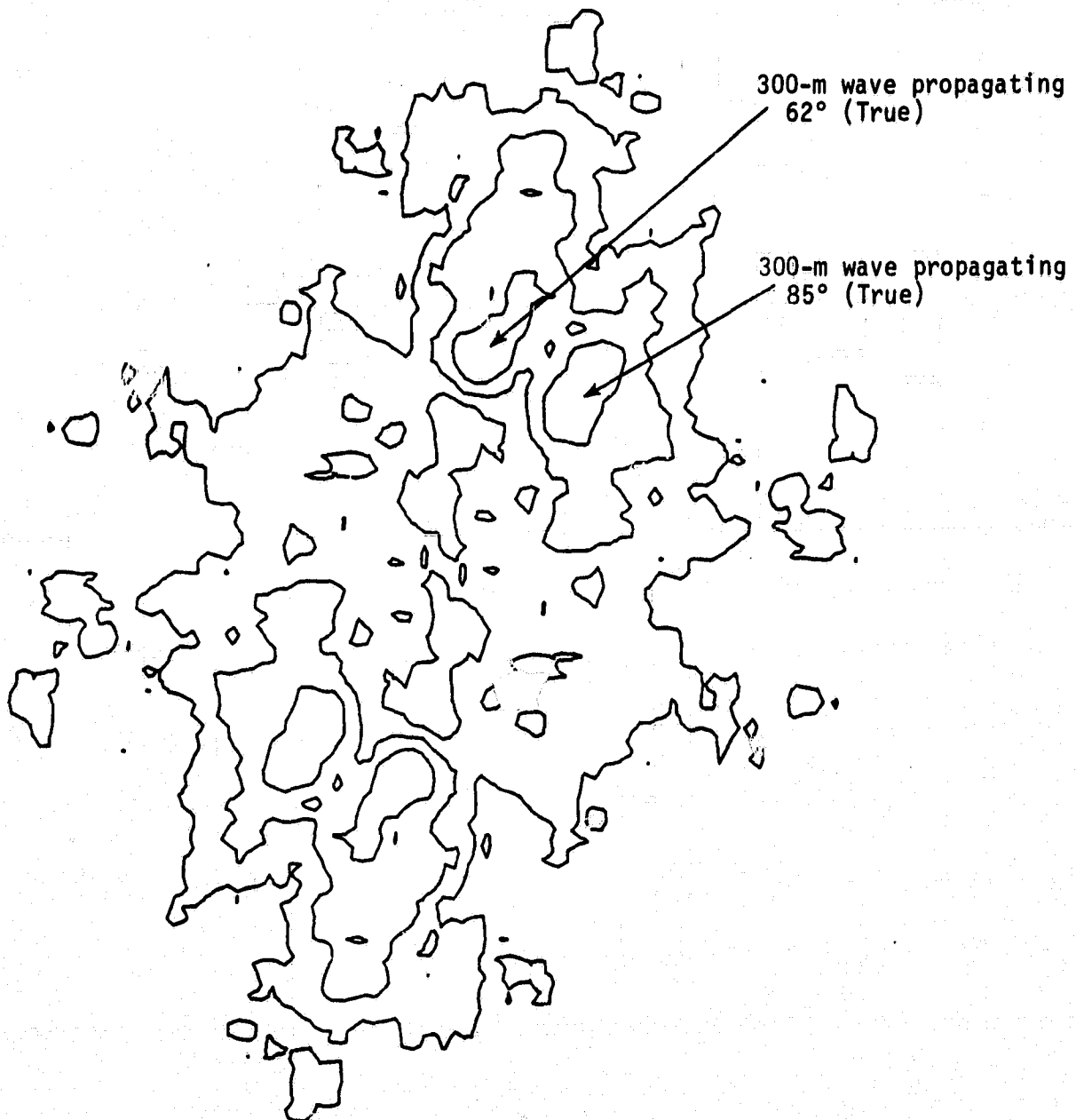


FIGURE 31. ENLARGEMENT OF TWO-DIMENSIONAL WAVE SPECTRA FROM AREA 4, SEASAT REV. 1049 SHOWING TWO WAVE COMPONENTS OF EQUAL SPECTRAL STRENGTH.

average directional width at the -3 dB contour of about 20 degrees. For this data set, it therefore appears that two wave trains present in a transformed region would have to be separated by a minimum of 20 degrees to be detected using the spectral estimation process employed here. This is supported by area 4 where two wave trains were discriminated varying 23 degrees in direction. The reader should be reminded that this -3 dB criterion holds for all cases. When waves are not imaged as clearly as those presented here, typically the directional spread of the -3 dB contour increases, thereby reducing the resolving ability of the spectral estimate.

In summary, it appears that Seasat SAR can directionally resolve more than one wave component. Due to the synoptic capability of the Seasat SAR, we were able to track the waves over 25 km, thus allowing us to observe: (1) the waves prior to diffraction, (2) the islands causing diffraction, and (3) the shadow region downwave of the islands where diffraction effects are present.

3.4 SUMMARY

The results presented in part one of this report may be summarized as follows:

1. Wave spectral estimates obtained from Seasat SAR data are not adversely affected by motion effects, and are not significantly improved by making compensations for these motion effects.
2. On the basis of synthetically generated wave data with Gaussian noise added, the semicausal spectral estimation technique appears to yield more accurate results than the FFT when small apertures are used, but
3. Using actual Seasat SAR data, the spectral estimates obtained from the semicausal technique are not significantly better than those obtained from FFT methods, even when the aperture size is reduced to approximately five wavelengths.

4. Two wave trains within a Seasat SAR image can be resolved using FFT methods if their propagation directions are separated by at least 20 degrees.

It should be noted that results (3) and (4) were obtained using Seasat data where the wave trains were very clearly imaged. It is possible that in cases where the wave image is less clearly defined, the semicausal spectral estimation technique may yield results superior to the FFT. In such cases also, the directional resolution may be reduced so that a separation of more than 20 degrees is needed to detect more than one wave component.

It is not known at the present time whether the SC model yields more accurate (higher resolution) directional and wave number information than the FFT. This is because there is no presently available sea truth accurate enough to answer this question. Additionally, very high resolution directional and wave number information is needed if we are ever to calculate currents using SAR data and wave/current interaction models. The SC spectral analysis method may, in some cases, yield slightly finer directional information than the FFT.

In view of the demonstrated utility of the optical Fourier transform technique for the measurement of the dominant wavelength and direction and the relatively high cost of generating fast Fourier transforms, the OFT technique was selected for use in the case study presented in part two of this report. This study is described in the following section of this report.

4

WAVE REFRACTION STUDIES

The purpose of this study is to investigate the capability of a spaceborne, imaging radar system to detect subtle changes in the propagation characteristics of ocean wave systems. Specifically, an evolving surface gravity wave system, emanating from hurricane "Ella" and propagating towards Cape Hatteras, North Carolina formed the basis of this case study. This wave system was successfully imaged by the Seasat Synthetic Aperture Radar (SAR) during Rev. 974 on 3 September 1978. The ground coverage of the Seasat SAR for Rev. 974 in the Cape Hatteras region is presented in Figure 32.

The acquisition of this comprehensive data set and subsequent analyses have resulted in the study of three phenomena associated with the propagation of ocean surface wave systems: the generation of the gravity waves from a hurricane, the interaction between gravity waves and a major ocean current, and the refraction of the gravity waves as they entered shallow water. To study these phenomena, the following tasks were undertaken: (1) accurate location of the generation region of these wave trains by hindcast projections; (2) detection of subtle changes in ocean surface wave propagation direction and wave number for a spatially evolving wave system; (3) measurement of the effect of a major ocean current system (the Gulf Stream) on the propagation characteristics of surface waves; (4) mapping of the magnitude and direction of major ocean current systems from these observed wave/current interactions; and finally (5) observation of bathymetric refraction in shallow water, and ultimately, extraction of depth information from these observations. This documentation and evaluation of Seasat SAR ocean surface wave imaging capability in each of these five tasks represents a definitive statement as to the potentials of a spaceborne microwave imaging system to provide routine, accurate, and reliable estimates of the dynamics of the upper ocean on a global scale.

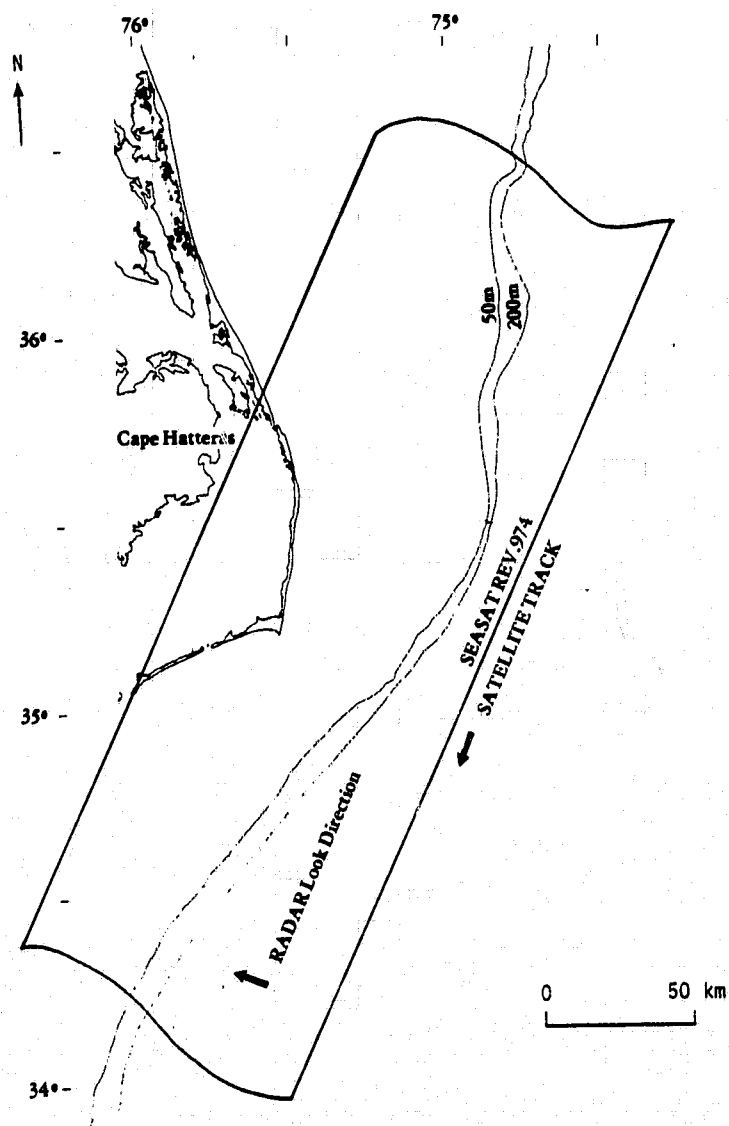


FIGURE 32. SAR GROUND COVERAGE OF SEASAT REV. 974, 3 SEPTEMBER 1978, IN THE CAPE HATTERAS, NORTH CAROLINA COASTAL REGION.

4.1 BACKGROUND

The successful completion of the five tasks outlined above can be largely attributed to the recent development of two ocean remote sensing tools. These are an analytical wave/current interaction model initially developed by Phillips (1981) and refinement of two-dimensional, Fourier transform techniques applied to ocean wave remote sensing (Shuchman, et al., 1979a). The Environmental Research Institute of Michigan (ERIM) has utilized these state-of-the-art techniques to investigate the spatial evolution of ocean surface gravity wave propagation.

During the initial ERIM study of Seasat SAR gravity wave data collected off Cape Hatteras during Rev. 974, Shuchman, et al. (1979) demonstrated it was possible to monitor the changes of wavelength and propagation direction of a gravity-wave field in coastal regions with Seasat SAR. This was accomplished by comparing depths obtained from navigational charts to depths calculated from gravity wave shoaling models which used SAR estimates of wavelength and direction as inputs. It should be noted that these results were obtained using optical Fourier transforms (OFTs) of Jet Propulsion Laboratory optically correlated SAR data.

In the previous section of this report, work was presented which evaluated various analysis techniques to precision process Seasat SAR data from Rev. 974. The investigation, utilizing scatterer motion compensation techniques to enhance Seasat SAR images of ocean waves, experimentally determined that special motion adjustments during processing of the SAR signal histories are not necessary to produce optimum wave imagery. This determination allowed the present refraction study to utilize the JPL stationary focused optical data as the primary input source.

Also discussed in the previous section was a high resolution, two-dimensional, spectral analysis technique, the semicausal (SC) model. The SC model investigation indicated that, given Seasat SAR data with its resolution of 25 meters and aperture sizes which generally include two wave trains or more, semicausal estimation techniques have no apparent advantage at the present time over the use of fast Fourier transform techniques. Furthermore, assuming that the same aperture size is used, SC methods presently possess a disadvantage with respect to higher computation cost.

The results of spectral analysis presented in the previous section further indicated the following generalizations: (1) OFT estimates of dominant wavelength and direction do not significantly vary from those produced from FFTs; and (2) fast Fourier transform analysis can be used on Seasat SAR data to differentiate between two distinct wave trains present within the same area. Thus, based on image enhancement and spectral analysis work, ERIM has confidence in its ability to properly analyze both film as well as digital products from Rev. 974.

4.2 METHODOLOGY

The purpose of this case study of gravity waves imaged by the Seasat SAR during Rev. 974 is to document and explain, through oceanographic theory, the observed changes of gravity waves as they propagate from deep water, across the Gulf Stream, and eventually into shallow water. The initial (first year) study revealed significant variations in the SAR derived wave field which could not be totally accounted for using only bathymetric wave refraction theory. In particular, the direction of propagation of the deep water waves varies considerably throughout the imaged scene. It was decided to divide this wave study into two parts: (1) analysis of deep water (>200 m depth) wave transformations; and (2) further analysis of shallow water (<200 m depth) wave transformations.

The deep water analysis explores reasons for the observed dramatic change in the gravity wave field characteristics in the deep water areas east of Cape Hatteras on the day the Seasat SAR data was collected. Reasons explored include gravity wave interactions with the Gulf Stream and the spatial variation in the evolving gravity wave field generated by hurricane Ella.

The shallow water (<200 m depth) wave analysis which follows includes comparing the Seasat observed wavelengths and directions to those obtained from a sophisticated computer-based wave refraction program. In addition, more accurate (than last year's analysis) water depth information was obtained from NOAA. Therefore, the wave refraction model used last year was also run to determine if improved results could be obtained.

As previously stated, the overall objective of this section of the report is to utilize the wave information obtainable from Seasat SAR imagery to document the complex oceanographic conditions which were responsible for wave transformations observed on SAR imagery collected during Rev. 974. The source of the waves was identified both from meteorological records as well as by wave hindcast projections. Wave rays from this source were then constructed. Using the wave/current interaction theory of Phillips (1981), these projected wave rays were refracted through the Gulf Stream, and were statistically compared to the observed set of wave rays constructed from SAR observed wave directions. Finally, using inputs from the deep water analysis, several shallow water wave refraction models were run, and the results from these models were compared to SAR observed data.

The major steps utilized for this wave refraction analysis are presented in Figure 33 and are summarized below:

1. After visual inspection of the available Seasat SAR imagery and considering known environmental conditions, 116 positions were selected to obtain two-dimensional optical Fourier transforms.



FIGURE 33. FLOW DIAGRAM OUTLINING METHODOLOGY OF EXAMINATION OF DEEP AND SHALLOW WATER WAVE REFRACTION USING SEASAT SAR DATA.

2. The 116 optical Fourier transforms, which were concentrated in the deep water region of Rev. 974, were produced and estimates of wavelength and direction were generated. From these data, wave ray diagrams were constructed.
3. The source of the gravity wave field present off the coast of Cape Hatteras at the time Seasat made its overpass was identified as hurricane Ella. Wave rays from hurricane Ella to Cape Hatteras were constructed on the basis of wave travel time which was calculated using the group velocity of the gravity waves.
4. The generating region for these waves was further confirmed as hurricane Ella by hindcast projections which utilized the SAR-derived directional spectra information.
5. Using the best available sea truth information, a velocity and directional profile of the Gulf Stream off Cape Hatteras was constructed.
6. The oceanographic theory of interactions between gravity waves and ocean currents was investigated and a wave/current interaction model selected.
7. The projected wave rays from the hurricane were refracted using the wave/current interaction model and new wave rays constructed.
8. Both the hurricane projected wave rays and the Gulf Stream refracted wave rays were then compared to the SAR observed wave rays.
9. The wave/current interaction model was inverted to estimate current velocities using wave information inputs from the two-dimensional OFTs of Seasat SAR data.
10. Using estimates of dominant wavelength and direction from the deep water analysis, two shallow water wave refraction

models were run and their results compared to SAR-derived values generated during the previous study.

11. A detailed comparison between theoretical and Seasat SAR-derived wavelengths and directions was completed.

4.2.1 DATA DESCRIPTION

Data utilized in this investigation consisted primarily of three types. These included (1) SAR-observed spectral estimates of direction and wave number of surface gravity waves emanating from hurricane Ella; (2) bathymetric data for the western North Atlantic in the region of Cape Hatteras, North Carolina; and (3) flow profiles across the Gulf Stream of surface current magnitude and direction.

In order to investigate the observed changes in surface gravity wave propagation characteristics in deep water regions off Cape Hatteras, a set of 116 optical Fourier transforms were generated from the Seasat SAR data. The areas transformed were from sub-swaths 1 and 2 from Rev. 974. The 116 locations are summarized in Figure 34. The positions are separated 12.5 kms in the azimuth direction and by 10 kms in the range direction. The circular aperture utilized to generate the OFTs had an effective ground size of 44 km^2 , or covered approximately 40 cycles of wave data. Digital analysis techniques were not employed for this study because of the large number of positions selected for investigation.

From the optical Fourier transforms, estimates of dominant wavelength and direction were obtained by choosing the area of highest light intensity on the two-dimensional spectra. By measuring the distance between the two points of highest intensity, an estimate of dominant wavelength is obtained. By measuring the relative angle of the spectral peaks, and knowing the direction of the satellite at the time the data was collected, an estimate of the dominant wave direction is obtained (for a more detailed discussion, see Shuchman, et al., 1979a). Two-dimensional wave spectra were not detectable on

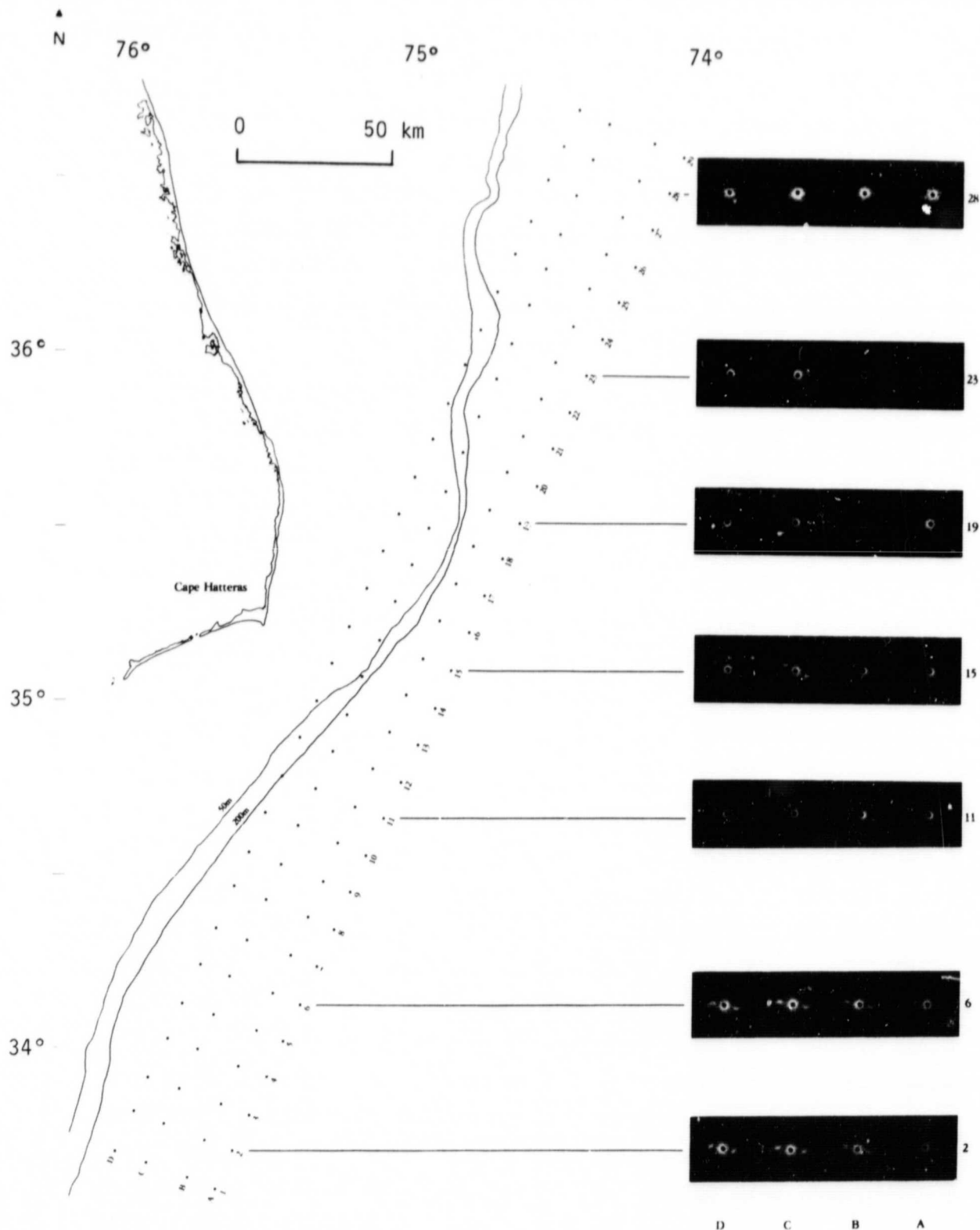


FIGURE 34. POSITIONS OF 116 OPTICAL FOURIER TRANSFORMS WITH EXAMPLES OF OFT SPECTRA. (Seasat Rev. 974, 3 September 1978.)

all the OFTs. Estimates of dominant wavelength were obtained from 99 positions and wave directions from 101 positions.

An error analysis was performed to determine the "level of uncertainty" associated with the OFT method. This analysis, presented in Appendix D, considered not only the precision of the OFT technique, but also the sources of variation in the method. It was determined that two positions had to have a difference of 5 meters in wavelength or 1.0° in wave direction before they could be considered statistically different from one another.

The bathymetric data utilized in this investigation were obtained from several sources. The first source was digital U.S. coastal hydrographic data obtained from NOAA's National Geophysical and Solar-Terrestrial Data Center in Boulder, Colorado. The data, available on a computer compatible tape (CCT) were digitized from National Ocean Survey (NOS) Smooth Sheets dating from 1930 to 1973. The area for which this digital data was obtained is outlined in Figure 35. The other source of data, for the areas studied which were outside the coverage in Figure 35, was from NOAA and Defense Mapping Agency navigational charts.

The position as well as the velocity of the Gulf Stream is temporally varying. One observation of the Gulf Stream meander reported by Fuglister and Worthington (1951) indicates the Gulf Stream shifts its position in an easterly or westerly direction at a rate of approximately 20 kilometers per day. Earlier estimates of the Gulf Stream surface velocity range from 1 to 1.2 m/sec by the dynamic computation method (Iselin, 1936) and from 2 to 2.5 m/sec by the Loran system and bathythermography (Iselin and Fuglister, 1948). Many other investigators (Worthington, 1954; Von Arx, 1962) also found that the maximum surface speed is around 2 m/sec. The speed is a maximum near the center of the Gulf Stream and decreases gradually toward both boundaries. In general, the rate of decrease is slower in the outer (eastern) side than in the inner (western) side

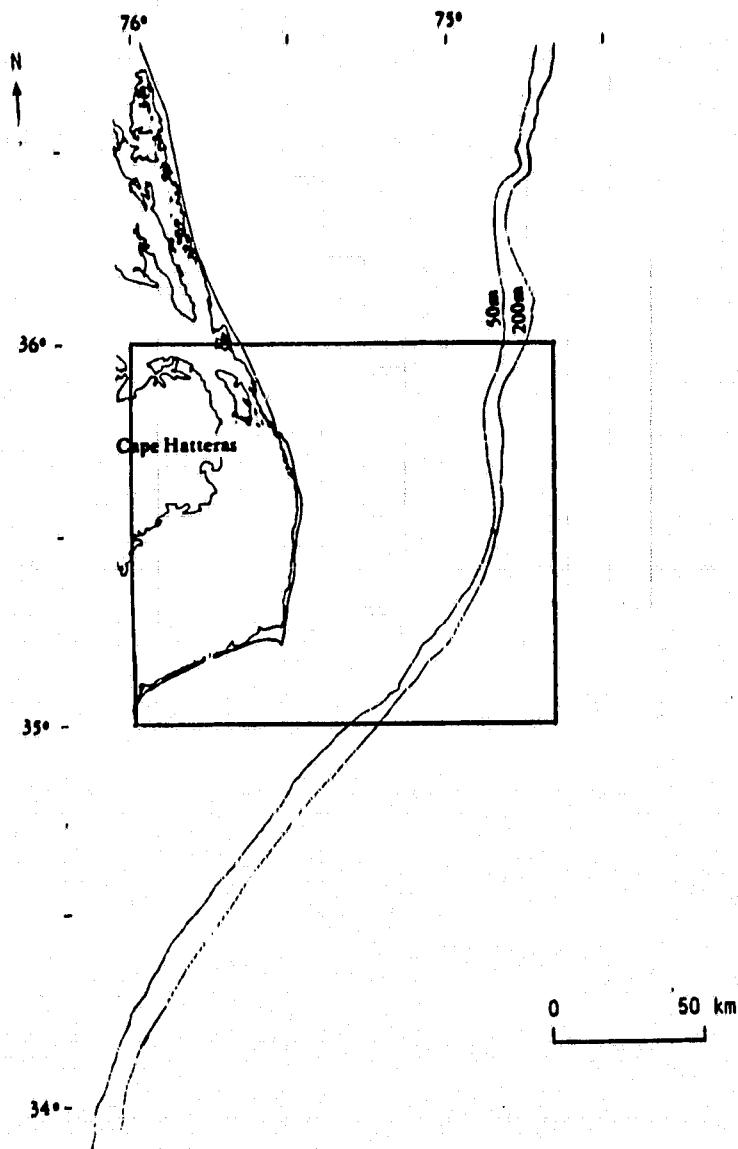


FIGURE 35. AREA OF DIGITAL DEPTH DATA AVAILABLE FROM NOAA NATIONAL OCEAN SURVEY SMOOTH SHEETS, 1930-1973.

of the Stream. The United States Coast Guard Oceanographic Unit has been publishing weekly sea current charts for specific areas, which include the Gulf Stream region. These charts are produced by a subjective analysis of all available data: bathythermographs (BT), airborne radiation thermometry (ART), satellite slope files, shelf files and other miscellaneous sources such as weather charts and current charts produced by other agencies. In order to study wave/current interactions across the Gulf Stream, available sea truth information was obtained from the weekly sea current chart prepared by the U.S. Coast Guard on August 30, 1978 (Anonymous, 1978). Figure 36 was reproduced from the southwestern part of this chart. The current speed is observed to be highest (2 m/sec) in the center portion of the Stream and to decrease gradually toward either side. The figure also shows that the rate of decrease in current speed is slower toward the outer boundary than toward the inner boundary.

The surface gravity wave fields studied in this investigation were generated by hurricane Ella. By consulting meteorological weather maps, it was determined that hurricane Ella was situated southeast of the Gulf Stream at about Latitude $32^{\circ}30'N$ and Longitude $72^{\circ}30'W$ and moving toward the northeast when the Seasat SAR made its overpass of Cape Hatteras (including the Gulf Stream) on September 3, 1978 (see Figure 37). However, since the hurricane generated waves require time to propagate to the Gulf Stream, the hurricane position from which these waves were generated would have been some place southwest of the above-mentioned position. These waves were also assumed to be generated and to be propagating in a direction tangential to the hurricane radius of 30 kilometers (a little less than 1.5 times of the radius of maximum wind velocity (Ross, 1981)), with an average group velocity of 30 km/hr. This group velocity was calculated from the average wave number measured by the SAR near the outer boundary of the Gulf Stream. The required traveling time from the above-mentioned hurricane center to the outer boundary of the

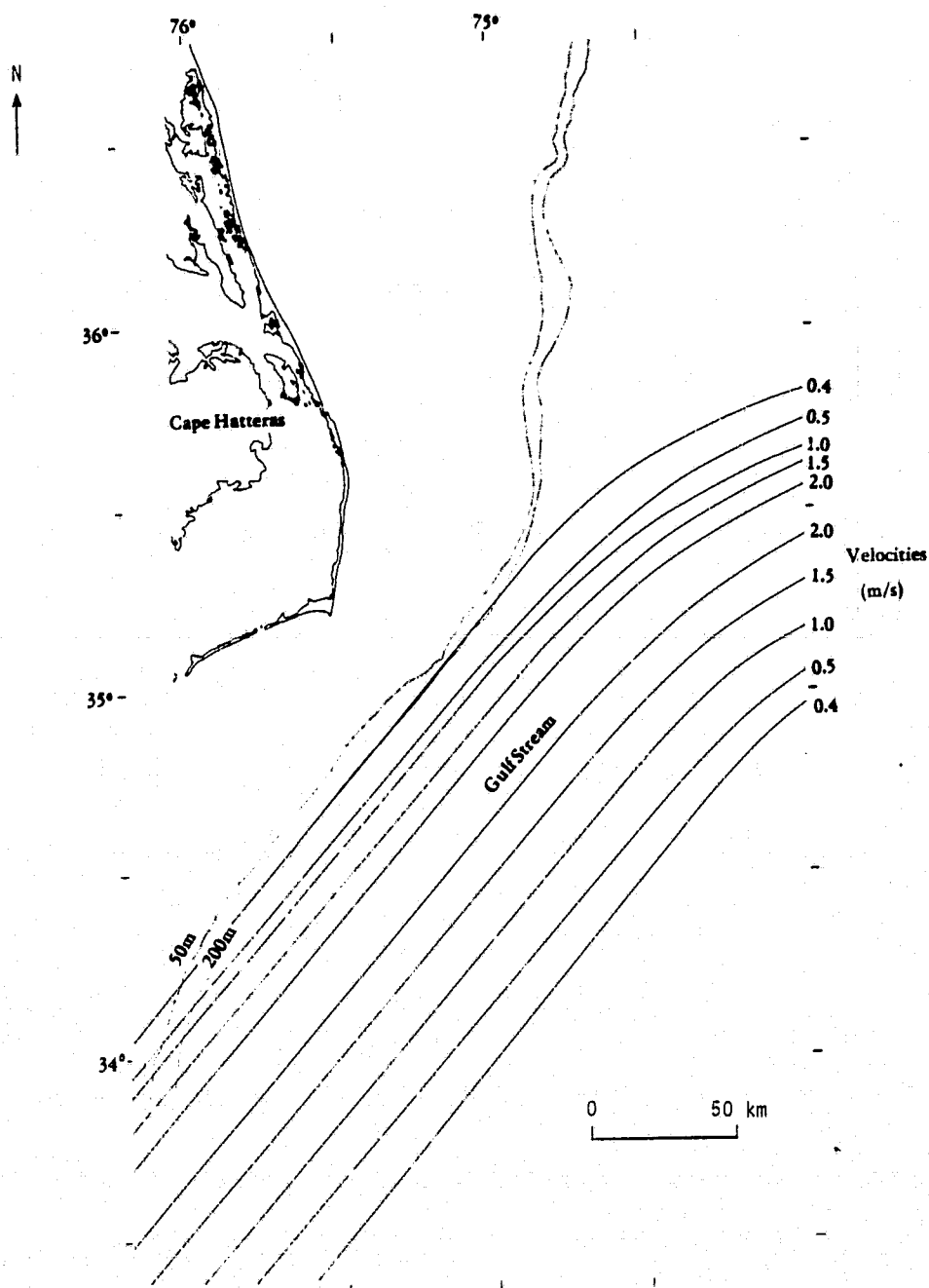


FIGURE 36. GULF STREAM FLOW CONDITIONS ON 30 AUGUST 1978.
(Taken from U.S. Coast Guard Sea Current Chart.)

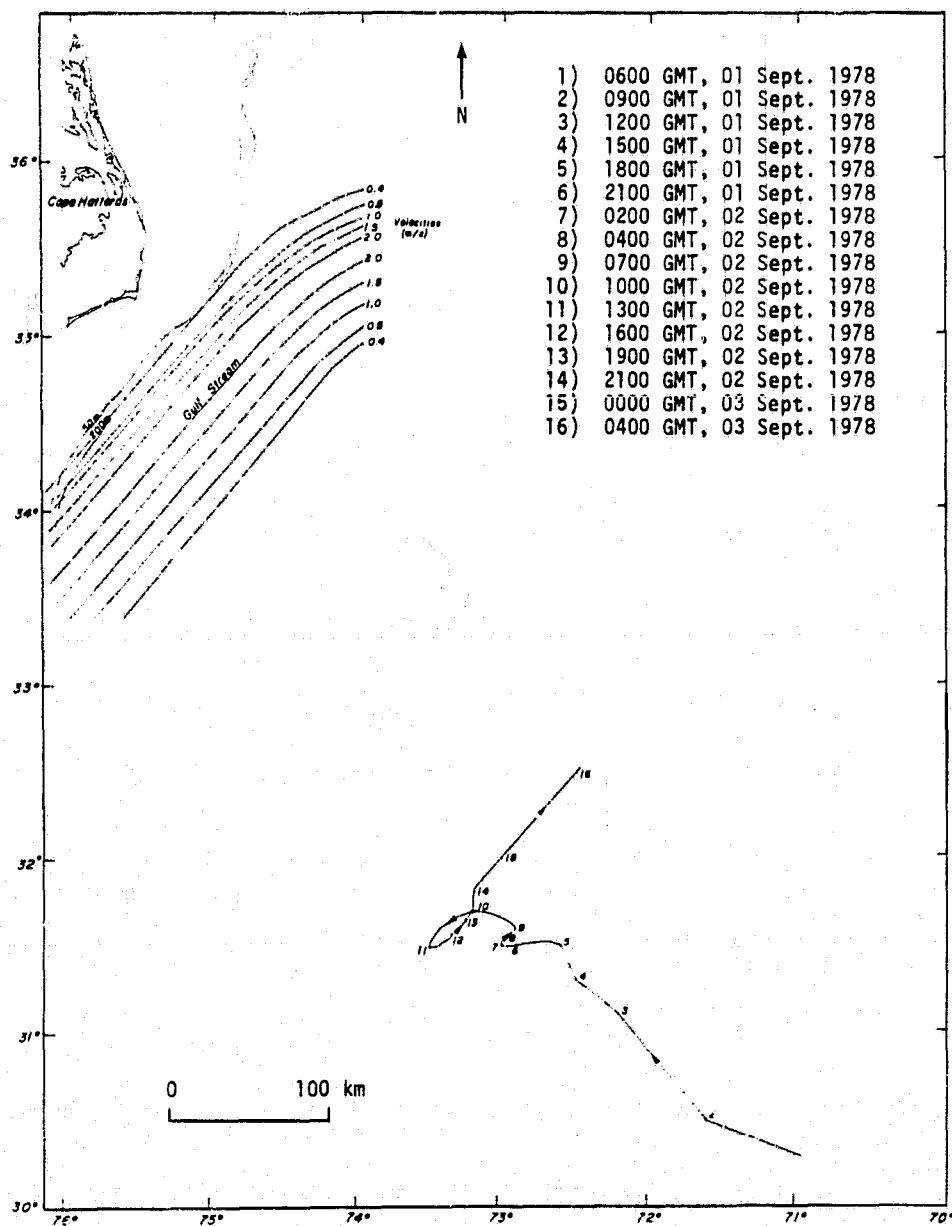


FIGURE 37. POSITION OF HURRICANE ELLA FROM 1 THROUGH 3 SEPTEMBER 1978.

Gulf Stream in the southern portion of the study area is approximately 10 hours. This time period allows us to locate, from the trace of the hurricane center, the actual area responsible for the wave propagation to the Gulf Stream. This actual center is located at Latitude $31^{\circ}30'N$ and Longitude $73^{\circ}14'W$. The input sea conditions (wave rays) were obtained from the extension of the tangential lines from a circle of radius 30 kilometers from the hurricane center. The position of hurricane Ella at the estimated time of wave propagation into the northern sector of Cape Hatteras, along with the projected wave rays, is presented in Figure 38. Figure 39 illustrates an enlargement of the Cape Hatteras region with the projected wave rays. Note these projected wave rays do not include the effect of wave/current interaction after entering the Gulf Stream.

Once the waves from hurricane Ella have been refracted by the Gulf Stream and emerged from the western edge of the stream, a shallow water (<200 m depth), bathymetrically-controlled refraction analysis was performed. Using dominant wavelengths and directions determined by the deep water analysis as inputs, two shallow water wave refraction models were run. The first model was based on Airy wave theory, while the second model was a computer-based program developed under NASA sponsorship (Poole, et al., 1977). The shallow water wavelengths and directions obtained from these models were statistically compared to SAR estimates generated during the initial study of Rev. 974 (Shuchman, et al., 1979).

4.3 ANALYSIS OF DEEP WATER WAVE TRANSFORMATIONS

Upon detailed examination, it was concluded that considerable variation existed in the dominant wavelengths and directions in the deep water regions off Cape Hatteras which were covered by Seasat Rev. 974, at 0300 (GMT) on 3 September 1979 (see Figure 32). In order to more accurately assess the shallow water wave refraction models, it was first necessary to explain this deep water variation.

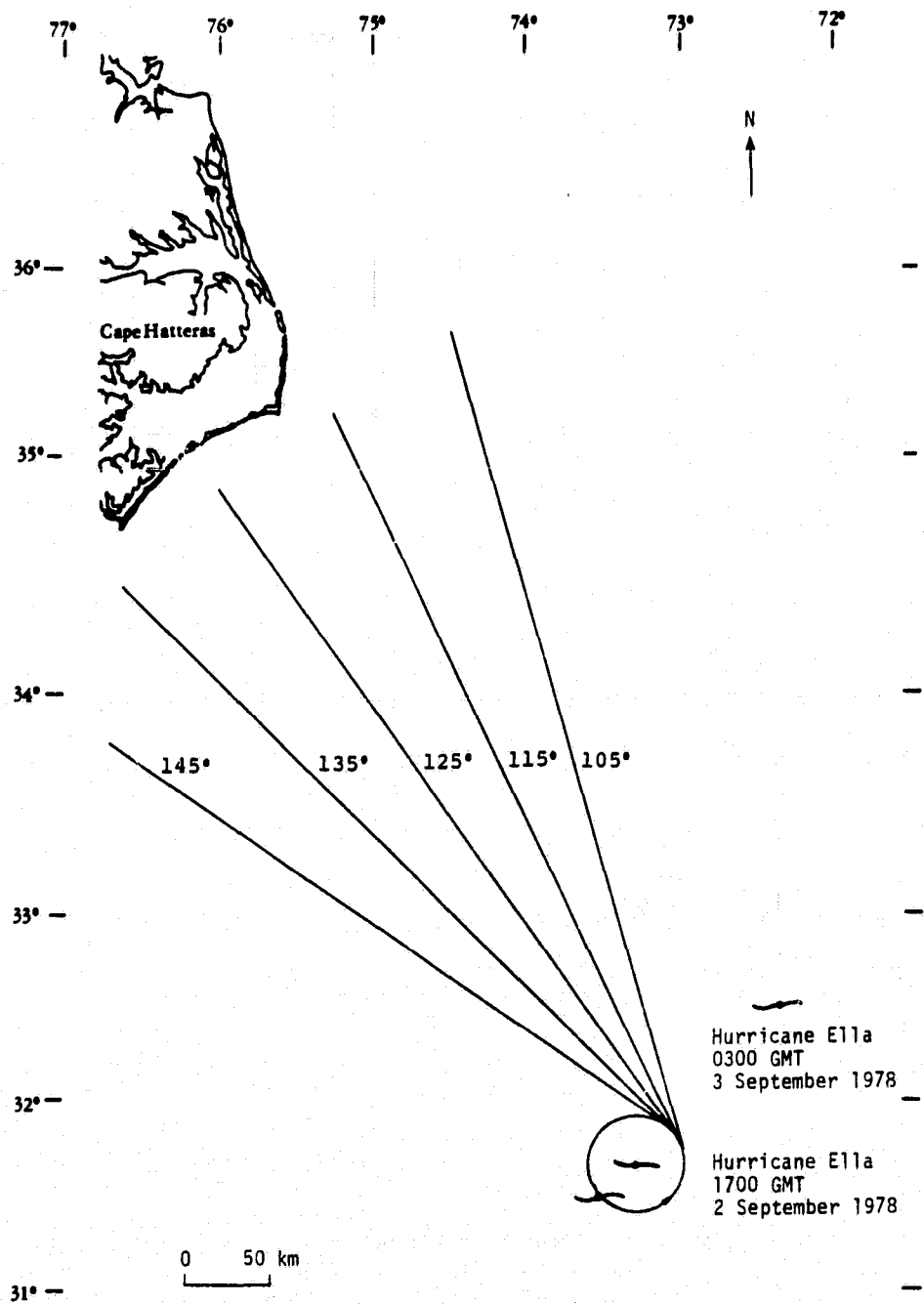


FIGURE 38. INPUT SEA CONDITIONS FROM HURRICANE ELLA.
(Angles measured from the east and
counterclockwise.)

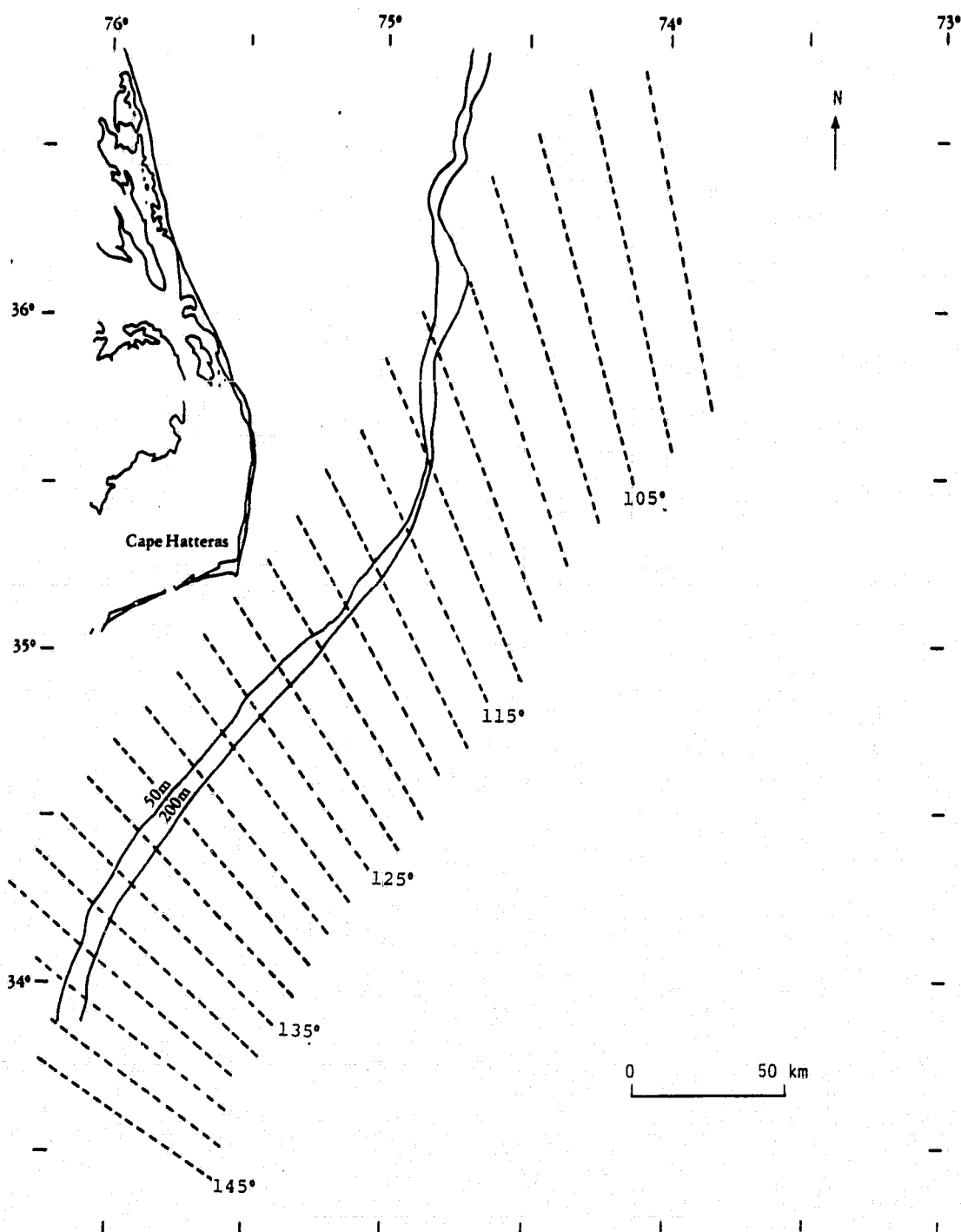


FIGURE 39. PROJECTED WAVE RAYS IN THE CAPE HATTERAS REGION FROM HURRICANE ELLA. (Angles measured from the east and counterclockwise.)

The positions of the 116 optical Fourier transforms from the deep water regions off Cape Hatteras obtained from Seasat Rev. 974, plus several examples of OFTs, were presented in Figure 34. From Figure 34 it can be observed that in the southern portion of the pass (rows 1-11) the direction of the waves is nearly perpendicular to the SAR flight direction while in the northern portion (rows 19-29), the waves are traveling 30° - 45° off perpendicular. A summary of the position, the OFT estimated dominant wavelength and direction and the water depth at each point is presented in Table 9.

From Table 9, it is clear that there are significant changes occurring in the deep-water dominant wavelength and direction at the time when Seasat made its overflight. Two factors were considered as the source of this variation: (1) a wave-current interaction between the Gulf Stream and the gravity wave field; and (2) the source of the gravity waves, in this case hurricane Ella.

In the following sections we will first review wave/current interaction theory as it applies to this study. Next, we will discuss the gravity wave field in the Cape Hatteras area and trace its origin to hurricane Ella. The Seasat observed wavelengths and directions will then be compared to those predicted from the wave/current interaction model using the deep water inputs projected from hurricane Ella. Finally, a discussion on the use of SAR wave observations as a large scale ocean surface current mapping tool will be presented.

4.3.1 WAVE/CURRENT INTERACTION THEORY

Ocean waves can generally interact with other ocean waves or with environmental conditions such as currents, eddies, bottom topographic features, etc. When an ocean wave interaction occurs, the wave is refracted or even reflected and the wave ray turns away from its original propagation direction accordingly. Wave/current refraction is expected to be particularly significant in the strong western

TABLE 9. SUMMARY OF SAR-PREDICTED (OFT) DOMINANT WAVELENGTH AND DIRECTION FROM DEEP-WATER AREAS OF SEASAT REV. 974.

Column A					
Row	Latitude	Longitude	Water Depth** (m)	Wavelength* (m)	Wave* Direction (°T)
1	33° 35'	75° 43'	999.0	171.8	306.0
2	34° 43'	75° 39'	999.0	176.2	306.0
3	33° 48'	75° 36'	999.0	176.2	304.0
4	34° 55'	75° 32'	999.0	185.7	308.5
5	34° 01'	75° 28'	999.0	171.8	307.5
6	35° 08'	75° 25'	999.0	180.8	305.0
7	34° 14'	75° 21'	999.0	180.8	305.0
8	35° 20'	75° 19'	999.0	190.8	306.5
9	34° 27'	75° 14'	999.0	202.1	313.0
10	34° 33'	75° 11'	999.0	195.7	315.0
11	34° 39'	75° 07'	999.0	202.1	317.5
12	34° 46'	75° 04'	999.0	188.5	318.5
13	34° 52'	75° 00'	999.0	185.7	318.5
14	34° 59'	74° 57'	999.0	188.5	321.5
15	35° 05'	74° 53'	999.0	196.3	326.0
16	35° 12'	74° 50'	999.0	195.7	325.0
17	35° 18'	74° 46'	999.0	221.6	327.5
18	35° 24'	74° 42'	999.0	212.0	332.0
19	35° 31'	74° 39'	999.0	208.2	334.0
20	35° 37'	74° 35'	999.0	--	--
21	35° 43'	74° 32'	999.0	202.1	339.0
22	35° 50'	74° 28'	999.0	--	--
23	35° 57'	74° 25'	999.0	--	--
24	36° 03'	74° 21'	999.0	--	--
25	36° 09'	74° 18'	999.0	--	--
26	36° 15'	74° 14'	999.0	--	349.0
27	36° 21'	74° 11'	999.0	--	--
28	36° 28'	74° 07'	999.0	--	--
29	36° 34'	74° 04'	999.0	--	--

* (--) indicates no data extractable from OFT.

**999 indicates depths greater than 999 m.

TABLE 9. SUMMARY OF SAR-PREDICTED (OFT) DOMINANT WAVELENGTH AND DIRECTION FROM DEEP-WATER AREAS OF SEASAT REV. 974.
(Continued)

Column B					
Row	Latitude	Longitude	Water Depth** (m)	Wavelength* (m)	Wave* Direction (°T)
1	33° 37'	75° 48'	999.0	171.8	304.0
2	34° 44'	75° 41'	999.0	180.8	310.5
3	33° 50'	75° 41'	999.0	180.8	304.0
4	34° 56'	75° 38'	999.0	190.8	309.0
5	34° 03'	75° 34'	999.0	180.8	304.0
6	35° 09'	75° 34'	999.0	190.8	307.0
7	34° 16'	75° 27'	999.0	190.8	309.0
8	35° 22'	75° 23'	999.0	196.3	308.0
9	34° 29'	75° 20'	999.0	196.3	309.5
10	34° 35'	75° 16'	999.0	195.7	316.0
11	34° 41'	75° 13'	999.0	190.8	318.0
12	34° 48'	75° 10'	999.0	195.7	320.5
13	34° 54'	75° 06'	999.0	202.1	321.0
14	35° 01'	75° 02'	999.0	195.7	319.5
15	35° 07'	74° 59'	999.0	196.3	321.5
16	35° 14'	74° 55'	999.0	195.7	322.5
17	35° 20'	74° 52'	999.0	202.1	321.5
18	35° 26'	74° 49'	999.0	188.5	329.5
19	35° 33'	74° 45'	999.0	190.8	331.0
20	35° 39'	74° 41'	999.0	190.8	334.0
21	35° 46'	74° 38'	999.0	190.8	335.0
22	35° 52'	74° 34'	999.0	214.0	344.0
23	35° 58'	74° 31'	999.0	190.8	350.0
24	36° 05'	74° 27'	999.0	--	347.0
25	36° 11'	74° 24'	999.0	171.8	346.0
26	36° 18'	74° 20'	999.0	--	--
27	36° 24'	74° 17'	999.0	--	--
28	36° 30'	74° 13'	999.0	--	--
29	36° 36'	74° 10'	999.0	--	--

* (--) indicates no data extractable from OFT.

**999 indicates depths greater than 999 m.

TABLE 9. SUMMARY OF SAR-PREDICTED (OFT) DOMINANT WAVELENGTH AND DIRECTION FROM DEEP-WATER AREAS OF SEASAT REV. 974.
(Continued)

Column C					
Row	Latitude	Longitude	Water Depth** (m)	Wavelength* (m)	Wave* Direction (°T)
1	33° 40'	75° 57'	999.0	180.8	306.0
2	34° 47'	75° 50'	999.0	176.2	306.0
3	33° 53'	75° 50'	999.0	180.8	303.0
4	35° 00'	75° 46'	999.0	185.7	308.0
5	34° 06'	75° 43'	999.0	180.8	308.5
6	35° 12'	75° 39'	999.0	176.2	305.5
7	34° 18'	75° 36'	999.0	176.2	306.5
8	35° 25'	75° 32'	999.0	190.8	306.0
9	34° 32'	75° 29'	999.0	190.8	312.0
10	34° 38'	75° 25'	999.0	195.7	316.0
11	34° 44'	75° 22'	999.0	196.3	317.5
12	34° 51'	75° 18'	999.0	188.5	321.0
13	34° 57'	75° 15'	999.0	190.8	323.5
14	35° 04'	75° 11'	999.0	195.7	316.5
15	35° 10'	75° 08'	75.0	190.8	322.0
16	35° 17'	75° 05'	36.6	169.6	321.5
17	35° 23'	75° 01'	33.9	171.8	320.5
18	35° 30'	74° 57'	42.1	169.6	320.0
19	35° 36'	74° 54'	58.6	167.6	325.5
20	35° 42'	74° 52'	140.9	176.2	330.0
21	35° 49'	74° 47'	999.0	202.1	335.0
22	35° 55'	74° 44'	999.0	--	--
23	36° 02'	74° 40'	999.0	180.8	345.5
24	36° 08'	74° 37'	999.0	--	--
25	36° 14'	74° 33'	999.0	180.8	352.0
26	36° 21'	74° 29'	999.0	--	352.
27	36° 27'	74° 26'	999.0	180.8	352.0
28	36° 33'	74° 23'	999.0	221.7	353.0
29	36° 40'	74° 20'	999.0	208.2	353.0

* (--) indicates no data extractable from OFT.

** 999 indicates depths greater than 999 m.

TABLE 9. SUMMARY OF SAR-PREDICTED (OFT) DOMINANT WAVELENGTH AND DIRECTION FROM DEEP-WATER AREAS OF SEASAT REV. 974.
(Concluded)

Column D					
Row	Latitude	Longitude	Water Depth** (m)	Wavelength* (m)	Wave* Direction (°T)
1	33° 42'	76° 03'	999.0	185.7	305.0
2	34° 49'	75° 56'	999.0	180.8	305.5
3	33° 54'	75° 56'	999.0	176.2	305.0
4	34° 02'	75° 53'	999.0	190.8	310.5
5	34° 08'	75° 50'	999.0	190.8	305.5
6	35° 14'	75° 46'	999.0	180.0	305.0
7	34° 20'	75° 42'	999.0	196.3	305.5
8	35° 27'	75° 38'	999.0	190.8	307.0
9	34° 34'	75° 35'	999.0	196.3	309.0
10	34° 40'	75° 32'	999.0	195.7	315.0
11	34° 48'	75° 28'	999.0	196.3	315.5
12	34° 53'	75° 25'	119.0	195.5	322.0
13	35° 00'	75° 21'	73.2	190.8	322.5
14	35° 06'	75° 18'	47.6	175.5	317.5
15	35° 13'	75° 14'	18.3	159.8	319.5
16	35° 19'	75° 11'	25.6	159.0	318.5
17	35° 26'	75° 07'	28.4	167.6	319.5
18	35° 32'	75° 05'	42.1	169.6	319.0
19	35° 39'	75° 00'	51.2	171.8	321.5
20	35° 45'	74° 57'	62.2	167.6	327.0
21	35° 51'	74° 53'	82.4	196.3	331.0
22	35° 57'	74° 50'	89.7	245.0	380.0
23	36° 04'	74° 47'	119.0	190.8	352.0
24	36° 10'	74° 43'	999.0	208.5	345.0
25	36° 17'	74° 40'	999.0	190.8	350.5
26	36° 24'	74° 36'	999.0	190.8	352.0
27	36° 30'	74° 33'	999.0	190.8	353.0
28	36° 35'	74° 29'	999.0	214.8	352.5
29	36° 42'	74° 26'	999.0	163.6	353.0

* (--) indicates no data extractable from OFT.

**999 indicates depths greater than 999 m.

boundary current area of the North Atlantic where the Gulf Stream borders the edge of the continental margin. In many cases, surface waves are affected by more than one of these factors at the same time. This will result in additional or less refraction depending on the combined effect of these factors. A strong western boundary current flowing near or over the continental margins is an obvious example. This portion of the study is a presentation of wave refraction resulting from wave/current interaction in deep water without the inclusion of bathymetric effects on the wave rays.

Consider a wave field riding upon the Gulf Stream in deep water of uniform depth (i.e., beyond the 200 m contour). The Gulf Stream is assumed to be in steady state (compared to the travel time of a wave group across the stream) with a velocity which varies slightly across it. The minimum velocity occurs at both outer boundaries of the stream, while the maximum velocity is in the center portion. These assumptions are generally satisfied by the Gulf Stream in the region near Cape Hatteras. When the wave propagates close to the continental slope, the sudden change of the water depth will cause the initiation of topographic refraction and will affect the wave direction and the wave number. This situation will be addressed in more detail later in this section.

For a detailed derivation of the governing analytical expressions for wave/current interaction, see Appendix E. The methodology utilized in this investigation parallels the wave/current interaction theory developed by Phillips (1981). Only a brief summary of this development will be presented here.

For waves riding on or across a current with a slowly changing velocity as shown in Figure 40, the angles α_i are the angles of incidence or refraction the wave rays make with the current streamlines. When the waves are incident upon the current with an average velocity range of u_0 to u_1 , the shear per unit width is $u_0 - u_1$, and conservation of wave frequency becomes:

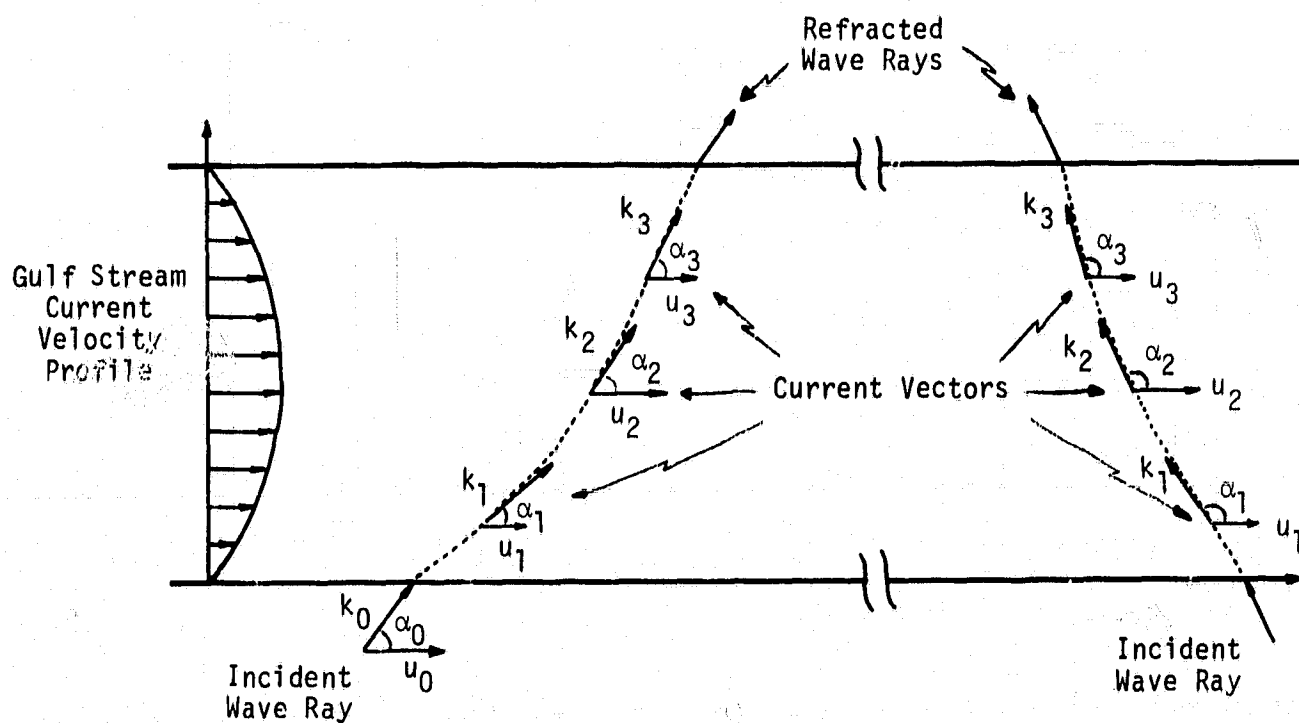


FIGURE 40. ILLUSTRATIONS OF WAVE AND CURRENT INTERACTIONS IN A SLOWLY VARYING CROSS CURRENT.

$$\sigma_0 = \sigma_1 + k_1(u_1 - u_0) \cos \alpha_1 \quad (5)$$

where σ_0 and σ_1 are the radian wave frequencies of the wave in the undisturbed and disturbed fluid respectively. Similarly, k_1 is the radian wave number in the disturbed fluid and conservation of wave numbers becomes:

$$k_0 \cos \alpha_0 = k_1 \cos \alpha_1 = \text{const} \quad (6)$$

Eq. (5) gives:

$$\cos \alpha_1 = \frac{\sigma_0 - \sigma_1}{k_1(u_1 - u_0)} = K_1/k_1 \quad (7)$$

Substituting k_1 from Eq. (6) into (7) gives:

$$\cos \alpha_0 = \frac{\sigma_0 - \sigma_1}{k_0(u_1 - u_0)} = K_1/k_0 \quad (8)$$

where $K_1 = (\sigma_0 - \sigma_1)/(u_1 - u_0)$, and for deep water gravity waves the intrinsic frequency is $\sigma^2 = gk$. Theoretically, the angles of incidence and refraction can be calculated from Eqs. (7) and (8) when both the shear of the current between two current strips and the wave numbers in these two current strips are known. Conversely, the current shear can be solved for by utilizing SAR-observed gravity wave propagation directions and wave numbers. Wave propagation angles observed by the SAR will be compared with wave refraction angles calculated from these theoretical results.

4.3.2 DATA ANALYSIS

Figure 41 shows the direction of the wave crests at the 101 positions where wave spectra were visible on the OFTs (well defined wave spectra were not resolved on 15 of the OFTs). Figure 42 is a diagram of orthogonals to these crests. From these orthogonals, a wave ray diagram can be constructed, as is shown in Figure 43. Three analyses of these wave rays were conducted. First, the wave rays

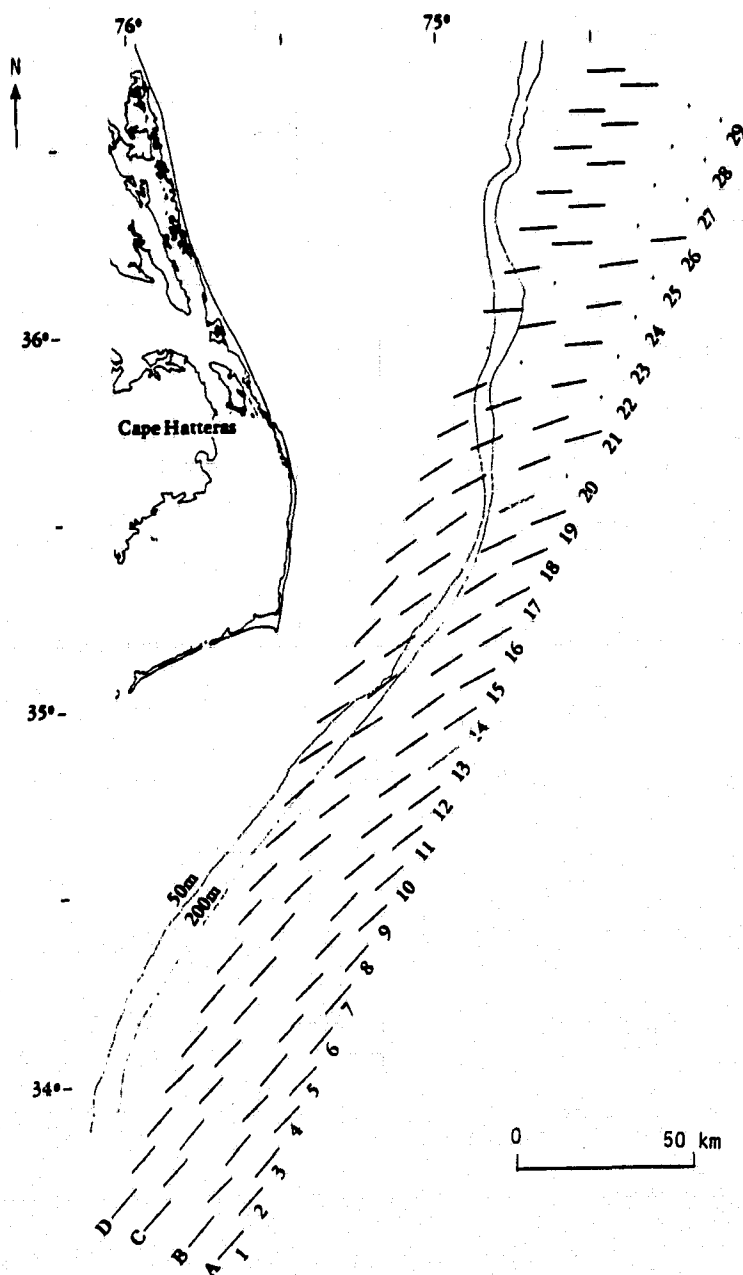


FIGURE 41. SUMMARY OF SEASAT-SENSED (OFT) DOMINANT WAVE CRESTS.
(Rev. 974, 3 September 1978.)

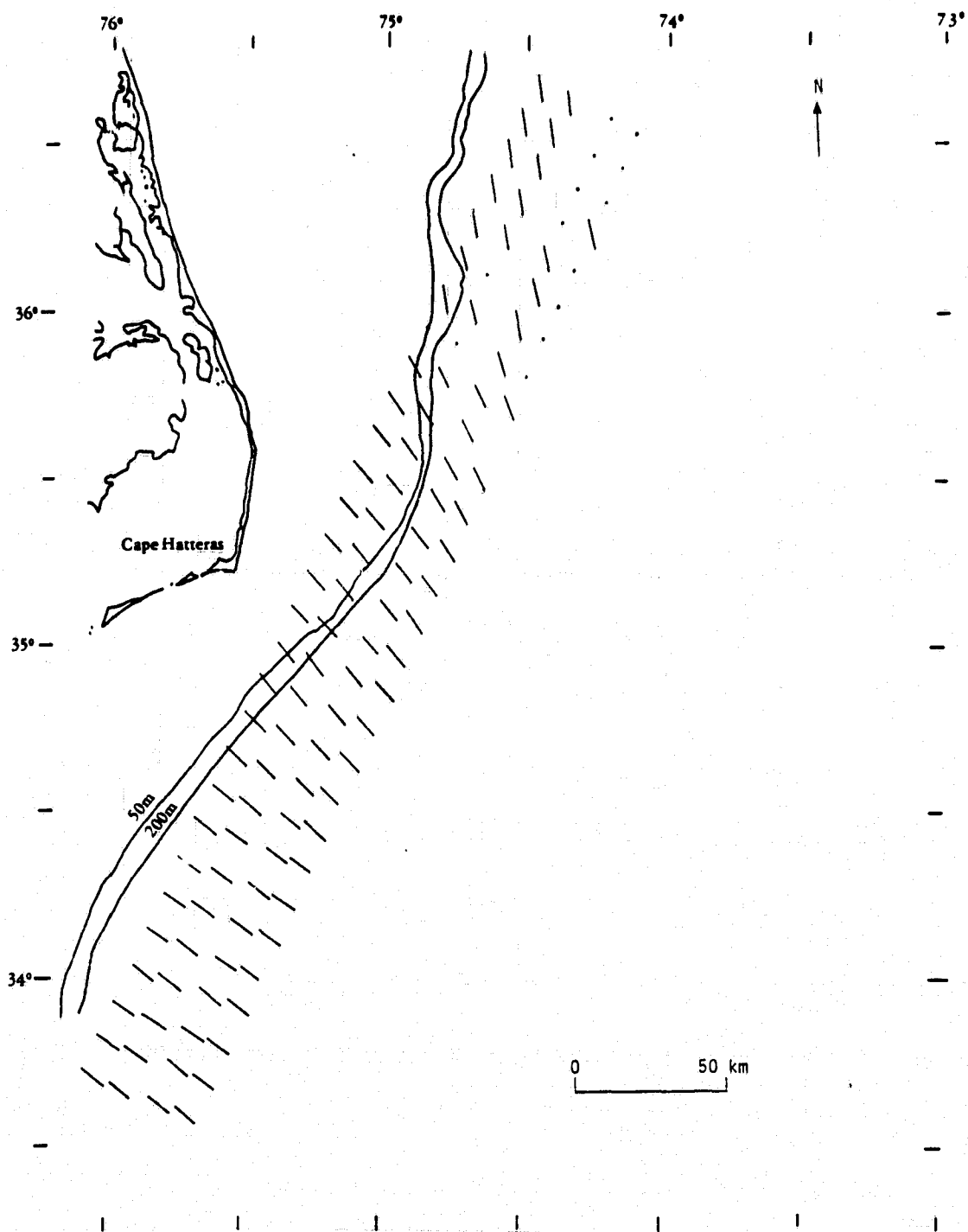


FIGURE 42. SEASAT SAR-OBSERVED DOMINANT WAVE DIRECTIONS.

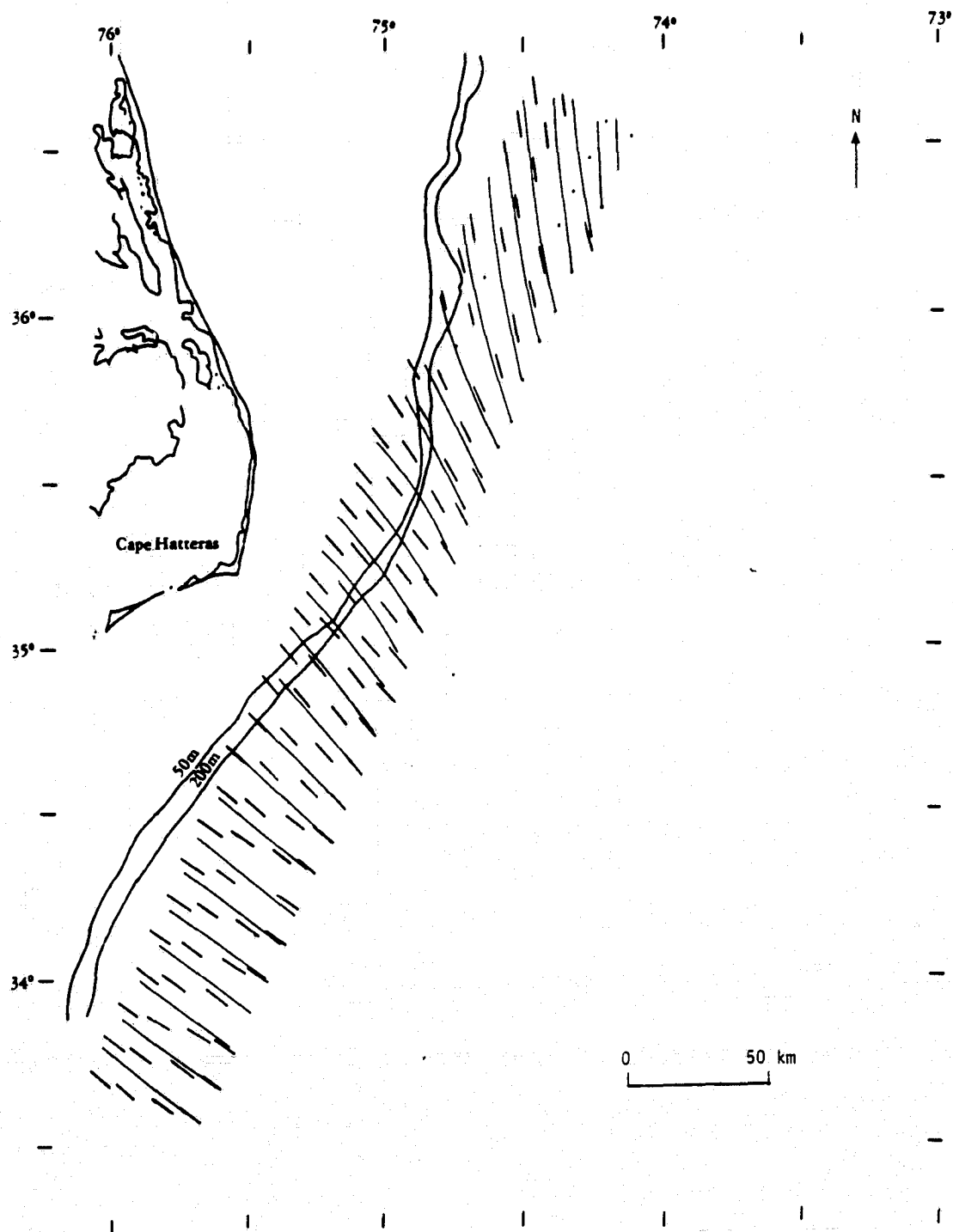


FIGURE 43. AVERAGE WAVE RAYS CONSTRUCTED FROM ORTHOGONALS TO SEASAT SAR-OBSERVED WAVE CRESTS. (The orthogonals [short lines] depict the observed dominant wave direction.)

determined from the OFT analysis were hindcast to locate the wave generation region of hurricane Ella. Second, they were compared to the projected wave rays from hurricane Ella without consideration of the Gulf Stream. Finally, the wave rays were compared to wave rays constructed using Phillip's (1981) wave/current interaction model.

Figure 44 shows the result of the wave ray hindcast projections to locate the wave generation region of hurricane Ella. These wave rays fall into two general groupings of approximately 50 x 50 km dimensions. The southern most group was derived from waves incident in the northern region of Cape Hatteras. The northern group of hind-cast rays originated from the southern most OFTs. It is interesting to note that the spatial separation of these two grouping corresponds to the wave travel time difference from the hurricane position to the OFT sensed positions at the time of satellite overpass. These projections agree well with the National Weather Service reported hurricane positions for the day in question.

4.3.2.1 Comparison of Hurricane Projected Wave Rays with Seasat SAR Wave Observations

The comparison of Seasat SAR observed wave rays with hurricane projected wave rays without consideration of the Gulf Stream's existence is shown in Figure 45.

In order to conduct a qualitative analysis of the Figure 45, we have divided the observed wave ray refraction into three groups. The forcing mechanism of the observed wave rays in each group is apparently different. The first four observed wave rays is named Group 1; the 5th to 19th, Group 2 and; the 20th to 28th, Group 3. In order to better explain the wave/current interaction in Section 4.3.2.3, we subdivided Group 2 into two subgroups: 2A (5th to 10th) and 2B (11th to 19th).

In Group 1, the observed and projected wave rays seem to match quite well, while in Group 2, the angle deviations between the Seasat

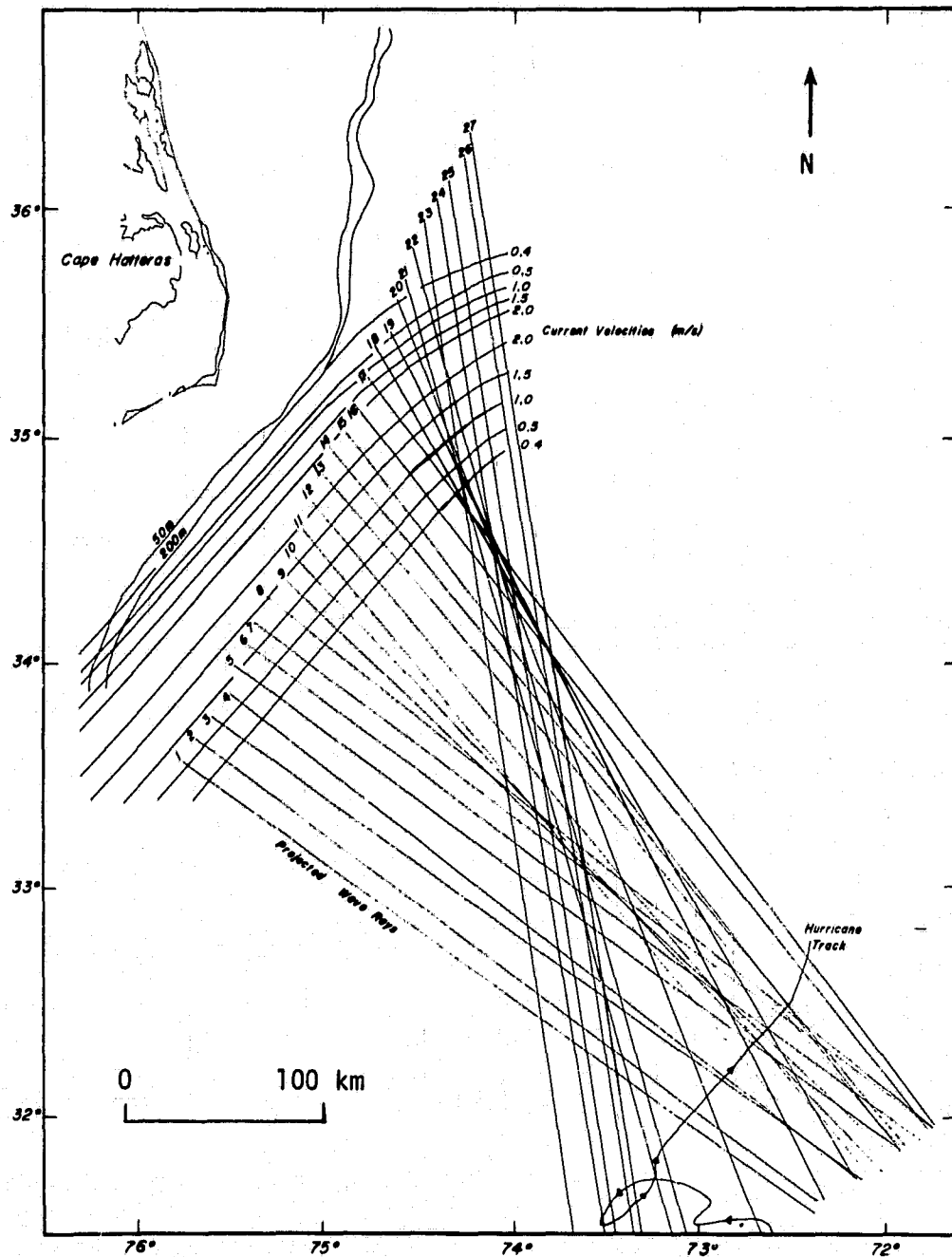


FIGURE 44. SAR WAVE RAY HINDCASTS TO DETERMINE WAVE GENERATION REGIONS.

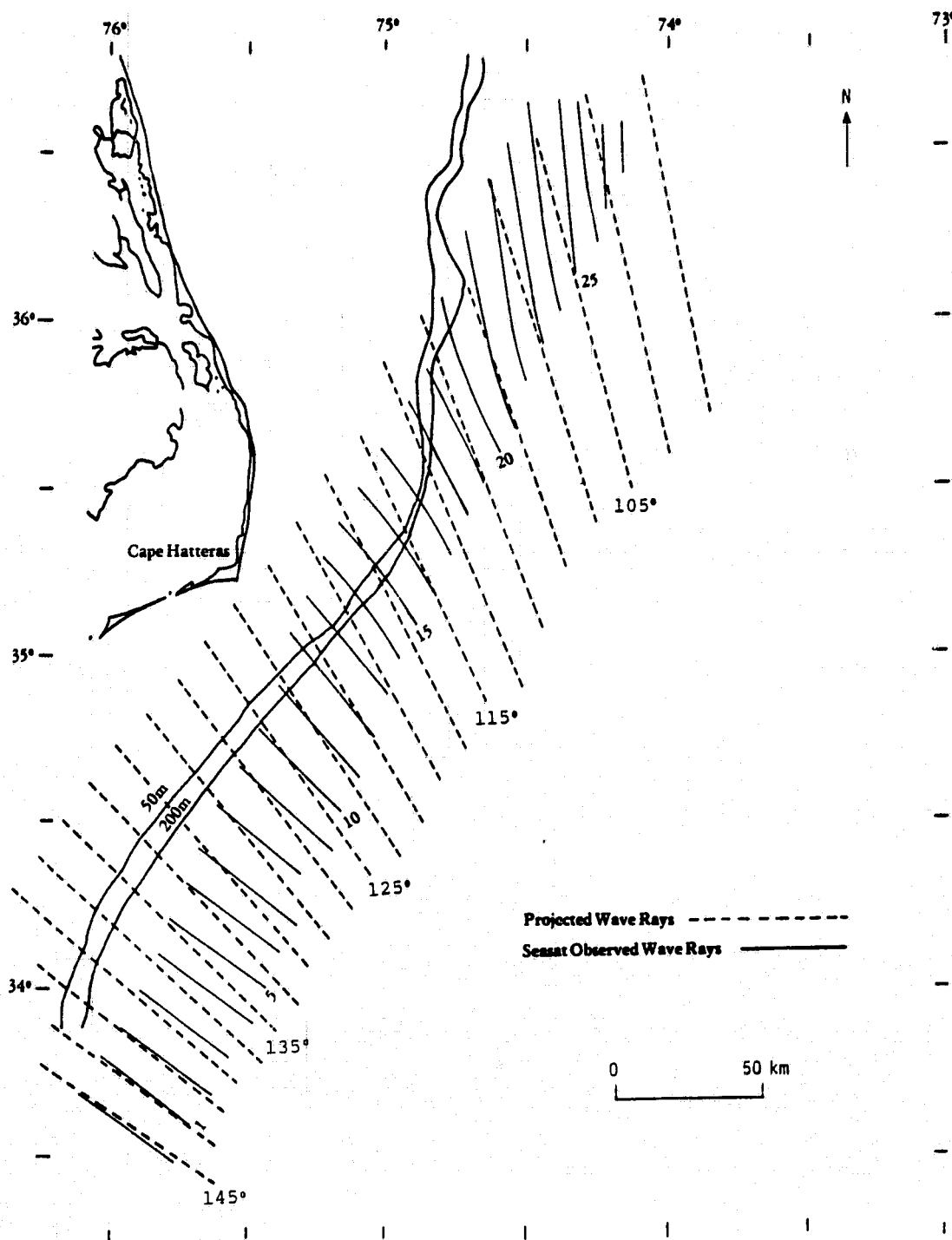


FIGURE 45. COMPARISON OF SAR-OBSERVED WAVE RAYS WITH PROJECTED WAVE RAYS WITHOUT CONSIDERATION OF THE CORRECTION OF THE REFRACTION DUE TO THE GULF STREAM.

observed and the predicted rays becomes larger. One common characteristic of the wave rays in these two groups is that the observed wave rays appear always cross the projected wave rays from the right to the left when viewed in the direction of propagation. In Group 3, the angle deviations seem to be smaller than those in Group 2 but larger than in Group 1. The characteristic of wave ray crossing in Group 3 is opposite to the first two groups: the observed rays always cross the projected wave rays from the left to the right.

Up to this point, we have assumed that all the waves imaged by Seasat during Rev. 974 originated from hurricane Ella at a single point of time. In actuality, the situation is not quite so simple. The waves in the northern portion of the Cape Hatteras region had to have been traveling longer from their point of origin than those in the southern region at the end of the Seasat overpass. Just prior to the time of the overpass, hurricane Ella was moving from southwest to northeast; and when the waves in the northern portion were generated, hurricane Ella was southwest of its position in Figure 38. The source of the projected wave rays has to be adjusted accordingly. This adjustment turns out to be approximately 1° clockwise for every 55 km north (relative to ray 1). For the second subgroup of Group 2, we therefore should adjust the hurricane projected wave rays by 1° to 2° clockwise.

In Group 3, the waves are outside the body of the Gulf Stream current as well as located offshore of the 200 m contour. In this case, the wave/current interaction and bottom refraction should be minimal, but the adjustment for the repositioning of hurricane Ella should be 2° to 4° .

In summary, a qualitative assessment of the transformation of the waves observed by Seasat during Rev. 974 seems to indicate that although there are deviations between the Seasat observed and predicted wave rays, the two groups match fairly well and are in agreement with the complicated oceanographic/meteorological conditions present at the time.

Quantitative studies of the observed wave rays refraction without consideration of the Gulf Stream can be referred to in Table 10. From this table, the angle differences (deviations) from the observed wave rays to projected wave rays are on the order of 4° for the first 4 wave rays (Group 1) with the smallest deviation on ray 1, where the deviation is less than 2° . The angle differences are on the order of 11° for rays 5 to 10 (subgroup A of Group 2) with the maximum deviation between rays 6 and 8; on the order of 9° for rays 11 to 19 with the maximum deviation between rays 15 and 17; on the order of -5° for ray 20 and up with the maximum negative deviation between rays 22 to 24. The negative sign means the observed wave rays are on the right-hand side of the projected wave rays.

Previous studies (see Vesecky and Stewart, 1981) indicate that SAR observed absolute wave directions are within $\pm 11^\circ$ of surface measured wave direction in experiments where both were simultaneously obtained. By identifying the source of the gravity wave field present in the deep water regions east of Cape Hatteras as hurricane Ella, and simultaneously tracking these waves over a large distance (on the order of 500 km), we have successfully identified the major source of this wave field's directional variation. The question now arises as to whether or not the deviation between the observed and predicted directions can be further reduced by implementing a wave/current refraction model.

4.3.2.2 Comparison of Wave/Current Interaction Model Results with Seasat SAR Wave Observations

As deep water waves propagate from the relatively undisturbed ocean and enter the Gulf Stream, their direction of propagation and wavelength will change. The refraction angle and resultant direction will depend mainly on the current shear, the wave numbers and incidence angle of the wave rays. Recall that the projected wave rays from hurricane Ella, presented in the previous section, did not incorporate the current refraction induced by the presence of the Gulf

TABLE 10. COMPARISON OF SAR-OBSERVED WAVE RAYS WITH HURRICANE ELLA-PROJECTED WAVE RAYS
(The case of projected wave ray without considering refraction due to the Gulf Stream.)

Wave Ray No.	Ob. Positions Group No.	Direction of Observed Wave Ray (1)				Direction of Projected Wave Ray (1)				Angle Difference Between Observed Wave Ray and Projected Wave Ray (2)				Average Angle Difference (degrees)
		A	B	C	D	A	B	C	D	A	B	C	D	
1	I	144.0	146.0	144.0	144.7	143.0	143.0	142.9	142.8	1.0	3.0	1.1	1.9	1.8
2		144.0	139.5	145.5	145.2	140.7	140.8	140.9	141.3	3.3	-1.3	4.6	3.9	2.6
3		146.0	146.0	144.5	145.5	138.3	138.4	138.6	140.0	7.7	7.6	5.9	5.5	6.7
4		141.5	141.0	141.7	144.5	135.7	136.5	136.5	137.0	5.8	4.5	5.2	7.5	5.8
5	IIA	142.5	146.0	143.0	145.0	134.0	134.5	134.5	134.8	8.5	11.5	8.5	10.2	9.7
6		144.5	142.0	144.0	144.5	132.0	132.5	132.5	133.0	12.5	9.5	11.5	11.5	11.3
7		145.0	141.0	143.7	143.0	130.2	130.5	131.0	131.2	14.8	10.5	12.7	11.8	12.5
8		143.5	141.2	141.0	141.0	128.0	128.1	128.8	129.1	15.5	13.1	12.2	11.9	13.2
9		137.0	136.7	134.0	135.0	126.0	126.3	127.0	127.2	18.0	10.4	7.0	7.8	9.1
10		135.0	133.0	132.5	134.5	124.5	124.7	125.1	125.5	10.5	8.3	7.4	9.0	8.8
11	IIB	132.5	130.7	129.0	128.0	122.6	122.8	123.0	123.2	9.9	7.9	6.0	4.8	7.2
12		131.5	129.0	126.5	131.5	121.1	121.2	121.2	121.3	10.4	7.8	5.3	10.2	8.4
13		131.5	129.5	130.5	130.5	119.2	119.5	119.8	121.8	12.3	10.0	10.7	8.7	10.4
14		128.5	129.5	127.5	132.0	117.9	118.0	118.0	120.1	10.6	11.5	8.7	11.9	10.7
15		124.0	128.2	127.5	131.0	116.2	116.5	117.8	118.6	7.8	11.7	9.7	12.4	10.4
16		125.0	128.2	129.7	130.7	115.0	115.2	116.4	117.8	10.0	13.0	13.3	12.9	12.3
17		125.0	128.2	127.7	128.5	114.0	114.2	115.3	116.1	11.0	14.0	12.4	12.4	12.5
18		118.0	119.0	120.0	123.0	112.1	112.2	113.7	114.2	5.9	6.8	6.3	8.8	7.0
19		116.0	116.0	115.0	119.0	111.0	111.1	111.2	112.0	5.0	4.9	3.8	7.0	5.2
20	III	113.5	115.0	119.7	98.0	110.5	110.0	112.4	110.2	3.0	5.0	7.3	-12.2	0.8
21		111.0	106.0	103.5	102.7	109.2	109.0	109.5	108.6	1.8	-3.0	-6.0	-5.9	-3.3
22		---	100.0	98.0	98.0	---	108.0	107.3	107.2	---	-8.0	-9.3	-9.2	-8.8
23		---	103.0	98.0	97.0	---	106.9	106.5	106.3	---	-3.9	-8.5	-9.3	-7.2
24		---	102.0	98.0	97.5	---	106.2	105.5	106.3	---	-4.2	-7.5	-8.8	-6.8
25		101.0	---	97.0	---	104.2	---	104.7	---	-3.2	---	-7.7	---	-5.5
26		101.0	---	97.0	---	104.2	---	103.9	---	-3.2	---	-6.9	---	-5.1
27		---	---	---	---	---	---	---	---	---	---	---	---	---
28		---	---	---	---	---	---	---	---	---	---	---	---	---
29		---	---	---	---	---	---	---	---	---	---	---	---	-4.8

NOTE: (1) The direction is measured from the east and counterclockwise;
(2) Angle difference between observed and projected wave ray = direction of observed wave ray - direction of projected wave ray;
(3) The average angle difference in each group is shown inside the rectangle;
--- Data not available.

Stream. In order to produce a more physically complete comparison with the observed wave rays, the refraction of the projected rays due to the Gulf Stream should also be taken into consideration. This situation is presented in Figure 46.

For the case being studied, as the waves enter the Gulf Stream, they are first refracted in a clockwise direction as they encounter an increasing velocity region of the current profile on the outer (eastern) edge of the Gulf Stream boundary. Similarly, they are refracted counterclockwise as they encounter the decreasing velocity region of the current profile on the inner (western) edge of the Gulf Stream. This concept is presented in Figure 47. Unless total internal trapping or reflection occurs, the direction of a wave departing the influence of the Gulf Stream should be the same as when the wave entered the Gulf Stream. However, the point of departure of that wave ray will be upstream of the position the wave ray would have been if it had not encountered the Gulf Stream. This distance was calculated to be on the order of 0.2 kilometers for the conditions encountered during this study.

The refracted wave angles can be calculated using Phillips' model as presented in Eq. (E-10); (see Appendix E). After a wave is generated by the hurricane, it is assumed to propagate in the same direction as the projected wave ray toward the Gulf Stream. After this wave enters the outer boundary of the Stream, it is refracted as stated in Phillips' model. The projected wave ray directions from hurricane Ella were used as input conditions into the wave/current refraction model. The average wave number, as measured by the Seasat SAR, was also used as an input. New projected wave rays, at 1° increments, were calculated, and the SAR observed directions were compared to the new projected rays.

The new projected wave rays are summarized in Table 11. The wave/current refraction angle is zero for the more southern wave rays and becomes larger as the incidence angle (measured from east and

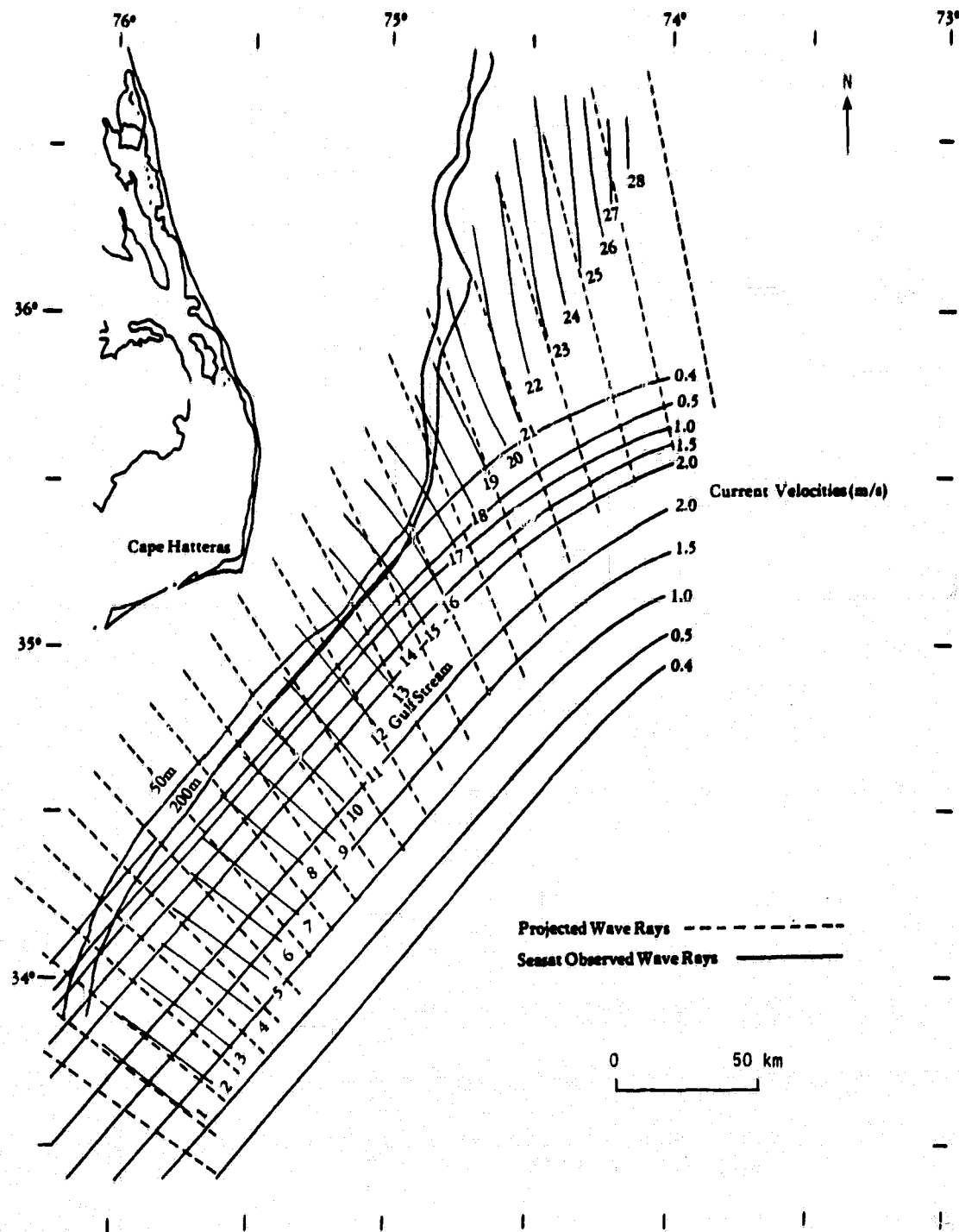


FIGURE 46. SAR-OBSERVED WAVE RAYS, HURRICANE-PROJECTED WAVE RAYS, AND THE GULF STREAM.

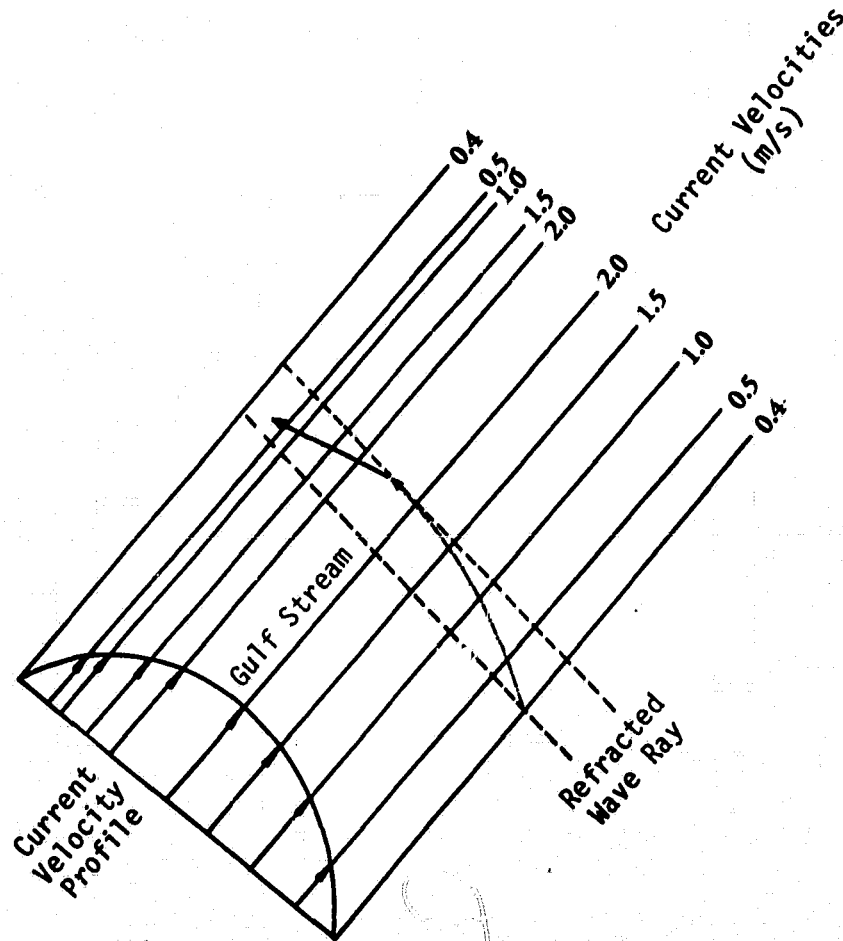


FIGURE 47. CLOCKWISE AND COUNTERCLOCKWISE BENDING OF PROJECTED WAVE RAY DUE TO REFRACTION WITHIN THE GULF STREAM'S NON-UNIFORM VELOCITY FIELD.

TABLE 11. COMPARISON OF SAR-OBSERVED WAVE RAYS WITH HURRICANE ELLA-PROJECTED WAVE RAYS.
(The case of projected wave ray considering refraction due to the Gulf Stream.)

Wave Ray No.	Ob. Positions Group No.	Direction of Observed Wave Ray (1)				Direction of Projected Wave Ray (1)				Angle Difference Between Observed Wave Ray and Projected Wave Ray (2)				Average Angle Difference (degrees)
		A	B	C	D	A	B	C	D	A	B	C	D	
1		144.0	146.0	144.0	144.7	143.0	143.0	143.5	142.8	1.0	3.0	1.1	1.9	1.8
2	I	144.0	139.5	145.5	145.2	140.7	140.8	140.9	141.3	3.3	-1.3	4.6	3.9	2.6
3		146.0	146.0	144.5	145.5	138.3	138.4	138.6	140.0	7.7	7.6	5.9	5.5	6.7
4		141.5	141.0	141.7	144.5	135.7	136.5	136.5	137.0	5.8	4.5	5.2	7.5	5.8
														4.2 (3)
5		147.5	146.0	143.0	145.0	134.0	134.5	134.5	134.8	8.5	11.5	8.5	10.2	9.7
6		144.5	142.0	144.0	144.5	132.1	132.6	132.6	133.1	12.4	9.4	11.4	11.4	11.2
7	IIA	145.0	141.0	143.0	143.7	130.4	130.7	131.2	131.4	14.6	10.3	12.5	11.6	12.3
8		143.5	141.2	141.0	141.0	128.4	128.5	129.2	129.5	15.1	12.7	11.8	11.5	12.8
9		137.0	136.7	134.0	135.0	126.4	126.7	127.4	127.6	10.6	10.0	6.6	7.4	8.7
10		135.3	133.0	132.5	134.5	125.3	125.5	125.9	126.3	9.7	7.5	6.6	8.2	8.0
														10.5 (3)
11		132.5	130.7	129.0	128.0	123.7	123.9	124.1	124.3	8.8	6.8	4.9	3.7	6.1
12		131.5	129.0	126.5	131.5	122.4	122.5	122.5	122.6	9.1	6.5	4.0	8.9	7.1
13		131.5	129.5	130.5	130.5	121.7	121.7	121.4	123.4	10.9	8.4	9.1	7.1	8.9
14		128.5	129.5	127.5	132.0	119.8	119.5	120.7	122.0	8.7	9.6	6.8	10.0	8.8
15	IIIB	124.0	128.2	127.5	131.0	118.4	118.7	120.0	120.8	5.6	7.5	10.8	10.2	8.2
16		125.0	128.2	129.7	130.7	117.5	117.7	118.9	120.3	7.5	10.5	10.8	10.4	9.8
17		125.0	128.2	127.7	128.5	116.8	117.0	118.1	118.9	8.2	11.2	9.6	9.6	9.7
18		118.0	119.0	120.0	123.0	115.3	115.4	116.9	117.4	2.7	3.6	3.1	5.6	3.8
19		116.0	116.0	115.0	119.0	114.5	114.5	114.7	115.5	1.5	1.5	0.3	3.5	1.7
														7.1 (3)
20		113.5	115.0	119.7	98.0	114.1	113.6	116.0	113.8	-0.6	1.4	3.7	-15.8	-2.8
21		111.0	106.0	103.5	107.7	113.4	113.2	113.7	112.8	-2.4	-7.2	-10.2	-10.0	-7.5
22		---	100.0	98.0	98.0	---	112.2*	111.5*	111.4*	---	-12.2	-13.5	-13.4	-13.0
23		---	103.0	98.0	97.0	---	111.1*	110.7*	110.5*	---	-9.2	-12.7	-13.5	-11.8
24	IIII	---	102.0	98.0	97.5	---	110.4*	109.7*	110.5*	---	-8.9	-11.7	-13.0	-11.0
25		101.0	---	97.0	---	108.4*	---	108.9*	---	-7.4	---	-11.9	---	-9.7
26		101.0	---	97.0	---	108.4*	---	108.1*	---	-7.4	---	-11.9	---	-9.7
27		---	---	---	---	---	---	---	---	---	---	---	---	---
28		---	---	---	---	---	---	---	---	---	---	---	---	---
29		---	---	---	---	---	---	---	---	---	---	---	---	-8.9 (3)

NOTE: (1) The direction is measured from the east and counterclockwise;
(2) Angle difference between observed and projected wave ray = direction of observed wave ray - direction of projected wave ray;
(3) The average angle difference in each group is shown inside the rectangle;
--- Data not available;
* Directions of projected wave rays are obtained by assuming the range refraction angle of wave ray No. 21 due to sea truth data (current speeds) not available for the refraction angle calculation.

counterclockwise) increases. This modified projected wave ray, which actually considers the effect of the Gulf Stream, can now be compared to the nearest observed wave ray. The results of this comparison are also shown in Table 11. From this table, for Group I (near normal incidence), we see that the angle differences remain the same as for those projected wave rays that did not account for current refraction (see Table 10). However, they become smaller for Group 2, and they also become smaller for Group 3. Since most of the angle differences are negative in Group 3, the absolute angle differences actually are larger. The angle differences therefore are still on the order of 4° for Group 1; on the order of 10° for Group 2; and on the order of -9° for Group 3.

Continuing the wave rays beyond the western boundary of the Gulf Stream places Rays 12 to 17 into intermediate and eventually shallow water with respect to wavelength. To account for topographically induced wave refraction these rays were numerically projected shoreward. The results of these computations are presented in Figure 48. Figure 48 was generated using a computer based wave refraction model (Poole, et al., 1977). This model will be discussed in more detail below. The projected wave ray directions presented in Tables 10 and 11 did take into account this bottom induced refraction.

Therefore, we have still not defined all the directional variation in the deep water wave field. Several possible explanations exist for these observations. First, the purely kinematic wave/current interaction model utilized in this investigation may underestimate the amount of surface gravity wave modification by the Gulf Stream. Second, the actual position of the northern portion of the Gulf Stream may have been displaced more northerly than predicted by the U.S. Coast Guard for 30 August 1978. Third, perturbations of the actual flow pattern of the Gulf Stream, such as rings and meanders, may have existed which were not resolved on the U.S. Coast Guard sea truth. And fourth, the projected wave ray directions put

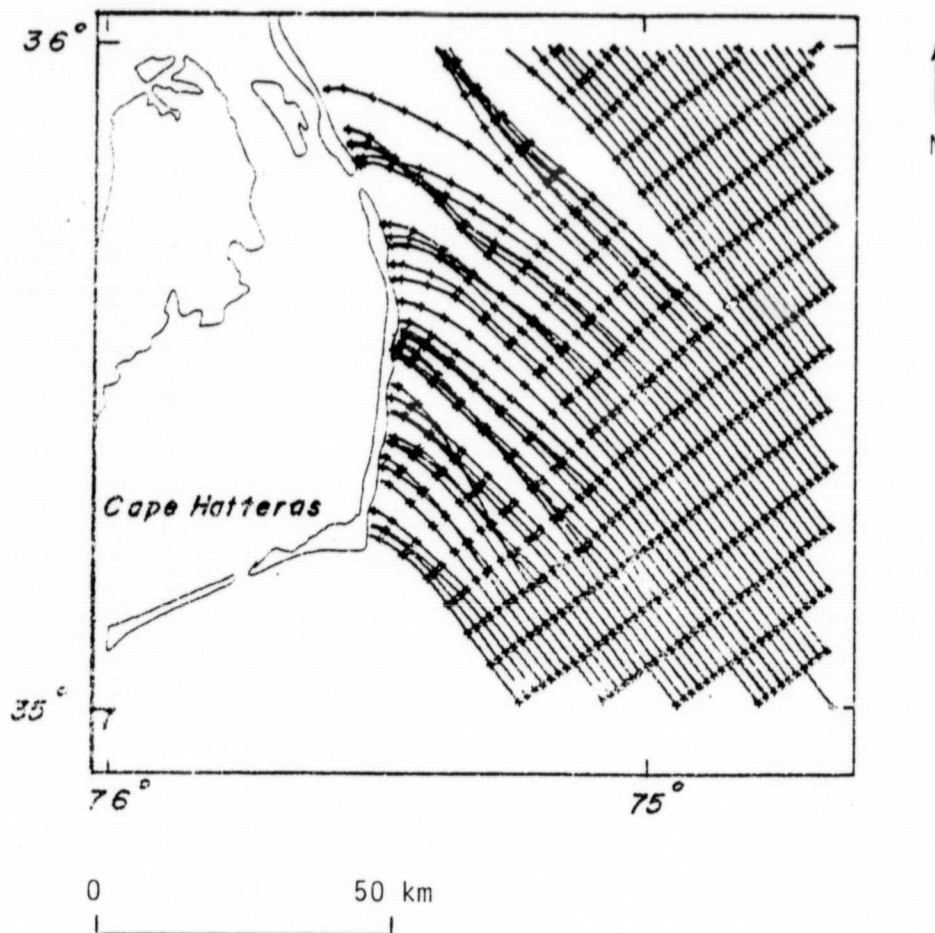


FIGURE 48. COMPUTER-GENERATED WAVE RAYS USING SAR-MEASURED DEEP WATER WAVE INPUTS SHOW THE EFFECTS OF TOPOGRAPHICALLY-INDUCED WAVE REFRACTION.

into the wave/current interaction model might actually vary more than was first thought. Any or all of these factors could have produced the observed deviations between the SAR sensed wave characteristics and those obtained from the wave/current interaction model.

4.3.3 CALCULATION OF THE SEASAT SAR INFERRED CURRENT FIELD

Perhaps the most useful application of this study of wave/current interaction is the quantification of the utility of SAR as a large scale ocean surface current mapping tool. SAR-sensed subtle changes in the propagation characteristics, wave direction, and dominant wave number have the potential to be used to analytically solve for the gross velocity field of the upper region of the ocean. The assumptions employed in this formulation appear to be quite harsh and require further detailed investigation. However, in spite of this uncertainty, the results obtained suggest that Seasat SAR is capable of producing reliable estimates of large scale ocean surface flow fields. The synoptic and repetitive coverage of large regions of the ocean surface which is provided by a satellite-borne radar system renders this technique extremely valuable as an eventual operational tool.

As suggested by Phillips (1981), conservation of wave number requires the following expression for the apparent wave frequency:

$$\sigma_0 = \sigma + \vec{k} \cdot \vec{u} \quad (9)$$

or alternately:

$$\sigma_0 = \sigma + ku \cos \alpha = \text{const} \quad (10)$$

where k is the local wave number ($k = 2\pi/L$), u is the flow velocity of the upper region of the ocean, σ_0 is the apparent wave frequency measured at a fixed point in a fluid assumed to be at rest, σ is the wave frequency ($\sigma = 2\pi/T$) observed in the moving fluid, and α is the angle between the local current and wave number vectors.

The two most directly observable characteristics of wave propagation from spaceborne SAR are the propagation direction and wave number of the dominant gravity wave components. As previously demonstrated, both of these quantities should be altered as a result of wave/current interactions and, hence, offer possible indicators of the underlying flow structure of the upper ocean. Published values for the absolute resolution of the dominant wave component direction from spaceborne SAR (Vesecky and Stewart, 1981) indicate reliable estimates can be obtained to $\pm 11^\circ$ absolute. The calculated changes in incident wave direction as a result of waves from hurricane Ella crossing the Gulf Stream, range from a few tenths of a degree to a few degrees, apparently far below the published limits of absolute SAR wave direction resolution. However, results from the error analysis performed as part of this investigation, indicate relative angular resolution of approximately 1° for successive OFT's obtained from the same Seasat pass. For a detailed discussion of the error analysis, see Appendix D. In addition, the SAR has been shown to be very sensitive to subtle changes in the dominant wave number of the ocean surface wave spectrum (Beal, 1980). Since the anticipated wave direction changes will be small, an analytical formulation that eliminates the angular change in wave propagation was chosen. This was accomplished by employing the following two stringent assumptions: First, the change in wave direction resulting from interaction with the Gulf Stream is assumed small (less than a few degrees); and second, all straining in the wave k vector field resulting from the Gulf Stream interaction is assumed to originate from only the current component in the direction of wave propagation, and that the orthogonal components of this strain can be treated independently. Employing these assumptions, changes in the direction of propagation of the dominant wave components can be analytically eliminated from this formulation.

From conservation of wave number component in the cross stream direction (y-direction):

$$k \sin \alpha = k_0 \sin \alpha_0 \quad (11)$$

where again the subscript, o, denotes the parameter value in the undisturbed fluid.

Combining Eqs. (10) and (11) gives:

$$(gk)^{1/2} + u[k^2 - k_0^2 \sin^2 \alpha_0]^{1/2} = \sigma_0 \quad (12)$$

and from Eq. (10), solving for $\cos \alpha$, gives:

$$\cos \alpha = \frac{\sigma_0 - \sigma}{ku} \quad (13)$$

Solving and substituting into Eq. (10) and assuming the total amount of straining induced in the surface wave field is the result of only the current component in the direction of wave propagation ($\alpha_0 = \alpha = \text{constant}$) gives:

$$(gk)^{1/2} + u[k^2 - k_0^2(1 - \cos^2 \alpha_0)]^{1/2} = \sigma_0 \quad (14)$$

Eq. (14) can be algebraically manipulated to give the following expression for u , the velocity of the underlying fluid required to produce the observed change in wave propagation characteristics:

$$u^2 = \frac{(\sigma_0 - \sigma)^2 \left(1 - \frac{k_0^2}{k^2}\right)}{(k^2 - k_0^2)} \quad (15)$$

or

$$u^2 = \frac{[(gk_0)^{1/2} - (gk)^{1/2}]^2}{k^2} \quad (16)$$

Utilizing this formulation and the wave number vectors of the dominant wave components resolved by the OFT analysis (Figure 49), orthogonal components of the current velocity field of the Gulf Stream

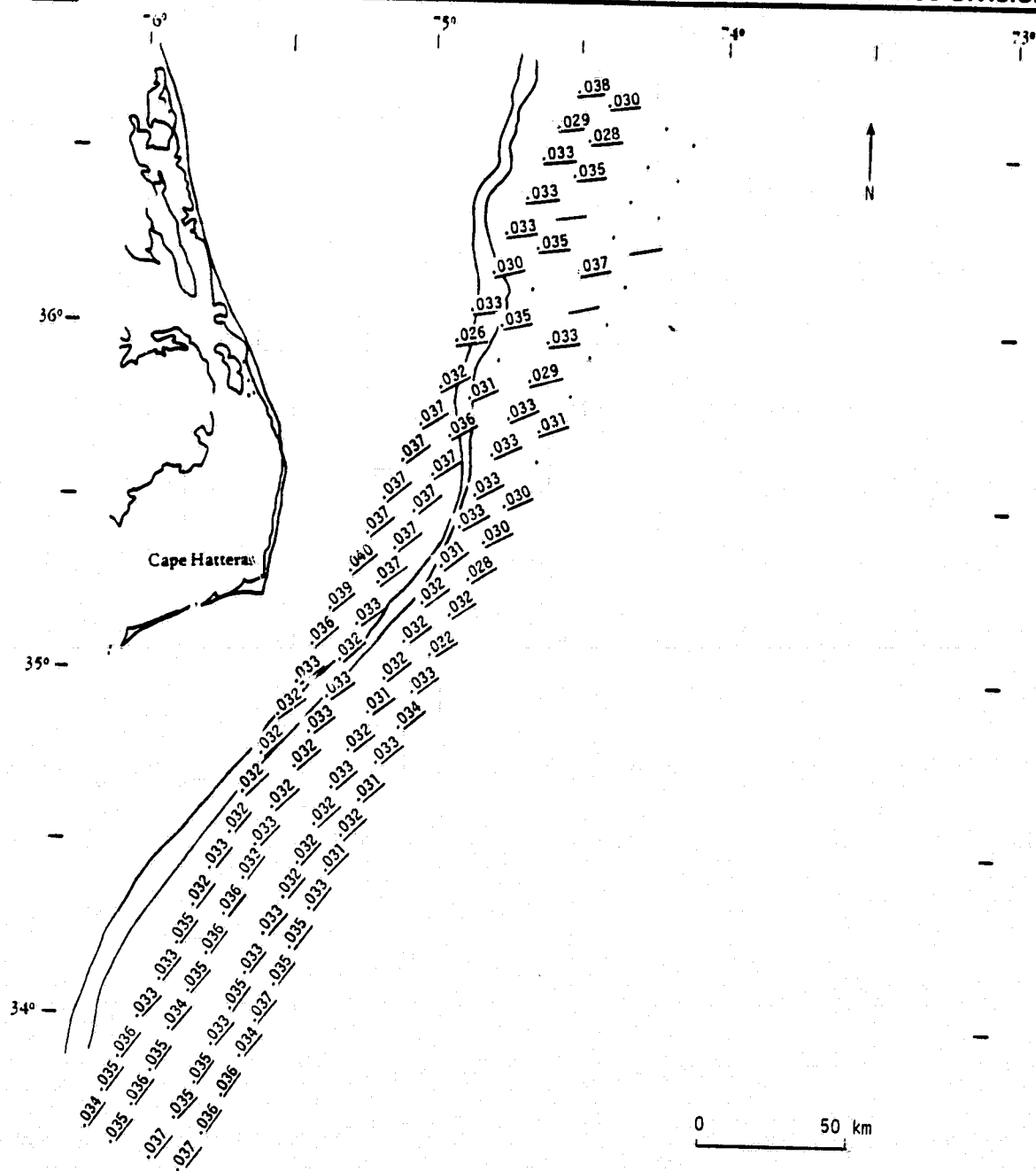


FIGURE 49. SAR-OBSERVED (OFT) WAVE NUMBERS AND VECTORS FROM SEASAT REV. 974 USED TO CALCULATE THE GULF STREAM CURRENT VELOCITY FIELD.

were calculated. These two orthogonal components are in the satellite cross track (Figure 50) and along track (Figure 51) direction. A total of 99 OFTs were used in this calculation. Figure 52 is the resulting vector magnitudes of the calculated upper ocean flow field. At each of the OFT locations, the total current magnitudes were then contoured on 0.5 m/s intervals to produce a visualization of the upper ocean flow structure. These current estimates were then smoothed with a 3 point moving average (corresponding to a spatial resolution of 34 km) in the along-track direction. These values were contoured and are presented in Figure 53. The agreement between these SAR derived velocities and those published by the U.S. Coast Guard for the time of this Seasat overpass (Figure 54) are in remarkably good agreement.

4.4 SHALLOW WATER ANALYSIS

It was shown in the previous section that considerable spatial variation occurred for the dominant deep water wave direction and wavelength due to the source of the gravity waves (hurricane Ella) and the interaction between the gravity waves and the Gulf Stream. In the initial study conducted by ERIM for NOAA/NESS on this data set (Shuchman, et al., 1979), the assumption was made that the deep water gravity waves in this area were uniform and relatively homogeneous (for dominant wavelength and direction).

It is now recognized that the assumption of a homogeneous deep water gravity wave field was not valid and that new, varying, deep water wavelengths and directions were necessary as inputs for the shallow water wave refraction models. Thus, the new approach described below was devised.

Eleven strata were defined to minimize the variation in the deep water wavelength and direction. These strata are illustrated in Figure 55. The deep water positions chosen for each strata were defined so as to include those points (see Figure 34) closest to the

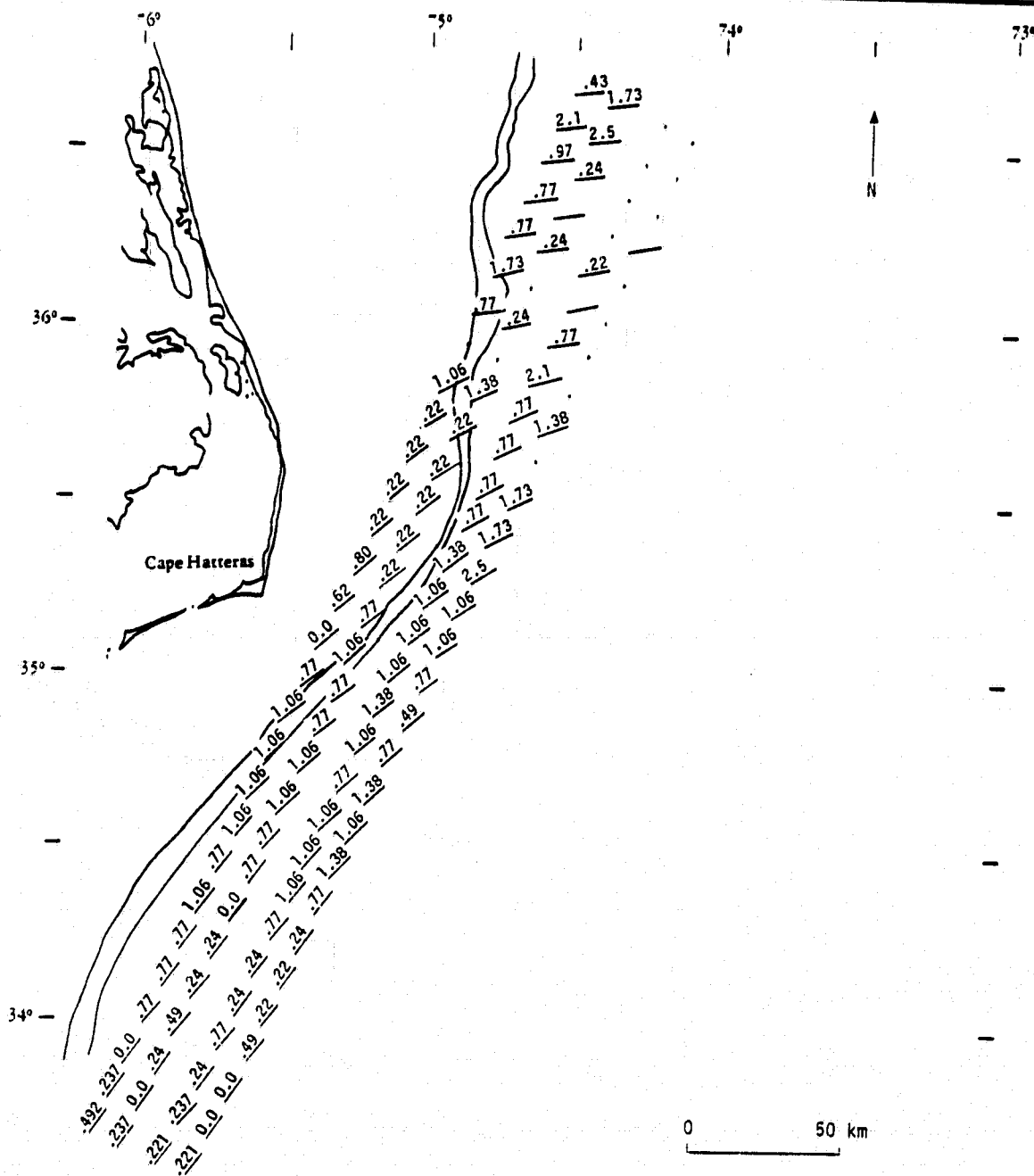
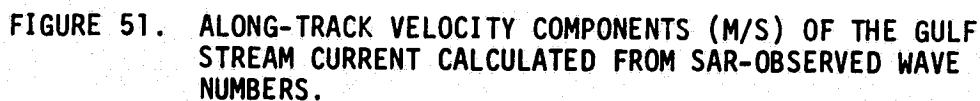


FIGURE 50. CROSS-TRACK VELOCITY COMPONENTS (M/S) OF THE GULF STREAM CURRENT CALCULATED FROM SAR-OBSERVED WAVE NUMBERS.





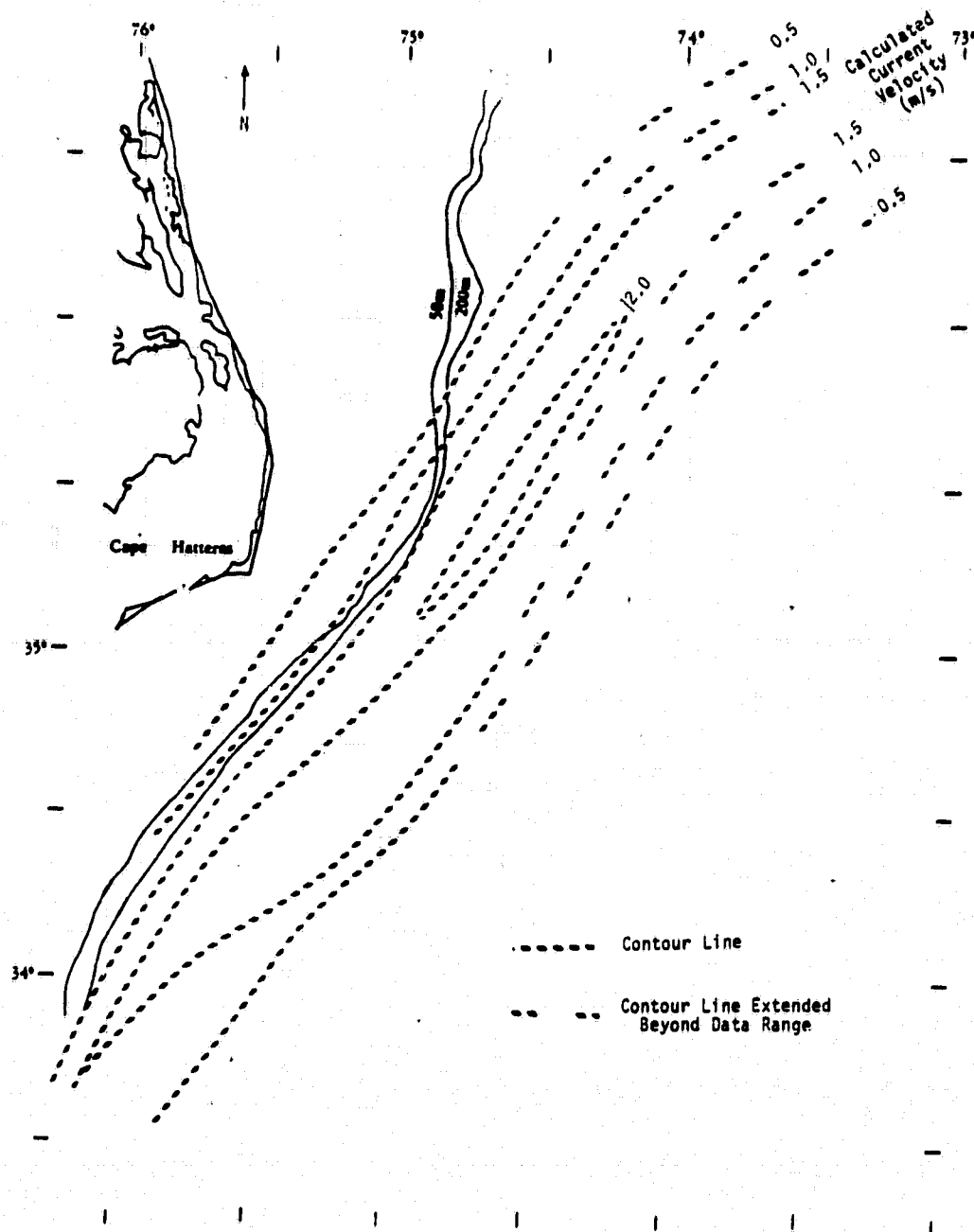


FIGURE 53. SPATIALLY-SMOOTHED (THREE-POINT MOVING AVERAGE) CURRENT VELOCITY PROFILE CALCULATED FROM SAR-OBSERVED WAVE NUMBERS.

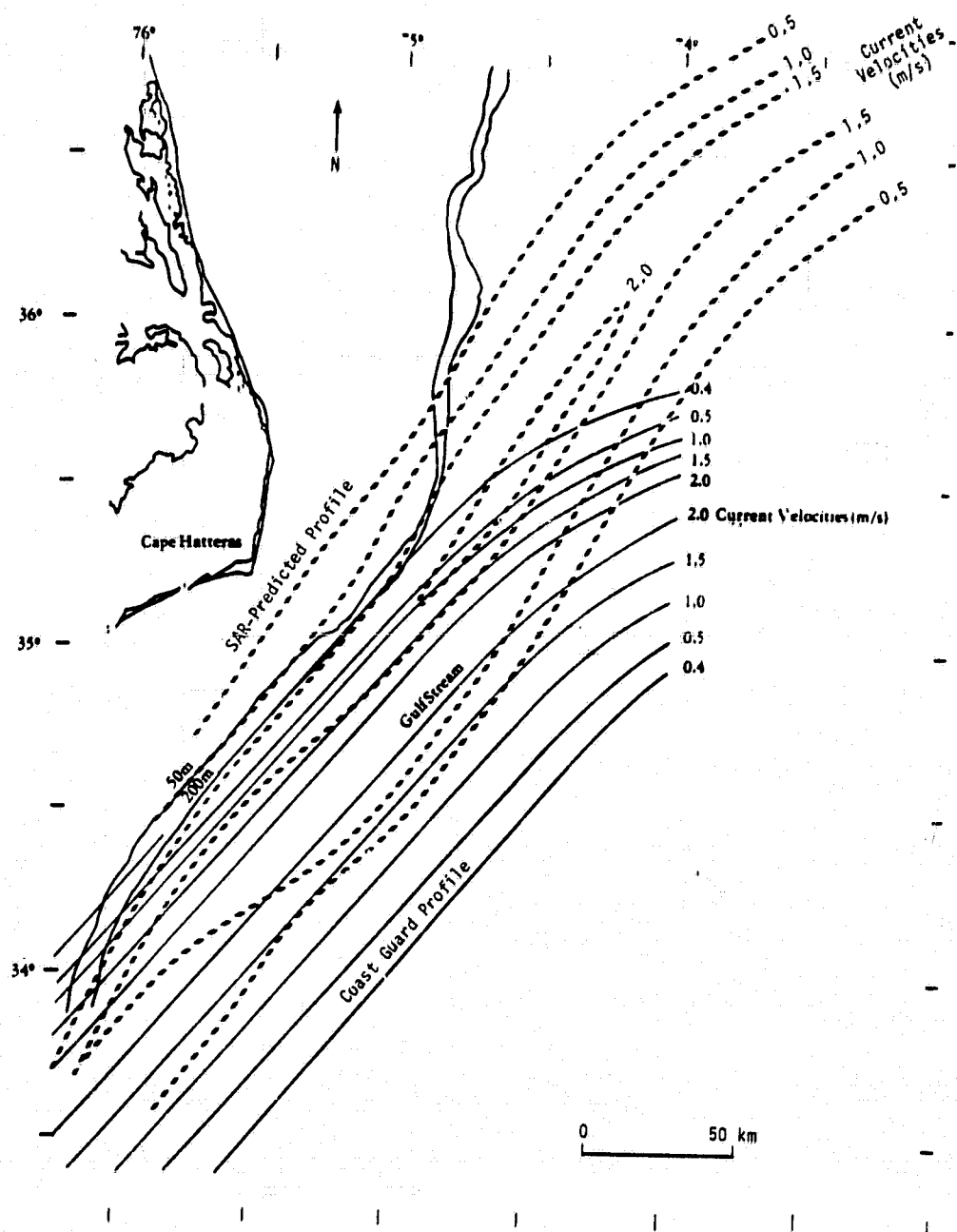


FIGURE 54. COMPARISON OF SAR-DERIVED CURRENT PROFILE TO U.S. COAST GUARD-PREDICTED CURRENT PROFILE. (Agreement is best [within 1 m/s] in the southern portion of the SAR coverage.)

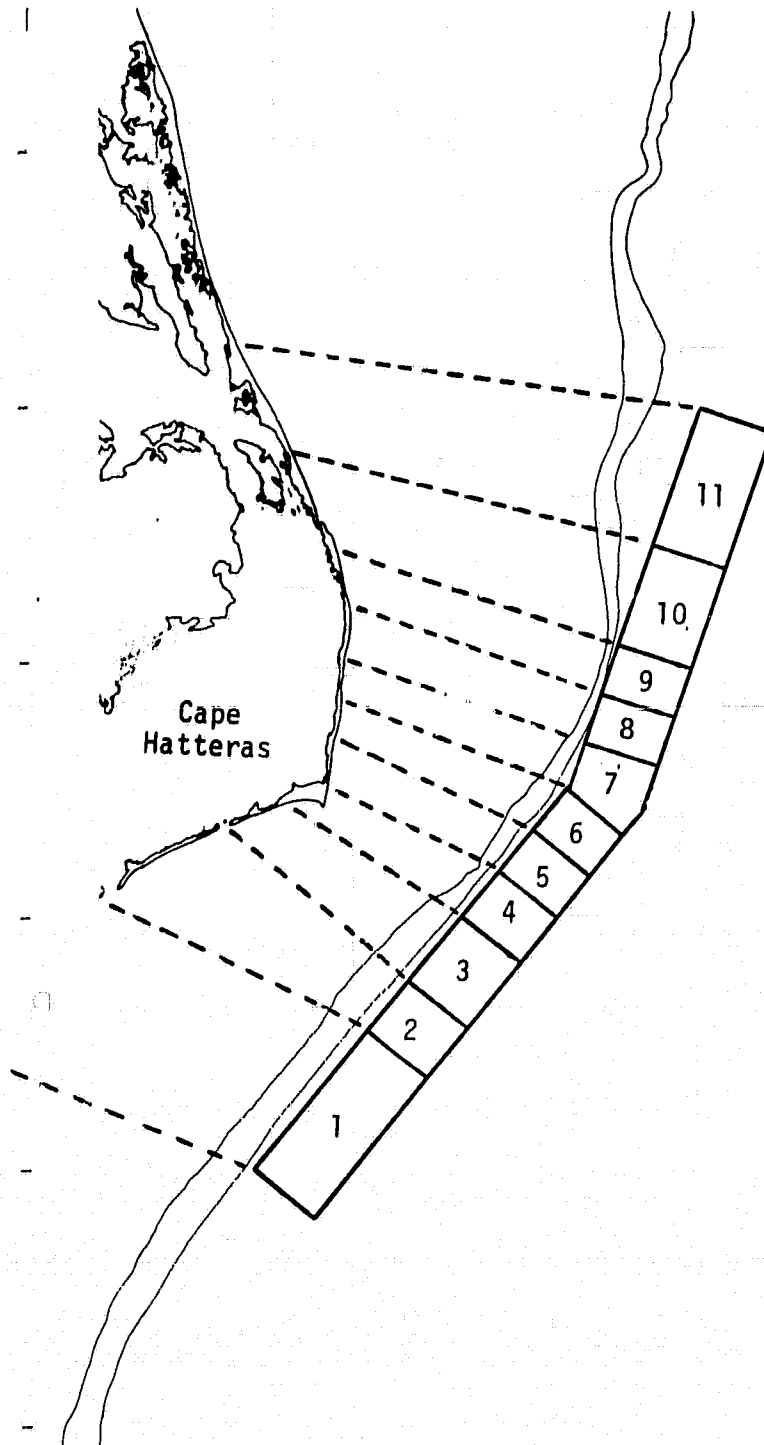


FIGURE 55. DEEP WATER WAVE STRATA LOCATIONS,
SEASAT REV. 974, 3 SEPTEMBER 1978.

200 meter contour still in deep water (>200 m). The wavelength and direction data for these points were then averaged for each strata and are summarized in Table 12.

Using these new deep water inputs, two wave refraction models were used to evaluate Seasat's ability to monitor changes in the gravity wave field as it propagates into shallow water. The first model is the wavelength comparison model developed during last year's study. Based on Airy wave theory (see Neumann and Pierson, 1966), this model computes a shallow water wavelength (L_1) as:

$$L_1 = L_0 \tanh \left(\frac{2\pi h}{L_1} \right) \quad (17)$$

where L_0 is the deep water wavelength, and
 h is the water depth at the position of L_1 .

This model can be algebraically reconfigured to compute a predicted water depth (h') using SAR measured wavelengths as inputs, as follows (after Shuchman, et al., 1979):

$$h' = \frac{L_1}{4\pi} \ln \left(\frac{1 + L_1/L_0}{1 - L_1/L_0} \right) \quad (18)$$

The water depths (h) used in the present study to compare to the predicted depths (h') were obtained from digital tapes of the bathymetric data obtained through NOAA's Environmental Data Information Service (EDIS) in Boulder, Colorado. For SAR data points outside the location of the area of coverage of the digital data, depths were extracted for input from navigation charts.

Since new water depths and new deep water wavelengths were available, last year's data were re-analyzed. Figure 56a shows a scatter plot of h' (predicted depth) versus h (actual depth) and Figure 57a shows a scatter plot of SAR-observed L_1 versus model predicted L_1 , both using last year's depth values and the new deep water

TABLE 12
DOMINANT WAVELENGTHS AND DIRECTIONS FOR
DEEP WATER STRATA

<u>Strata</u>	<u>Points</u>	<u>λ</u>	<u>θ</u>
1	9D, 10D, 11D	196.4 m	313.2°
2	11D, 12C	192.2 m	318.3°
3	12C, 13C	189.8 m	322.3°
4	13C, 14B	193.3 m	321.5°
5	14B, 15B	195.7 m	320.5°
6	15B, 16B	195.7 m	321.8°
7	16B, 17B	198.8 m	321.8°
8	17B, 18B	195.1 m	325.5°
9	18B, 19B	188.7 m	330.3°
10	19B, 20C	183.2 m	330.5°
11	20C, 21D	185.3 m	330.5°

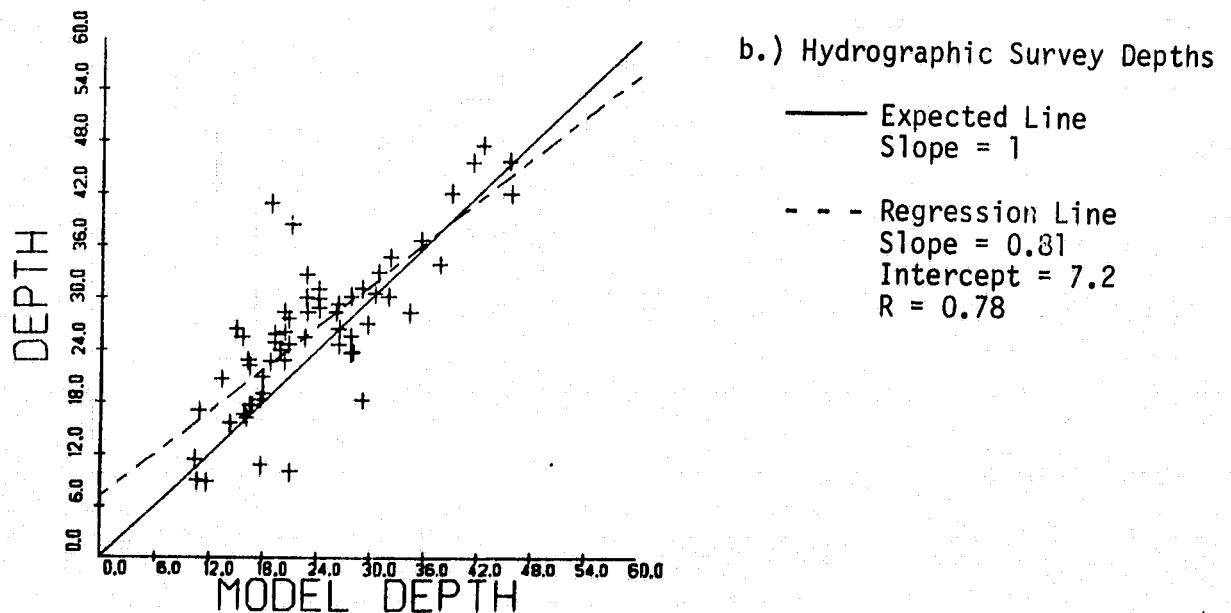
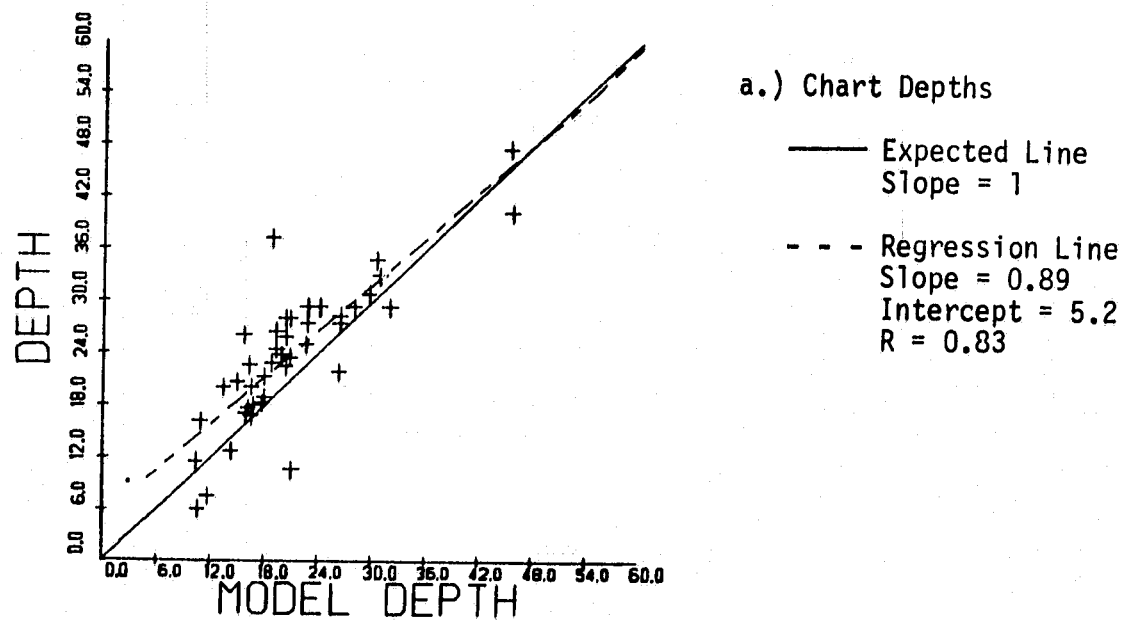


FIGURE 56. SAR-PREDICTED DEPTH (USING INVERTED AIRY WAVE THEORY MODEL) VERSUS ACTUAL DEPTH.

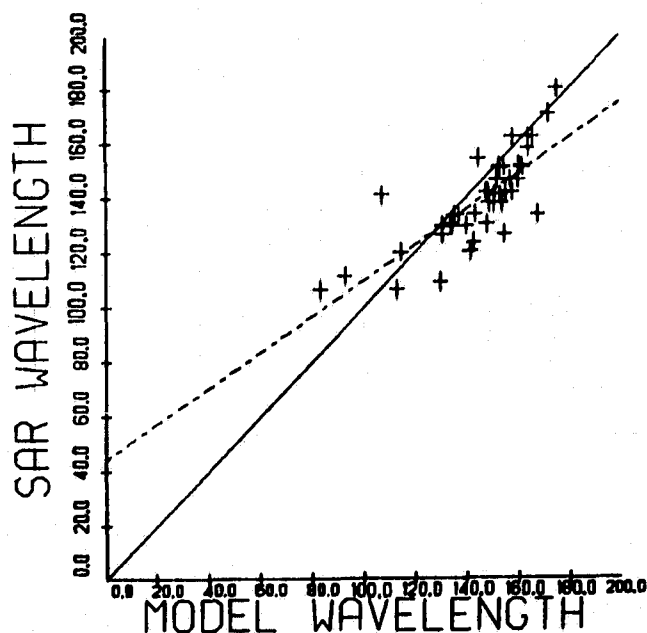
wavelengths as inputs. Figures 56b and 57b illustrate the same data using the new depth values. Relatively little difference exists between the two data sets. It can be seen that the Seasat SAR observed the wavelength changes quite well.

A second model was used to generate values to compare to the SAR-observed wavelengths and directions. This computer based model was obtained from NASA and is described in detail by Poole, et al. (1977). The depth values used for inputs to this model were from the NOAA/EDIS digital bathymetry tapes. Figure 35 previously outlined the area of coverage of digitized depth data and hence where the computer model was run. Figure 48 depicts a typical output plot from this program.

Not all shallow water points for which OFTs were generated were within the area previously outlined in Figure 35. Table 13 summarizes the points where data were available. The locations of the points summarized in Table 13 are presented in Figures 34, 58, and 59. Given in this table are the locations, the SAR observed wavelengths and directions and the model derived values for the point nearest the OFT point (all model values were derived from those depth data points closest to the OFT position, but no further than one nautical mile from the OFT position). The deep water inputs into the wave refraction model were varied according to the stratification scheme summarized in Figure 55 and Table 12.

Figure 60a summarizes the model predicted wavelengths versus the SAR observed wavelengths. As with the previous model (see Figure 57), we can see that the wave refraction model predicted longer wavelengths than were observed with the Seasat SAR.

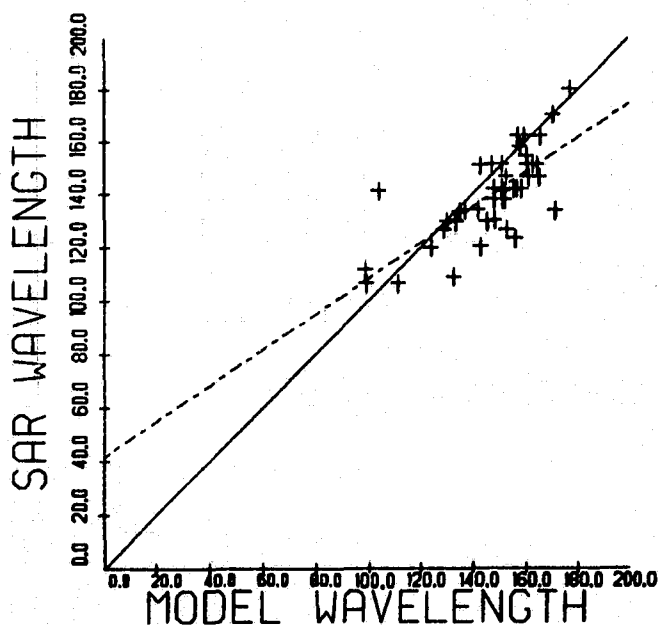
Figure 60b summarizes the directional data. As with the previous study of this data (Shuchman, et al., 1979), the directions produced by the SAR did not fit the wave refraction model results as well as the wavelength comparisons. A trend in the data is present, but it is not a strong trend.



a.) Using Chart Depths as Model Inputs

— Expected Line
Slope = 1.0

- - - Regression Line
Slope = 0.65
Intercept = 44.4
R = 0.78



b.) Using Hydrographic Survey Depths as Model Inputs

— Expected Line
Slope = 1.0

- - - Regression Line
Slope = 0.67
Intercept = 41.9
R = 0.75

FIGURE 57. COMPARISON OF WAVELENGTH FROM AIRY WAVE THEORY MODEL VERSUS SAR-OBSERVED WAVELENGTHS.

TABLE 13
DATA POINTS FOR COMPUTER WAVE REFRACTION
MODEL COMPARISONS

<u>Position</u> *	<u>Depth</u>	<u>SAR λ</u>	<u>Model λ</u>	<u>SAR ϵ</u>	<u>Model ϵ</u>
E19	22.200	129.90	147.19	129.00	138.11
E20	17.700	129.90	137.26	136.00	136.93
E21	27.000	162.40	157.06	140.50	133.34
E22	24.100	141.20	153.91	134.00	132.22
E23	16.300	129.90	----	134.50	----
E25	32.900	162.40	168.27	139.00	141.48
E26	30.500	158.40	168.58	137.50	141.00
E28	26.500	151.50	155.72	135.00	132.78
E29	15.600	120.30	119.66	123.50	123.00
E30	45.800	170.90	183.39	138.00	150.50
E31	23.800	151.00	147.28	139.00	145.69
C1	20.700	120.40	148.51	130.00	138.09
C2	17.100	109.40	138.92	126.50	129.22
C3	22.800	142.30	147.82	138.00	130.22
C4	22.800	130.50	151.71	136.00	135.38
C5	18.300	133.60	133.01	131.00	130.49
C6	17.700	130.50	137.26	133.50	136.93
C7	11.500	106.70	121.68	119.00	111.01
C9	26.100	142.30	156.41	139.00	132.59
C10	24.900	138.10	152.19	133.00	137.23
C11	22.700	138.10	150.46	133.00	130.25
C12	19.000	134.20	137.26	137.00	136.93
C15	28.800	151.70	161.20	137.00	128.98
C16	25.500	146.70	151.86	140.00	139.26
C17	24.700	142.30	147.35	134.00	135.29
C19	20.900	134.20	138.08	131.00	140.47
C20	8.9000	111.80	85.481	122.00	130.82
C24	29.900	151.50	163.70	140.00	129.45

TABLE 13
DATA POINTS FOR COMPUTER WAVE REFRACTION
MODEL COMPARISONS (Continued)

Position*	Depth	SAR λ	Model λ	SAR θ	Model θ
C25	28.400	142.30	156.36	138.50	136.50
C26	25.800	138.10	151.77	139.50	138.70
C29	26.400	123.60	137.98	121.50	140.92
C31	32.700	146.80	157.99	143.00	135.99
C32	27.600	142.30	152.27	141.50	143.09
C33	30.100	146.80	195.77	142.50	140.50
15D	18.300	159.80	140.45	139.50	136.36
16D	25.600	159.00	157.51	138.50	137.59
17C	33.900	171.80	195.08	140.50	145.50
17D	28.400	167.60	159.52	139.50	141.75
18C	42.100	169.60	189.88	140.00	150.30
18D	42.100	169.60	172.52	139.00	142.85
E34	30.200	159.00	155.73	140.50	136.12
E35	23.700	159.00	151.71	139.00	135.38
E36	10.800	133.90	120.64	134.00	123.71

*For location of the positions beginning with an "E", see Figure 58; beginning with a "C", see Figure 59; for the rest of the positions, see Figure 34.

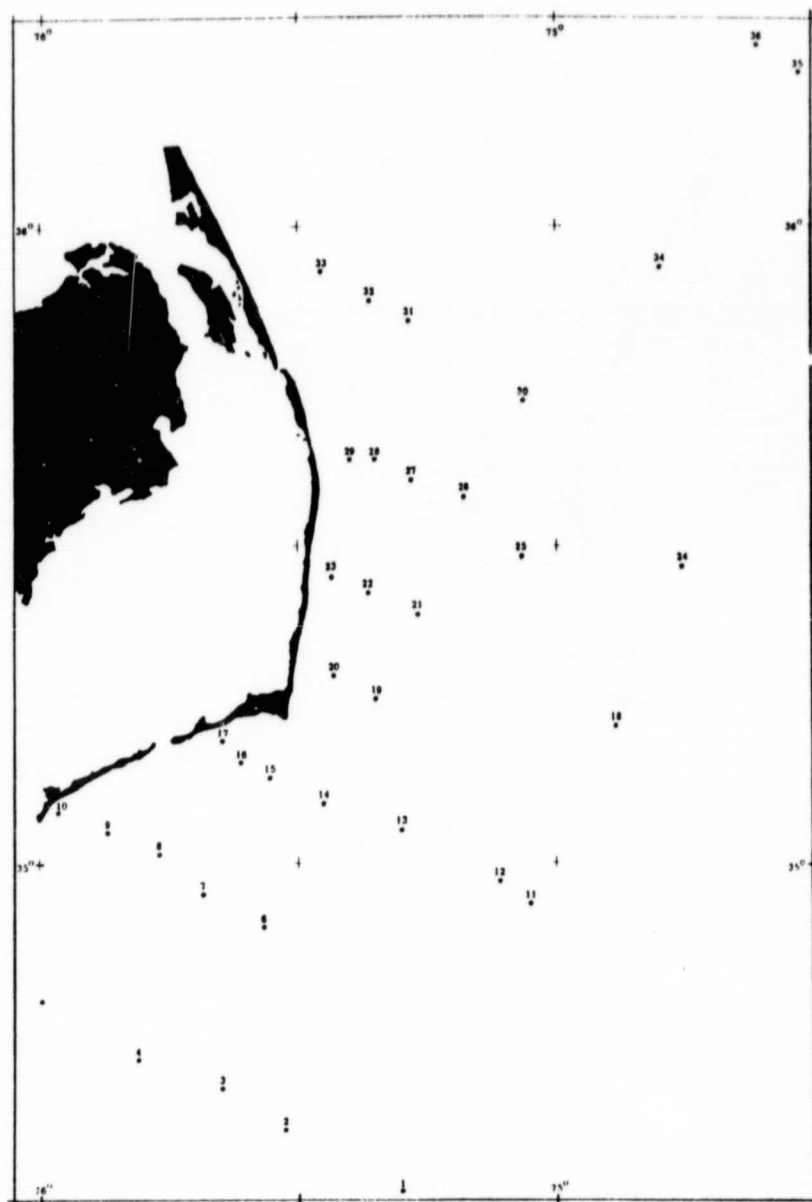


FIGURE 58. POSITION OF ERIM-GENERATED SHALLOW WATER OFTS.
(E prefix in Table 13.)

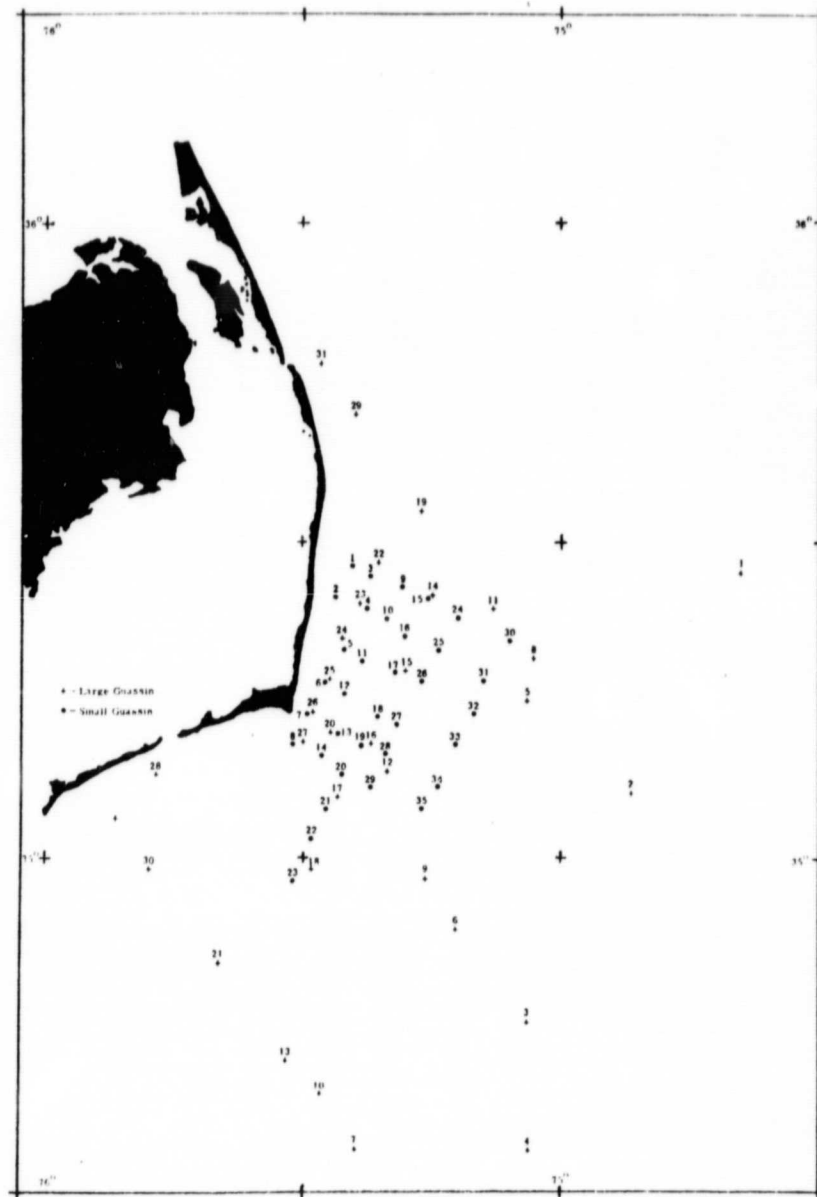
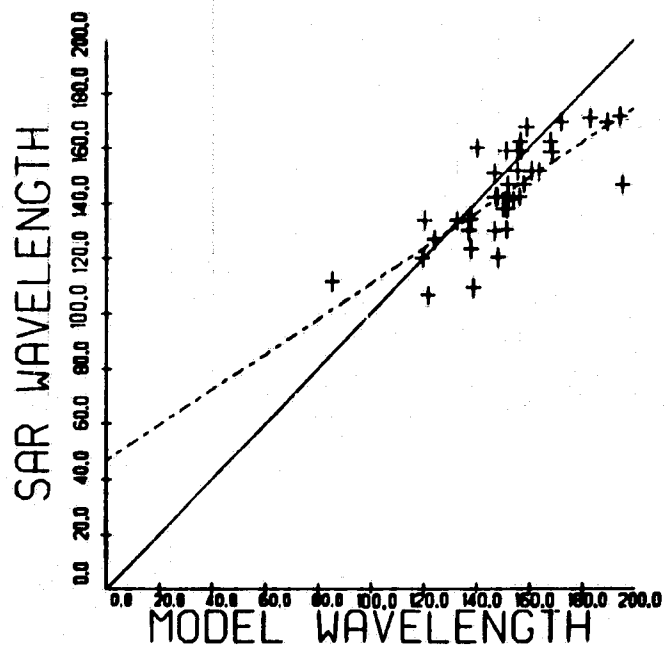
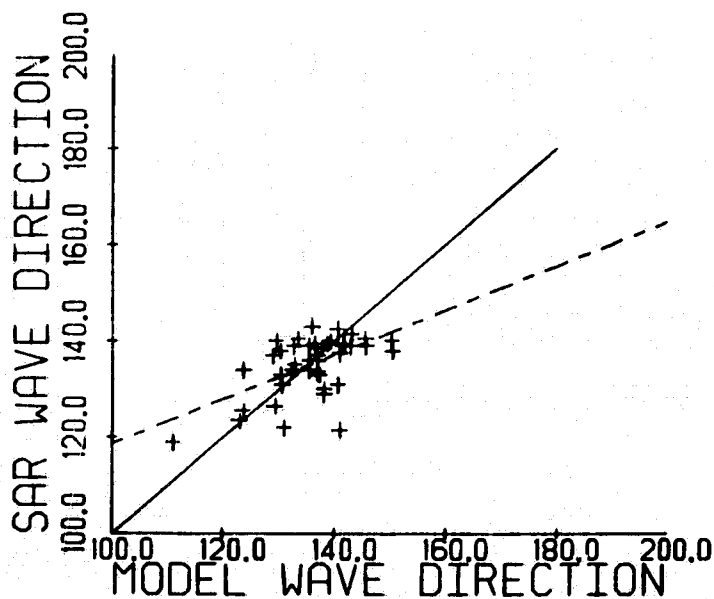


FIGURE 59. POSITION OF CERC-GENERATED SHALLOW WATER Ofts.
(C prefix in Table 13.)



a.) Wavelength Comparison

- Expected Line
Slope = 1
- - - Regression Line
Slope = 0.64
Intercept = 47.0
R = 0.77



b.) Wave Direction Comparison

- Expected Line
Slope = 1
- - - Regression Line
Slope = 0.69
Intercept = 42.9
R = 0.56

FIGURE 60. COMPARISON OF WAVELENGTHS AND DIRECTIONS FROM COMPUTER-BASED MODEL VERSUS SAR-OBSERVED VALUES.

One trend in the above wave refraction analyses was that the waves detected by the SAR had shorter wavelengths than were predicted by the wave refraction model. One of four reasons could account for this: (1) a bias exists in the manner the SAR observes gravity waves; (2) the water depths were less than the chart values, (3) a physical disturbance was present which decreased the wavelength a greater amount than would occur naturally; or (4) a bias exists in the manner in which the SAR images shoaling gravity waves. Previous studies of the ability of the Seasat SAR to estimate dominant wavelength have not detected a bias in the SAR data (Shuchman, et al., 1981a). The depth data to which comparisons were made were from actual hydrographic surveys and are not suspect, but are known to be conservative. Some oceanic factor could be the cause. In the region of the Eastern U.S. coastline, a countercurrent (to the Gulf Stream) is well documented. This current generally flows in a southerly direction and could be responsible for shortening the wavelengths in the near shore coastal region of Cape Hatteras. Finally, a bias in the way the SAR is imaging the waves in coastal waters could exist because of the non-stationary nature of gravity waves in shallow water.

The results obtained from all the wavelength comparisons between SAR observed values and the model estimates were essentially the same. The best linear fit to the data (see Figures 57 and 60) all have a slope of ~ 0.65 and a y-intercept of about 45 meters. If the SAR were truly imaging gravity wavelength, we would expect better agreement than this. Previous analyses of the ability of the Seasat SAR suggest that when the dominant ocean wavelength is on the order of 120 meters or less, the SAR has difficulty in imaging that wavefield (Kasischke, et al., 1981). We therefore have some justification for removing data points where the wave refraction models predict a wavelength of 120 meters or less. This was done for the Cape

Hatteras data set and new wavelength comparisons made. These results, summarized in Figure 61, indicate that the slope of the regression equation is now between 0.82 and 0.91 with a y-intercept between 5 and 19 meters. This is in much better agreement with the models.

4.5 DISCUSSION

This investigation represents an initial attempt to document and predict subtle changes in the propagation characteristics of a hurricane generated evolving gravity wave system. As a result of these efforts, several significant surface gravity wave and oceanographic phenomena have been investigated over a large spatial region of the ocean. The primary significance of this study is the documentation of the variation in gravity wave fields over a large area through the use of a large number of two-dimensional optical Fourier transforms, and the high resolution of this approach in both wave number and direction. By employing these techniques, we were able to accomplish the following tasks for Seasat Rev. 974:

1. Determination of the wave generation region of hurricane Ella by wave ray hindcasting to a 50 km square region.
2. Determination of non-uniform deep water wave conditions away from the wave generation region.
3. Observation and prediction of subtle changes in gravity wavelength and direction as a result of wave/current interactions with the Gulf Stream.
4. Use of these Seasat SAR-observed changes in wave propagation characteristics to analytically solve for the gross flow field of the upper ocean.
5. Extension of our predictive capability in shallow water regions based upon topography-induced gravity wave refraction observed by Seasat SAR.

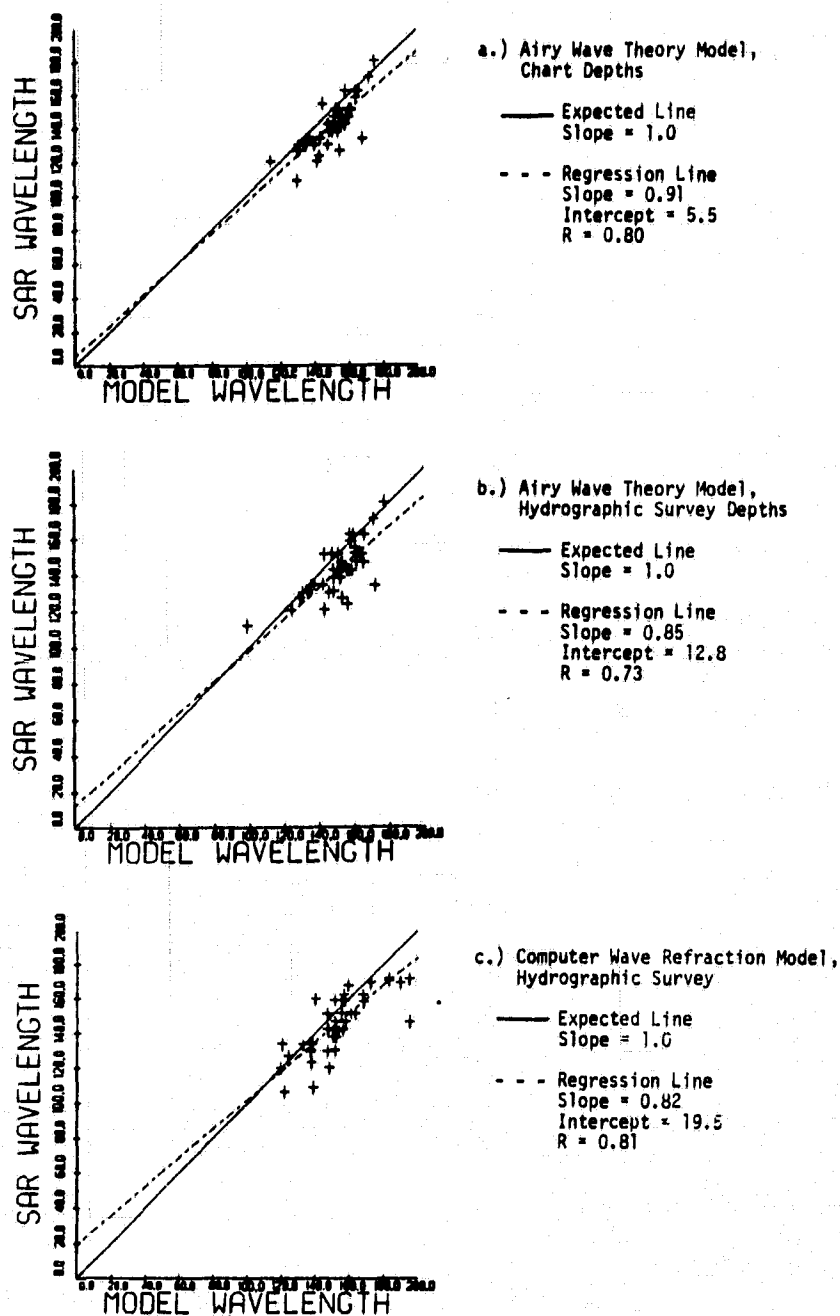


FIGURE 61. MODEL-PREDICTED WAVELENGTHS VERSUS SAR-OBSERVED WAVELENGTHS ELIMINATING POINTS WHERE WAVELENGTH (SAR) <120 METERS.

Although these tasks were accomplished, the methods employed in this investigation have strict limitations.

In an effort to quantify these limitations, a statistical analysis of the accuracy and reliability of the OFT estimates of two-dimensional wave spectra was performed. The results of this analysis indicate that the Seasat SAR is capable of producing an estimate of the wave propagation direction to within $1-2^\circ$. A similar estimate for SAR sensed gravity wave numbers was obtained to an accuracy of approximately 2 percent. This may be due in part to the fortuitous set of circumstances associated with Seasat Rev. 974. We strongly recommend that these tests be repeated for a case of non-hurricane generated waves.

We also recommend that the findings of the other portions of this investigation be rigorously evaluated with other Seasat SAR data. In particular, the demonstrated ability of SAR to (1) isolate the wave generation region of severe storms, (2) detect propagation characteristics of spatially evolving gravity wave systems, (3) document large scale wave/current interaction phenomena, and (4) ultimately predict and map major ocean current systems from these Seasat SAR observations is in need of further investigation. The limits of applicability and environmental ranges over which these techniques produced reliable results must be determined from additional Seasat revolutions. The results of this investigation, although encouraging, require a continued effort to verify and evaluate the methods and results obtained for Rev. 974.

In summary, as a result of this investigation, we have attempted to extend the current uses of Seasat SAR ocean wave data. We have demonstrated that through the use of a large number of OFTs, very reliable estimates of wave propagation characteristics and their spatial gradients can be obtained. These same procedures should also be attempted for digital Fourier transforms of Seasat SAR data. We have also demonstrated a capability to detect the dynamics of the

upper ocean with its major ocean current systems, utilizing SAR-sensed changes in the gravity wave field structure. Should this technique prove reliable with other Seasat SAR data sets, a potential for rapid, global surface current mapping may exist. Furthermore, we have utilized changes in SAR sensed wave characteristics in shallow water to provide an estimate of the topography in these regions. Refinement of the techniques and analytical formulations employed in this investigation may eventually lead to an operational, global ocean sensing capability for storm wave generation regions, and/or ocean surface currents and nearshore bathymetric changes.

5

RECOMMENDATIONS FOR ADDITIONAL INVESTIGATIONS

This report has presented results which show the usefulness of using Seasat SAR data to monitor and map large scale spatial variations in deep and shallow water gravity wave fields. This investigation has also studied an advanced spectral analysis technique, the semicausal model, and compared results obtained from it to those from the more conventional fast Fourier transform technique. This model needs further evaluation of its utility in generating spectral estimates from SAR wave data.

Continuation of efforts is needed in three general areas: (1) further evaluation of the semicausal model; (2) further analysis of the deep and shallow water spatial variation documented by the Seasat SAR during Rev. 974; and (3) analysis of other Seasat SAR data to further document the Seasat SAR's utility as a tool in monitoring the propagation characteristics of gravity wave fields.

To further test the semicausal model, the following areas should be addressed:

1. Compare semicausal spectral estimates to FFT spectral estimates using a wider variety of Seasat SAR imagery,
2. Investigate the effects of noise on the SC model by artificially adding noise to actual SAR data.

To further analyze the Seasat SAR data collected during Rev. 974, the following areas should be pursued:

1. Obtain optimally processed digital data for Rev. 974,
2. Further evaluate Seasat SARs ability to monitor shallow water wave refraction using digital analysis techniques,
3. Further evaluate wave/current interaction models using digital analysis techniques,

4. Evaluate Seasat SAR's ability to map large scale ocean currents by monitoring changes in direction and wavelength of the gravity waves.

Finally, to further evaluate the utility of spaceborne SARs to monitor gravity wave fields, the following areas should be addressed using Seasat SAR data other than Rev. 974:

1. Document large scale variations in gravity wave fields,
2. Isolate the wave generation regions of large storms,
3. Document the changes in wave characteristics near islands and in near shore regions,
4. Document large scale wave/current interactions,
5. Detect the propagation characteristics of spatially evolving gravity wave fields.

REFERENCES

Allan, T.D. and T.H. Guymer, Seasat and JASIN, Int. J. Remote Sensing, Vol. 1, pp. 261-267, 1980.

Anonymous, Weekly Sea Current Chart Production Manual, Oceanographic Unit Technical Report 78-3, U.S. Coast Guard, Department of Transportation, 1978.

Ausherman, D.A., Digital Versus Optical Techniques in Synthetic Aperture Radar (SAR) Data Processing, Optical Eng., Vol. 19, pp. 157-167, 1980.

Beal, R.C. Spaceborne Imaging Radar: Monitoring of Ocean Waves, Science, 204, pp. 1373-1375, 1980.

Beal, R.C., P.S. DeLeonibus and I. Katz (eds.), Spaceborne Synthetic Aperture Radar Imagery for Oceanography, Johns Hopkins Univ. Press, Baltimore, MD, 215 pp., 1981.

Burg, J.P., Maximum Entropy Spectral Analysis, Ph.D. Thesis, Stanford University, 1975.

Fuglister, F.C. and L.V. Worthington, Cyclonic Rings Formed by the Gulf Stream, 1965-66, in Studies in Oceanography: A Tribute George Wust on this 80th Birthday, A.L. Gordon, ed., Gordon and Breach, New York, pp. 137-168, 1951.

Gonzalez, F.I., R.A. Shuchman, D.B. Ross, C.L. Rufenach and J.F.R. Gower, Synthetic Aperture Radar Wave Observations During GOASEX, in Oceanography from Space, ed. J.F.R. Gower, Plenum Press, pp. 459-467, 1981.

Iselin, C.O.D., A Study of the Circulation of the Western North Atlantic, Pap. Phys. Oceanograph. and Meteor., 4(4), pp. 101, 1936.

Iselin, C.O.D., and F.C. Fuglister, Some Recent Developments in the Study of the Gulf Stream, J. Mar. Res., 7, pp. 317-329, 1948.

Jain, A.K. and S. Ranganath, Two-Dimensional Spectral Estimation, Proc. of the RADC Spectrum Estimation Workshop, 1978.

Kasischke, E.S., Extraction of Gravity Wave Information from Synthetic Aperture Radar Data, Univ. of Mich. M.S. Thesis, 108 pp., 1980.

Kasischke, E.S., A. Klooster and R.A. Shuchman, Verification of Synthetic Aperture Radar Focusing Algorithms, Proc. Thirteenth Int. Symp. Remote Sensing Environ., Ann Arbor, MI, pp. 1077-1092, 1979.

Kasischke, E.S. and R.A. Shuchman, The Use of Wave Contrast Measurements in the Evaluation of SAR/Gravity Wave Models, Proceedings of the Fifteenth International Symposium on Remote Sensing of Environment (in press), May 1981.

Kasischke, E.S., R.A. Shuchman, J.D. Lyden, R.F. Stewart, J.F. Vesecky and H.A. Assal, Seasat SAR Observations of Ocean Gravity Waves During the JASIN Experiment, submitted to J. Geophys. Res., 1981.

Neumann, G. and W.J. Pierson, Principles in Physical Oceanography, Prentice Hall, Inc., Englewood Cliffs, N.J., 1966.

Phillips, O.M., The Structure of Short Gravity Waves on the Ocean Surface, in Spaceborne Synthetic Aperture Radar for Oceanography, ed. by R.C. Beal, P.S. DeLeonibus, and I. Katz, Johns Hopkins Univ. Press, Baltimore, MD, pp. 24-31, 1981.

Poole, L.H., S.R. LeCroy and W.D. Morris, Minimal-Resource Computer Program for Automatic Generation of Ocean Wave Ray or Crest Diagrams in Shoaling Water, NASA Technical Memorandum 74076, NASA Langley Research Center, Hampton, Virginia 1977.

Raney, R.K., Synthetic Aperture Radar and Moving Targets, IEEE Trans. Aerospace Elect. Syst., Vol. AES-7, pp. 499-505, 1971.

Ross, D.B., Personal Communication, 1981.

Schaeffer, R.L., W. Mendenhall, and L.Ott, Elementary Survey Sampling, 2nd Ed., Duxburg Press, North Scituate, Mass., 278 pp., 1979.

Sheffe, H., The Analysis of Variance, John Wiley and Sons, Inc., New York, 477 pp., 1959.

Shuchman, R.A., Processing Synthetic Aperture Radar Data of Ocean Waves, Proceedings of the COSPAR/SCOR/IUCRUM Symposium on Oceanography from Space, Plenum Press, pp. 477-496, 1981.

Shuchman, R.A. and J.S. Zelenka, Processing of Ocean Wave Data from a Synthetic Aperture Radar, Boundary-Layer Meteorol., 13, pp. 181-191, 1978.

Shuchman, R.A., E.S. Kasischke, A. Klooster and P.L. Jackson, SAR Coastal Ocean Wave Analysis - A Wave Refraction and Diffraction Study, ERIM Final Report No. 138600-2-F, Ann Arbor, MI, 1979.

Shuchman, R.A., K.H. Knorr, J.C. Dwyer, P.L. Jackson, A. Klooster and A.L. Maffett, Imaging Ocean Waves with SAR - A SAR Ocean Wave Algorithm Development, ERIM Interim Technical Report No. 124300-5-T, Ann Arbor, MI, 123 pp., 1979a.

Shuchman, R.A., A.L. Maffett and A. Klooster, Static Modeling of a SAR Imaged Ocean Scene, IEEE J. Oceanic Eng., Vol. OE-6, (in Press), 1981a.

Shuchman, R.A., E.S. Kasischke, J.D. Lyden, and G.A. Meadows, The Use of Synthetic Aperture Radar (SAR) to Measure Ocean Gravity Waves, Proceedings of the National Academy of Sciences Special Conference on Wave Technology (in press), April 1981b.

Swingler, D.N., Burg's Maximum Entropy Algorithm versus the Discrete Fourier Transform as a Frequency Estimator for Truncated Real Sinusoids, J. Geophys. Res., 85, 1435-1438, 1980.

Vesecky, J.F. and R.H. Stewart, The Observation of Ocean Surface Phenomena Using Imagery from the Seasat Synthetic Aperture Radar - An Assessment, submitted to J. Geophys. Res., 1981.

Von Arx, W.S., An Introduction to Physical Oceanography, Pub. Co., Inc., Reading, MA, 422 p, 1962.

Worthington, L.V., Three Detailed Cross Sections of the Gulf Stream, Tellus, 6, pp. 116-123, 1954.

APPENDIX A

"HIGH RESOLUTION SPECTRAL ESTIMATION OF
SAR OCEAN WAVE IMAGERY"

Included in this Appendix is a copy of a journal article which
has been submitted to the Journal of Geophysical Research.

HIGH RESOLUTION SPECTRAL ESTIMATION OF
SAR OCEAN WAVE IMAGERY

P.L. Jackson*

Geological Sciences Department
The University of Michigan
Ann Arbor, Michigan 48109

and

R.A. Shuchman

Radar and Optics Division
Environmental Research Institute of Michigan
Ann Arbor, Michigan 48107

ABSTRACT

A new two-dimensional spectral estimation procedure, termed semicausal, is applicable to analysis of ocean wave gravity waves. Spectral estimates of both reference functions and actual synthetic aperture radar (SAR) data of ocean waves have been generated using semicausal techniques and compared to Fast Fourier Transform estimates of identical data sets. The semicausal method can successfully generate spectral estimates of truncated data sets and data sets with two closely spaced frequency components. The semicausal estimate is sensitive to the autoregressive order and exhibits spectral splitting in some cases. Its noise sensitivity is similar to that of the Fourier transform.

INTRODUCTION

The wave number and propagation direction of ocean gravity waves are readily computed from digitized imagery by two-dimensional spectral estimation. A commonly used type of wave spectra display, where the distance of peak values from the origin is proportional to the wave number, is shown in Figure 1. Peak values are shown by the contour levels. Propagation direction is along a line between the

*Also an ERIM consultant.

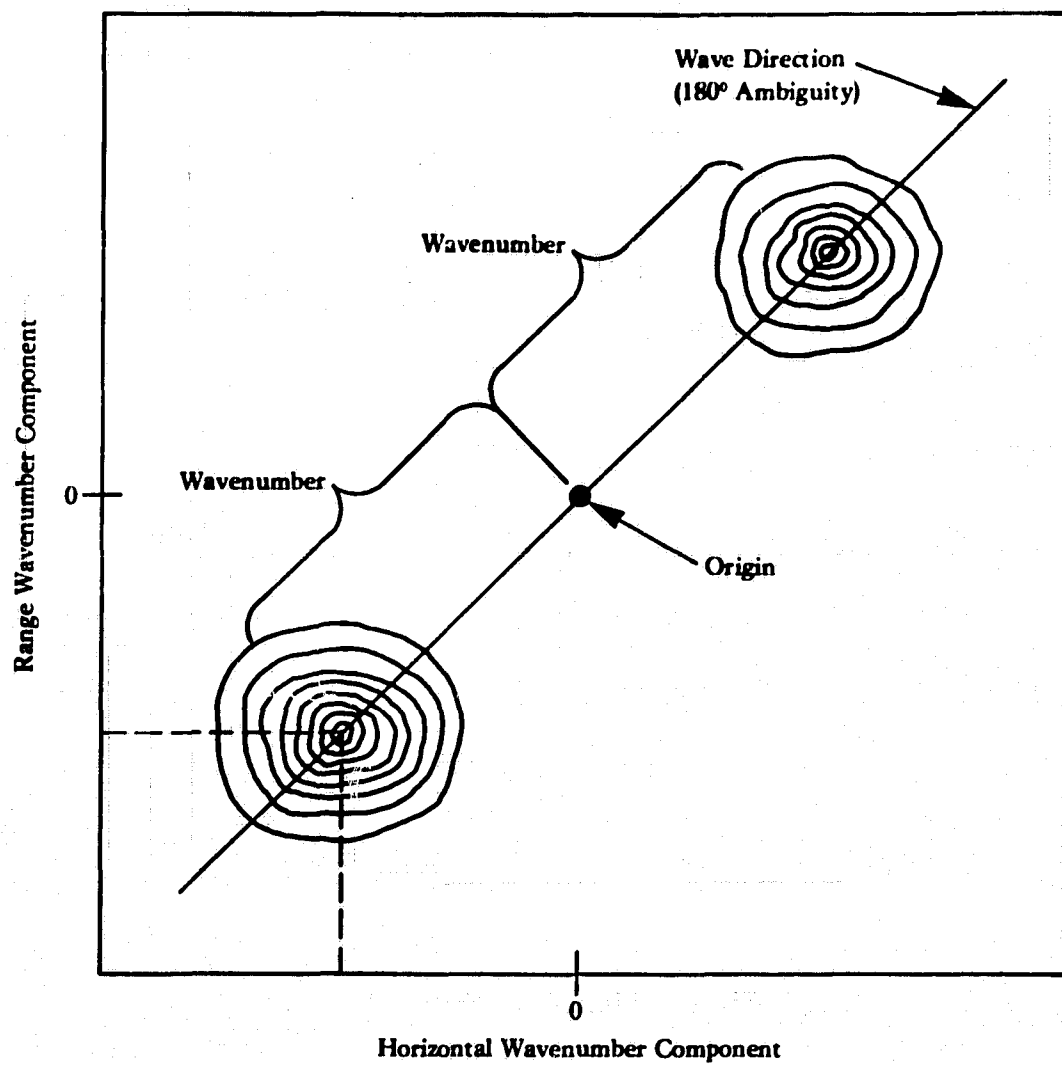


Figure 1. Two-dimensional spectral estimation of ocean waves.
(Schematic representation)

origin and the peak contour values, which are a direct but as yet undetermined function of wave height. Note, there is a 180° ambiguity with respect to direction of wave propagation. In present practice, ocean wave spectral estimates are produced by both digital (FFT) and optical (OFT) two-dimensional Fourier transforms (Shuchman, et al., 1979).

The limited resolution of the Fourier transform, however, impairs its usefulness in discriminating between two waves whose wave numbers are closely spaced, and in spectral estimation using truncated data sets. Since wave refraction produces curved wave fronts, the spectrum of severely truncated sets must be estimated. Truncation approximates a linear wave front, which enables accurate assessment of propagation direction at a specific location. Overcoming the restrictions of Fourier transform resolution would aid in more accurate determination of wave spectra.

Many investigators are involved in overcoming Fourier transform limitations. Since the introduction of autoregressive (AR) techniques by Parzen (1967) and the similar maximum entropy (MEM) by Burg (1967, 1975), contributions have been and are being made to the development of new high resolution spectral estimation. One-dimensional spectral estimation methods have been made more accurate and reliable. Frequency shifts have been reduced, and line-splitting eliminated (Marple, 1980). More two-dimensional high resolution spectral estimation methods are also being introduced (Roucos and Childers, 1980). A recent workshop by the Acoustics, Speech and Signal Processing Society of IEEE (Proceedings of the First ASSP Workshop on Spectral Estimation, 1981) demonstrated the wide extent and rapid development of this field.

To compare the semicausal method (SCM) and the FFT, both were used to obtain spectral estimations of SAR ocean wave imagery, and also of synthesized data for which the frequency components were

accurately known. The high resolution technique was developed by Jain and Ranganath (1979) and termed "semicausal," which we abbreviate to SCM. Jain (1981) also has described the SCM configuration in an image enhancement context. The SCM employs two-dimensional AR and is representative of the new high resolution techniques at this stage of development. The method does exhibit frequency shifts and line splitting. Its sensitivity to noise is illustrated in this paper. As the above publications by Jain and Ranganath are not readily accessible and do not fully describe the derivation, this AR algorithm and its derivation will be described here.

Of approximately 200 experiments on reference functions and approximately 30 on ocean wave data, a selection from those which most clearly compare the FFT with the SCM are presented here. The results of the comparison, which indicate the SCM can improve resolution over the FFT, are shown in the form of contour plots.

ALGORITHM

A two-dimensional AR scheme is employed in which the selection of data samples to form the AR order is "semicausal." This term refers to the two-dimensional treatment as an initial value problem (causal) in one direction and a boundary value problem (non-causal) in the perpendicular direction.

The algorithm can be developed as follows: We wish to find an AR sequence in a zero-mean two-dimensional random field U to predict a sample value $\hat{u}_{i,j}$. The mean square error between the actual value $u_{i,j}$ and $\hat{u}_{i,j}$ should be a minimum. The AR sequence will then enable spectral estimation by an all-pole rather than an all-zero model as in the FFT (Ulrych, 1972).

For the AR sequence, data samples are chosen which are interior to a window W as shown in Figure 2. Then,

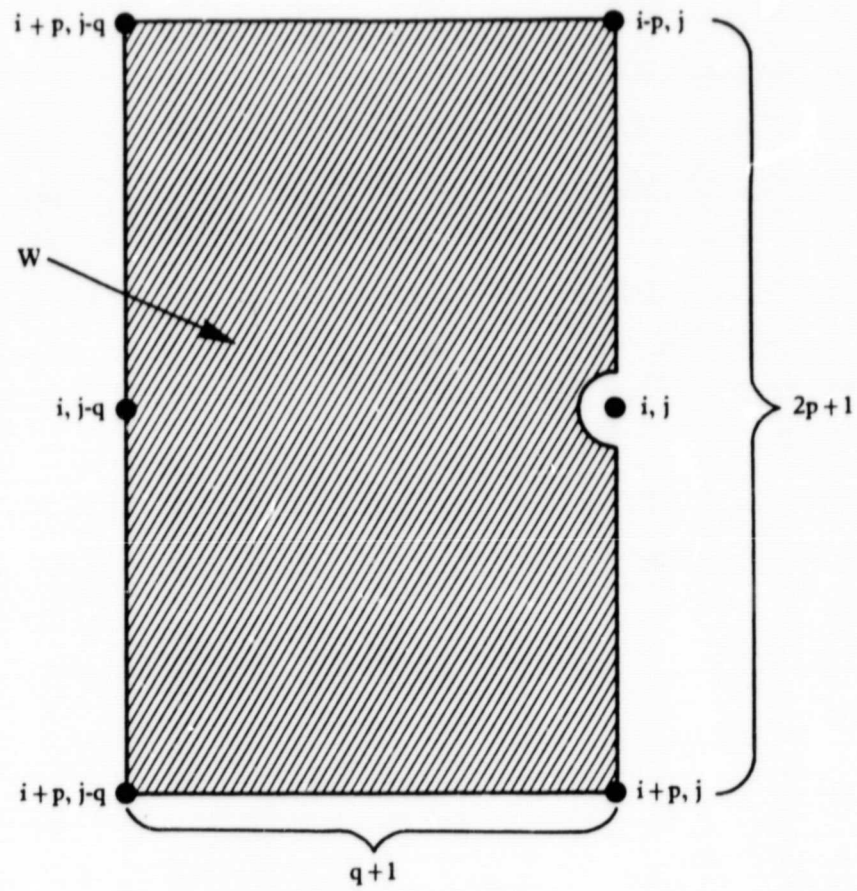


Figure 2. Window of two-dimensional field U used to predict a sample value $\hat{U}_{i,j}$ based on interior samples.

$$u_{i,j} = \hat{u}_{i,j} + \epsilon_{i,j} \quad (1)$$

where $u_{i,j}$ is the datum, $\hat{u}_{i,j}$ the predicted value, and $\epsilon_{i,j}$ the prediction error.

Substituting for $\hat{u}_{i,j}$, Eq. (1) becomes

$$u_{i,j} = \sum_{m=-p}^p a_{m,0} u_{i-m,j} + \sum_{m=-p}^p \sum_{n=1}^q a_{m,n} u_{i-m,j-n} + \epsilon_{i,j} \quad (2)$$

where the predicted $\hat{u}_{i,j}$ is written as a linear combination of samples within the window. The $a_{m,n}$ can be found from a mean-square-error criterion, which implies the observations are orthogonal to the error.

For any k, ℓ within the window, Eq. (1) can be multiplied by $u_{i-k,j-\ell}$ and expected values taken:

$$\begin{aligned} E(u_{i,j} u_{i-k,j-\ell}) &= \sum_{\substack{m=-p \\ m \neq 0}}^p a_{m,0} E(u_{i-m,j} u_{i-k,j-\ell}) \\ &\quad + \sum_{n=-p}^p \sum_{n=1}^q a_{m,n} E(u_{i-m,j-n} u_{i-k,j-\ell}) \\ &\quad + E(\epsilon_{i,j} u_{i-k,j-\ell}) \end{aligned} \quad (3)$$

If the data are stationary, Eq. (2) becomes

$$\gamma(k, \ell) = \sum_{\substack{m=-p \\ m \neq 0}}^p a_{m,0} \gamma(k-m, \ell) + \sum_{m=-p}^p \sum_{n=1}^q a_{m,n} \gamma(k-m, \ell-n) + 0, \quad (4)$$

since $E(\epsilon_{i,j} u_{i-k,j-\ell}) = 0$ by orthogonality. $\gamma(k, \ell)$ is the two-dimensional autocovariance function.

At $k = \ell = 0$, Eq. (4) becomes

$$\gamma(0,0) = \sum_{\substack{m=-p \\ m \neq 0}}^p a_{m,0} \gamma(-m,0) + \sum_{m=-p}^p \sum_{n=1}^q a_{m,n} \gamma(-m,-n) + E(\epsilon_{i,j} u_{i,j}), \quad (5)$$

where

$$E(\epsilon_{i,j} u_{i,j}) = E(\epsilon_{i,j} [\hat{u}_{i,j} + \epsilon_{i,j}]) = E(\epsilon_{i,j}^2), \quad (6)$$

as $E(\hat{u}_{i,j} \epsilon_{i,j}) = 0$ by the orthogonality principle. By definition,

$$E(\epsilon_{i,j}^2) = \beta^2, \quad (7)$$

is the variance of the prediction error.

Combining Eq. (4), (5), (6), and (7),

$$\gamma(k,\ell) - \sum_{\substack{m=-p \\ n \neq 0}}^p a_{m,0} \gamma(k-m,\ell) - \sum_{m=-p}^p \sum_{n=1}^q a_{m,n} \gamma(k-m,\ell-n) = \beta^2 \delta_{k,0} \delta_{\ell,0} \quad (8)$$

where $\delta_{k,0} \cong 1$ when $k = 0$ and $\delta_{\ell,0} \cong 1$ when $\ell = 0$, otherwise $\delta_{k,0} \cong \delta_{\ell,0} = 0$, so that $\beta \cong 0$ except at $k = \ell = 0$.

If $a_{0,0}$ is brought within the window and set equal to -1 , effectively subtracting the actual value $u_{i,j}$ from the predicted value $\hat{u}_{i,j}$, then

$$\sum_{m=-p}^p \sum_{n=0}^q a_{m,n} \delta(k-m,\ell-n) = -\beta^2 \delta_{k,0} \delta_{\ell,0} \quad (9)$$

where it is clear that β^2 is the error in prediction of $u_{i,j}$.

In matrix notation, Eq. (9) can be written as

$$\underline{R} \underline{a} = -\beta^2 \underline{1} \quad (10)$$

where \underline{a} and \underline{l} are column matrices of $(2p + 1)(q + 1)$ elements each, which is the number of elements within the window W plus one. \underline{a} is the AR sequence of coefficients. \underline{l} is a string of zeros except for the $(pq + p + 1)$ entry, which is unity, and represents $\delta_{k,0}\delta_{l,0}$ of Eq. (9). R is a block Toeplitz matrix of $[(2p + 1)(q + 1)]^2$ elements.

Equation (10) can be restated as

$$\underline{a} = -\beta^2 R^{-1} \underline{l} \quad (11)$$

Since $a_{0,0} = -1$

$$-1 = -\beta^2 [R^{-1}]_{(pq+p+1, pq+p+1)},$$

or

$$\beta^2 = 1/[pq+p+1, pq+p+1] \text{ element of } R^{-1}, \quad (12)$$

and

$$\underline{a} = -\beta^2 [(pq+p+1) \text{ column of } R^{-1}] \quad (13)$$

Since the column vector \underline{a} represents the least-mean-squares estimate of the AR coefficients, we have the samples to make an AR all-pole spectral estimation.

The algorithm to find the two-dimensional AR coefficients is straightforward except for some detailed bookkeeping to select the correct elements of the matrix R :

1. Obtain the covariance (autocorrelation) through the FFT.
2. Form the block Toeplitz matrix R from the $(2p+1)(q+1)$ elements of the window W on the autocovariance function. $\delta(0,0)$ is located in an analogous position to $u_{i,j}$ in Figure 2.
3. Invert the matrix R to obtain R^{-1} .

4. Select elements from R^{-1} which represent $-\beta^2$ and \underline{a} .
5. With $-\beta^2$ and \underline{a} , compute the power spectra estimation by the 2-D analog of the one-dimensional AR method (Ulrych, 1972).

$$S(k, \ell) = \frac{\beta^2 \sum_{m=-p}^p a_{m,0} \exp(-irmk)}{\sum_{m=-p}^p \sum_{n=0}^q a_{m,n} \exp(-ir[mk+n\ell])^2} \quad (14)$$

where $S(k, \ell)$ is the 2-D power spectrum, $i = \sqrt{-1}$, and $r = 2\pi/s$ where s is the number of samples in one period.

WAVE ANALYSIS BY SPECTRAL ESTIMATION

Background

A two-dimensional spectral estimation of SAR images of ocean waves shows the direction and wavelength of the waves. However, when waves are refracted, a range of directions is estimated if the image includes many wavelengths. A directional smearing in the spectral estimation prevents the assignment of a wave direction to a specific location. Since the amount of wave refraction reveals water depth, it is desirable to specify wave directions at specific locations. These specifications require spectral estimations of data sets truncated to a wavelength or less. As the main lobe of the FFT is inversely proportional to the size of the data sample, the lobe becomes large when data is severely truncated, and resolution is thereby degraded. Discrimination between two similar waves is also degraded because of the merging of FFT main lobes produced by each wave train.

Recent spectral estimation developments have concentrated on reducing the main lobe to improve resolution, and to reduce sidelobes. Historically, improved resolution has come with limitations:

spectral splitting, and frequency shifts. As noted above, limitations have been addressed and improvements made in the one-dimensional case (Marple, 1980). Spectral estimation by the SCM produces much narrower main lobes than the FFT, but shares in the above limitations.

Spectral Estimation of Wave Data

Spectral estimates of SAR ocean wave data from the 1975 Marineland Experiment (Shemdin, et al., 1978) and from the SEASAT JASIN Experiment (Allan and Guymer, 1980) were produced by both the FFT and the SCM. An example of Marineland imagery is shown in Figure 3. The spectral estimates are shown in Figures 4 and 5, where the wave number k is $2\pi/\lambda$ and λ is the ocean wavelength.

The vertical axis on the spectra in Figures 4 and 5 corresponds to the range dimension on the radar image while the horizontal axis is in the direction of the SAR platform motion. The angles of the frequency components with respect to the origin (at the center) indicate, with 180° ambiguity, the direction of ocean wave propagation.

In the 1975 Marineland Experiment, ocean waves were imaged with a SAR X-band (3 cm radar wavelength) aircraft system. A pitch and roll buoy operating at the time of data collection indicated a wave train identified as a swell (8 second period or 80 m wavelength, $k = 0.08$) was traveling in the approximate direction of 270° with respect to true north. The significant wave height ($H_{1/3}$) was 1.5 - 1.8 m. A complete comparison between the pitch and roll spectra and SAR derived spectra (utilizing FFT techniques) is given by McLeish, et al., (1980).

L-band (23.5 cm wavelength) SAR satellite data from SEASAT was collected during the JASIN Experiment (Allan and Guymer, 1980). A pitch and roll buoy was also operating during the JASIN SAR data collection (SEASAT Revolution 1049) and a wave train identified as swell (12.5 sec period or 244 m wavelength) was traveling in the approximate direction of 264° with respect to true north. The



Figure 3. Radar image from Marineland experiment (X-band, 3 cm).

FFT 10X10

SC SPECTRUM 10X10

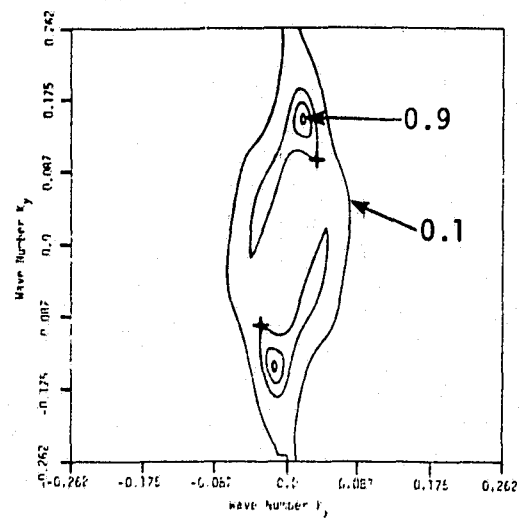
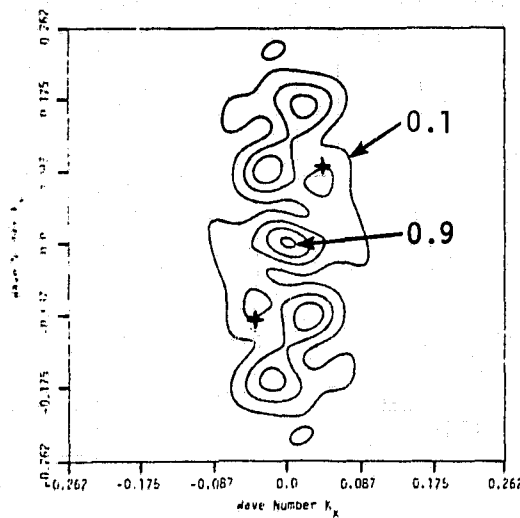


Figure 4. Two-dimensional spectral estimates of Marineland SAR data (X-band, 3 cm). (Approximately 1.5 period data length. Four equally spaced contour values from 0.1 to 0.9 of maximum values.)

FFT 50X50

SC SPECTRUM 50X50

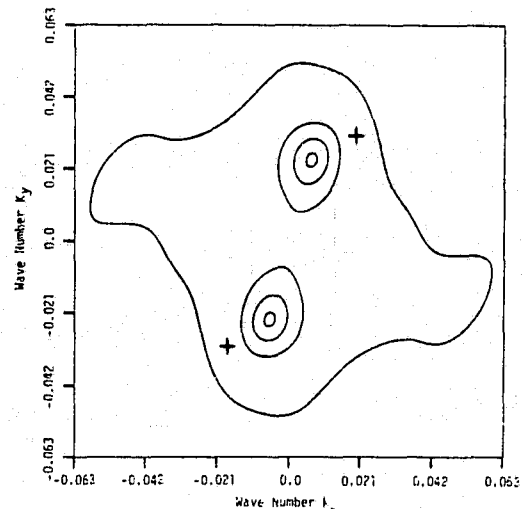
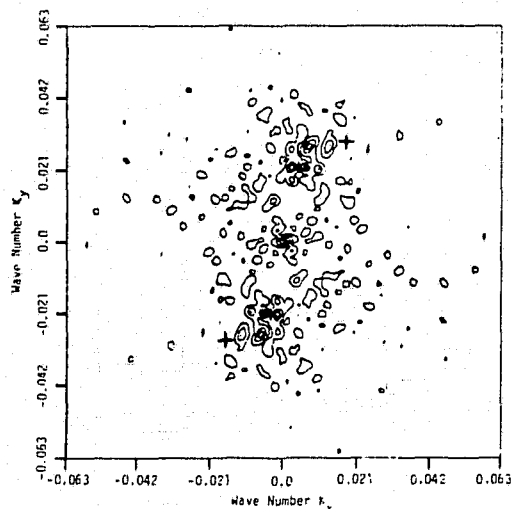


Figure 5. Two-dimensional spectral estimates of SEASAT SAR data (L-band, 23.5 cm). (Approximately 10 period data length. Contour values same as in Figure 4.)

significant wave height ($H_{1/3}$) for the JASIN case was approximately 5.0 meters. SEASAT SAR data have a resolution of approximately 25 meters while the aircraft data have a finer resolution of 3 meters.

Figures 4 and 5 indicate the SCM spectrum corresponds closely to the FFT spectrum and to data gathered at the ocean surface. Note that the ocean surface measurements of the gravity wave field as obtained from pitch and roll buoys are indicated on Figures 4 and 5 as crosses. Figure 4 illustrates the FFT and SCM spectrum for a short truncation (1.5 cycles) of ocean wave data. The SCM spectrum has definite peaks closely approximating the ocean surface measurements, and has no peak at the origin. The corresponding FFT has a peak at the origin, two lower peaks (one of which corresponds to ocean surface measurements), and has a more diffuse pattern.

In Figure 5, the spectral estimation of a comparatively large region of SAR ocean data shows different results with the two methods; the FFT appearing mottled. These data from SEASAT SAR represent 10 wave cycles. In the FFT, much energy goes into zero frequency, even when the bias has been removed from the data. A similar mottled appearance throughout the FFT frequency plane has been found in the approximately 50 FFT spectra of SAR ocean wave imagery which we have processed. It is necessary to look for clustering of small peaks to establish the dominant wave in the FFT. The pitch and roll data indicated only the major frequency component shown in the SCM spectrum.

Spectral Estimation of Synthetic Data

To evaluate the comparative attributes of SCM and FFT, synthetic data were also generated and spectrally estimated. Comparative spectral estimation of data characterized by short truncation, narrowly separated components, and various signal-to-noise ratios are shown in the power spectra of Figures 6 and 7. The synthetic data are sine waves generated with initial shifts of $\pi/4$.

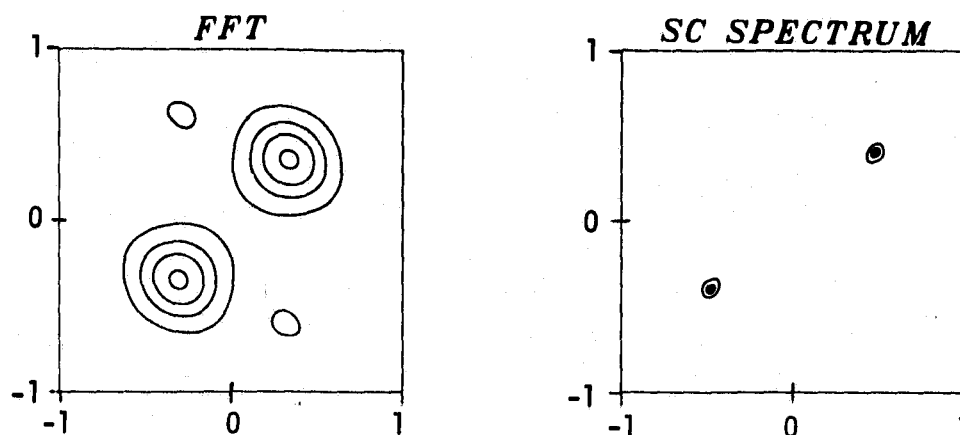


Figure 6. Spectral estimations of reference function with single frequency truncated to 2/3 of one cycle.
 $(\sin \frac{2\pi}{6}(i + j); i, j = 1-5. \text{ Initial phase } 60^\circ. \text{ Four equally spaced contour values from } 0.1 \text{ to } 0.9 \text{ of maximum value. SNR} = 10 \text{ dB. Frequency scale normalized.})$

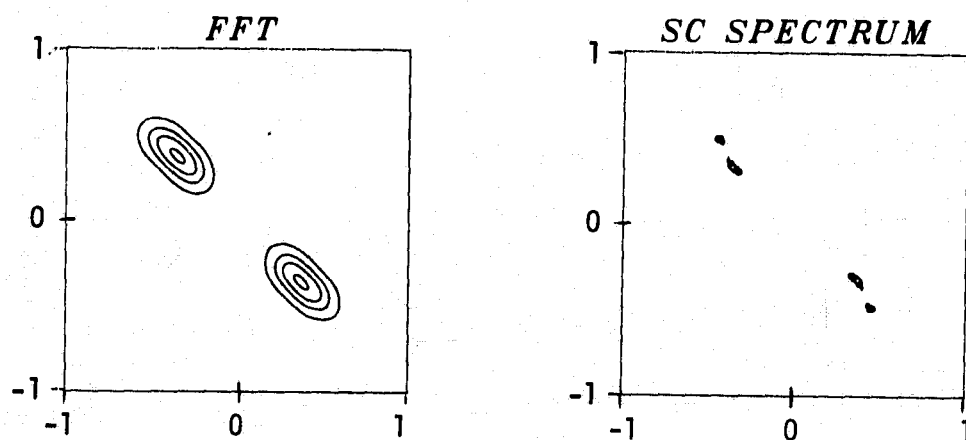


Figure 7. Spectral estimations of reference function with two closely spaced frequency components.
 $(\sin \frac{2\pi}{7}(i - j) + \sin \frac{2\pi}{5}(i - j); i, j = 1-11. \text{ Initial phases } 51^\circ \text{ and } 72^\circ. \text{ Contour intervals same as Figure 4. SNR} = 10 \text{ dB. Frequency scale normalized.})$

Figure 6 illustrates the comparative resolution of a single sine wave of less than 1 cycle with 10 dB SNR. Note the widths of the main lobes of the SCM are significantly smaller than those of the FFT.

In Figure 7, two closely spaced frequency components are separated in the SCM spectrum but merged in the FFT. One component is 1.43 cycles, the other 2 cycles long. The ratio of the frequencies is 1.4, which is closely approximated by the SCM spectrum.

One of the limitations of the new high resolution spectral estimation is occasional spectral splitting, where two peaks are formed for one frequency component. An example is shown in Figure 8. As spectral splitting has recently been eliminated in one-dimensional spectral estimation, probably a similar advance in two-dimensional spectral estimation can be expected.

Noise Effects

Experiments on severely truncated synthetic data show the main lobes of the SCM estimation significantly smaller than those of the FFT under additive noise conditions. Both fail to discriminate the synthesized frequency at and below a signal-to-noise ratio (SNR) of about -5 dB. The synthetic data were generated with sample intervals of 1/8 of a period. A total of 6 samples were used, giving a data length of 5/8 of a period. Initial phase was $\pi/4$. For these synthetic data, Figure 9 compares the -3 dB levels of main lobes of spectrum estimations for both the SCM and FFT at four SNR levels.

The FFT is sensitive to phase (Jackson, 1967; Marple, 1976), and the SCM was also found to be sensitive to phase, similar to the one-dimensional maximum entropy method (Chen and Stegen, 1974). In addition, noise individuality can cause moderate differences in the spectral estimation between two or more estimations at identical SNR levels, as is well known. The effects of phase, noise variations and AR orders, which are beyond the scope of this paper, remain

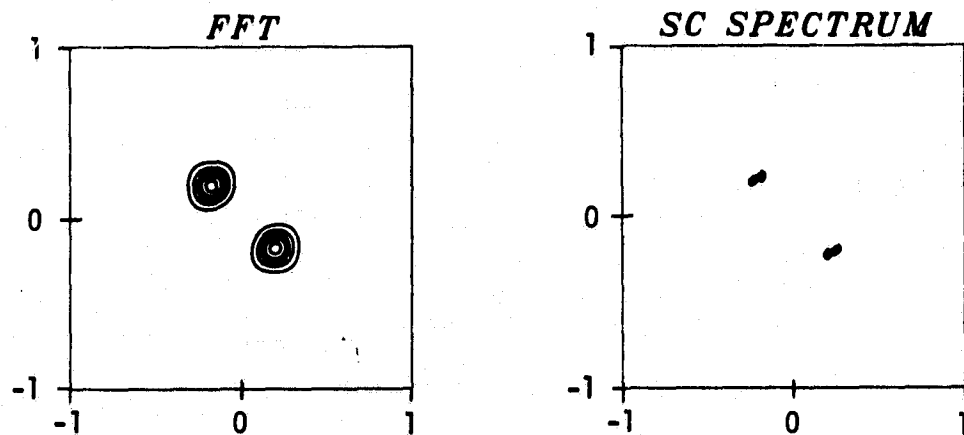


Figure 8. Example of spectral splitting in the SC reference function with a single frequency. $2/3$ of one cycle. $(\sin \frac{2\pi}{12}(i - j); i, j = 1-9$. Initial phase 30° . Five equally spaced contour values from 0.1 to 0.9 of maximum value. SNR = 10 dB. Frequency scale normalized.)

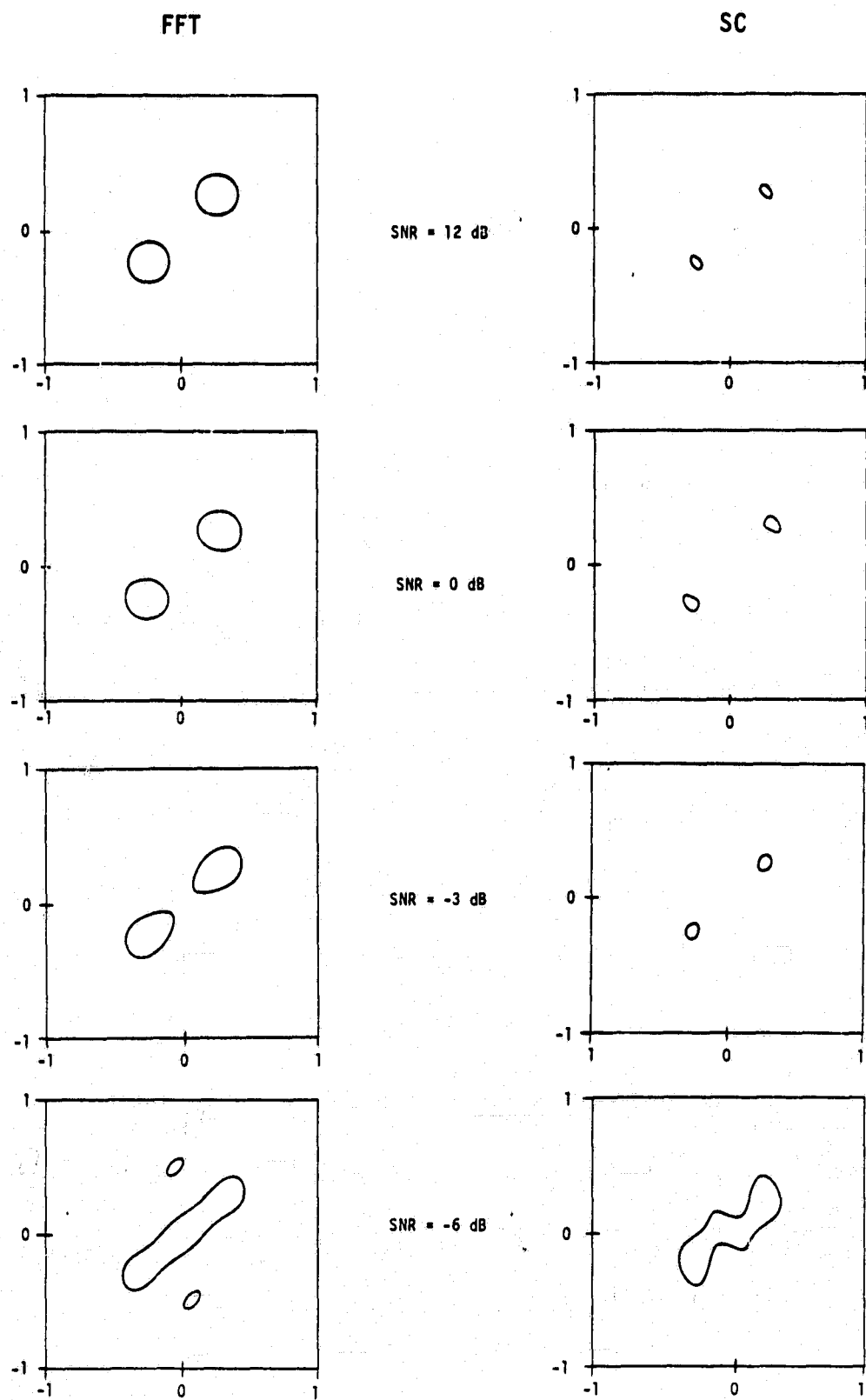


Figure 9. Spectral estimations of reference function truncated to 5/8 of one cycle with various signal-to-noise ratios. (Frequency scales normalized to unity.)

within a reasonable range and do not substantially alter the results illustrated in Figure 9. The AR orders used for the illustrated spectral estimations were $p = 4$ $q = z$ (see Figure 2).

SUMMARY

Examples of spectral estimation of SAR ocean imagery show that a new high resolution autoregression method can be used to obtain the wavelength and propagation direction of ocean gravity waves. The algorithm is termed the "semicausal method" (SCM). More pronounced spectral peaks, less mottling, and less energy at zero frequency were found with this method than with the commonly used FFT.

Synthetic data were generated to compare the SCM with the FFT. With a truncation of less than a single wavelength, the new method produces a main lobe significantly smaller than the width of the FFT main lobes. Also, two closely spaced sine wave components were discriminated where the FFT failed to discriminate.

Noise sensitivity was demonstrated by the comparative sizes of main lobes under different SNR conditions. For severe data truncations, the SCM main lobe continue to be smaller than that of the FFT for SNR conditions down to approximately -5 dB. Below -5 dB, both the FFT and the SCM fail to produce valid spectrums under conditons of severe data truncations.

High resolution frequency analysis using autoregression, moving-averages, maximum entropy and other concepts is a swiftly developing field in which many investigators are offering insights and improvements. The algorithm described and demonstrated here is representative of new techniques in this field. These techniques were developed to achieve high resolution and accuracy, and improvements in accuracy are being made. The SCM algorithm shows two limitations at this stage of development: spectral splitting and frequency shifts. These are well-known limitations in one-dimensional AR estimations and are being reduced or eliminated with new algorithms.

For short data truncations and for discriminating two similar wave trains, this algorithm can be an aid in specifying the wavelength and direction of ocean waves from airborne or satellite imagery.

ACKNOWLEDGEMENTS

This analysis was supported by Code 480 of the Office of Naval Research (ONR). The contract number was N00014-76-C-1048. The technical monitor for the ONR contract was Mr. Hans Dolezalek. The authors appreciate the assistance, comments, and suggestions of James Lyden of ERIM in preparing this paper.

REFERENCES

- Allan, T.D. and T.H. Guymer, Seasat and JASIN, Int. J. Remote Sensing, 1, pp. 261-267, 1980.
- Burg, J.P., Maximum entropy spectral analysis, paper presented at the 37th Annual International Meeting, Society of Exploration Geophysicists, Oklahoma City, Oklahoma, 1967.
- Burg, J.P., Maximum entropy spectral analysis, Ph.D Thesis, Stanford University, Xerox Microfilms No. 75-25-499, Ann Arbor, MI, 1975.
- Chen, W.Y. and G.R. Stegen, Experiments with maximum entropy power spectra of sinusoids, J. Geophys. Res., 79, pp. 3019-3022, 1974.
- Jackson, P.L., Truncations and phase relationships of sinusoids, J. Geophys. Res., 72, pp. 1400-1403, 1967.
- Jain, A.K., Advances in mathematical models for image processing, Proc. of the IEEE, 69, pp. 502-529, 1981.
- Jain, A.K. and S. Ranganath, Two-dimensional spectral estimation, Proc. of the RADC Spectrum Estimation Workshop, May 1978.
- Marple, L., Conventional Fourier, autoregressive, and special ARMA methods of spectrum analysis, Degree of Engineering Thesis, Stanford University, 1976.
- Marple, L., A new autoregressive spectrum analysis algorithm, IEEE Trans. on Acoustics, Speech, and Signal Processing, ASSP-28, pp. 441-454, 1980.
- McLeish, W., D. Ross, R.A. Shuchman, P.G. Teleki, S.V. Hsiao, O.H. Shemdin, and W.E. Brown, Synthetic aperture radar imaging of ocean waves: comparison with wave measurements, J. Geophys. Res., 85, pp. 5003-5011, 1980.
- Parzen, E., Statistical spectral analysis (single channel case) in 1968, Department of Statistics, Technical Report No. 11, Stanford University, Stanford, California, 1968.
- Roucos, S.E. and D.G. Childers, A two-dimensional maximum entropy spectral estimator, IEEE Trans. on Information Theory, IT-26, pp. 554-560, 1980.
- Shemdin, O.H., W.E. Brown, F.G. Staudhammer, R. Shuchman, R. Rawson, J. Zelenka, D.B. Ross, W. McLeish, and R.A. Berles, Comparison of in-situ and remotely sensed ocean waves off Marineland, Florida, Boundary-Layer Meteorology, 13, pp. 193-202, 1978.
- Shuchman, R.A., E.S. Kasischke, A. Klooster, and P.L. Jackson, SEASAT SAR coastal ocean wave analysis - a wave refraction and diffraction study, ERIM Final Report to NOAA, Report No. 138600-2-F, November 1979.
- Ulrych, T.J., Maximum entropy power spectrum of truncated sinusoids, J. Geophys. Res., 82, p. 1051, 1972.

APPENDIX B**AN ASSESSMENT OF JPL DIGITALLY PROCESSED SEASAT
SAR DATA FROM REV. 974**

APPENDIX B
AN ASSESSMENT OF JPL DIGITALLY PROCESSED SEASAT
SAR DATA FROM REV. 974

To more rigorously analyze the wave information available in Seasat SAR data, it is felt that the data must be digitally processed using fast Fourier transforms (FFTs). To this end, ERIM obtained two digitally processed scenes of Seasat SAR data from the Jet Propulsion Laboratory (JPL). The geographic coverage of these two tapes are presented in Figure B1. Selected areas from these tapes were fast Fourier transformed to extract gravity wave information from the SAR data.

A comparison of the estimates of dominant wavelength and direction from the FFTs to those obtained from an OFT analysis of JPL optically processed data produced dramatically different results. A previous ERIM study of Seasat-SAR data collected during the JASIN experiment showed that OFTs and FFTs produced essentially the same estimate of dominant wavelength and direction (Kasischke, 1980). The early results produced from an analysis of the JPL digital data of Rev. 974 were therefore somewhat disconcerting.

Upon a visual comparison of the JPL-digitally processed data and the JPL-optically processed data, it was noticed that the quality of the digitally processed data was poorer than that of the optically processed data in that waves were more visible on the optically processed image. An example of the same area from Rev. 974 from both digitally and optically processed JPL imagery is presented in Figure B2. Note the ship in each picture provides a common frame of reference. The wave images are much more distinct in the optically processed image than in the digitally processed image.

Figure B3 shows a digital fast Fourier transform of an area using both ERIM Hybrid digital imagery and JPL digital imagery. (The position of these FFTs are from 10D in Figure 34.) Note that where

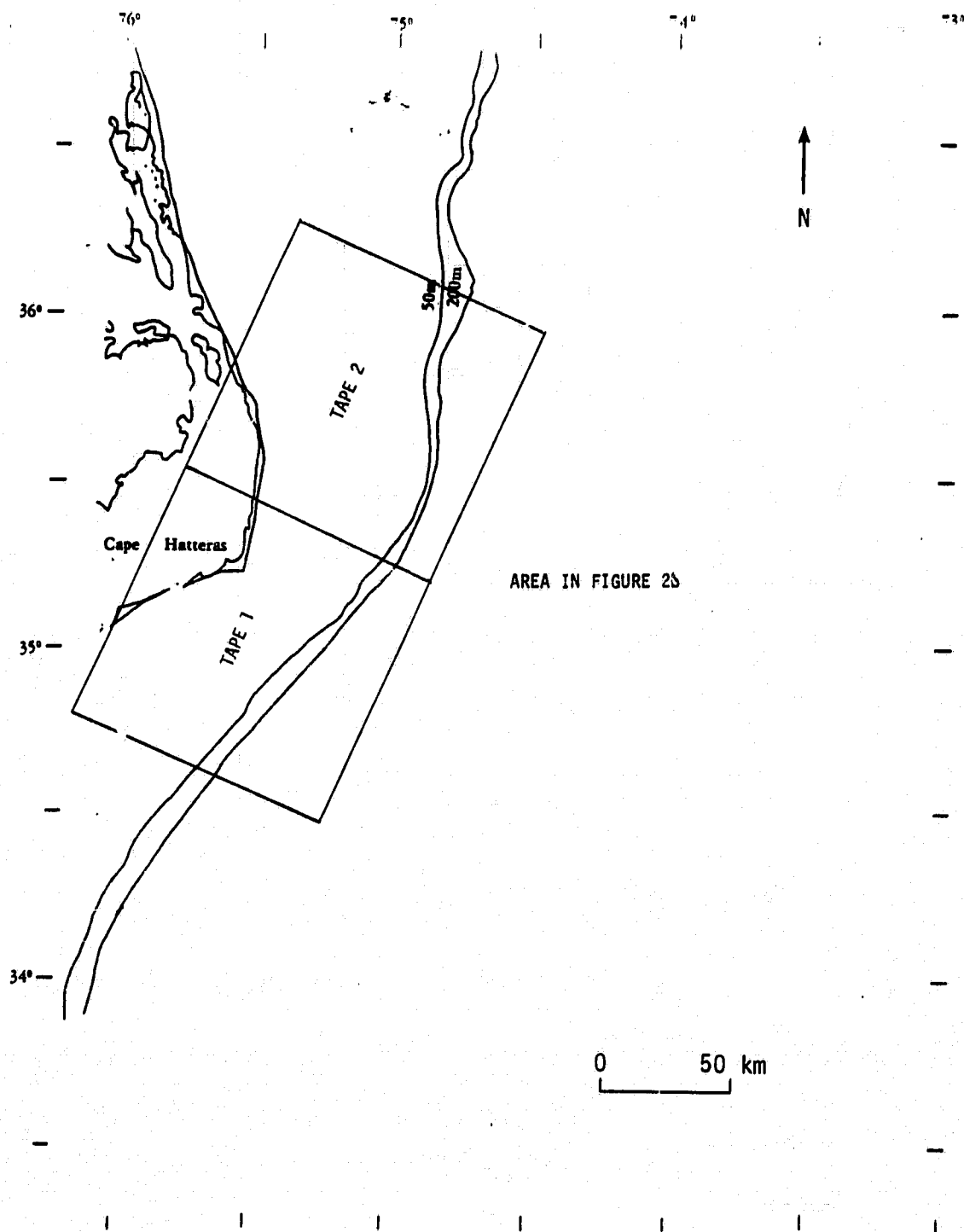


FIGURE B1. GEOGRAPHICAL LOCATION OF JPL-DIGITAL SEASAT SAR DATA, REV. 974.

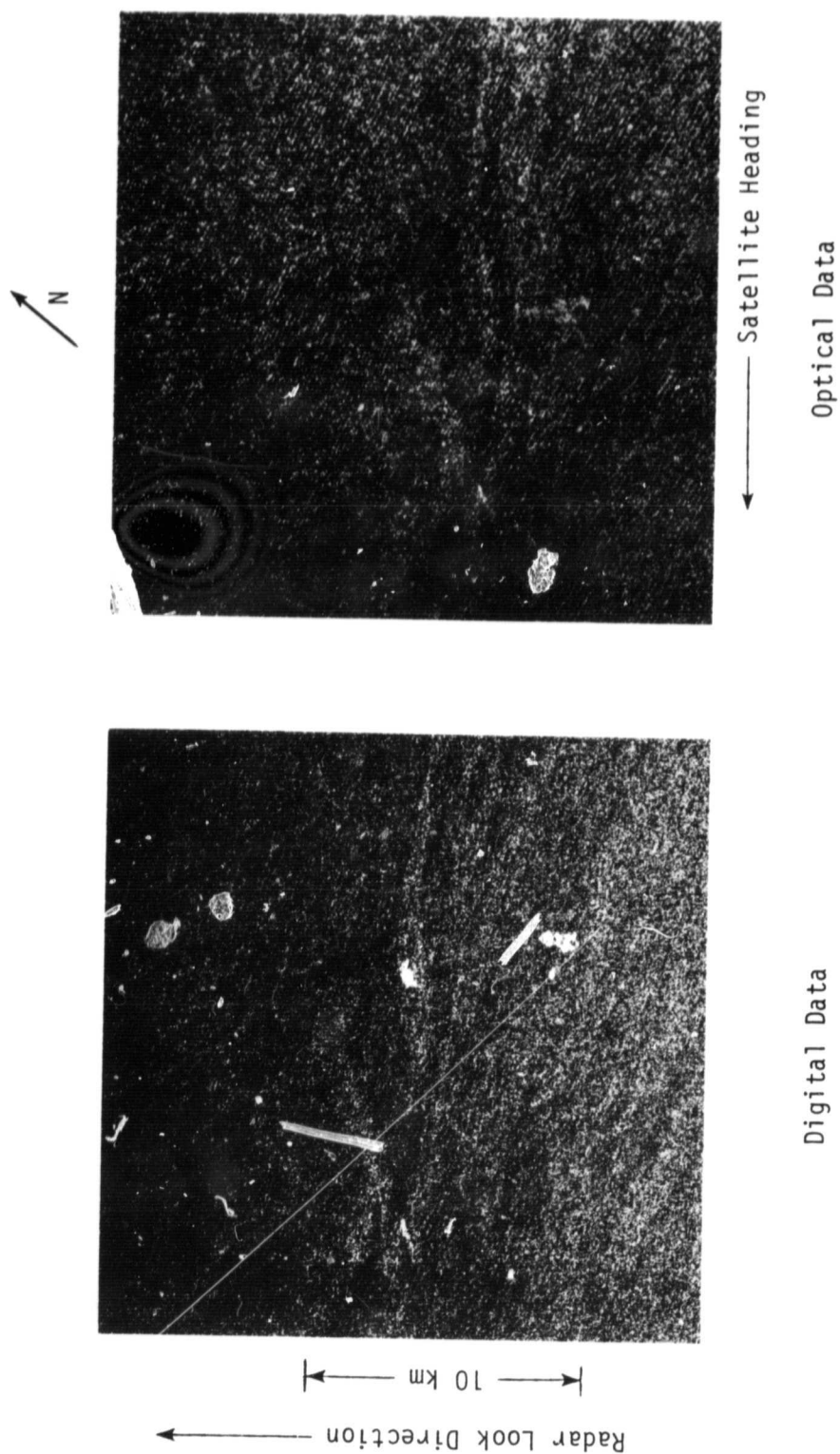
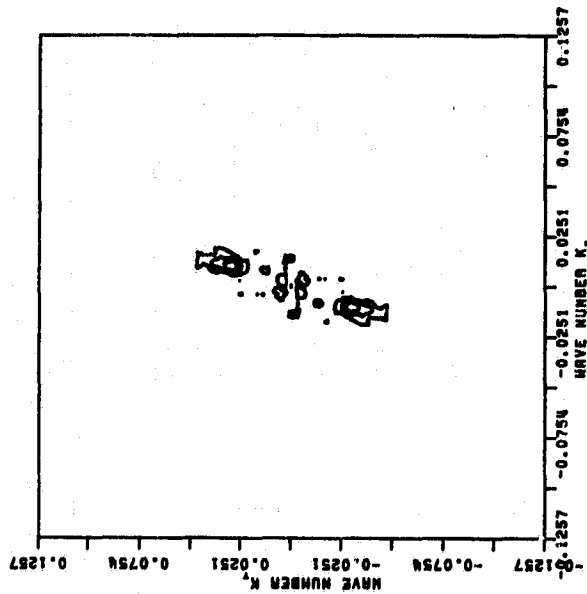
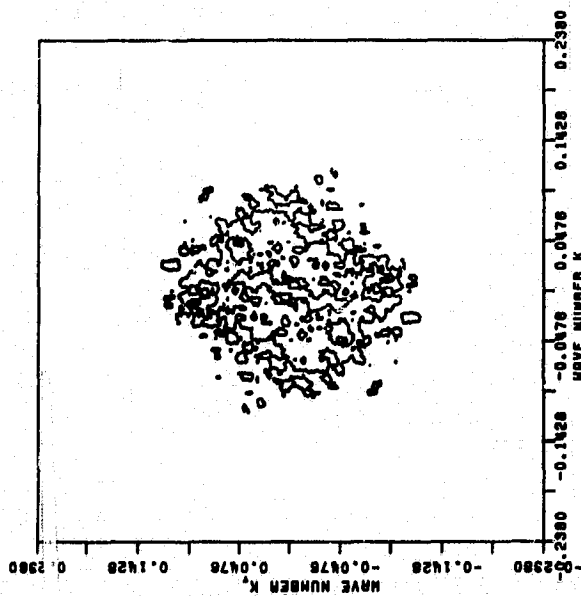


FIGURE B2. COMPARISON OF JPL DIGITALLY-GENERATED VERSUS OPTICALLY-GENERATED SEASAT SAR DATA, REV. 974.



ERIM HYBRID DIGITAL DATA



JPL DIGITAL DATA

FIGURE B3. COMPARISON OF FAST FOURIER TRANSFORMS
GENERATED FROM JPL-DIGITALLY PROCESSED
DATA AND ERIM-HYBRID DIGITAL DATA,
SEASAT REV. 974, POSITION 10D.

the spectra are clearly evident on the ERIM image there is no clear dominant spectra on the JPL image.

The following observations were made when comparing the optical and digital data:

1. The southernmost digital tape (Tape 1) had waves evident on imagery generated from the tape, but these waves were not as visible as those on the optical data and the imagery produced marginal data when fast Fourier transformed. The same areas of JPL optically generated imagery, when digitized and fast Fourier transformed, produced good estimates.
2. Imagery from the northernmost digital tape (Tape 2) had few visible waves and produced no spectral estimates when fast Fourier transformed. The optical imagery from the same area, when processed, produced fair to good spectral estimates.
3. The apparent degradation of the digitally processed imagery was worse in the northern region of Tape 1 than in the southern portion of Tape 1.
4. The small overlap area between the two tapes had the same quality of data.

The conclusion drawn from these observations was that when digitally processed the Rev. 974 data were not optimally focused, resulting in poor wave images. Examination of other JPL digital tapes of ocean areas shows that waves were just as clear on these data as on optical data, indicating the problems encountered with Rev. 974 data were probably specific to that pass.

APPENDIX C

**FURTHER SEMICAUSAL VERSUS FAST FOURIER
TRANSFORM COMPARISONS**

APPENDIX C
FURTHER SEMICAUSAL VERSUS FAST FOURIER
TRANSFORM COMPARISONS

In addition to the results presented in Section 3.2.3, other tests were performed on the semicausal model using a variety of aperture sizes. For this study, unsmoothed Seasat SAR data from Rev. 974 positions A, B, C, and D were used. Again, five separate aperture sizes (sampling every other pixel) were used to vary the number of wave cycles sampled (128 x 128 pixels, 64 x 64 pixels, 32 x 32 pixels, 16 x 16 pixels, and 8 x 8 pixels). Two-dimensional contour plots were generated from each method for each aperture size. These plots were manually interpreted for dominant wavelength and direction by locating the peak in the two-dimensional spectrum, as described in Section 3.1.2. The results of these comparisons are summarized in Tables C-1 through C-4 and the contour plots are presented in Figures C1 through C4. Also presented in Table C-1 are the results obtained from position A using smoothed data and the digital analysis techniques described in Section 3.1.2 (i.e., integrating the spectrum over angles).

From Table C-1, we can see that the manually interpreted results are close to those produced digitally. From Tables C-2 through C-4, we can see that the same trend is evident in all the data; the SC and FFT estimates of dominant wavelength and direction are close to one another and to the 256 x 256 FFT estimate through the first three aperture sizes. When an aperture size of 16 x 16 pixels or 8 x 8 pixels is used, neither technique produces spectra which match the 256 x 256 pixel FFT results.

TABLE C-1
COMPARISON OF SEMICAUSAL SPECTRAL ESTIMATES VERSUS
FAST FOURIER TRANSFORM SPECTRAL ESTIMATES
USING VARIABLE APERTURE SIZES*

Aperture Size	Wave Cycles/ Aperture	FFT (digital)		FFT (manual)		SC (digital)		SC (manual)	
		λ	θ	λ	θ	λ	θ	λ	θ
128 x 128 pixels	18.6	178 m	308°	179 m	307°	179 m	306°	177 m	307°
64 x 64 pixels	9.3	179 m	306°	178 m	307°	179 m	311°	178 m	312°
32 x 32 pixels	4.7	187 m	301°	183 m	301°	179 m	309°	168 m	310°
16 x 16 pixels	2.3	396 m	247°	366 m	298°	396 m	301°	413 m	302°
8 x 8 pixels	1.2	N/D**	N/D**	N/D**	N/D**	440 m	306°	450 m	308°

* Seasat Rev. 974, Position A; A 256 x 256 FFT of this area results in a dominant wavelength of 172 meters and a dominant wave direction of 307° (T). To generate the data in this study, every other pixel was sampled, resulting in ~3 samples per wave cycle.

** N/D: not discernible.

TABLE C-2
COMPARISON OF SEMICAUSAL SPECTRAL ESTIMATES VERSUS
FAST FOURIER TRANSFORM SPECTRAL ESTIMATES
USING VARIABLE APERTURE SIZES*

Aperture Size	Wave Cycles/ Aperture	FFT		SC	
		λ	θ	λ	θ
128 x 128 pixels	16.9	175 m	308°	171 m	307°
64 x 64 pixels	8.5	189 m	309°	176 m	307°
32 x 32 pixels	4.2	202 m	311°	162 m	305°
16 x 16 pixels	2.1	123 m	309°	134 m	311°
8 x 8 pixels	1.1	535 m	354°	535 m	355°

*Seasat Rev. 974, Position B; A 256 x 256 FFT of this area results in a dominant wavelength of 189 meters and a dominant wave direction of 308° (T). To generate the data in this study, every other pixel was sampled, resulting in ~4 samples per wave cycle.

TABLE C-3
COMPARISON OF SEMICAUSAL SPECTRAL ESTIMATES VERSUS
FAST FOURIER TRANSFORM SPECTRAL ESTIMATES
USING VARIABLE APERTURE SIZES*

Aperture Size	Wave Cycles/ Aperture	FFT		SC	
		λ	θ	λ	θ
64 x 64 pixels	16.3	194 m	313°	180 m	313°
32 x 32 pixels	8.2	168 m	309°	166 m	312°
16 x 16 pixels	4.1	188 m	310°	162 m	310°
8 x 8 pixels	2.0	N/D**	N/D**	256 m	310°
4 x 4 pixels	1.0	N/D**	N/D**	229 m	294°

*Seasat Rev. 974, Position C; A 256 x 256 FFT of this area results in a dominant wavelength of 196 meters and a dominant wave direction of 313° (T). To generate the data in this study, every other pixel was sampled, resulting in ~4 samples per wave cycle.

**N/D: Not discernible.

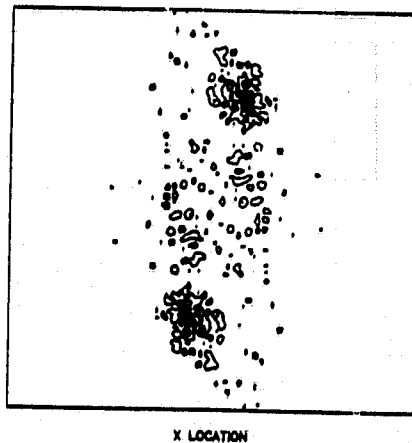
TABLE C-4
COMPARISON OF SEMICAUSAL SPECTRAL ESTIMATES VERSUS
FAST FOURIER TRANSFORM SPECTRAL ESTIMATES
USING VARIABLE APERTURE SIZES*

Aperture Size	Wave Cycles/ Aperture	FFT		SC	
		λ	θ	λ	θ
128 x 128 pixels	20.9	164 m	316°	154 m	319°
64 x 64 pixels	10.5	164 m	317°	156 m	319°
32 x 32 pixels	5.2	163 m	317°	165 m	319°
16 x 16 pixels	2.6	692 m	339°	N/D**	N/D**
8 x 8 pixels	1.3	233 m	355°	284°	346°

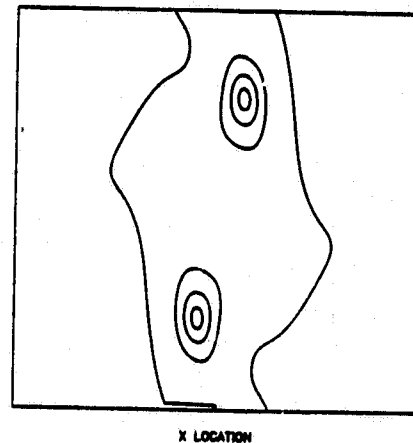
*Seasat Rev. 974, Position D; A 256 x 256 FFT of this area results in a dominant wavelength of 153 meters and a dominant wave direction of 318° (T). To generate the data in this study, every other pixel was sampled, resulting in ~3 samples per wave cycle.

**N/D: Not discernible.

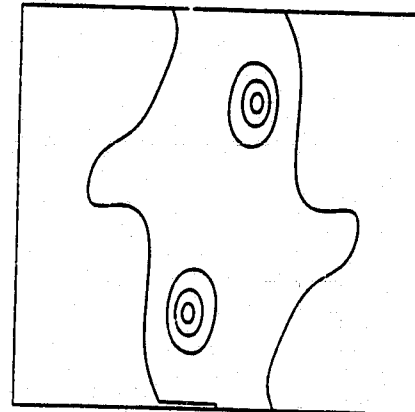
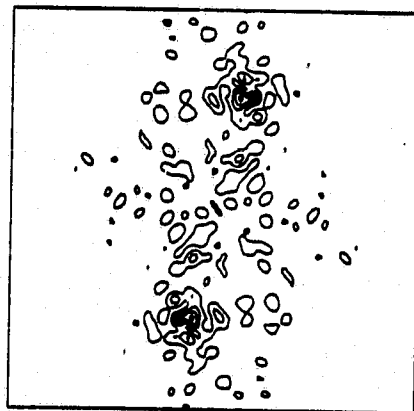
FFT



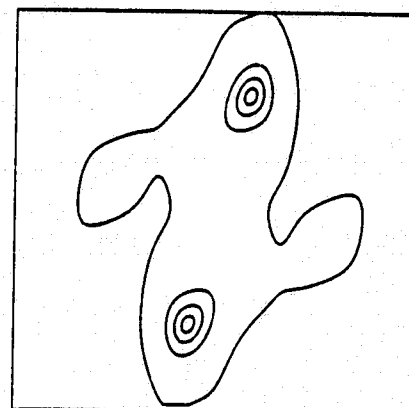
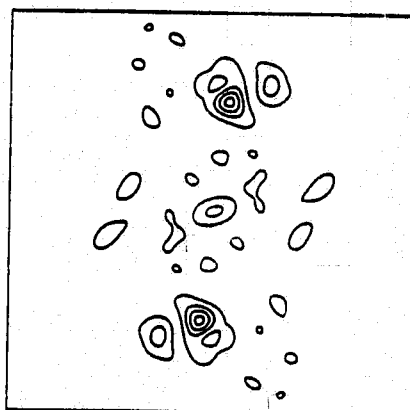
SC



18.6 Wave Cycles per Aperture
(128 x 128 pixels)



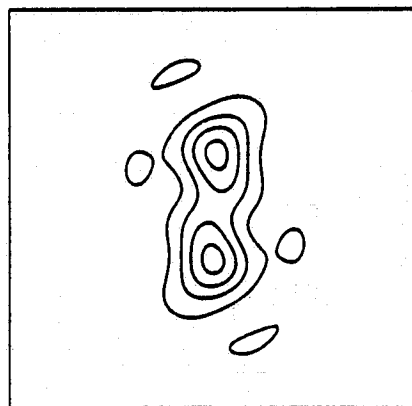
9.3 Wave Cycles per Aperture
(64 x 64 pixels)



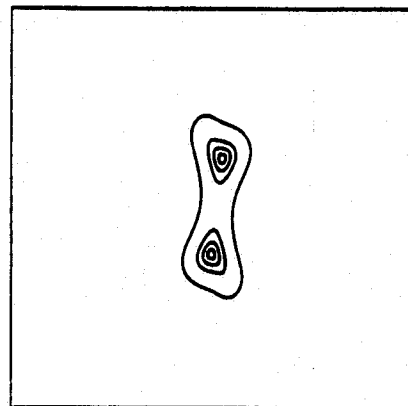
4.7 Wave Cycles per Aperture
(32 x 32 pixels)

FIGURE C1. FAST FOURIER TRANSFORM VERSUS SEMICAUSAL TWO-DIMENSIONAL SPECTRA USING A VARIABLE NUMBER OF WAVE CYCLES PER APERTURE. (Rev. 974, Area A)

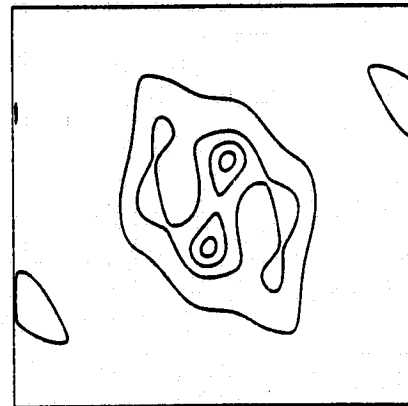
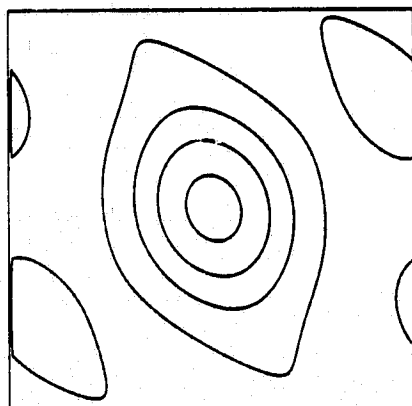
FFT



SC



2.3 Wave Cycles per Aperture
(16 x 16 pixels)

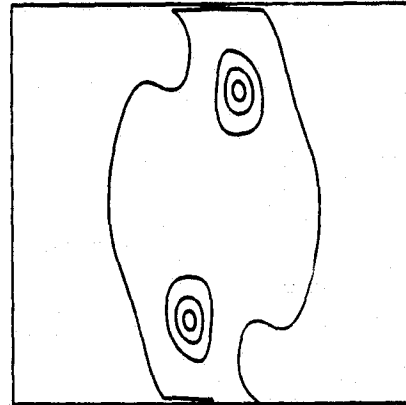
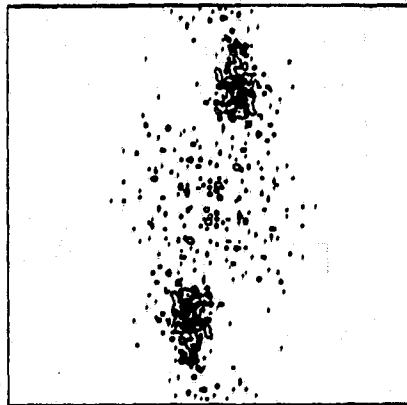


1.2 Wave Cycles per Aperture
(8 x 8 pixels)

FIGURE C1. FAST FOURIER TRANSFORM VERSUS SEMICAUSAL TWO-DIMENSIONAL SPECTRA USING A VARIABLE NUMBER OF WAVE CYCLES PER APERTURE. (Rev. 974, Area A)
(concluded)

FFT

SC



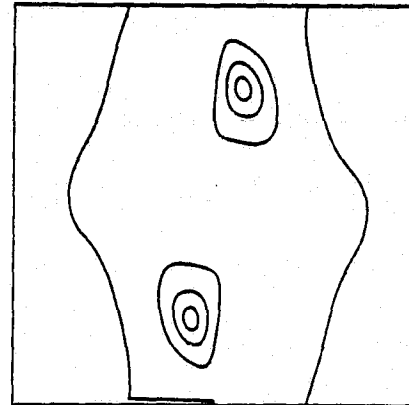
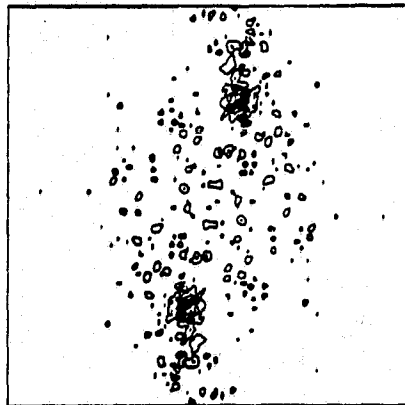
X LOCATION

X LOCATION

Y LOCATION

Y LOCATION

16.9 Wave Cycles per Aperture
(128 x 128 pixels)



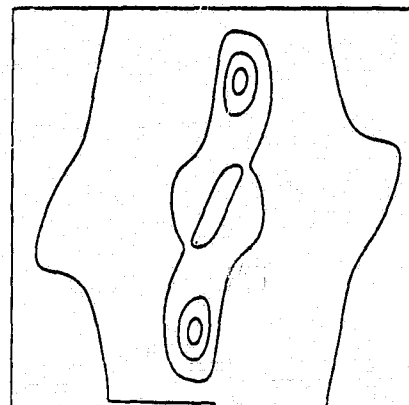
X LOCATION

X LOCATION

Y LOCATION

Y LOCATION

8.5 Wave Cycles per Aperture
(64 x 64 pixels)



X LOCATION

X LOCATION

Y LOCATION

Y LOCATION

4.2 Wave Cycles per Aperture
(32 x 32 pixels)

FIGURE C2. FAST FOURIER TRANSFORM VERSUS SEMICAUSAL TWO-DIMENSIONAL SPECTRA USING A VARIABLE NUMBER OF WAVE CYCLES PER APERTURE.
(Rev. 974, Area B)

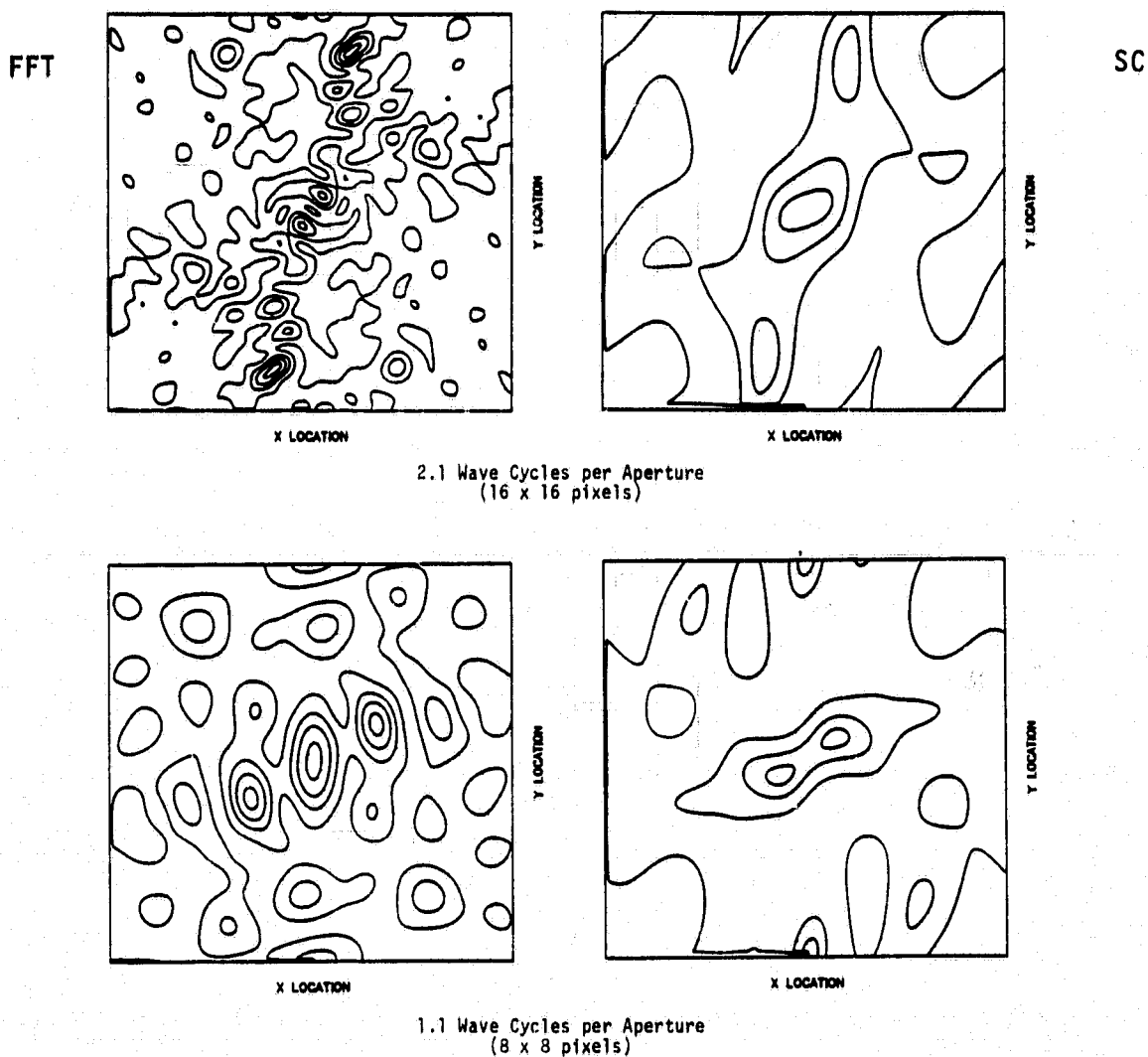
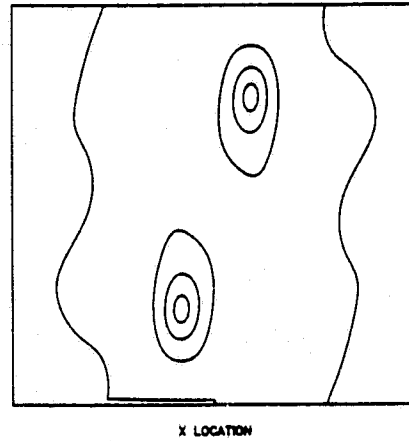
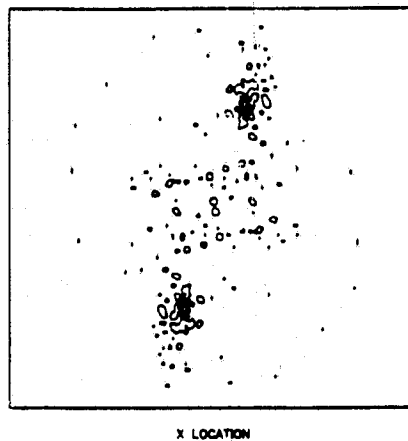


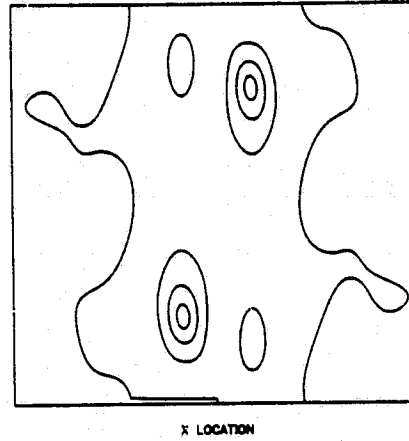
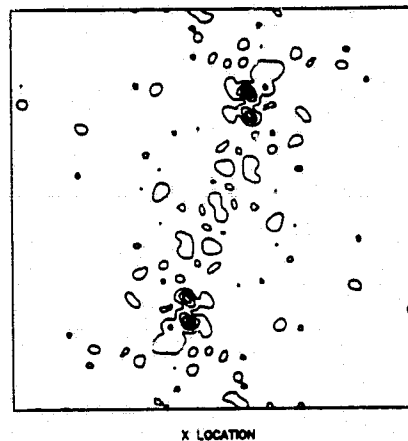
FIGURE C2. FAST FOURIER TRANSFORM VERSUS SEMICAUSAL TWO-DIMENSIONAL SPECTRA USING A VARIABLE NUMBER OF WAVE CYCLES PER APERTURE.
(Rev. 974, Area B)
(concluded)

FFT

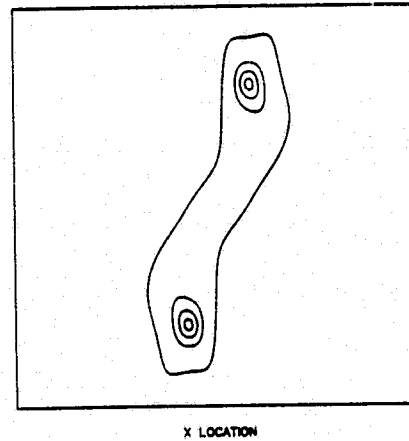
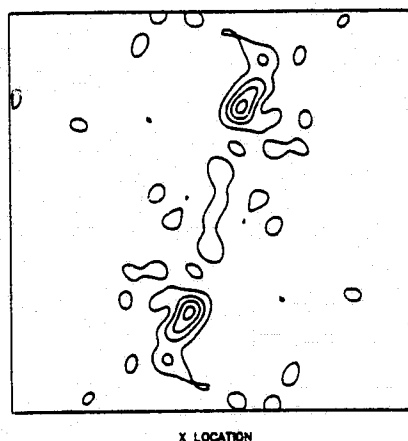
SC



16.3 Wave Cycles per Aperture
(128 x 128 pixels)



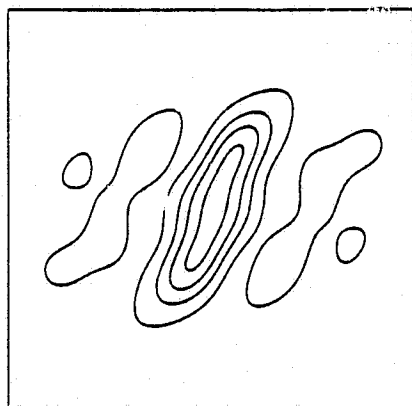
8.2 Wave Cycles per Aperture
(64 x 64 pixels)



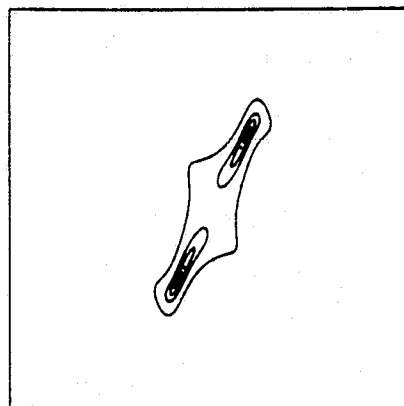
4.1 Wave Cycles per Aperture
(32 x 32 pixels)

FIGURE C3. FAST FOURIER TRANSFORM VERSUS SEMICAUSAL TWO-DIMENSIONAL SPECTRA USING A VARIABLE NUMBER OF WAVE CYCLES PER APERTURE. (Rev. 974, Area C)

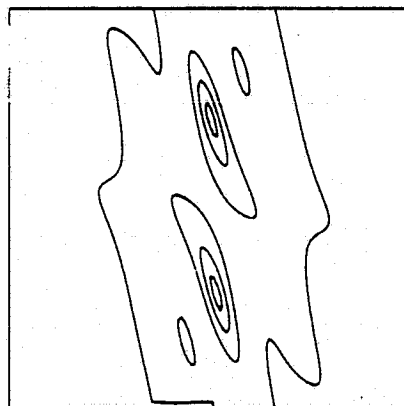
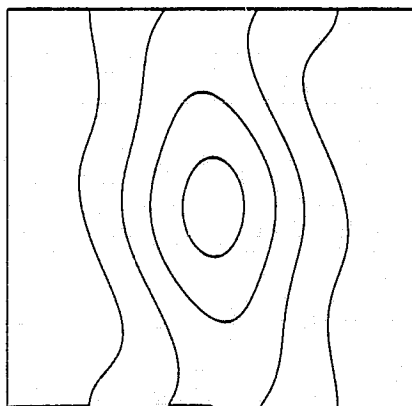
FFT



SC



2.0 Wave Cycles per Aperture
(16 x 16 pixels)

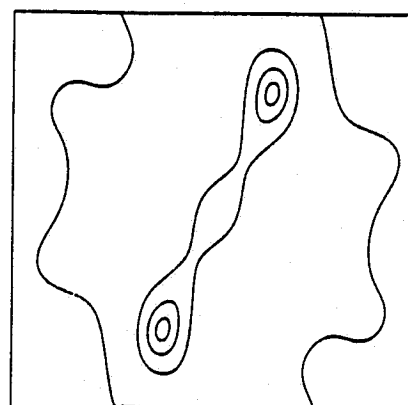
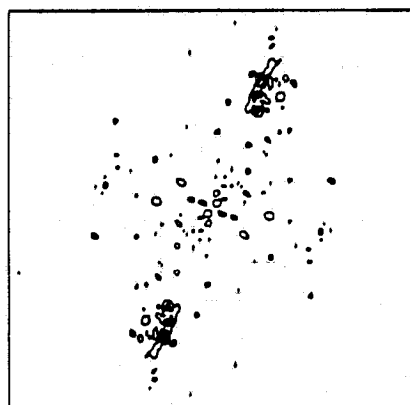


1.0 Wave Cycles per Aperture
(8 x 8 pixels)

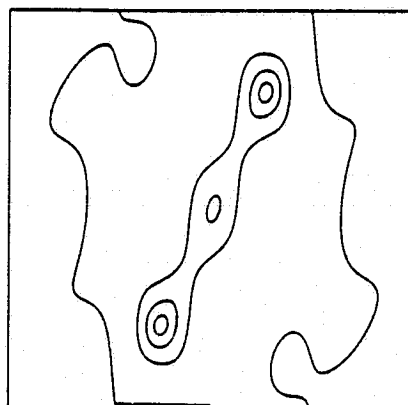
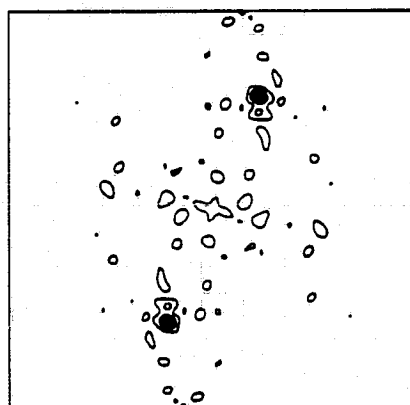
FIGURE C3. FAST FOURIER TRANSFORM VERSUS SEMICAUSAL TWO-DIMENSIONAL SPECTRA USING A VARIABLE NUMBER OF WAVE CYCLES PER APERTURE.
(Rev. 974, Area C)
(concluded)

FFT

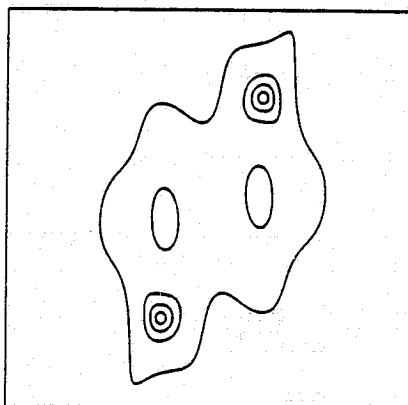
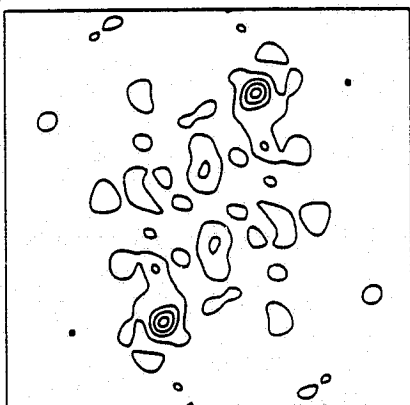
SC



20.9 Wave Cycles per Aperture
(128 x 128 pixels)



10.5 Wave Cycles per Aperture
(64 x 64 pixels)



5.2 Wave Cycles per Aperture
(32 x 32 pixels)

FIGURE C4. FAST FOURIER TRANSFORM VERSUS SEMICAUSAL TWO-DIMENSIONAL SPECTRA USING A VARIABLE NUMBER OF WAVE CYCLES PER APERTURE. (Rev. 974, Area D)

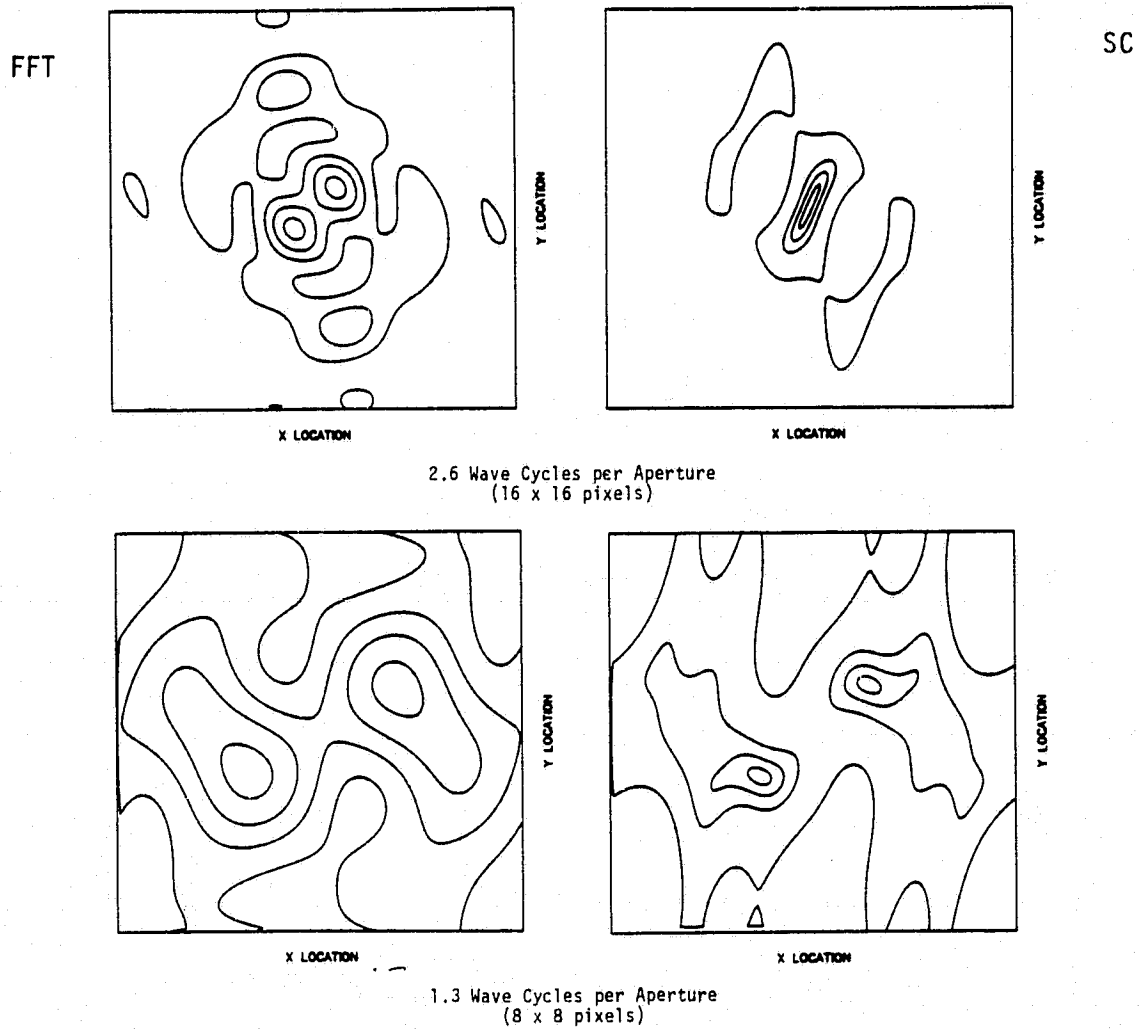


FIGURE C4. FAST FOURIER TRANSFORM VERSUS SEMICAUSAL TWO-DIMENSIONAL SPECTRA USING A VARIABLE NUMBER OF WAVE CYCLES PER APERTURE.
(Rev. 974, Area D)
(concluded)

APPENDIX D

PRECISION AND ACCURACY OF OPTICAL FOURIER TRANSFORMS

APPENDIX D

PRECISION AND ACCURACY OF OPTICAL FOURIER TRANSFORMS

Throughout this report, we have extensively used optical Fourier transforms (OFTs) to extract estimates of dominant wavelength and direction from SAR ocean wave data. We have used the estimates to monitor changes in wavelength and direction of a spatially evolving wave field. In order to assess whether these changes are significant, we must know the "level of uncertainty" associated with the measurement technique (i.e., the OFT).

To define this level of uncertainty of the OFT measurements, we must look at the accuracy of the measurements, the precision of the measurements, and the variability of the measurements. In determining the accuracy of a measurement, we usually compare the results obtained from the measuring device against a standard. In determining the accuracy of the OFTs, we could use standard oceanographic techniques (such as pitch and roll buoys, wave rider buoys, etc.) as our standard, but the accuracy of these techniques is really not that high. It may be, in fact, that OFTs are more accurate (in the absolute sense) than the present day standard oceanographic techniques. Fortunately, for the present study, we are interested in relative measurements, not absolute; therefore, we can ignore any systematic error in the OFT method in terms of absolute accuracy (if one does indeed exist). In the remainder of this discussion, we will address the questions of precision and variability in the OFT technique, and in the end, come up with a level of uncertainty for the OFT estimates of wavelength and direction.

Precision of the OFT Measurements

The orientation of the peak of the optical Fourier transform spectra was measured by the human interpreter with a precision of $\pm 0.25^\circ$ using a protractor measurement on a 70 mm polaroid print.

The distance between the peaks of the symmetrical spectra were measured with a precision of ± 0.25 mm. This distance (r) was then put into the formula (after Shuchman, et al., 1979):

$$\lambda = \frac{2K}{kr} \quad (D-1)$$

where λ = the dominant ocean wavelength,
 K = ocean wave image scale factor, and
 k = spectrum scale factor.

While there might be some measurement uncertainties in K or k that would affect the precision of λ , these uncertainties will be constant throughout the experiment and should be considered a bias in the entire data set rather than a source of error in an individual calculation.

In using Eq. (D-1) to calculate wavelength, the precision of the wavelength calculation depends on the value of r . The smallest r measured in the Rev. 974 data set was 14.0 mm. The wavelength associated with this r is 245 meters, and introducing the ± 0.25 mm uncertainty, this wavelength ranges from 240.7 m to 249.5 or ± 4.5 m, which equals ± 1.8 percent.

The precision of the OFTs are therefore $\pm 0.25^\circ$ in direction and ± 1.8 percent in wavelength for this set of measurements.

Variability in the OFT Measurements

For the purposes of this study, we will define variability in terms of the 95 percent confidence interval of the population mean (after Shaeffer, et al., 1979) calculated as $2\sigma_x$, where σ_x (the standard error of the estimate) is:

$$\sigma_x = \frac{s_x}{n} \quad (D-2)$$

where s_x is the standard deviation of the mean, and
 n is the number of samples in the experiment.

The sources of variation considered for this experiment were:

1. Natural variation within the wave field being imaged by the SAR,
2. Variation in the generation of the OFT, and
3. Variation in the measurement of the dominant wavelength and direction from the OFT.

The wave field being imaged by the SAR has its own variation, so that if the same wave field is measured at different geographic locations, a naturally occurring variation will exist. There is often variation in OFTs obtained from the same nominal position. Finally, if the same OFT is measured more than once, there will be a variability associated with the interpreter making the separate measurements. Each one of these sources of variation was estimated.

A deep water area from Rev. 1049 was used to determine the variability in the wave field. Nine independent OFTs were generated from nine different areas. The average direction for these nine areas was 40.8° with a 95 percent confidence interval of 1.1° . The average r value calculated for these nine positions was 16.3 mm with a 95 percent confidence interval of 0.18 mm. Using Eq. (D-1) results in a wavelength of 210.4 m with a 95 percent confidence interval of 2.4 m or 1.1 percent.

Next, a fixed location in the SAR ocean image was resampled five times to determine the variability in this stage of the OFT technique. An area of Rev. 974 was selected for this study. The average direction calculated was 61.0° with a 95 percent confidence interval of 0.3° . This average r value was 20.5 mm with a 95 percent confidence interval of 0.32 mm, which results in a wavelength of 167.3 m with a 95 percent confidence interval of 2.7 m or 1.6 percent.

Finally, four separate OFTs were selected from the Rev. 974 data set and each was remeasured five times. The results from this study are summarized in Table D-1. From Table D-1, we can see the average 95 percent confidence interval was 0.9° for direction and 2.2 meters or 1.2 percent in wavelength.

In summary, the variability in the measurement of the wavelength was approximately the same for independent OFTs from a uniform wave field, for overlapping OFTs from the same position within the image, and for repeated measurements on the same OFT. Further, the variability is approximately equal to the precision of the measurement (these values are summarized in Table D-2). Therefore, a change in the measured wavelength within a given SAR image may be considered to be significant if it is greater than this value (i.e., approximately 1.8 percent of the wavelength).

For wave direction, the greatest variation in the measurements is approximately 1° . The greatest variation in the data appears to come from the variation within a given wave field. Thus, for the measurement techniques used in this study, a change in the wave direction on the order of 1° within a given image may be considered significant.

TABLE D-1
SUMMARY OF MEASUREMENTS FOR OFT VARIABILITY STUDY

Area	Average	r			Direction	
		95 Percent Confidence Interval			95 Percent Confidence Interval	
		r	Wavelength	Percent	Average	
A	18.3 mm	0.40 mm	4.2 m	2.2	106.0°	1.2°
B	18.3 mm	0.24 mm	2.5 m	1.3	103.8°	1.0°
C	21.3 mm	0.24 mm	1.9 m	1.2	116.1°	0.6°
D	20.5 mm	0 mm	0 m	0	122.9°	0.8°
		Average	2.2 m	1.2		0.9°

TABLE D-2
SUMMARY OF PRECISION AND VARIABILITY DATA FOR OPTICAL
FOURIER TRANSFORM MEASUREMENT OF WAVELENGTH
AND DIRECTION

<u>Source</u>	95 Percent Confidence Intervals	
	<u>Wavelength</u>	<u>Direction</u>
Precision of Measurement	1.8 percent	0.25°
Natural variation in wave data	1.1 percent	1.1°
Variation in taking multiple OFTs of same position	1.6 percent	0.3°
Variation in measurement of wavelength and direction from the same OFT	1.2 percent	0.9°

APPENDIX E

WAVE/CURRENT INTERACTION ANALYTICAL DEVELOPMENT

APPENDIX E WAVE/CURRENT INTERACTION ANALYTICAL DEVELOPMENT

For the first-order approximation of the propagation of waves in water of uniform depth (d) with a constant atmospheric pressure, the dispersion relation is:

$$\sigma^2(k) = k(g + \gamma k^2) \tanh kd \quad (E-1)$$

where $k = |\vec{k}|$, \vec{k} is the vector wave number (k_1, k_2), g is the gravitational acceleration, γ is the ratio of surface tension to water density, and σ is the intrinsic frequency. In deep water, the water depth is much larger than the wavelength, and kd is much smaller than unity. The phase velocity $c = (\sigma/k)$ then has a minimum when $k = (g/\gamma)^{1/2}$ or when the wavelength $\lambda = 2\pi(\gamma/g)^{1/2}$. For waves shorter than this wavelength, the restoring force is dominated by surface tension, and for waves larger than this, the capillary force is no longer predominant. Gravity waves are those whose restoring force is mainly due to gravity and have wavelengths greater than $2\pi(\gamma/g)^{1/2}$. For deep water gravity waves the dispersion relation in Eq. (E-1) is therefore reduced to:

$$\sigma^2 = gk \quad (E-2)$$

For longer period waves such as tides and Rossby waves, the assumption of $kd \gg 1$ may be no longer valid and the simple dispersion relation in Eq. (E-2) will result in significant error. However, under field conditions, there are no good indications that Eq. (E-2) is not an adequate approximation when the wavelength is less than approximately half the water depth (Phillips, 1981).

When a wavetrain enters shoaling water, refraction occurs as a result of water depth and possibly current variations. In the case where these variations are slow, the dispersion relation in Eq. (E-1) for gravity waves becomes

$$\sigma^2 = gk \tanh kd \quad (E-3)$$

where $d = d(x)$ is the local water depth.

If a wave is moving in a medium with a velocity $\vec{u}(x, t)$ relative to an observation point, the observed or apparent frequency of waves, n , measured at a fixed point, should include a Doppler shift to the intrinsic frequency:

$$n = \sigma(k) + \vec{k} \cdot \vec{u} \quad (E-4)$$

The velocity \vec{u} is actually the variation or shear of the current; therefore, when a wave is moving along or across a current with slowly changing current velocities, \vec{u} should be the vector sum of the two neighboring velocities. It is convenient to assume that a current can be divided into many small portions or strips with slowly varying velocities, which are steady and uniform in each portion or strip.

For waves riding on or across a current with slowly changing velocities as shown in Figure 40, the angles α_1 are the incidence angles or refraction angles. When the waves are incident upon the current which has an average velocity range of u_0 to u_1 , the shear per unit distance is $u_0 - u_1$, and the conservation of frequency in Eq. (E-4) becomes:

$$\sigma_0 = \sigma_1 + k_1(u_1 - u_0) \cos \alpha_1 \quad (E-5)$$

The conservation of wave numbers is:

$$k_0 \cos \alpha_0 = k_1 \cos \alpha_1 = \text{const} \quad (E-6)$$

Eq. (E-5) gives:

$$\cos \alpha_1 = \frac{\sigma_0 - \sigma_1}{k_1(u_1 - u_0)} = K_1/k_1 \quad (E-7)$$

Substituting k_1 from Eq. (E-6) into (E-7) gives:

$$\cos \alpha_0 = \frac{\sigma_0 - \sigma_1}{k_0(u_1 - u_0)} = K_1/k_0 \quad (\text{E-8})$$

where $K_1 = (\sigma_0 - \sigma_1)/(u_1 - u_0)$, and for deep water gravity waves the intrinsic frequency $\sigma^2 = gk$. Theoretically, the incidence and the refraction angles can be calculated from Eqs. (E-7) and (E-8) when both the shear of the current between two current strips and the wave numbers in these two current strips are known.

Equations (E-5) and (E-6) have been reduced to another useful presentation (Phillips, 1981):

$$\cos \alpha_1 = \frac{gk_0 \cos \alpha_0}{[\sigma_0 - k_0(u_1 - u_0) \cos \alpha_0]^2} \quad (\text{E-9})$$

or

$$\cos \alpha_1 = \frac{\cos \alpha_0}{\left(1 - \frac{u_1 - u_0}{c_0} \cos \alpha_0\right)^2} \quad (\text{E-10})$$

where $c_0 = (g/k_0)^{1/2}$ is the initial phase velocity of the wavetrain and the term $(u_1 - u_0)/c_0 \cos \alpha_0$ is usually much less than unity. This term can be positive or negative depending on the signs of $(u_1 - u_0)$ and $\cos \alpha_0$. If the incidence angle α_0 is less than 90° , the wave ray will turn away from its normal when it is traveling across a slowly increasing current; otherwise, if the wave is traveling across a slowly decreasing current, the wave ray will shift towards its normal. Similarly, if α_0 is greater than 90° , the wave ray will turn toward or away from its normal depending on an increasing or a decreasing current. These concepts are illustrated in Figure 40. In order to have very small or no refraction of the wave ray, the incidence angle α_0 should be both/either close to 90° and/or the ratio of shear to the initial

phase velocity of the wavetrain should be very small. With a particular incidence angle, when the refraction angle becomes zero, the wave no longer penetrates further into the current, but is reflected by the current. The condition of total reflection of the wave ray is obtained by setting $\alpha_1 = 0$ in Eq. (E-10) or $(u_1 - u_0)/c_0 = [1 - (\cos \alpha_0)^{1/2}]/\cos \alpha_0$. For small incidence angles, even a small shear will result in reflection.